Modelling and Measurement of Sealing Effectiveness and Heat Transfer in a Rotor-Stator System with Ingress

Pountney, Oliver

Award date:
2012

Awarding institution:
University of Bath

Modelling and measurement of sealing effectiveness and heat transfer in a rotor-stator system with ingress

Oliver James Pountney

A thesis submitted for the degree of Doctor of Philosophy

University of Bath

Department of Mechanical Engineering

August 2012

Abstract

This thesis investigates, both theoretically and experimentally, the phenomenon of ingress through gas turbine rim seals. The work presented focuses on modelling and measuring the required sealing flow levels to purge the wheelspace against combined ingress and the effect of externally-induced ingress on the surface temperature and heat transfer to the rotor.

Combined ingress is driven by a pressure difference between the mainstream annulus and wheelspace cavity resulting from the combination of the asymmetric external pressure profile in the annulus and the rotation of fluid in the rotor-stator wheelspace cavity. Ingress can be prevented by pressurising the wheelspace through the supply of sealant flow. The Owen (2011b) combined ingress orifice model was solved to predict the required levels of sealant flow to prevent ingress into the wheelspace. The model was validated using pre-published data and data collected experimentally over the course of this research.

Gas concentration measurements were made on the *stator* of the Bath single-stage gas turbine test rig to determine the variation of sealing effectiveness with sealant flow rate for an axial clearance seal geometry at design and off-design operational conditions. The measured variation of the required sealant flow rate with the ratio of the external and rotational Reynolds numbers, Re_W / Re_ϕ, was consistent with the findings of other workers: at low values of Re_W / Re_ϕ, ingress levels were influenced by the combined effects of the disc rotation and the annulus pressure profile and were therefore considered to fall into the combined ingress region; the influence of rotation diminished as Re_W / Re_ϕ increased and the ingress levels were dominated by the annulus pressure field (externally-induced ingress). The orifice model was in good agreement with the experimental measurements and the pre-published experimental data.

Thermochromic liquid crystal (TLC) was used to determine effect of ingress on the heat transfer coefficient, h, and adiabatic wall temperature, T_{ad}, on the *rotor* of the Bath gas turbine rig. Concurrent gas concentration measurements were made on the stator to compare the effects of ingress on the two discs. Data was collected at the design condition, where $Re_W / Re_\phi = 0.538$ and at an overspeed off-design condition, where $Re_W / Re_\phi = 0.326$.

The comparison between a newly defined adiabatic effectiveness, ε_{ad}, on the rotor and the concentration effectiveness, ε_c, on the stator, showed that the rotor was protected against the

effects of ingress relative to the stator. The sealing air, which is drawn into the rotor boundary layer from the source region, thermally buffers the rotor against the ingested fluid in the core. A thermal buffer ratio, η, was defined as the ratio of the minimum sealant flow required to purge the stator against ingress to the minimum sealant flow required to purge the rotor against ingress. The thermal buffer is dependent upon the flow structure in the wheelspace, which itself is governed the turbulent flow parameter, λ_T. A hypothesis relating η to λ_T was developed and shown to be in good agreement with the experimental data.

The local Nusselt numbers, Nu_r, on the rotor were shown to be fairly constant with radius and increased as λ_T was increased. The latter finding can be explained by the flow structure in the wheelspace: as λ_T is raised, the swirl in the fluid core reduces, which results in an increase in the moment coefficient and Nu_r on the rotor.

Difficulties in measuring T_{ad} during the experiments suggested a new technique from which to solve for h and T_{ad} using TLC surface temperature measurements. The solution Fourier's equation for a step-change in the temperature of a fluid flowing over a solid of semi-infinite thickness (the 'semi-infinite solution') is limited to relatively low Fourier numbers if T_{ad} is to be calculated accurately. A two-layer composite substrate made from, for example, polycarbonate and Rohacell, could be used to achieve accurate estimates of h and T_{ad} over a larger range of Biot numbers than for a single material substrate. TLC could be used to measure the surface temperature history of the composite substrate during an experiment; this would allow h and T_{ad} to be solved from the numerical solution of Fourier's equation or from a combination of the semi-infinite and steady-state solutions.

The work presented in this thesis has uncovered some interesting findings in areas where research was limited. The measurements of the minimum sealant flow required to purge the wheelspace at off-design operation for a rotor-stator system with blades and vanes and the measurements of the adiabatic effectiveness on a rotating disc affected by ingress are unique and provide a platform for further experimental studies and validation of CFD models.

Acknowledgements

First and foremost I would like to thank my supervisor Professor Gary Lock for giving me the opportunity to work on such an interesting and exciting research project. Gary has provided me with invaluable advice and support throughout my three years as a PhD student and his input has had a significant impact upon my development as a researcher.

I would also like to thank Professor Mike Owen for the guidance he has provided. The enthusiasm that Mike brings to his research has proved inspiring and will be something that I will remember during the course of my career.

Dr. Mike Wilson has been a valuable second supervisor and has always been eager to offer support, particularly on the theoretical side of the project.

Guy Brace, Alan Jeffries and Vijay Rajput have all provided crucial technical advice and helped the experiments to run smoothly. I should thank James Mayhew for teaching me the art of spraying and calibrating liquid crystals. My colleagues in the aero-thermo group, particularly Carl Sangan, Kunyan Zhou, Luke Tregidgo, James Scobie and GeonHwan Cho, must be credited for providing their help when needed and making the office such an enjoyable place to work.

Finally, and most importantly, I want to thank my family and fiancée for their endless support. Luce has been with me through the good times and bad times and this thesis is dedicated to her.

Contents

List of figures

List of tables

Nomenclature

Symbols

a	speed of sound
A	empirical constant in combined ingress orifice equations
A'	empirical constant in combined ingress orifice equations
b	radius of seal
Bi	Biot number [= hL/k]
$\overline{Bi}$	corrected Biot number [= $\bar{h}L/k$]
c	concentration; empirical constant; ratio of temperatures [= Θ_1/Θ_{ss}]
C	resultant velocity at exit from vanes; empirical constant
$C_{d,e}$ $C_{d,i}$	discharge coefficients for egress and ingress
C_M	moment coefficient [= $M/(1/2\rho\Omega^2 b^5)$]
c_p	specific heat of solid
$c_{p,air}$	specific heat of air
C_p	pressure coefficient [= $(p_a - \bar{p}_a)/(1/2\rho\Omega^2 b^2)$]
$C_{p,max}$	pressure coefficient [= $\Delta p/(1/2\rho W^2)$]
C_w	non-dimensional flow rate [= $\dot{m}/\mu b$]
$C_{w,e}$, $C_{w,i}$	values of C_w for egress and ingress
$C_{w,0}$	non-dimensional sealing flow rate
$C_{w,min}$	minimum value of $C_{w,0}$ to prevent ingress
$C_{\beta 1}$	modified internal swirl ratio [= $\beta_1^2(1 - r_1^2/r_2^2)$]
D	mass diffusion coefficient
e	relative error in Bi
f	normalised pressure [= $(p_2 - p_{2,min})/\Delta p$]; function
g	function
Fo	Fourier number [= $\alpha t/L^2$]
$\overline{Fo}$	corrected Fourier number [= $Fo(1-\bar{\phi})$]
Fo_0	value of Fo at measured liquid crystal isotherm
G	gap ratio [= S/b]
G_c	seal-clearance ratio [= s_c/b]
h	heat transfer coefficient; annulus height
$\bar{h}$	corrected heat transfer coefficient
h_m	mass transfer coefficient
h_{seal}	depth of seal insert
i	i^{th} value of N points
I_{min}	integral for EI ingress orifice equations
I_{min}'	integral for combined ingress orifice equations
k	thermal conductivity of solid
k_{air}	thermal conductivity of air
K	empirical constant for seal ranking and in thermal buffer hypothesis
L	thickness of solid
m	number of terms in exponential series temperature rise
$\dot{m}$	mass flow rate
M	Mach number; moment on disc
n	power in power-law relationship
N	sample size
Nu_r	local Nusselt number [= hr/k_{air}]

p	static pressure
P	95% uncertainty
p_a	static pressure on vane platform
p_{in}	non-dimensional ingress-predicting pressure [= $\{ (p - p_a) / p_a \} \times 10^3$]
$P_{\overline{K}}$	95% uncertainty in $\overline{K}$
P_{max}	non-dimensional pressure parameter [= 1/2 $C_{p,max}$ Re_W^2]
Pr	Prandtl number of air [= $\mu/\rho\alpha$]
q	heat flux at surface
r	radius
R	thermocouple recovery factor; fluid dynamic recovery factor
Re_W	axial Reynolds number in annulus [= $\rho W b/\mu$]
Re_ϕ	rotational Reynolds number [= $\rho \Omega b^2/\mu$]
S	axial clearance between rotor and stator
s_c	seal clearance
Sc	Schmidt number [= $\mu/\rho D$]
Sh	Sherwood number [= $h_m r/D$]
t	time; time to activate liquid crystal isotherm; t-value for 95% uncertainty
T	temperature
T_a	temperature of fluid; temperature of air in annulus
T_{ad}	adiabatic disc temperature
T_{ad}*	adiabatic disc temperature for $\Phi_0 = \Phi_{min}$
T_{in}	initial temperature of system
T_3	turbine-entry-temperature
U	bulk-mean velocity of sealing air through rim seal [= $\dot{m}_0 / 2\pi\rho b s_c$]
u_e	external axial velocity
u_m	average radial velocity through seal
V	velocity relative to blades; freestream velocity; voltage
v	velocity component in wheelspace
W	axial velocity in annulus
x	non-dimensional radius [= r/b]; normal co-ordinate
X	non-dimensional normal co-ordinate [= x/L]; function of G
y	lateral co-ordinate
Y	non-dimensional lateral co-ordinate [= y/L]
z	axial co-ordinate in wheelspace
α	vane exit angle; thermal diffusivity of rotor [= $k / \rho c_p$]
β	blade angle; swirl ratio in wheel-space [= $v_\phi / \Omega r$]
β_n	eigenvalue in quenching solution
β_0	blade angle for the design case
Γ_c	ratio of discharge coefficients [= $C_{d,i} / C_{d,e}$]
$\Gamma_{\Delta p}$	ratio of driving forces for EI and RI ingress [= $\Delta C_p / C_{\beta 1}$]
δ	uncertainty; boundary layer thickness
δ_{ad}	uncertainty in T_{ad}
δ_a	uncertainty in T_a
δ_{ad}*	uncertainty in T_{ad}*
δ_ε	uncertainty in ε_{ad}
δt	time increment of digital camera
ΔC_p	non-dimensional pressure difference [= $\Delta p / (1/2 \rho \Omega^2 b^2)$]
Δp	peak-to-trough pressure difference in annulus
Δp_b	pressure drop in combustion chamber
Δt	active period of liquid crystal colour change
ΔT	frictional temperature increase on rotor; bandwidth of liquid crystal
ε	sealing effectiveness [= $C_{w,0} / C_{w,e} = \Phi_0 / \Phi_e$]
ε_{ad}	adiabatic effectiveness for rotor [= $(T_{ad} - T_a)/(T_{ad}$*$- T_a)$]

ε_c	concentration effectiveness [= $(c_s - c_a) / (c_0 - c_a)$]
ε_M	dimensionless coefficient for calculation of C_M
η	thermal buffer ratio [= $\Phi_{min,c}/\Phi_{min,ad}$]; composite parameter [= $(1+Bi_A/Bi_B)$]
θ	normalized angle between vanes
θ_∞	non-dimensional air temperature [= $(T_{core} - T_{in})/(T_0 - T_{in})$]
θ_E	non-dimensional temperature in engine [= $(T_a - T)/(T_a - T_0)$]
Θ	non-dimensional temperature difference [= $(T - T_{in})/(T_{ad} - T_{in})$]
λ_T	turbulent flow parameter [= $C_w / Re_\phi^{0.8}$]
$\lambda_{T,min}$	value of λ_T when $C_w = C_{w,min}$
μ	dynamic viscosity of air
ρ	density
σ	standard deviation
τ	time constant
ϕ	correction parameter for lateral conduction = [$(\partial^2\Theta/\partial Y^2) / (\partial^2\Theta/\partial X^2)$]
$\overline{\phi}$	average value of correction parameter for lateral conduction
ϕ_0	correction parameter at $X = 0$, $Y = 0$
Φ	sealing flow parameter [= $C_w / 2\pi G_c Re_\phi$]
Φ_e	value of Φ when $C_w = C_{w,e}$
Φ_i	value of Φ when $C_w = C_{w,i}$
Φ_i*	value of Φ_i when $\Phi_0 = 0$
Φ_{min}	value of Φ_0 when $C_{w,0} = C_{w,min}$
Φ_0	value of Φ when $C_w = C_{w,0}$
Φ_h, Φ_{Tad}	amplification parameters for h and T_{ad}
χ	parameter in semi-infinite solution [= $BiFo^{1/2}$]
χ_{av}	correction factor
ψ	empirical constant in combined ingress orifice model
Ω	angular velocity of rotor

Subscripts

a	annulus
ad	adiabatic
ax	axial clearance
A	material A
B	material B
c	concentration
CI	combined ingress
e	egress
E	engine
EI	externally-induced ingress
h	relating to heat transfer coefficient
hot	hot junction
i	ingress or individual value; interface of composite substrate
j	j^{th} value of *m*
in	initial, inlet
L	back face
min	minimum
overlap	overlap clearance
r	radial component; value at radius *r*
rad	radial clearance
ref	reference junction
RI	rotationally-induced ingress
s	sample point; surface

ss	steady-state value
T	relating to temperature
Tad	relating to adiabatic disc temperature
TC	thermocouple reading
w	rotor wall
z	axial component
ϕ	tangential component
0	superposed flow
1	wheelspace; first crystal isotherm; value for one-dimensional conduction
2	annulus; second crystal isotherm
∞	infinite time

Superscript

–	average value
+	value for upper 95% uncertainty limit
–	value for lower 95% uncertainty limit
*	value with zero ingress
^	improved value (see Appendix B)
′	value at $\varepsilon_c = 0.95$

Chapter 1. Introduction

1.1 A brief history of the gas turbine engine for industrial power generation

The importance of the gas turbine engine in modern industry is unquestionable. From propulsion of aircraft and marine vehicles to electrical power generation, the gas turbine has evolved rapidly since conception. Historical accounts often focus on the importance of Frank Whittle and Hans von Ohain during the 1930's in the birth and advancement of the turbojet. Whilst these two individuals remain arguably the greatest pioneers in the history of gas turbines, much work of note was undertaken on industrial turbines prior to their involvement.

Diakunchak *et al.* (2008) provide an overview of early gas turbine work. John Barber established a patent for a gas turbine engine in 1791, nearly 150 years before the first tests of the Whittle WU engine took place in 1937. Barber's design remained a concept until the early 20th Century when the first power-producing turbine was built by Rene Armengaud and Charles Lemale in France in 1906. This early power turbine was limited to an operational efficiency of less than three percent.

Hunt (2011) wrote a paper that laid tribute to the pioneers of gas turbine technology. John Barber, Rene Armengaud and Charles Lemale all featured, as did a number of individuals from Switzerland that provided impetus to gas turbine research and development at Brown Boveri from 1905 to 1940. The work carried out in this period led to Brown Boveri commissioning and building the first operational industrial gas turbine engine in 1939 at the Neuchâtel power plant facility. The Neuchâtel engine had a 4MW power output capability and operated with an efficiency of 17.4 percent: the first truly economical gas turbine engine. The Brown Boveri engine provided a significant step in the evolution of gas turbine design, as demonstrated by the subsequent award of ASME International Historic Mechanical Engineering Landmark status in 1988 (see ASME (1988)). A simple schematic of the Neuchâtel turbine is shown in Fig. 1.1; the engine featured an axial compressor, single combustor and axial rotor all driven along a common shaft. An inline generator was installed to produce electricity.

Parallel to the development gas turbines for power generation was the drive for a new propulsive system in aircraft. The aforementioned Whittle and von Ohain were the principals

in this field. Both realised the great potential that the gas turbine offered as a means of propulsion and they simultaneously conceived and built independent versions of the jet engine. Meher-Homji (1998) and Meher-Homji and Prisell (2000) provide detailed accounts of Whittle and von Ohain's journeys from idea to creation.

By 1939 the first jet powered flight was made using von Ohain's HeS3 engine: a gas turbine featuring a centrifugal compressor, annular combustor and centrifugal turbine. A Whittle-inspired flight soon followed in 1941 with the W.1X-powered Gloster E28/E29. The W.1X differed to the HeS3 in that it had a two-stage axial turbine driving the compressor. The jet engine revolution continued with the German-developed Junkers Jumo 004 and the American manufactured Westinghouse WE19A in the 1940's, both of which had axial compressor and axial turbine sections. The Jumo 004 and WE19A engines in particular had a significant impact upon gas turbine design for power generation post WWII.

The 1950's saw an explosion in gas turbine design for industrial power purposes. Manufacture of power turbines was becoming a global affair, with the UK, Western Europe, the USA and Japan all contributing to post-war advancement. Hunt (2011) provides a detailed history of the development of industrial power turbines between 1950 and 1990. General Electric and Westinghouse feature heavily in this history, as do Siemens. All three companies benefitted from their early work into the design and build of aero engines. The transfer of knowledge between aero and industrial engines is well-demonstrated by the Siemens VM1 (an industrial turbine completed in 1956), which borrowed technologies employed in the Jumo 004. The Siemens VM3 (shown in Fig. 1.2) and VM5 soon followed, with the latter achieving a power output of 5.6 MW at an efficiency of 29 percent. Diakunchak *et al.* (2008) claim that the VM5 was the 'first truly commercial gas turbine'. In the ten years since the final commissioning of the Neuchâtel gas turbine, engine efficiencies had almost doubled.

From the 1960's to present day, industrial gas turbines have been improving in efficiency and power performance from one design to the next. The Westinghouse 501 series engines were developed progressively over seven models from 1968 to 1999. During this time, output power was increased from 45 to 249 MW and engine efficiency from 27.0 to 38.6 percent. General Electric and Siemens (which acquired Westinghouse in 1999) made similar performance gains in this time period.

Modern stationary gas turbines are versatile as a power unit and consequently they are used in an array of industries and the power they produce can be used in a variety of ways. Examples include but are not limited to: commercial electrical generation, drive of

compression pumps in natural gas pipelines, and supply of power to auxiliary machines on oil rigs. Gas turbine manufacturers need to consider the requirements of their customer and thus most large companies offer engines with a range of power outputs. State of the art high-power industrial gas turbines, such as the Siemens SGT5-8000H engine (shown in Fig. 1.3), are used in large scale power stations as part of combined heat and steam cycles. The SGT5-8000H, which first fired in 2007, is capable of producing 530 MW in combined cycle operation at an efficiency level in excess of sixty percent. Smaller engines, such as the 5MW rated Siemens SGT-100, are suited to small manufacturing facilities looking to produce their own electricity and heated water supplies.

The gas turbine has revolutionised industry in little over a hundred years. Simple engine efficiencies have doubled and power capabilities have increased by over two orders of magnitude between 1939 and present day. With small, medium and large scale industrial units being designed and built to suit a range of applications, the gas turbine is vital to modern industry. Climate change is at the forefront of social conscience and so engine designers must continue improving efficiencies to ensure that gas turbines are a significant contributor to future industrial power generation.

1.2 Gas turbine theory

Lock (2007) provides a summary of engine classification and design. A basic gas turbine—or core engine as it is sometimes referred—comprises a compressor, combustor and turbine. Air is drawn through an intake, pressurised in a compressor and then heated in a combustion chamber to form a high pressure and temperature air-fuel gas mixture. This hot gas mixture is then expanded through a turbine to drive the compressor unit via a coupled shaft. At exit from the turbine, the way in which the hot gas is used depends upon application: in an aero engine it is accelerated through an exhaust nozzle to create thrust; in an industrial unit it is used to drive a secondary power turbine and generate electricity. A simple gas turbine system for power generation is shown in Fig. 1.4.

Two gas turbine cycles are shown as temperature-entropy diagrams in Fig. 1.5: (a) an ideal gas turbine Brayton cycle, and (b) a cycle for a gas turbine with a separate power turbine. In an ideal Brayton cycle there is isentropic compression from 1 to 2′ and isentropic expansion from 3 to 4′. An engine will be non-isentropic due to the frictional and aerodynamic losses associated with viscous flow. Consequently, when the fluid flows through the compressor and turbine sections entropy will be generated; hence compression will occur from 1 to 2 and expansion from 3 to 4. Using the ideal Brayton cycle,

Saravanamuttoo *et al.* (2009) show that turbine cycle efficiency is dependent only upon pressure ratio (PR = p_2/p_1), whereas the specific work output of the engine is dependent upon both PR and turbine entry temperature (TET=T_3). It follows that an engine designer would aim to maximise both PR and TET so as to obtain the most efficient and powerful engine. This is demonstrated by the development of the Westinghouse 501 series engines (see Diakunchak *et al.* (2008)) where PR and TET increased from 7 to 19.5 and 1236 K to 1773 K respecitvely between 1968 and 1999. These changes in PR and TET yielded an increase in power output from 45 MW to 249 MW and engine efficiency from 27.0 percent to 38.6 percent.

The marked trend in rising TET has pushed turbine design beyond the limits of current metallurgic technology. As Cumpsty (2003) highlights, single-crystal Nickel alloys from which modern turbine blades are manufactured have typical melting points of around 1550 K. This is significantly less than the TETs of current industrial turbines, which can exceed 1800 K at full operational load. To prevent failure of components under sustained operation, it is necessary to implement cooling in the regions of the turbine exposed to high gas temperatures.

1.3 Internal cooling

Lock (2007) and Saravanamuttoo *et al.* (2009) provide an overview of internal cooling in gas turbines. A gas turbine being used for industrial power generation follows a cycle as illustrated in Fig. 1.5 (b). The drop in total pressure across the combustion chamber (Δp_b), which arises due to skin-friction and turbulence, is beneficial to a designer of gas turbine cooling systems as it provides a favourable pressure gradient between the compressor and turbine. This pressure difference allows a proportion of the compressor exit air, which is relatively cool at around 900 K, to be bled off and fed to the areas of the turbine that require cooling. Any air bled from the compressor will not be used for power generation and will thus impact engine performance: for every one percent of air drawn from the compressor for use as coolant a one percent drop in isentropic efficiency will follow (see Cumpsty (2003)). It is thus important to design effective cooling systems so as to maximise engine efficiency.

The transportation of coolant to the turbine section is achieved through a network of complicated channels. Coolant flow is directed not only to the turbine blades, but also to the stator vanes, bearing chambers, seals and turbine cavities. A typical gas turbine cooling network is shown in Fig. 1.6.

The first-stage nozzle guide vanes and turbine blades are the components exposed to the highest working temperatures. Modern vanes and blades are complex in design and make use of a number of techniques to prevent damage from exposure to high gas temperatures. These techniques include: film cooling, by forcing coolant through holes on the blade surface; convection cooling, by feeding coolant through multi-pass internal blade ducts; and thermal barrier protection, by coating the blades with ceramics. A typical first-stage turbine blade employing current technology is shown in Fig. 1.7.

Hot gas entering the turbine is problematic not only to the blades and vanes, but also to the stator and rotor discs. Figure 1.8 shows a first-stage rotor-stator setup typical of that in an industrial turbine. If mainstream gas passes between the clearance separating the rotor and stator, it will enter the cavity (or wheelspace) between the two discs and potentially lead to overheating and damage of the turbine hub and blade roots. Fluid can be drawn from the annulus into the wheelspace when a pressure difference exists between the two regions. Any overheating, particularly of highly stressed rotating components, can result in catastrophic component failure in the turbine section. The unwanted flow of the hot mainstream gas from the annulus into the wheelspace is termed ‘ingress’ and is something that engine designers strive to minimise.

Ingress levels are controlled by supplying sealant flow to the wheelspace. The sealant flow has the dual effect of lowering temperatures in the wheelspace and preventing influx of fluid from the annulus by pressurising the cavity. An important objective of secondary air-system designers is to limit ingress to levels that, once mixed with the cool sealant flow, do not exceed the maximum working temperatures of the turbine components. The amount of coolant required to limit ingress to acceptable levels can be reduced with effective rim seal design. Experiments, theoretical models and Computational Fluid Dynamics (CFD) have all played, and continue to play, an important role in furthering understanding of the fundamental fluid dynamics and heat transfer associated with ingress and in optimising seal performance.

1.4 Off-design operation

Saravanamuttoo *et al.* (2009) provide a summary of the performance of gas turbines at a range of operational design conditions. An industrial gas turbine engine will generally be designed for maximum overall efficiency at the peak-load requirement: this is referred to as ‘on-design’ operation. If the engine is being used to supply a variable demand of electricity then it will sometimes work at part-load (i.e. it will operate ‘off-design’). The circumferential pressure distribution and the peak-to-trough pressure levels in the annulus

will be dependent upon the operational condition (see Section 4.1.3 for a detailed discussion on the relationship between non-dimensional pressure in the annulus and the operational condition of the turbine). The use of industrial turbines as part of a system (for example, to supplement unreliable renewable energy sources) can result in operation over a range of off-design conditions. It is important that engine designers understand how ingress levels are affected by off-design operation so that the cooling system can be designed accordingly.

1.5 Thesis aim and objectives

The answers to the following three questions are of interest to engineers working in gas turbine secondary air-system design:

Q1. How can the sealing flow levels required to prevent hot gas ingress into the wheelspace be predicted?

Q2. How does ingress affect the flow structure in the wheelspace?

Q3. What is the effect of ingress on the temperature of the rotor disc?

In order to answer these questions, the following aim was set: to investigate the effect of hot gas ingress on the fluid dynamics in the wheelspace and the heat transfer to the rotor of a first-stage high-pressure gas turbine. An extensive review of literature showed that this aim could be fulfilled with completion of the following objectives:

Obj 1. Solve the Owen (2011b) Combined Ingress Orifice Model, used to predict ingress levels, and validate it using pre-published and self-collected data.

Obj 2. Measure the sealing effectiveness on the stator of the Bath gas turbine test rig by making CO_2 concentration measurements across a range of operational conditions.

Obj 3. Make temperature measurements using thermochromic liquid crystal to investigate the effect of ingress upon the temperatures and heat transfer levels on the rotor surface.

The experimental technique used in the work for Objective 3 was susceptible to large uncertainties. A fourth objective was proposed to reduce these uncertainties for future experiments:

Obj 4. Develop a composite substrate technique to improve the accuracy of thermochromic liquid crystal for adiabatic surface temperature measurements.

1.6 Thesis overview

Chapter 1 gives an overview of the history, the basic theory and the associated internal cooling flow challenges of industrial gas turbines. The phenomenon of ingress and its associated problems are introduced to the reader. The aims and objectives of this thesis and a list of publications resulting from the work in this thesis are provided.

Chapter 2 provides an introduction to ingress through gas turbine rim seals. The fundamental fluid dynamics pertinent to the phenomenon are discussed. This is followed by a review of the existing experimental and theoretical research into rotationally-induced, externally-induced and combined ingress; this review includes an overview of past ingress research carried out on the Bath gas turbine test rig.

Chapter 3 presents analytical and numerical solutions of an orifice model developed for the case of combined ingress. The model is validated against pre-published experimental data for the cases of constant and variable discharge coefficients with various annular pressure profiles. The possibility of using the model as a tool for extrapolating data from rig to engine operating conditions is briefly discussed.

Chapter 4 presents concentration sealing effectiveness measurements made on the stator of the University of Bath single-stage gas turbine rig for an axial clearance seal geometry; the measurements show the effect of off-design operation on the minimum sealing flow required to purge the wheelspace against ingress. Finally, experimental uncertainty levels and practical implications are considered.

Chapter 5 gives an overview of thermochromic liquid crystal (TLC) as a technique for determining the heat transfer coefficient and adiabatic wall-temperature in transient heat transfer experiments. Transient and steady-state heat transfer methods are covered prior to a review of the existing research into heat transfer in rotor-stator systems.

Chapter 6 presents effectiveness and heat transfer coefficient measurements on the rotor of the Bath gas turbine test rig. An adiabatic effectiveness is defined and used to determine the effects of ingress on the rotor. A buffer ratio hypothesis relating the adiabatic effectiveness on the rotor to the concentration effectiveness on the stator is suggested; this hypothesis is tested with the collected data. Finally, the local Nusselt numbers on the rotor

are presented for different sealant flow rates and discussed in relation to the fundamental fluid dynamics of rotor-stator systems.

Chapter 7 discusses the limitations associated with the use of TLC to determine the adiabatic wall temperature from the so called ‘semi-infinite solution’ for a substrate made from a single material. The ‘quenching solution’ is used to check when the back face boundary condition of the substrate starts to affect the values of Biot number calculated from the semi-infinite solution. Numerical and analytical solutions for determining the heat transfer coefficient and adiabatic wall temperature from TLC measurements are shown for a two-layer composite substrate; the advantages of using a composite substrate over a single substrate for transient TLC measurements is discussed.

Chapter 8 presents the conclusions of this thesis and suggests some possible future research.

1.7 Publications

The following journal publications were made during the course of this thesis:

1. Sangan, C. M., **Pountney, O. J.**, Zhou, K., Wilson, M., Owen, J. M. and Lock, G. D., 2011, "Experimental measurement of ingestion through turbine rim seals. Part 1: Externally-induced ingress," ASME Paper GT2011-45310, to appear in ASME J. Turbomach.
2. Sangan, C. M., **Pountney, O. J.**, Zhou, K., Wilson, M., Owen, J. M. and Lock, G. D., 2011, "Experimental measurements of ingestion through turbine rim seals. Part 2: Rotationally-induced ingress," ASME Paper GT2011-45313, to appear in ASME J. Turbomach.
3. Owen, J. M., Zhou, K., **Pountney, O. J.**, Wilson, M. and Lock, G. D., 2012, "Prediction of ingress through turbine rim seals. Part I: Externally induced ingress," ASME J. Turbomach., 134(3), pp. 031012.
4. Owen, J. M., **Pountney, O. J.** and Lock, G. D., 2012, "Prediction of ingress through turbine rim seals. Part II: Combined ingress," ASME J. Turbomach., 134(3), pp. 031013.
5. Sangan, C. M., **Pountney, O. J.**, Scobie, J. A., Wilson, M., Owen, J. M. and Lock, G. D., 2012, "Experimental measurements of ingestion through turbine rim seals. Part 3: Single and double seals," ASME Paper GT2012-68493, to appear in ASME J. Turbomach.

6. **Pountney, O. J.**, Sangan, C. M., Lock, G. D. and Owen, J. M., 2012, "Effect of ingestion on temperature of turbine discs," ASME Paper GT2012-68496, to appear in ASME J. Turbomach.
7. **Pountney, O. J.**, Cho, G., Lock, G. D. and Owen, J. M., 2012, "Solutions of Fourier's equation appropriate for experiments using thermochromic liquid crystal," Int. J. Heat Mass Transfer, 55(21-22), pp. 5908-5915

1.8 Figures

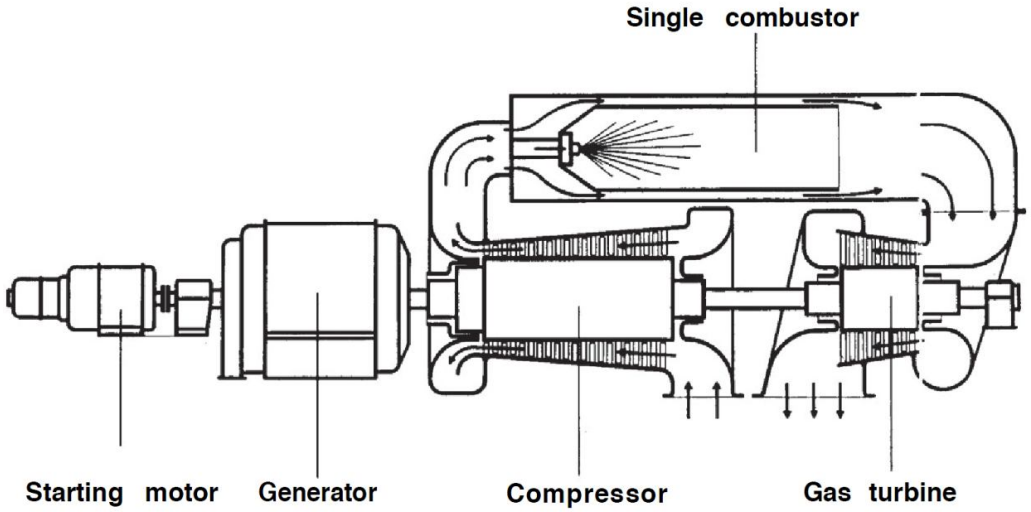

Figure. 1.1: Schematic of single-stage Brown Boveri gas turbine installed at the Neuchâtel power plant (from ASME (1988)).

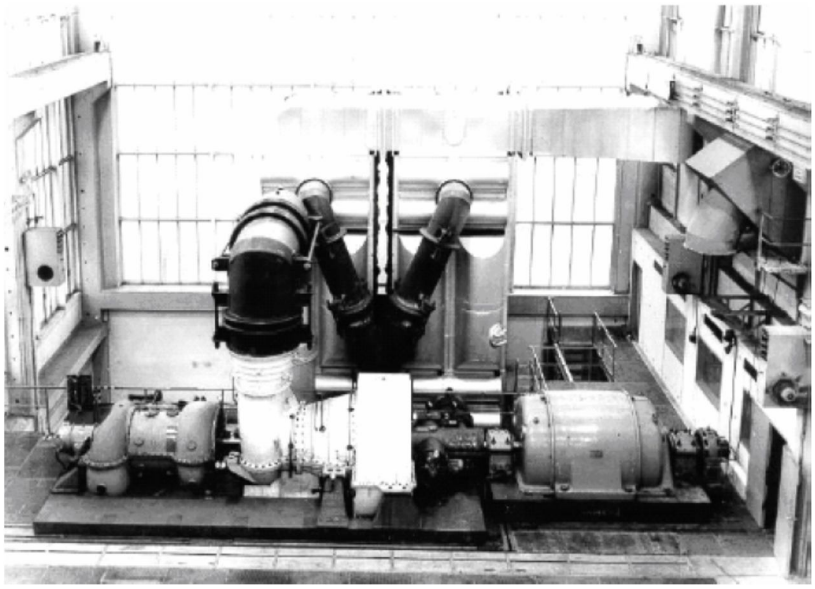

Figure. 1.2: Siemens VM3 gas turbine (from Diakunchak *et al.* (2008)).

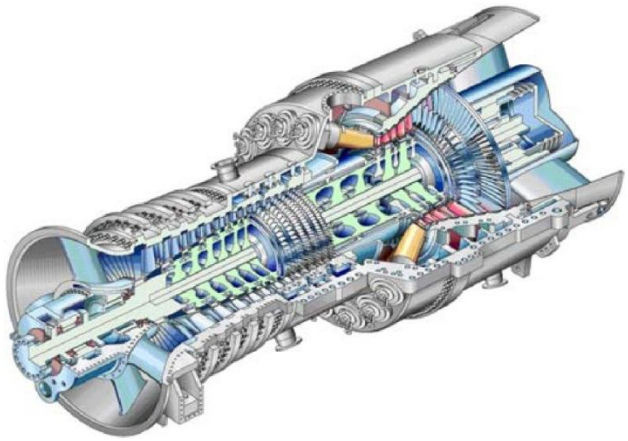

Figure. 1.3: Siemens SGT5-8000H industrial gas turbine engine (from Diakunchak *et al.* (2008)).

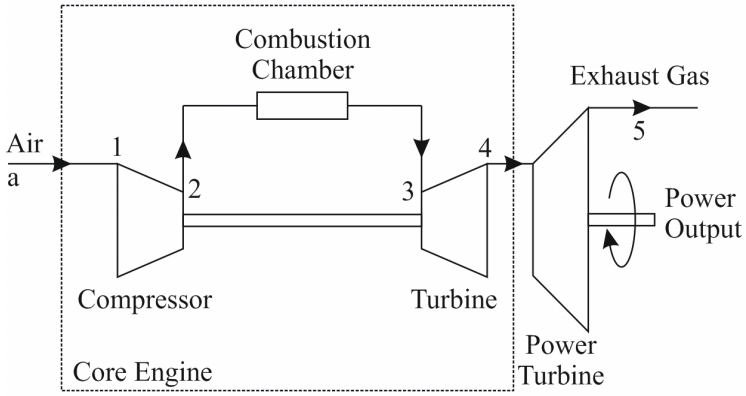

Figure. 1.4: A gas turbine system for power generation (adapted from Cumpsty (2003)).

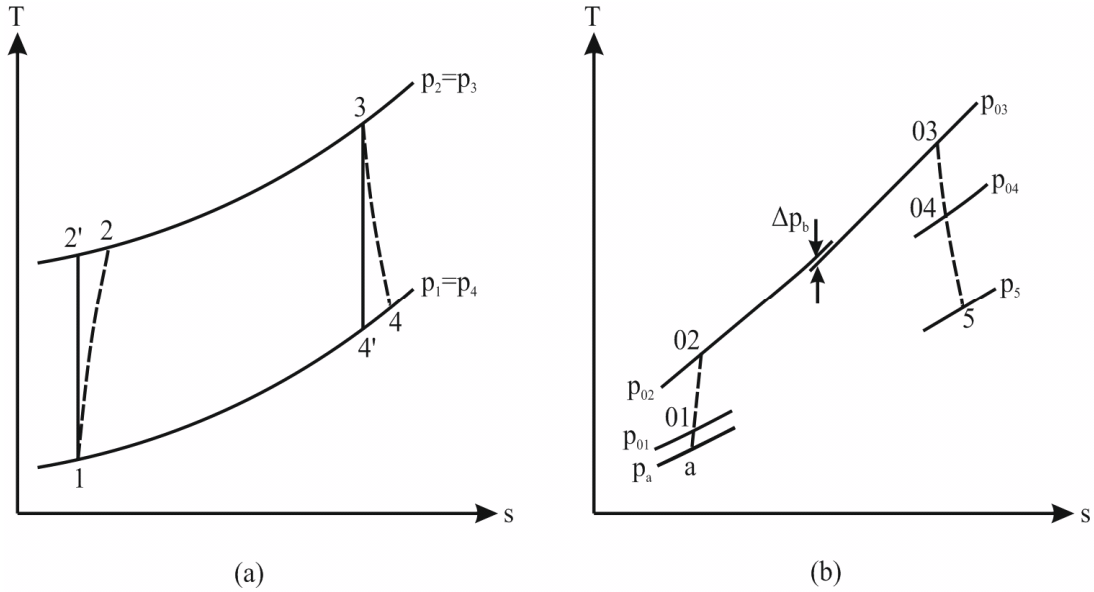

Figure. 1.5: Temperature-entropy plots for gas turbine cycles (stations are shown in Fig. 1.4): (a) Brayton cycle, (b) cycle for a gas turbine with separate power turbine (adapted from Cumpsty (2003)).

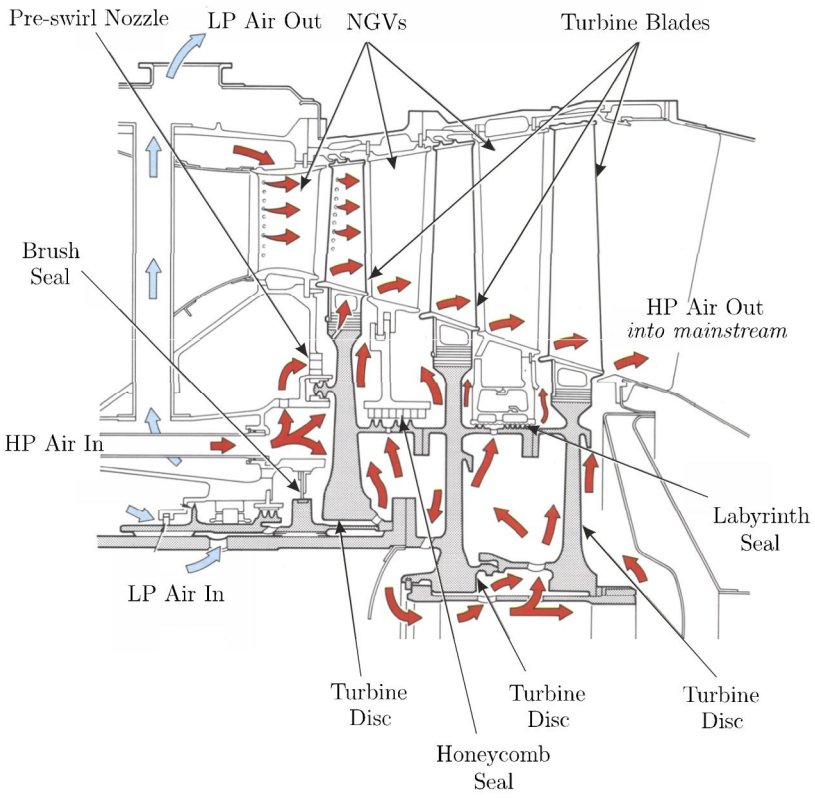

Figure. 1.6: Typical gas turbine cooling network (from Rolls-Royce (1996)).

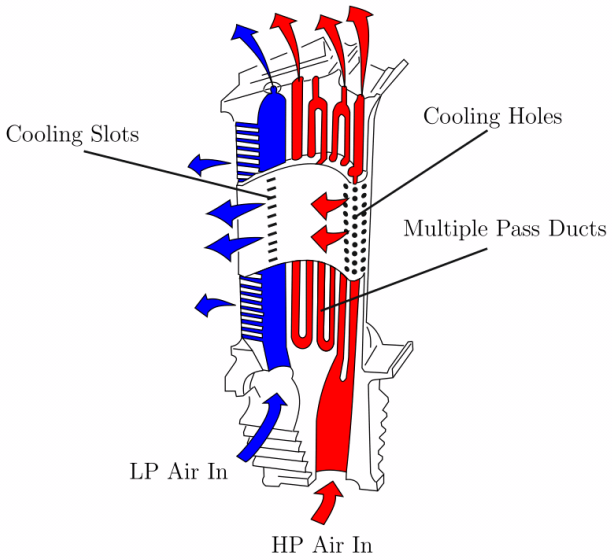

Figure. 1.7: First-stage turbine blade with multi-pass ducts for convection cooling and slots and holes for film cooling (adapted from Rolls-Royce (1996)).

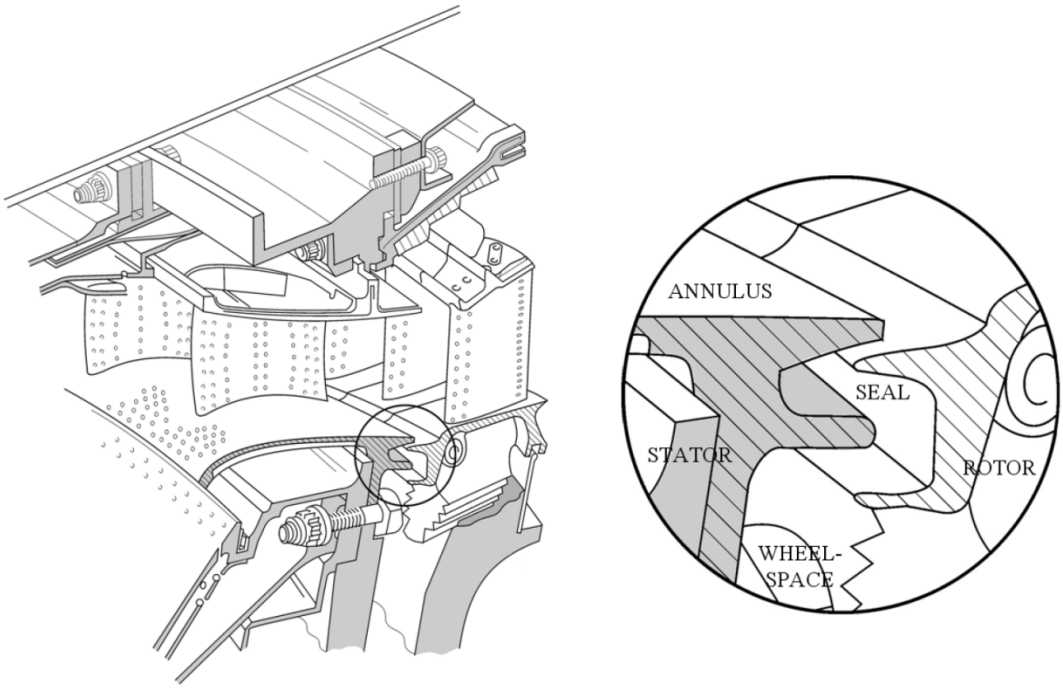

Figure. 1.8: Rotor-stator section including detail of rim-seal region (from Sangan *et al.* (2011a)).

.

Chapter 2. Literature review part I: ingress

This chapter provides an introduction to ingress through gas turbine rim seals. The fundamental fluid dynamics for a free-disc and various rotor-stator configurations are discussed. This is followed by a review of the existing experimental and theoretical research into rotationally-induced, externally-induced and combined ingress and a brief discussion on the contribution of CFD in furthering the understanding of the ingress phenomenon. Finally, pre-published research into ingress carried out on the University of Bath gas turbine test rig is presented.

2.1 The free-disc

Schlichting (1979), Owen and Rogers (1989) and, more recently, Childs (2011) examined a disc rotating with uniform angular velocity in an initially stationary fluid; this case is referred to as the free-disc. To satisfy the no-slip condition on the surface of the disc, the fluid must accelerate from zero velocity outside the rotor boundary layer to the disc speed, Ωr, on the surface. The centrifugal forces resulting from the shear between the disc and fluid lead to a radial outflow of fluid in the rotor boundary layer (often termed disc-pumping). It is necessary that fluid is axially entrained into the boundary layer to conserve mass and facilitate the radial outflow of fluid. The free-disc radial and tangential boundary layers are shown in Fig. 2.1.

2.2 Rotor-stator systems

A rotor-stator system is made up of a rotating disc and a stationary disc separated by an axial clearance that forms a cavity known as a wheelspace. The flow physics associated with rotor-stator systems are more complex than the free-disc case and require careful consideration. A rotor-stator system with an open periphery and low radius supply of fluid is shown in Fig. 2.2.

With reference to the geometric parameters defined in Fig. 2.2, the following non-dimensional ratios can be expressed:

$$G_c = \frac{s_c}{b} \tag{2.1}$$

and

$$G = \frac{S}{b} \tag{2.2}$$

where s_c is the seal clearance, S is the axial spacing between the rotor and stator and b is the radius of the shroud. G_c is referred to as the seal clearance ratio and G as the gap ratio.

2.2.1 Non-dimensional variables

It is useful to define a set of fluid dynamic non-dimensional variables commonly used in the study of rotor-stator systems: rotational Reynolds number, Re_ϕ; axial Reynolds number, Re_W; non-dimensional flow rate, C_w; turbulent flow parameter, λ_T; and swirl ratio, β. All of these variables, which are defined in equations 2.3 to 2.7, influence the flow structure that forms in the rotor-stator wheelspace region.

$$Re_\phi = \frac{\rho \Omega b^2}{\mu} \tag{2.3}$$

$$Re_W = \frac{\rho W b}{\mu} \tag{2.4}$$

$$C_w = \frac{\dot{m}}{\mu b} \tag{2.5}$$

$$\lambda_T = \frac{C_w}{Re_\phi^{0.8}} \tag{2.6}$$

and

$$\beta = \frac{v_\phi}{\Omega r} \tag{2.7}$$

where W is the axial velocity of the fluid in the external annulus, ρ is the density, μ is dynamic viscosity and $\dot{m}$ is the mass flow rate of the fluid. It is typically assumed that there are no thermal gradients in the discs and that axisymmetric flow exists in the wheelspace for the theoretical system described below.

2.2.2 Flow regimes

Owen and Rogers (1989) and Childs (2011) provide detailed analysis of flow regimes for enclosed rotor-stator systems and open rotor-stator systems operating with radial inflow and outflow. The work carried out in this thesis is focused on rotor-stator systems with clearance at the periphery and thus open systems are of chief interest here.

Axial entrainment of fluid into the radial and tangential boundary layers on a rotating disc is limited by λ_T. Free-disc entrainment occurs when $\lambda_T \leq 0.22$; when λ_T exceeds this value fluid will no longer flow into the rotor boundary layer.

If fluid is supplied to a rotor-stator system at low radius then it will form a source region. The fluid in the source region will be drawn into the rotor boundary layer and pumped up the disc. Generally, if λ_T is less than the limit for full disc entrainment then the fluid in the wheelspace will adhere to a model similar to that proposed by Batchelor (1951). Batchelor flow comprises separate rotor and stator boundary layers with a rotating fluid core located between; the tangential velocity component in the core is less than the disc speed, Ωr. Fluid flows radially outward on the rotor and radially inward on the stator. The rotor boundary layer is supplied with fluid from the core region to satisfy entrainment and so thickens with radius. The mass of fluid leaving the core is balanced by an influx of fluid from the stator boundary layer, which thins as it flows radially inwards. A simplified schematic of Batchelor-type flow in an open rotor-stator system is shown in Fig. 2.3.

The rotating core will adhere to the Taylor-Proudman theorem, which states that for a fluid rotating in a system with solid boundaries:

$$v_r = 0 \tag{2.8}$$

and

$$\frac{\partial v_\phi}{\partial z} = \frac{\partial v_z}{\partial z} = 0 \tag{2.9}$$

where v_r, v_ϕ and v_z are the tangential, radial and axial components of velocity respectively and z is the axial displacement across the wheelspace. It follows that the flow of fluid across the wheelspace will take place along a line of fixed radius with constant tangential and axial velocity components. Corresponding velocity profiles are presented in Fig. 2.4 (a) to (c).

If λ_T is above the free-disc entrainment rate then the flow in the wheelspace will follow the Stewartson (1953) flow model: v_ϕ will reduce from the disc speed to zero outside the rotor boundary layer; v_r will be positive across the wheelspace (i.e. radially outwards); and v_z will be positive (towards the rotor) to satisfy entrainment into the rotor boundary layer. Velocity profiles for Stewartson flow are presented in Fig. 2.4 (d) to (f).

Daily and Nece (1960) carried out an experimental and theoretical study of fluid flow inside an enclosed rotor-stator system for G and Re_ϕ values in the following ranges: $0.0127 < G < 0.217$ and $1 \times 10^3 < Re_\phi < 1 \times 10^7$. Empirical correlations relating the moment coefficient on the disc, C_m, to G and Re_ϕ were determined from disc torque measurements for

a variety of flow regimes. These flow regimes, which were ascertained from measurement of velocity profiles in the wheelspace, were defined by Daily and Nece as:

Regime 1: Laminar flow, small clearance with merged rotor-stator boundary layers

Regime 2: Laminar flow, large clearance with separate rotor-stator boundary layers

Regime 3: Turbulent flow, small clearance with merged rotor-stator boundary layers

Regime 4: Turbulent flow, large clearance with separate rotor-stator boundary layers

The Daily and Nece moment coefficient correlations enabled rotor-stator flow to be categorised by G and Re_ϕ, as shown in Fig. 2.5.

Daily *et al.* (1964) made measurements of the core swirl ratio at four values of G for an enclosed disc system. Their measurements yielded the following correlation between β and G for a system with no superposed flow:

$$\beta = 0.49 - 0.57G \tag{2.10}$$

The Daily and Nece (1960) and Daily *et al.* (1964) correlations are useful to engine designers and experimentalists looking to predict the fluid dynamics in the wheelspaces of rotor-stator systems.

2.3 Rotationally-induced ingress

A radial pressure gradient exists in any body of rotating fluid. For the case of fluid rotating in the core in a rotor-stator system, this radial pressure gradient can lead to sub-annular pressures in the wheelspace. If the system is open to atmosphere at the periphery, a pressure difference will exist that causes fluid to be ingested through the seal clearance into the wheelspace: a phenomenon referred to here as rotationally-induced (RI) ingress.

Figure 2.6 shows the sealant flow, ingress and egress paths for a rotor-stator system operating with RI ingress. Subscripts 0, i and e denote sealant flow, ingress and egress respectively; locations 1 and 2 correspond to the wheelspace and atmosphere (or annulus when there is no external flow). When the system is fully sealed, $C_{w,i} = 0$ and $C_{w,0} = C_{w,e} = C_{w,min}$; subscript *min* is used to define the minimum value of sealant flow required to seal the system.

Bayley and Owen (1970) conducted experiments at the University of Sussex on a disc rotating near a shrouded stator with axial clearance at the periphery (i.e. an axial clearance

seal). This work supported their earlier study of a shroudless rotor-stator configuration (see Bayley and Owen (1969)). $C_{w,0}$ was supplied to the wheelspace at low radius through a delivery pipe at the centre of the stator and, in the absence of an annulus, expelled to atmosphere through the clearance at the shroud. Pressure readings were made on the stator wall using static taps; sub-atmospheric readings indicated the presence of ingested fluid in the wheelspace. By increasing the sealant flow rate to pressurise the wheelspace, Bayley and Owen showed that the system could be protected from ingestion. $C_{w,min}$, was measured at two values of G_c (0.0033 and 0.0067) and Re_ϕ values in the range $0.4 - 4 \times 10^6$. For $G >> G_c$ and $Re_\phi < 4 \times 10^6$, the following empirical relationship, often termed the Bayley-Owen correlation, was presented for RI ingress:

$$C_{w,min} = 0.61 G_c Re_\phi \tag{2.11}$$

Further research into RI ingress in rotor-stator systems was carried out at the University of Sussex between 1982 and 1988. Phadke and Owen (1982) investigated a simple shrouded rotating disc system with a radial outflow of coolant for $0.0025 < G_c < 0.04$ at a fixed gap ratio. Pressure measurements and flow visualisation techniques were used to determine $C_{w,min}$; these measurements yielded the following correlation:

$$C_{w,min} = 0.14 G_c^{0.66} Re_\phi \tag{2.12}$$

Phadke and Owen (1983) followed up their 1982 study by investigating the sealing behaviour of a number of radially spaced shroud geometries (shown in Fig 2.7). These geometries were considered to represent the complex designs found in gas turbine engines. For $Re_\phi < 1 \times 10^6$, a non-dimensional 'ingress-predicting pressure', p_{in}, was determined from static pressure measurements, p, made at a single radial location in the stator wall (r/b = 0.975 for seals A to D and r/b = 0.955 for seal E). p_{in} was defined by:

$$p_{in} = \frac{(p - p_a)}{p_a} \times 10^3 \tag{2.13}$$

where p_a is the ambient pressure outside the wheelspace.

Figure 2.8 shows effect of $C_{w,0}$ on the variation of p_{in} with Re_ϕ for the five test geometries. p_{in} was seen to decrease monotonically with Re_ϕ at relatively low values of $C_{w,0}$ for all geometries; however, at the highest value tested ($C_{w,0}$ = 11900), a 'pressure-inversion effect' was observed for geometries B, C and D. The authors presented a number of explanations for this pressure inversion effect, but did not reach a firm conclusion.

Phadke and Owen found that $C_{w,min}$ was lower for radial seal geometries when compared to an axial geometry for a common clearance (i.e. $G_{c,ax}$=$G_{c,rad}$). The radial seals with the best sealing performance were those with the greatest overlap: increasing the overlap at the periphery magnified the pressure-inversion effect and thereby prevented ingestion into the wheelspace.

Graber *et al.* (1987) carried out an experimental ingress study using a rig featuring a rotor-stator system with an external annulus. The disc setup comprised a shrouded and bladeless rotor separated axially from a shroudless and vaneless stator. Four peripheral geometries were tested: an axial clearance seal; a radial clearance seal with no overlap; and two overlapping radial clearance seals, each with a different $G_{c,rad}$. The sealant flow was seeded with tracer gas (CO_2) and delivered to the wheelspace stator side. Unseeded external flow was fed through the annulus at two different values of swirl, β_2. Tracer gas concentration levels were measured on the stator wall to determine how much unseeded air had been ingested from the annulus into the wheelspace (note: without ingress, the CO_2 concentration on the stator wall would equal the seeded value in the sealant flow). The authors found that that β_2 had little impact upon sealing performance for their experimental setup; consequently, ingress would have been rotationally-induced despite the presence of an external flow path.

Graber *et al.* measured CO_2 concentration at a number of sample points at different radial locations on the stator wall; the mean of these samples ($\bar{c}_s$) was taken to represent the concentration in the wheelspace. The authors defined the following system effectiveness based upon their concentration measurements:

$$\bar{\varepsilon}_c = \frac{\bar{c}_s - c_a}{c_0 - c_a} \tag{2.14}$$

where c_a and c_0 were the measured concentration levels in the annulus and sealant flow line respectively. By definition $\bar{\varepsilon}_c \rightarrow 0$ as $C_{w,0} \rightarrow 0$ and $\bar{\varepsilon}_c \rightarrow 1$ as $C_{w,0} \rightarrow C_{w,min}$. The typical variation of $\bar{\varepsilon}_c$ with $C_{w,0}$ is shown in Fig. 2.9.

The results presented by Graber *et al.* showed that increasing shroud overlap and reducing $G_{c,rad}$ of radial clearance geometries reduced the amount of sealant flow required to purge the wheelspace of ingress, which agreed with the findings of Phadke and Owen (1983). However, in contrast to the Phadke and Owen study, the authors found that a basic radial geometry (which featured no overlap) offered no performance benefit over an axial geometry for $G_{c,ax}$=$G_{c,rad}$. This contradiction may have arisen, as suggested by Owen (2011a), due to the difference in experimental setup between the two studies: Phadke and

Owen performed experiments with shrouds on both discs, whereas Graber *et al.* investigated a shroudless stator and shrouded rotor setup.

Phadke and Owen (1988a) carried out an ingress study on a rotor-stator system open to atmosphere at the periphery. The authors tested seven shroud geometries and found that, as suggested by previous studies, $C_{w,min} \propto Re_{\phi}$. Flow visualisation techniques helped to explain the previously discovered pressure-inversion phenomenon. For two of the radial shroud geometries, the fluid pumped up the rotor formed an impinging jet on the stator disc/shroud that created an ingress preventing 'fluid-curtain'.

Chew *et al.* (1992) extended RI ingress research to more complex seal geometries than those previously tested. Two engine representative radial seals were tested alongside an axial seal for baseline performance checks. The pressure difference between the atmosphere and wheelspace was measured using static pressure taps in the shroud and stator wall; $C_{w,min}$ was taken as the value of $C_{w,0}$ at which this differential was zero. The authors used this pressure criterion to show that the realistic radial geometries required lower purge flow rates to seal the system compared with the axial seal for $G_{c,ax}$=$G_{c,rad}$.

Chew *et al.* developed an empirical relationship relating $C_{w,min}$ to $G_{c,ax}$ and Re_{ϕ} for an axial seal. This relationship agreed well with the Bayley and Owen (1970) and Phadke and Owen (1983) correlations, shown in equations 2.11 and 2.12 respectively, for $G_{c,ax}$ = 0.01. However, the agreement at smaller values of $G_{c,ax}$ was less good, owing to, as suggested by the authors, difficulty in accurately setting small seal clearances.

Subsequent research has focused on externally-induced ingress over RI ingress as the former is representative of ingress is gas turbine engines. There is a resulting gap in RI ingress research between the abovementioned studies and Owen (2011a).

Owen (2011a) developed a theoretical model to predict ingress through the clearance of rotor-stator shroud geometries in the absence of external flow. This model—termed the RI orifice model—was derived for compressible and incompressible inviscid swirling flow from first principles. The seal clearance was treated as an orifice ring with inflow area, δA_i, and an outflow area, δA_e; this setup is shown in Fig. 2.10. Two discharge coefficients were built into the theory to account for viscous losses: $C_{d,i}$ for ingress and $C_{d,e}$ for egress.

Owen solved the incompressible RI orifice equations to form a relationship between a non-dimensional sealing parameter, Φ_0, and a sealing effectiveness, ε, where:

$$\Phi_0 = \frac{C_{w,0}}{2\pi G_c Re_\phi} \tag{2.15}$$

and

$$\varepsilon = 1 - \frac{\Phi_i}{\Phi_e} = \frac{\Phi_0}{\Phi_e} \tag{2.16}$$

Assuming that the effect of external swirl, β_2, was negligible, the relationship between Φ_0 and ε was shown to be a function of $\Phi_{min,RI}$, the minimum value of Φ_0 required to seal the system, and Γ_c, the ratio of the discharge coefficients, where:

$$\Gamma_c = \frac{C_{d,i}}{C_{d,e}} \tag{2.17}$$

and

$$\Phi_{min,RI} = C_{d,e} C_{\beta_1}^{1/2} \tag{2.18}$$

The modified internal swirl ratio, $C_{\beta 1}$, was defined as:

$$C_{\beta_1} = \beta_1^2 \left(1 - \left(\frac{r_1}{r_2}\right)^2\right) \tag{2.19}$$

For Γ_c =1 and $\Phi_{\text{min,RI}}$ = 0.097 (as taken from Bayley and Owen (1970)), the RI orifice model was fitted to the experimental data of Graber *et al.* (1987). The theory provided a good fit to the data for a range of G_c, β_2 and Re_ϕ values and both axial and radial seal geometries for most sealant flow rates. The model tended to over-predict the effectiveness values as $\Phi_0 \rightarrow \Phi_{\text{min,RI}}$. Owen suggested this to be a limitation of the model in which diffusion was not accounted for.

2.4 Externally-induced and combined ingress

In a gas turbine engine, hot post-combustion gas will be directed through a set of nozzle guide vanes to the rotor blades. The flow of fluid over the vanes and blades produces a circumferentially asymmetric pressure field in the annulus (this pressure field is also 3D and unsteady). The circumferential variation in pressure above the seal clearance can result in regions where the pressure in the annulus exceeds that in the wheelspace, thereby leading to ingress of fluid from the annulus into the wheelspace. Conversely, the fluid pressure in the annulus may fall below that in the wheelspace, thus causing an egress of fluid from the wheelspace into the annulus. Ingress of hot gas into the wheelspace owing to the pressure field in the annulus is termed externally-induced (EI) ingress. A schematic representing EI

ingress is shown in Fig. 2.11. Combined ingress occurs when the effects of rotation and external flow are both important.

The importance of external flow on the sealing performance of turbine rim seals was first made apparent in an early study by Campbell (1978). The author put forward the argument that the static pressure variation in the annulus resulting from flow through the vane and blade passages would result in regions where the annular pressure exceeded the pressure radially inward of the rim seal, thus leading to ingress of external flow into the wheelspace. This suggestion paved the way for future research into EI ingress.

Abe *et al.* (1979) carried out an experimental study into ingress on a rig comprising a 1.5-stage stator-rotor-stator setup with external flow supply. Two wheelspaces were formed by this setup: the first, an upstream cavity between the upstream stator and rotor; the second, a downstream cavity between the rotor and downstream stator. The two wheelspaces were independently supplied with sealing flow through their respective stator discs. An asymmetric annular pressure profile was generated by installing nozzle guide vanes on the peripheral stator shrouds; the rotor shroud was bladeless. Propane density measurements were made at a range of radial locations on the stator walls to determine the amount of fluid ingested from the annulus into the two wheelspace cavities. For a range of complex engine representative seal geometries the authors found that, for a fixed Re_ϕ, increasing the annular flow rate necessitated an increase in the coolant flow required to prevent ingress into the wheelspaces for a given seal geometry (the sealing characteristic were broadly similar for the two wheelspaces). This confirmed the proposition made by Campbell (1978) that the annular flow conditions played an important part in the ingress phenomenon.

Phadke and Owen (1988b, c) explored rim seal performance characteristics on a rotor-stator system with quasi-axisymmetric and asymmetric annular flow. The annular flow was supplied through a mesh, onto which, in the absence of blades and vanes, honeycomb sections were installed to generate circumferential pressure asymmetries. Sealant flow was provided to the wheelspace through a central line in the stator. $C_{w,min}$ was determined using three experimental techniques: flow visualisation and concentration and static pressure criterions.

Phadke and Owen (1988b) determined $C_{w,min}$ for $0 < Re_\phi < 10^6$ and $0 < Re_W < 10^6$ for three seal geometries: two axial seals, the first with clearance stator-side, the second with clearance rotor-side; and a radial clearance seal. Their measurements for quasi-axisymmetric external flow showed that:

- In the absence of external flow (i.e. $Re_W = 0$) for the axial clearance seals $C_{w,min}$ was proportional to Re_ϕ. This agreed with the findings of Bayley and Owen (1970).

- For the largest values of Re_W tested, $C_{w,min}$ was proportional to Re_W and independent of Re_ϕ for all seal geometries (this is shown in Fig. 2.12 for one of the axial seals).

- At small values of Re_W, there was an initial decrease in $C_{w,min}$ with increasing Re_W. Owen (2011b) suggested that this undershoot behaviour was evidence of a region of combined ingress, where ingestion levels were dictated by the combined effects of fluid rotation in the wheelspace and the pressure profile in the annulus.

Phadke and Owen (1988c) furthered their investigation into EI ingress by looking into the effect of pressure asymmetry on the sealing performance of the three seal geometries tested in Phadke and Owen (1988b). These seals were tested for different pressure profiles to ascertain the effects of the maximum circumferential pressure difference in the annulus ($C_{p,max}$ in non-dimensional form) and Re_W on $C_{w,min}$. The pressure coefficient was defined as:

$$C_{p,max} = \frac{\Delta p}{1/2 \rho W^2} \tag{2.20}$$

where

$$\Delta p = p_{2,max} - p_{2,min} \tag{2.21}$$

$p_{2,max}$ and $p_{2,min}$ were the maximum and minimum static pressures measured on the outside wall of the annulus.

The variation of $C_{w,min}$ with Re_W was measured at multiple levels of $C_{p,max}$; the rotor disc was kept stationary (i.e. $Re_\phi = 0$) to ensure that ingress into the wheelspace was driven purely by the pressure asymmetry in the annulus and not by the rotation of the disc. The authors found that under EI ingress conditions, $C_{w,min}$ was proportional to Re_W and increased with $C_{p,max}$. This is demonstrated by Fig. 2.13, which shows $C_{w,min}$ against Re_W for a simple axial clearance seal; in the figure $C_{p,max}$ increases monotonically with asymmetry number.

Phadke and Owen (1988c) also measured the variation of $C_{w,min}$ with Re_W and Re_ϕ at $C_{p,max} = 0.48$ (the largest value tested) for one of their axial seals. The authors discovered that when comparing the asymmetric and quasi-axisymmetric measurements for the same seal, the two cases proved qualitatively similar: for $Re_W = 0$, $C_{w,min}$ was proportional to Re_ϕ; at relatively large values of Re_W, the data for all Re_ϕ tended towards an asymptote formed by the $Re_\phi = 0$ case (often referred to as the EI asymptote); and at small values of Re_W, there was an undershoot region. Figure 2.14 shows the experimental data for $C_{p,max} = 0.48$; it is

clear from the figure that the asymmetric and quasi-axisymmetric cases tended towards different EI asymptotes.

Phadke and Owen correlated the results for all their seals at G_c = 0.005, 0.01 and 0.02 for Re_ϕ = 0 (i.e. EI ingress) using the following relationship:

$$C_{w,min} = 2\pi G_c K P_{max}^{1/2} \tag{2.22}$$

where K is an empirical constant and

$$P_{max} = \frac{1}{2} C_{p,max} Re_W^{\,2} \tag{2.23}$$

A value of K = 0.6 provided a good fit to the experimental data.

In light of the Phadke and Owen (1988b, c) findings, Hamabe and Ishida (1992) carried out further research into EI ingress. Gas concentration was measured in the wheelspace of a single-stage experimental rig to determine $C_{w,min}$ for a simple axial clearance seal; pressure asymmetries were generated in the annulus by directing the annular flow through a set of inlet nozzle guide vanes installed on the peripheral shroud of the stator (the rotor was bladeless). The authors used a theoretical orifice model to fit their experimental data. The model was solved for three theoretical pressure profiles and the measured pressure profile to give predictions of the variation of ε with $C_{w,0}$. It was observed that the predicted variation of ε with $C_{w,0}$ was dependent upon the pressure profile used in the model. Good agreement was found between the experimental data and the model when the measured profile was used; Hamabe and Ishida therefore concluded that knowledge of the pressure form in the annulus was necessary to accurately evaluate ingestion levels.

Dadkhah *et al.* (1992) undertook an empirical study into EI ingress on a rig with a reversible rotor-stator assembly. Interchanging the disc positions enabled the authors to investigate ingestion into upstream and downstream wheelspace cavities. Figure 2.15 shows the rim seal geometries for the upstream (a) and downstream (b) cavities; the upstream cavity featured an ‘upward rotor lip’ seal and the downstream cavity featured an ‘upward stator lip’ seal. No vanes or blades were installed on the stator or rotor shrouds, thus the circumferential pressure profile in the annulus was measured as quasi-axisymmetric. The sealant flow was seeded with tracer gas so that concentration measurements could be made in the wheelspace to determine ingestion levels. Concentration taps were installed at four radial locations and, for each radial location, at seven axial locations in the wheelspace. The sealing effectiveness, ε, was determined from the average value of the concentration measurements made at all sample points in the wheelspace.

The Dadkhah *et al.* concentration measurements showed that upon entering the wheelspace, the ingested fluid travelled across to and down the stator before being entrained across the wheelspace into the rotor boundary layer. The rotor surface showed the 'least-contamination' against the ingested fluid; in contrast, the stator surface was exposed to the greatest levels of ingestion. The authors concluded that if a value of ε = 0.95 could be tolerated by engine designers, then a significant amount of sealing flow (approx. 35%) could be saved over a fully sealed system. Comparison of the sealing performance of the two abovementioned seals ranked the stator-lip seal as most effective; however, owing to the different external flow direction for the two cavities, a caveat was placed upon this ranking.

Chew *et al.* (1994) used N_2O as a tracer gas in central fed sealant flow to make experimental measurements of sealing effectiveness on a single-stage gas turbine rig featuring a bladeless rotor. Only one rim seal was tested: a simple axial geometry with clearance $G_{c,ax}$ = 0.01 rotor-side. Superposed external flow was fed through nozzle guide vanes to generate asymmetric external flow in the annulus. The authors compared their experimental measurements with those obtained by complimentary CFD and predictions made using the model developed by Hamabe and Ishida (1992).

Chew *et al.* measured the variation of the egress and ingress discharge coefficients, $C_{d,e}$ and $C_{d,i}$ respectively, with the ratio of the axial annular flow velocity (u_e) to average radial velocity through the rim seal (u_m); these measurements, which are shown in Fig. 2.16, were made without vanes for Re_ϕ = 0. The authors found that the Hamabe and Ishida theoretical model, which was solved using the measured discharge coefficients, over-estimated ingestion levels when compared with their experimental measurements. It was suggested that the neglect of the tangential component of velocity through the rim seal in the model may have resulted in this over-prediction.

The Chew *et al*. CFD model under-predicted ingress levels when compared with their experiments at high sealant flow rates. The authors suggested that this disagreement could be attributed to the fact that the CFD was modelled as a steady case and thus could not capture the unsteady 3D pressure profile in the annulus. Unsteady CFD models require computations at multiple blade-passing angles (i.e. the angle of the blade relative to the vane) to produce representative time-averaged results; this is computationally demanding compared with steady CFD codes, which model the rotor in a single fixed position. Computational limitations restricted the development of complex unsteady CFD codes at the time of the Chew *et al.* study; consequently, experimental studies remained vital in improving engine designers understanding of the ingestion phenomenon.

Green and Turner (1994) carried out an experimental study into EI ingress on the same rig as Chew *et al.* (1994) with the addition of blades on the rotor; measurement techniques were the same for two studies. Experiments were performed with and without blades so that their impact upon ingestion levels could be observed. Gas concentration readings in the wheelspace showed that the inclusion of blades on the rotor reduced the amount of ingestion into the wheelspace relative to the bladeless case. The authors concluded that the effect of blades on ingress to be 'complex' and researchers should not oversimplify rig design, but instead match as closely as possible real engines for experimental studies to be meaningful.

Bohn *et al.* (1995) measured EI ingress levels on a turbine rig with a bladeless rotor. Circumferential pressure asymmetries were generated in the annulus by feeding the mainflow through a set of inlet guide vanes. The static pressure profile was measured across two vane pitches at three locations axially downstream of the vane trailing edge. The authors showed that the magnitude of the peak-to-trough pressure variation in the annulus decayed with distance from the vane trailing edge; as a result, ingestion levels increased as the vanes were moved closer to the rim seal.

Bohn *et al.* (1999) made sealing effectiveness measurements on an upstream cavity rig with vanes and blades. Sealant flow, which was seeded with CO_2 as a tracer gas, was supplied through a central line in the stator. The circumferential pressure variation in the wheelspace was measured via static pressure taps on the stator shroud, 1.5mm axially downstream of the vane trailing edge. The results presented in the study showed that ingestion levels increased with increasing Re_W / Re_ϕ owing to a consequential rise in driving pressure, ΔC_p, where:

$$\Delta C_p = \frac{\Delta p}{1/2\rho\Omega^2 b^2} \tag{2.24}$$

Δp was the peak-to-trough pressure difference measured in the annulus, as defined by Eq. 2.21.

Khilnani and Bhavnani (2001) investigated the sealing performance of an axial seal on an upstream cavity rig without blade and vanes. CO_2 sampling and static pressure measurements were used to determine $C_{w,min}$ at a range of Re_W and Re_ϕ values. The measurements showed good agreement with those of Phadke and Owen (1988c) for asymmetric external flow. As can be seen in Fig. 2.17, the study returned two main findings: first, at low values of Re_W, the influence of Re_ϕ on $C_{w,min}$ was significant; and second, as Re_W increased, $C_{w,min}$ began to converge for all Re_ϕ. The authors experimented with lower values of Re_W / Re_ϕ (almost half) compared with Phadke and Owen; consequently, although

converging, their measurements of $C_{w,min}$ did not become independent of Re_ϕ at high Re_W (i.e. they did not reach the EI asymptote). It is therefore suggested that the Khilnani and Bhavnani experiments were conducted for combined ingress.

Bohn and Wolff (2003) conducted an EI ingress study on a 1.5-stage rig with vanes and blades. Four seal geometries were tested: a shroudless setup, config. 1; an axial seal with clearance rotor-side, config. 2; a radial clearance seal, config. 3; and a double seal, config. 4. The mainflow gas path was fed through a set of upstream vanes to generate pressure asymmetries in the annulus. A low radius supply of sealant flow (seeded with CO_2) was directed to the wheelspace through the stator; $C_{w,min}$ was determined from concentration measurements on the stator wall. The authors correlated their results using $C_{w,min} = 2\pi G_c K P_{max}^{1/2}$ (P_{max} is defined in Eq. 2.23), where K, an empirical constant, was chosen to give the least squares error to the experimental data for each seal geometry. Figure 2.18. shows the experimental data and fitted correlations for the four geometries; the data was best represented by an individual value of K for each seal. It was suggested by the authors that the single value of K = 0.6 used by Phadke and Owen (1988c) to correlate their data for multiple seals was overly conservative.

The Bohn and Wolff correlations showed that the radial clearance seal (config. 3) offered a significant improvement in sealing performance over the axial clearance seal (config. 2), which agreed with the findings of numerous existing studies. The double radial overlap seal (config. 4) provided the best sealing performance of those tested.

Johnson *et al.* (2006) used time-averaged pressure distributions obtained from CFD in conjunction with a single discharge coefficient (C_d) orifice model to estimate ingress and egress through turbine rim seals. A value of C_d = 0.4 provided a good fit of the model to the experimental data of Bohn *et al.* (2003) for two vane and blade configurations (1a and 1c, narrow and wide spacing between the vanes and blades respectively); the fit for config. 1c is shown in Fig. 2.19. The authors concluded that, given the good agreement between the fits and experimental data, the model would prove useful to engine designers by offering efficiency in solution over complex CFD codes.

Johnson *et al.* (2008) extended the single discharge coefficient orifice model developed in Johnson *et al.* (2006) to incorporate two discharge coefficients: $C_{d,i}$ and $C_{d,e}$ for ingress and egress respectively. The results produced by the model for unequal values of $C_{d,i}$ and $C_{d,e}$ provided better agreement with the experimental sealing effectiveness data than those obtained for $C_{d,i} = C_{d,e}$. The model was further developed by adding a term from the radial momentum equation to account for the effects of swirl. It was shown that the predictions

made by the model with swirl could be matched by the model without swirl by modifying the discharge coefficients in the latter; given this agreement, the authors concluded that the swirl term could be ignored to simplify the model.

Owen (2011b) extended the RI orifice theory presented in Owen (2011a) to EI and combined RI and EI ingress cases. The EI and combined ingress orifice equations were derived for compressible and incompressible inviscid swirling flow from first principles. Two discharge coefficients were built into the theory to account for viscous losses: $C_{d,i}$ for ingress and $C_{d,e}$ for egress. The circumferential variation of pressure in the annulus was assumed to follow a 'saw-tooth' profile (shown in Fig. 2.20) so as to allow the orifice equations to be solved analytically. For EI ingress with negligible internal and external swirls (i.e. $\beta_1 = \beta_2 = 0$) the relationship between ε and Φ_0 was shown to be a function of $\Phi_{min,EI}$ and Γ_c (defined in Eq. 2.17), where:

$$\Phi_{min,EI} = \frac{2}{3} C_{d,e} \Delta C_p^{1/2} \tag{2.25}$$

The non-dimensional pressure difference, ΔC_p, is given in Eq. 2.24.

The combined ingress orifice equations were solved for negligible external swirl to give the following relationship between the minimum sealant flow to prevent ingress for the combined case, $\Phi_{min,CI}$, and $\Phi_{min,RI}$:

$$\frac{\Phi_{min,CI}}{\Phi_{min,RI}} = \frac{2}{3} \frac{C_{d,e,CI}}{C_{d,e,RI}} \frac{(1+\Gamma_{\Delta p})^{3/2} - 1}{\Gamma_{\Delta p}} \tag{2.26}$$

where $C_{d,e,CI}$ and $C_{d,e,RI}$ are the egress discharge coefficients for combined and RI ingress respectively, and

$$\Gamma_{\Delta p} = \frac{\Delta C_p}{C_{\beta_1}} \tag{2.27}$$

The modified internal swirl, $C_{\beta 1}$, is defined in Eq. 2.19.

The EI orifice equations were fitted to the Johnson *et al.* (2008) experimental effectiveness data using equal discharge coefficients ($\Gamma_c = 1$); the agreement between the theory and data was good. Owen suggested that $\Gamma_c = 1$ would not necessarily provide good fits to all experimental data and that a least-squares fit would be needed to accurately determine an appropriate value of Γ_c. The combined ingress orifice equations were not validated owing to a lack of published data for test cases where the combined effects of RI and EI ingress determine the relationship between ε and Φ_0.

2.5 Computational fluid dynamics

A comprehensive review of literature relevant to CFD in ingress research is provided by Zhou *et al.* (2011a); the interested reader is referred to this study for a fuller understanding of the methodology behind CFD and the modelling considerations pertinent to ingress.

CFD is an important tool for all gas turbine engine designers, including those looking to minimise the expenditure of coolant in preventing ingress. CFD allows the complex fluid dynamics in the wheelspace of rotor-stator systems and the gas path interactions radially outward of the rim seal to be investigated in a level of detail that is difficult to achieve experimentally. However, the three-dimensional unsteady pressure fields present in the annulus can be difficult to capture with simple CFD models; modelling the wheelspace over a 360° sector (for example see Wang *et al.* (2012)) is required to fully capture the flow physics associated with ingestion. These large models require significant computational power and, consequently, are expensive and time-consuming to run.

Experiments have played, and will play for the foreseeable future, a crucial role in the success of CFD; the results obtained on experimental rigs have been used to validate models prior to their use as design tools. An important future aspect of CFD will be its use in scaling measurements made at incompressible flow conditions on rigs to the compressible flow conditions in engines; Teuber *et al.* (2012) presented a preliminary study on scaling methods.

2.6 State of the art

The majority of the studies discussed above were focused on generic rim seal geometries. State of the art seal geometries are often much more complex than those tested in experiments (generic geometries are used on rigs so that the fundamental physics of certain design features can be understood). Engines typically operate with double seal type geometries (see Fig. 2.21); these are used to constrain ingested fluid in the outer wheelspace, thereby preventing the penetration of hot air inner wheelspace region. Fig 1.8 provides an example of a complex seal design that may be found in an engine.

2.7 Experimental ingress research at the University of Bath

The work discussed in this section was the basis of three journal paper publications on all of which the author of this thesis was co-author and a significant contributor. The findings of these publications are significant to the work conducted in Chapters 3 and 4 of this thesis,

and so an overview is provided to aid with the understanding of the work in these later chapters. The interested reader is referred to the complete papers, which are provided in Appendix D.

Sangan *et al.* (2011a) measured the effect of Re_ϕ on the variation of ε with Φ_0 in the upstream cavity of a single-stage gas turbine rig in the presence of external flow for axial and radial clearance seals; all measurements were made 'on-design' (i.e. for balanced velocity triangles in the mainstream annulus). Concentration sealing effectiveness, ε_c, was determined on the stator wall from CO_2 sample measurements at r/b = 0.958 (the sealant flow was seeded). ε_c was defined as:

$$\varepsilon_c = \frac{c_s - c_a}{c_0 - c_a} \tag{2.28}$$

where c_s, c_a and c_0 were the measured concentration levels on the stator wall and in the annulus and sealant flow line respectively. By definition $\varepsilon_c \rightarrow 0$ as $\Phi_0 \rightarrow 0$ and $\varepsilon_c \rightarrow 1$ as $\Phi_0 \rightarrow \Phi_{min}$. The non-dimensional ingress flow into the wheelspace, Φ_i, was determined from the measurements of ε and Φ_0 using:

$$\Phi_i = \Phi_0 (\varepsilon^{-1} - 1) \tag{2.29}$$

The authors used the EI orifice model developed by Owen (2011b) to form an explicit relationship between ε and Φ_0, as given in Eq. 2.30 below (for the Sangan *et al.* (2011a) experiments, $\varepsilon = \varepsilon_c$). This equation—referred to as the 'EI effectiveness equation'—was fitted to the experimental variation of ε and Φ_0 using the statistical technique presented by Zhou *et al.* (2011b). Equation 2.31, which was formed from Eqs. 2.29 and 2.30, was used to fit the experimental variation of $\Phi_{i,EI}$ with Φ_0.

$$\frac{\Phi_0}{\Phi_{min,EI}} = \frac{\varepsilon}{[1 + \Gamma_c^{-2/3}(1-\varepsilon)^{2/3}]^{3/2}} \tag{2.30}$$

and

$$\frac{\Phi_{i,EI}}{\Phi_{min,EI}} = \frac{1-\varepsilon}{[1 + \Gamma_c^{-2/3}(1-\varepsilon)^{2/3}]^{3/2}} \tag{2.31}$$

Sangan *et al.* (2011b) measured the variation of ε with Φ_0 at three values of Re_ϕ for RI ingress. The same geometries were tested as those in Sangan *et al.* (2011a): a simple axial clearance seal and a radial clearance seal. The authors developed the RI orifice model from Owen (2011a) to form the 'RI effectiveness equation' given in Eq. 2.32 below. This equation was fitted to the experimental variation of ε and Φ_0 using the statistical fitting

method of Zhou *et al.* (2011b). Equation 2.33, derived from Eqs. 2.29 and 2.32, was fitted to the experimental variation of $\Phi_{i,RI}$ with Φ_0.

$$\frac{\Phi_0}{\Phi_{min,RI}} = \frac{\varepsilon}{[1+(1-\varepsilon)^{1/2}][1+\Gamma_c^{-2}(1-\varepsilon)]^{1/2}} \tag{2.32}$$

and

$$\frac{\Phi_{i,RI}}{\Phi_{min,RI}} = \frac{1-\varepsilon}{[1+(1-\varepsilon)^{1/2}][1+\Gamma_c^{-2}(1-\varepsilon)]^{1/2}} \tag{2.33}$$

The Sangan *et al.* (2011a, b) experimental measurements of ε with Φ_0 are plotted in Fig. 2.22 for the axial and radial seals for RI and EI ingress alongside the aforementioned theoretical fits. As predicted by the orifice equations, ε versus Φ_0 was invariant with Re_ϕ for both RI and EI ingress. The fits were in good agreement with the data and yielded $\Phi_{min,EI}$ = 0.326 for the axial seal and $\Phi_{min,EI}$ = 0.0915 for the radial seal; consequently, the radial seal outperformed the axial seal by a factor of approximately 3.5. Given the good agreement between the data and the theory, the authors concluded that the orifice model could be useful as a tool for engine designers, particularly if used in combination with CFD to extrapolate data collected on test rigs up to engine representative operating conditions.

The ratio of $\Phi_{min,EI}$ to $\Phi_{min,RI}$ was measured as 3.9 and 2.9 for the axial and radial seals respectively. The authors tentatively suggested that, based upon the fit of the EI asymptote to the axial seal data of Phadke and Owen (1988c), for $\Phi_{min,EI} / \Phi_{min,RI} > 2$ then EI ingress occurs; when $\Phi_{min,EI} / \Phi_{min,RI} < 2$ then ingress will be effected by rotation and would thereby fall into the combined ingress region.

Sangan *et al.* (2012) used the Bath test rig to measure the sealing effectiveness of a range of generic single and double seals for EI ingress; the double seal geometries were chosen to represent the state of the art seals found in typical gas turbine engines. The study showed that double seals restrict ingress to the outer wheelspace cavity (see Fig. 2.21). The outer wheelspace attenuates the circumferential pressure asymmetry, thereby leading to less ingestion through the inner seal clearance (i.e. the inner wheelspace is partly protected from the ingested fluid). The performance limit for a double seal was shown to be where the pressure asymmetry in the outer wheelspace has been completely damped out and RI ingress occurs across the inner seal.

2.8 Summary

This chapter has provided an extensive review of the literature relevant to ingress through gas turbine rim seals. It was shown that the phenomenon can be broken down into three main categories: rotationally-induced (RI), externally induced (EI) and combined ingress.

RI ingress occurs when there is no mainflow through the turbine annulus. For the case of fluid rotating in the core in a rotor-stator system, a radial pressure gradient exists, which can lead to the pressures in the wheelspace falling below those radially outward of the rim seal. The difference in pressure across the rim seal will cause fluid to be drawn through the seal clearance into the wheelspace.

EI ingress is caused by the asymmetric pressure field in the annulus. The flow of fluid over the vanes and blades produces circumferential variation in pressure above the rim seal; this pressure variation can result in regions where the pressure in the annulus is greater than that in the wheelspace, leading to ingress. Combined ingress occurs when the rotational effects of the fluid in the wheelspace and the external pressure profile in the annulus are both important in the ingestion process (i.e. a combination of RI and EI ingress).

The study of existing literature has shown that RI and EI ingress are well-researched topics; however, there has been little work into the understanding and predicting of combined ingress. Combined ingress is of practical importance in aero engines, which frequently operate off-design, and in double seals where the pressure asymmetry in the annulus can be attenuated in a buffer cavity, resulting in combined ingress occurs through the inner seal clearance. There is clearly scope for theoretical and experimental research into combined ingress.

2.9 Figures

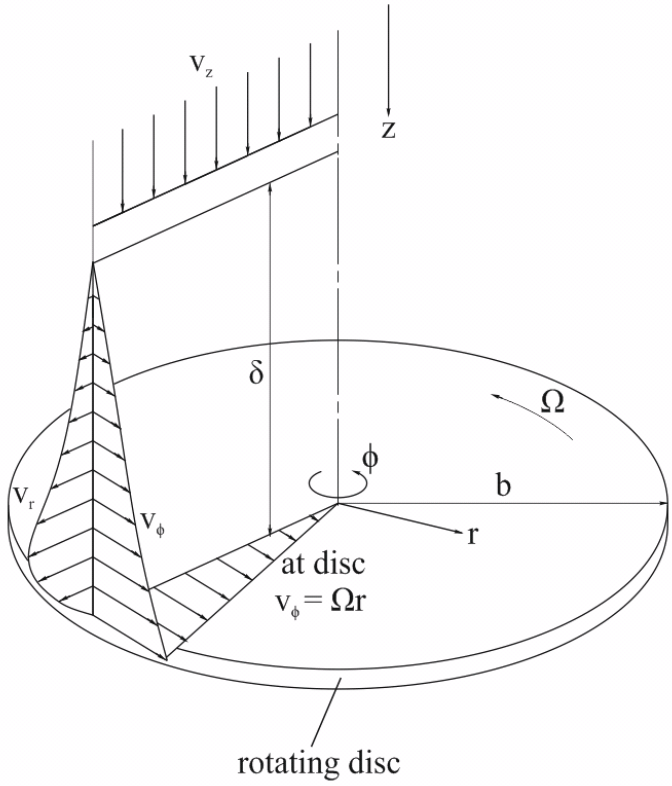

Figure. 2.1: Free-disc radial and tangential boundary layers (adapted from Childs (2011)). v_z, v_r and v_ϕ are the axial, radial and tangential fluid velocities respectively.

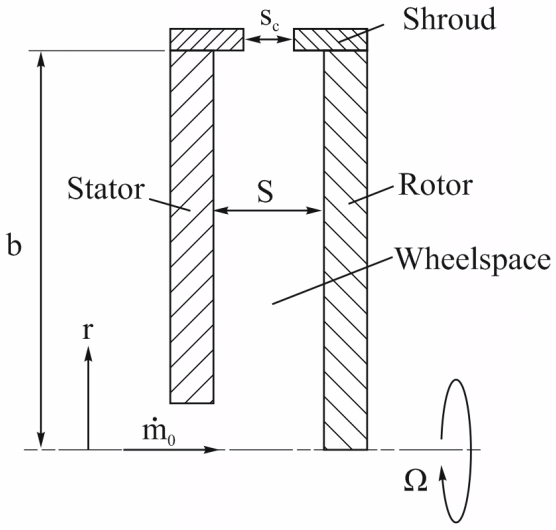

Figure. 2.2: Rotor-stator system with axial shroud clearance and supplied mass flow.

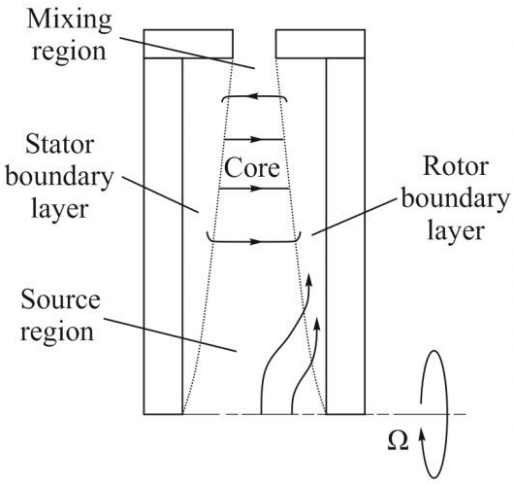

Figure. 2.3: Batchelor-type flow in an open rotor-stator system.

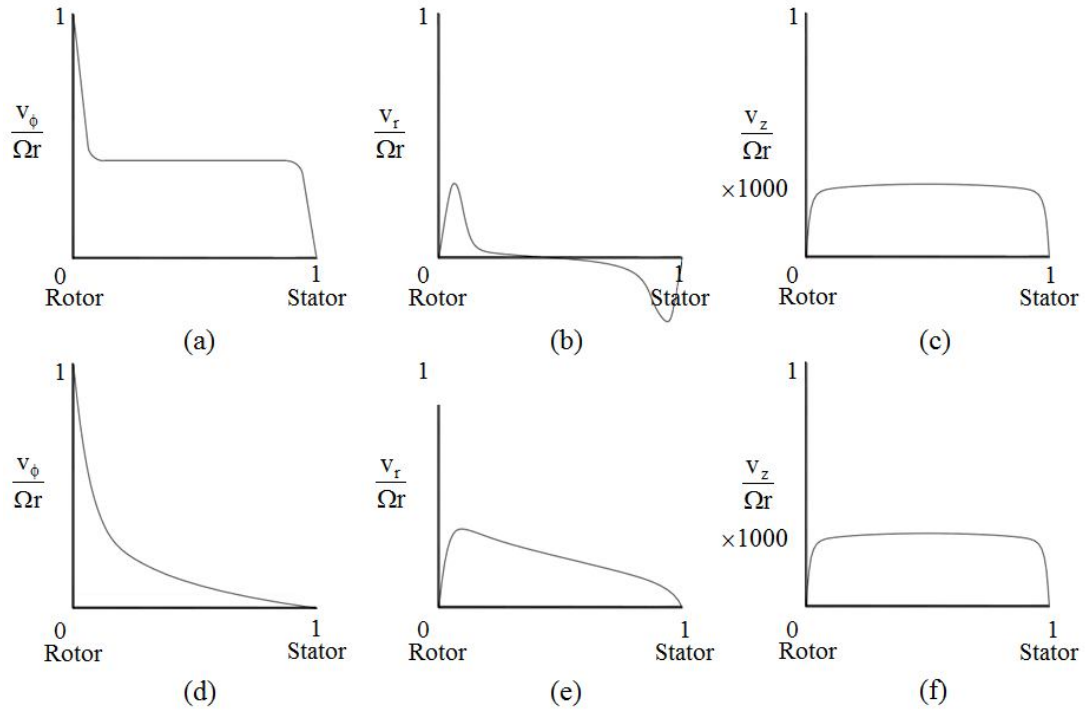

Figure. 2.4: Typical velocity profiles for a rotor-stator system: (a) to (c) Batchelor flow; (d) to (f) Stewartson flow (adapted from Childs (2011)).

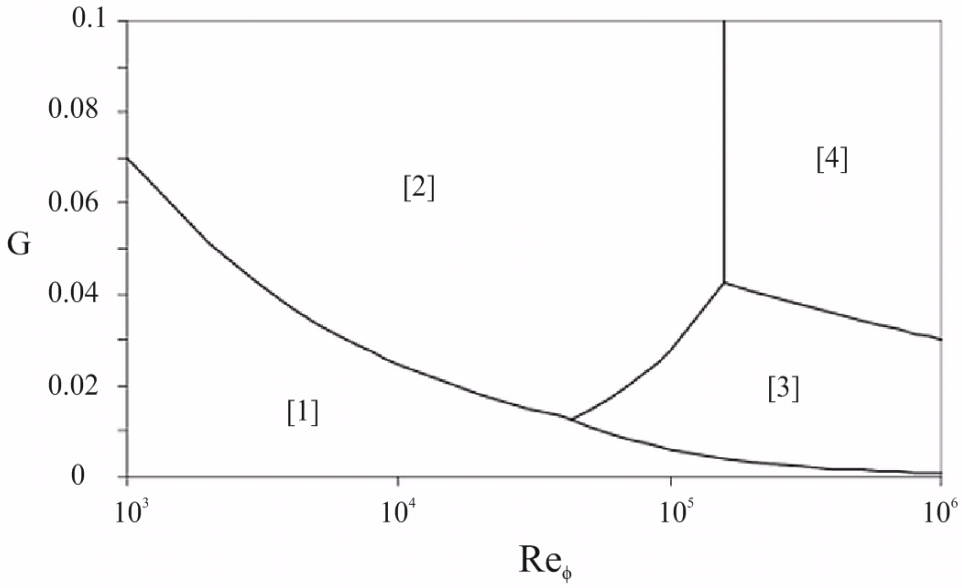

Figure. 2.5: Rotor-stator flow regimes (adapted from Childs (2011)): [1] Laminar flow, small clearance; [2] Laminar flow, large clearance; [3] Turbulent flow, small clearance; and [4] Turbulent flow, large clearance.

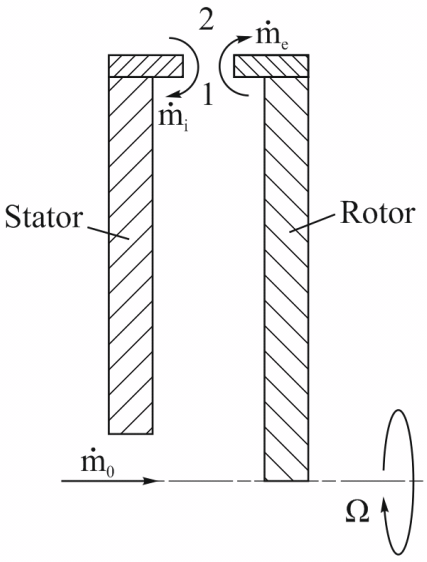

Figure. 2.6: Rotor-stator system with ingress, egress and sealant mass flow paths $\dot{m}_i$, $\dot{m}_e$ and $\dot{m}_0$ respectively.

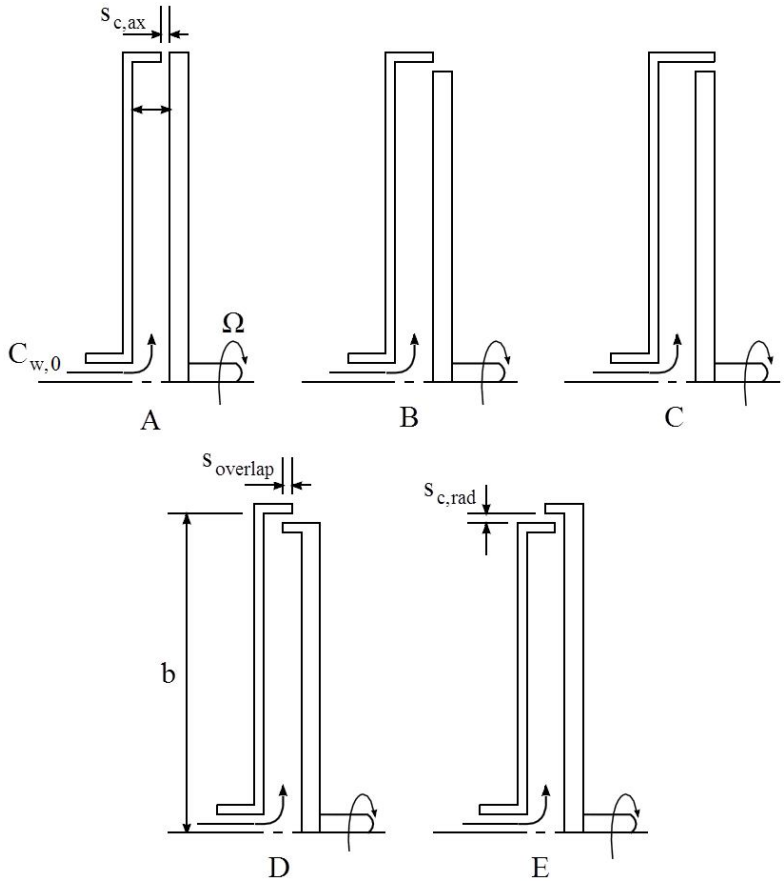

Figure. 2.7: Shroud geometries tested by Phadke and Owen (1983). Subscripts *ax* and *rad* refer to axial and radial clearances respectively.

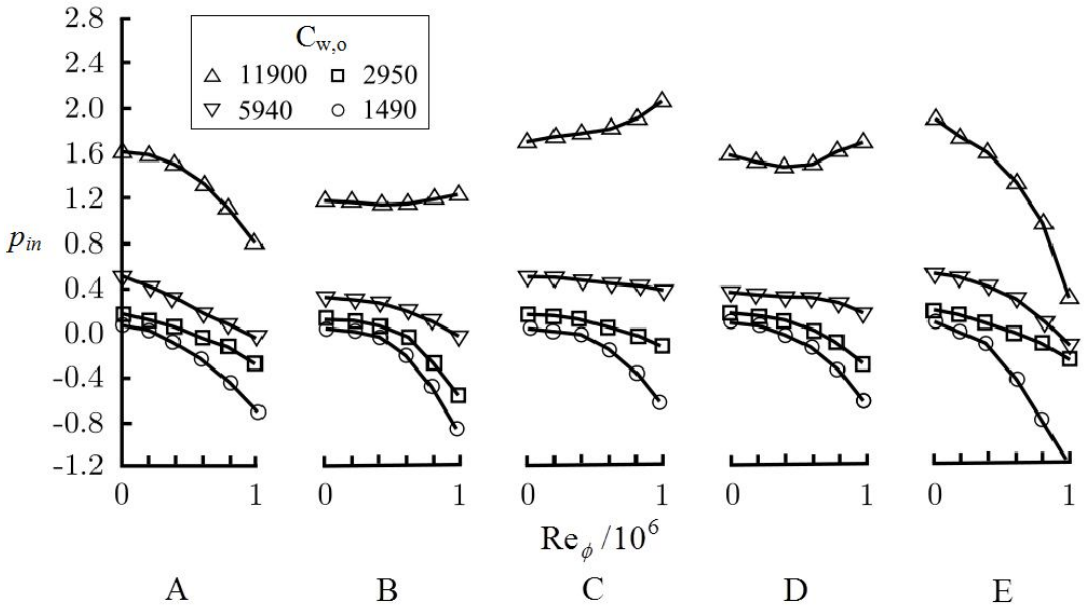

Figure. 2.8: Variation of ingress predicting pressure, p_{in}, with Re_ϕ for Phadke and Owen test geometries at four values of $C_{w,0}$ (adapted from Phadke and Owen (1983)).

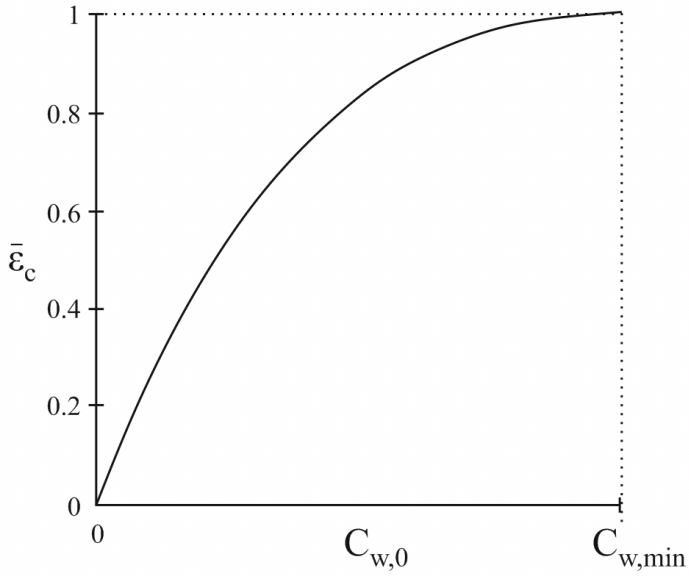

Figure. 2.9: Typical variation of $\bar{\varepsilon}_c$ with $C_{w,0}$ (adapted from Graber *et al.* (1987)).

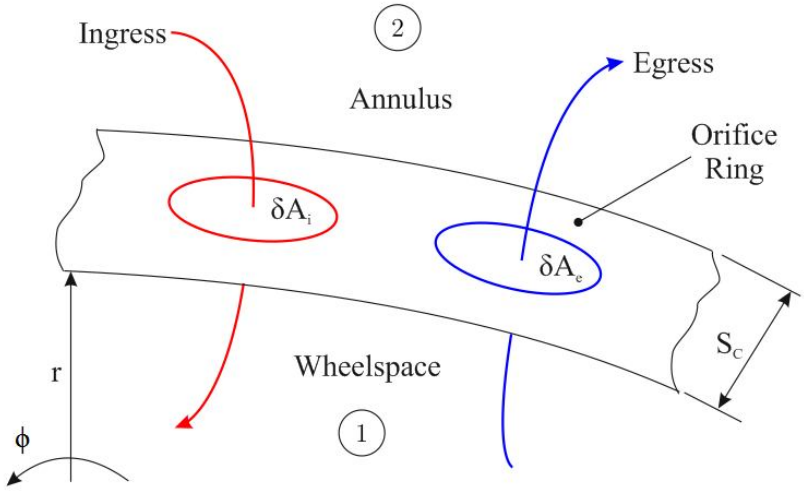

Figure. 2.10: Orifice model setup (adapted from Owen (2011a)).

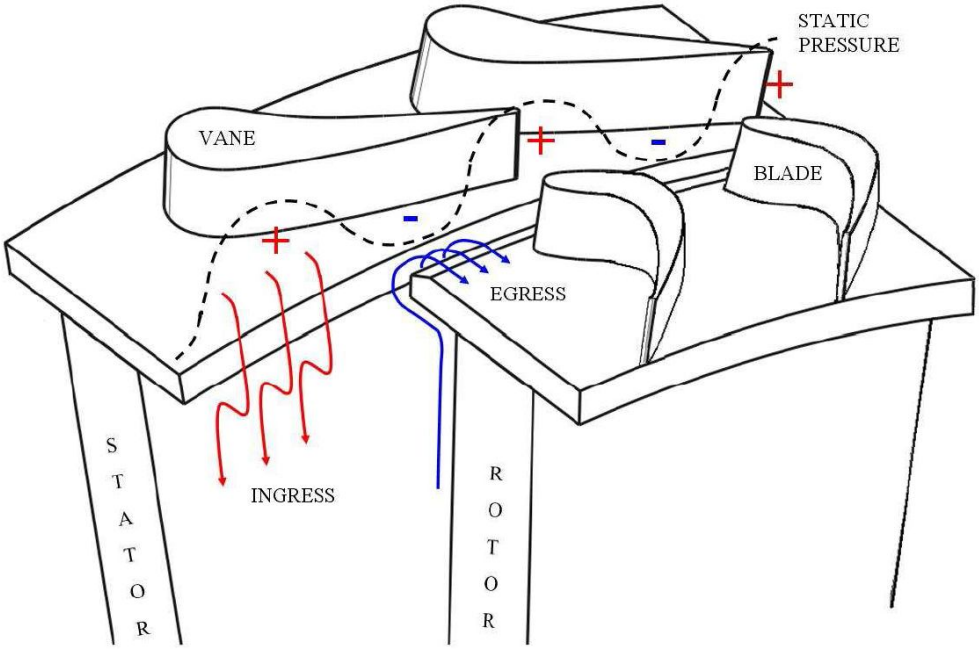

Figure. 2.11: Static pressure variation in annulus owing to flow over vanes and blades. Corresponding ingress and egress flow paths are shown (from Sangan *et al.* (2011a)).

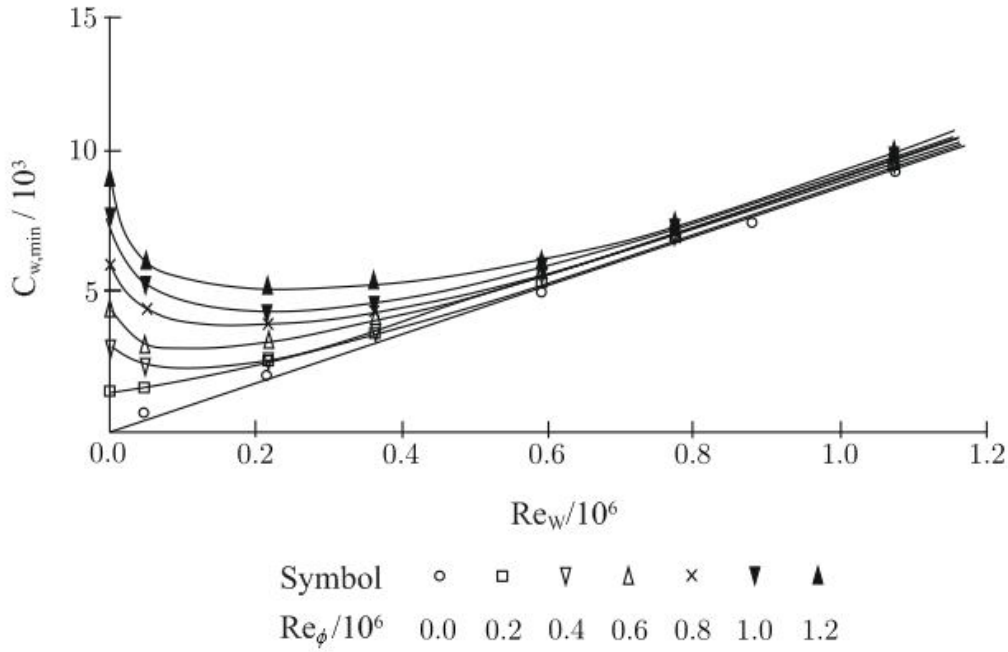

Figure. 2.12: Effect of Re_ϕ on the relationship between $C_{w,min}$ and Re_W for quasi-axisymmetric annular flow for an axial seal with clearance stator-side (adapted from Phadke and Owen (1988b)).

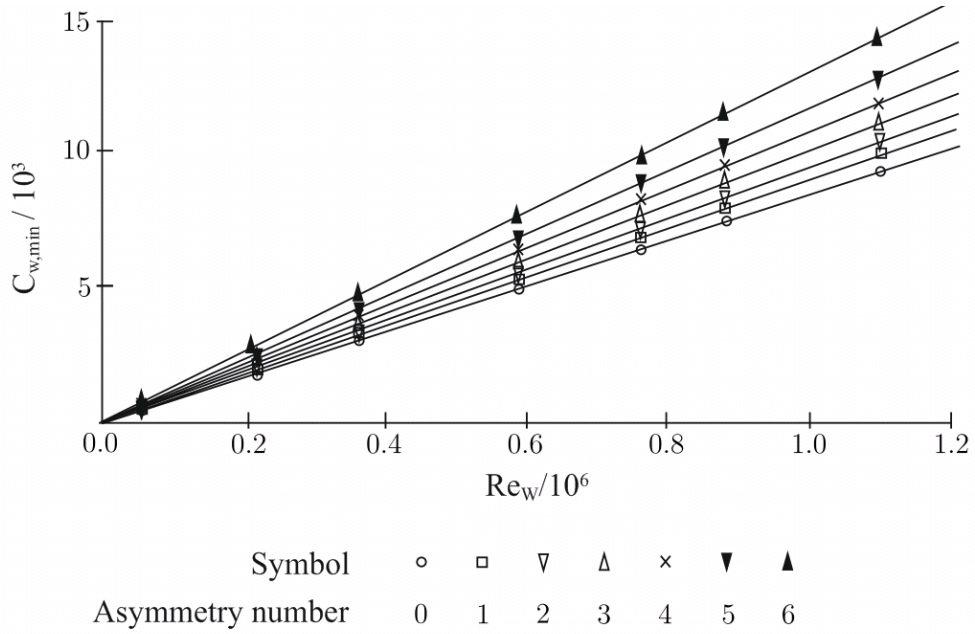

Figure. 2.13: Effect of $C_{p,max}$ on the relationship between $C_{w,min}$ and Re_W for an axial seal with clearance stator-side (adapted from Phadke and Owen (1988c)). $C_{p,max}$ increases monotonically with asymmetry number.

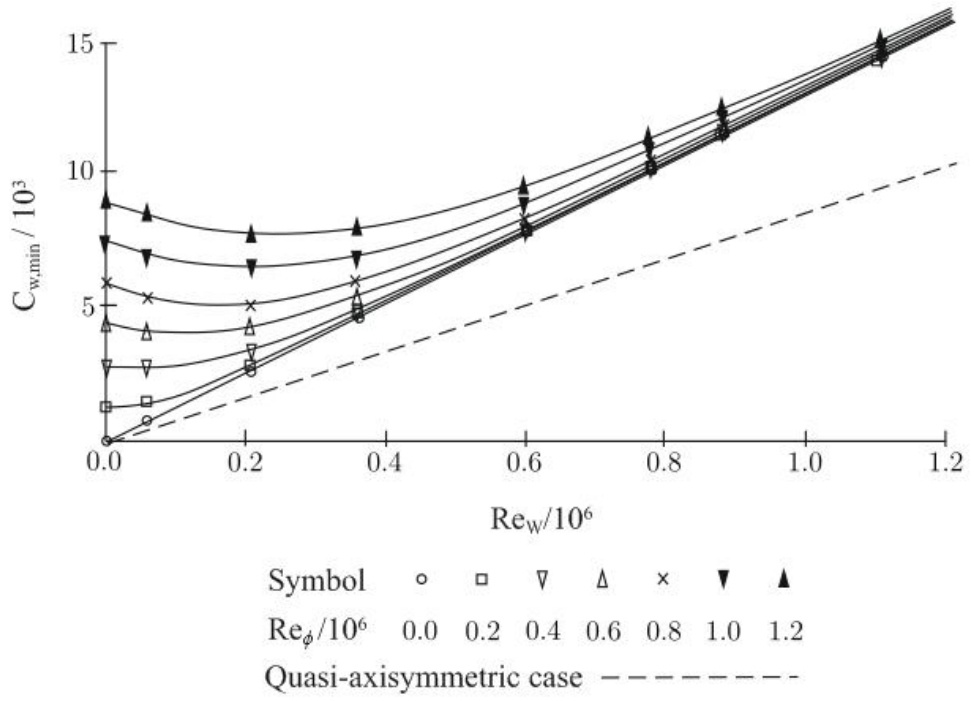

Figure. 2.14: Effect of Re_ϕ on the relationship between $C_{w,min}$ and Re_W for asymmetric annular flow with $C_{p,max}$ = 0.48 for an axial seal with clearance stator-side (adapted from Phadke and Owen (1988c)). The dashed line represents the EI asymptote for the quasi-axisymmetric case.

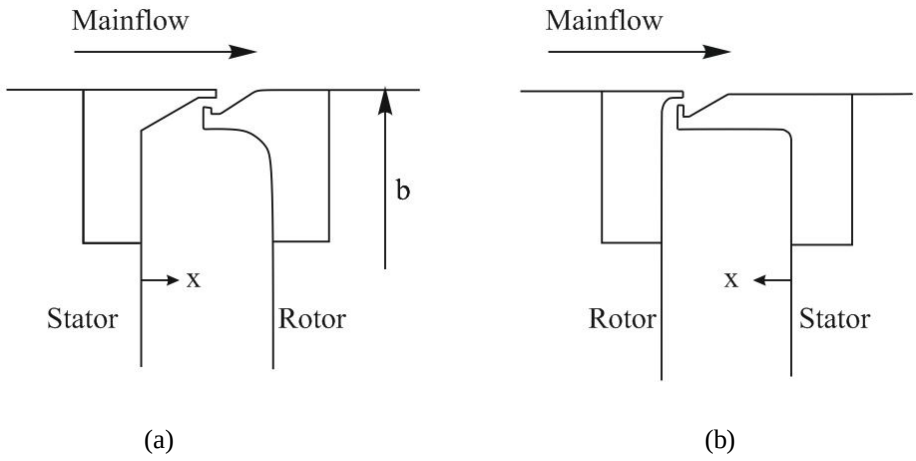

(a) (b)

Figure. 2.15: Rim seal arrangements: (a) upstream cavity with rotor-lip seal for, (b) downstream cavity with stator-lip seal (adapted from Dadkhah *et al.* (1992)).

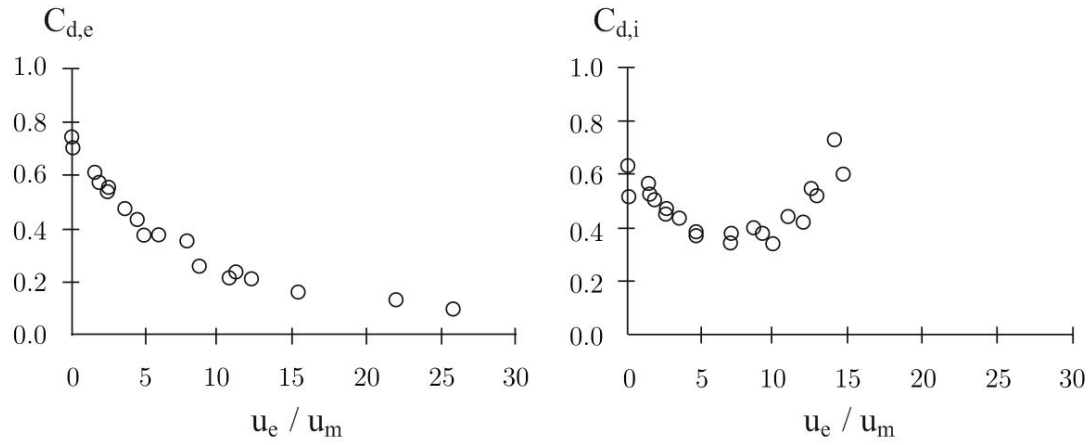

(a) (b)

Figure. 2.16: Relationship between rim seal discharge coefficients and u_e/u_m for $Re_\phi = 0$, as measured by Chew *et al.* (1994): (a) Egress coefficient; (b) Ingress coefficient.

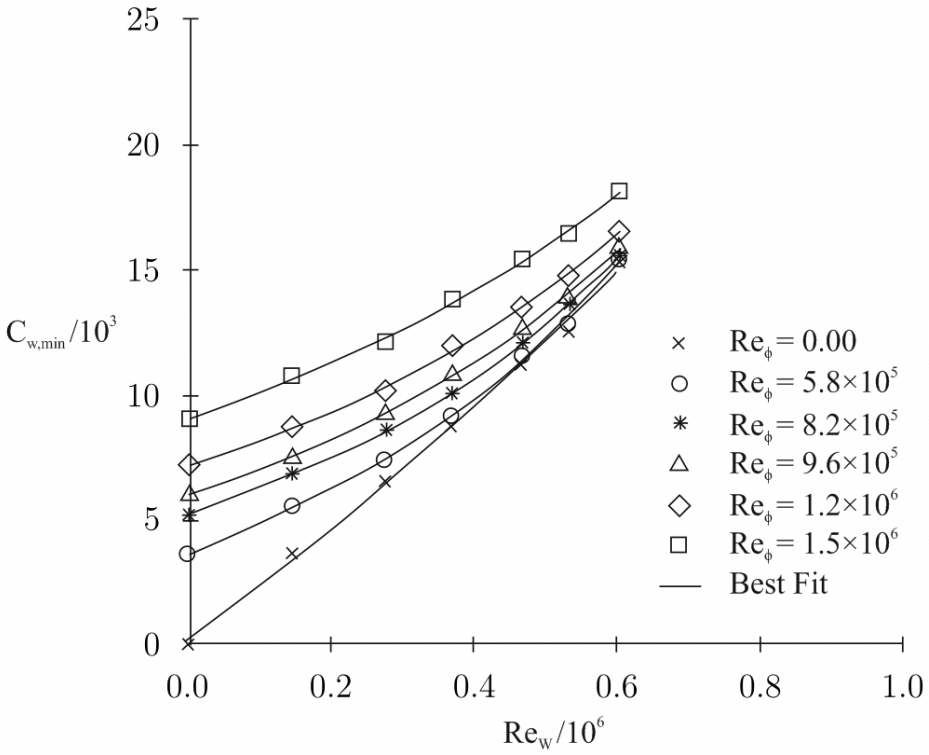

Figure. 2.17: Variation of $C_{w,min}$ with Re_W and Re_ϕ for an axial seal with clearance rotor-side (adapted from Khilnani and Bhavnani (2001)).

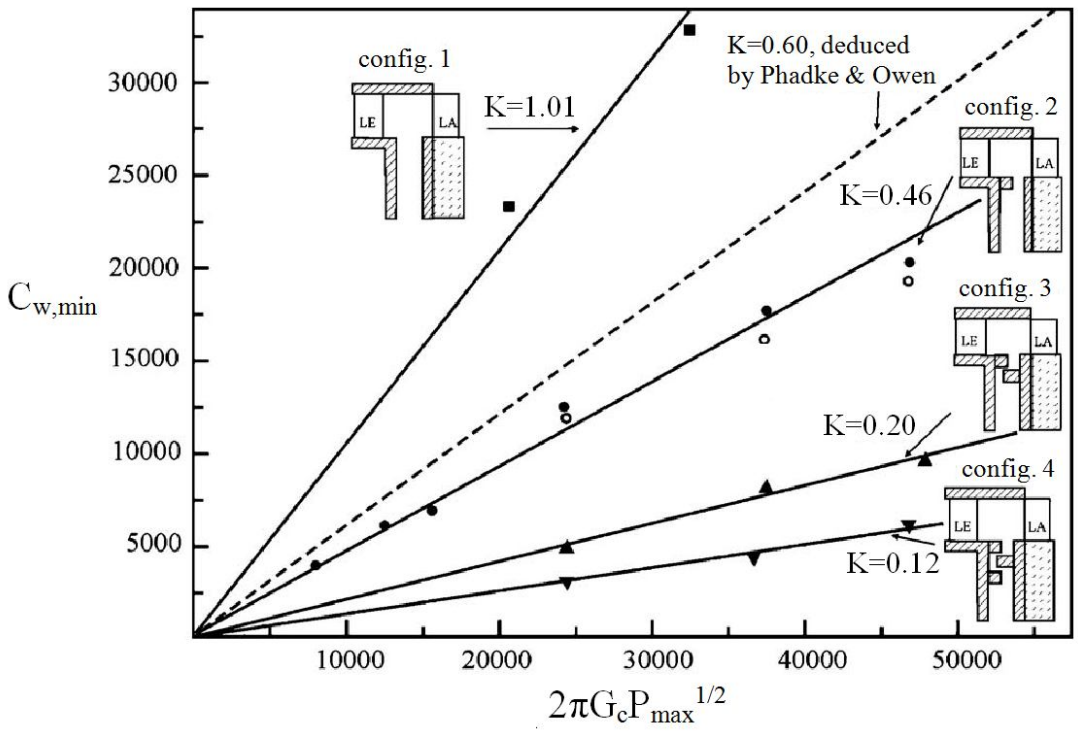

Figure. 2.18: Variation of $C_{w,min}$ with $2\pi G_c P_{max}^{1/2}$ for four seal geometries. K is the empirical correlating factor (adapted from Bohn and Wolff (2003)).

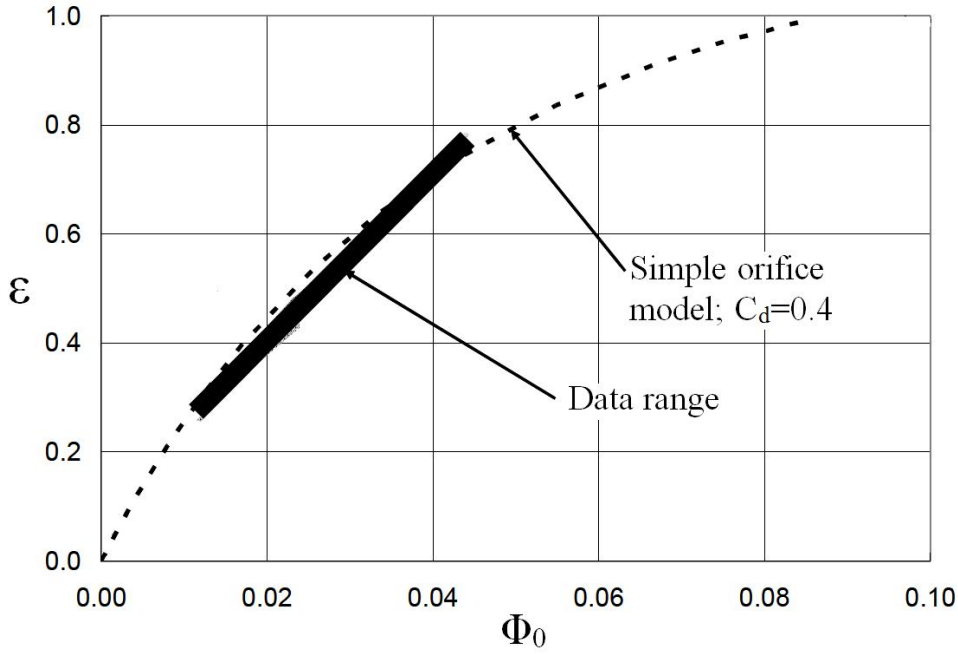

Figure. 2.19: Distribution of ε with Φ_0 in the downstream wheelspace cavity for config. 1c (adapted from Johnson *et al.* (2006)). The experimental data is contained in the black envelope; the prediction made by the simple orifice model with C_d = 0.4 is represented by the dashed line.

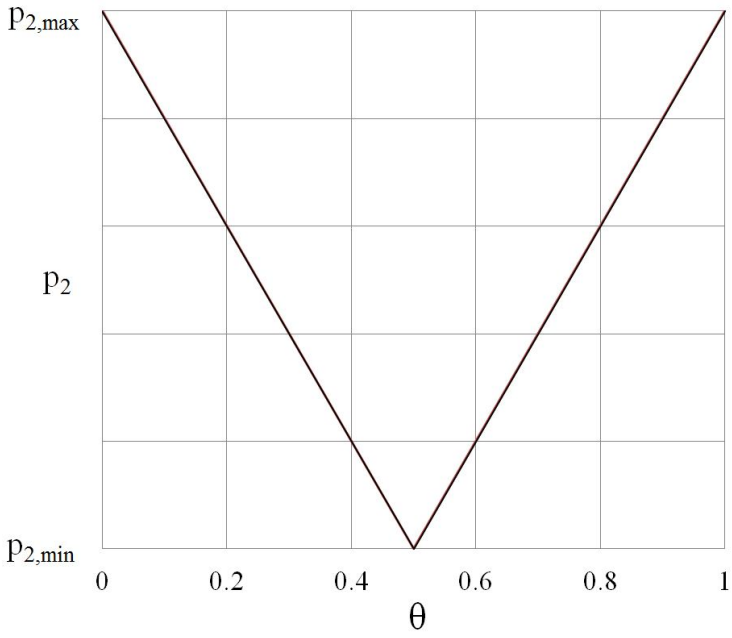

Figure. 2.20: Saw-tooth pressure profile (adapted from Owen (2011b)). p_2 is the static pressure in the annulus and θ is the non-dimensional circumferential angle across one vane pitch.

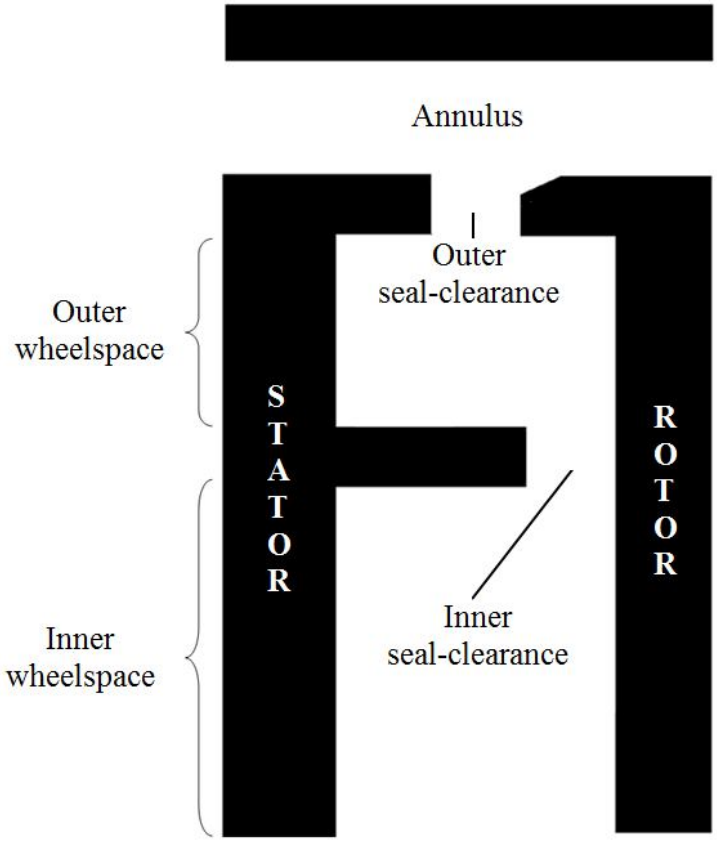

Figure. 2.21: Double seal arrangement (adapted from Sangan *et al.* (2012)).

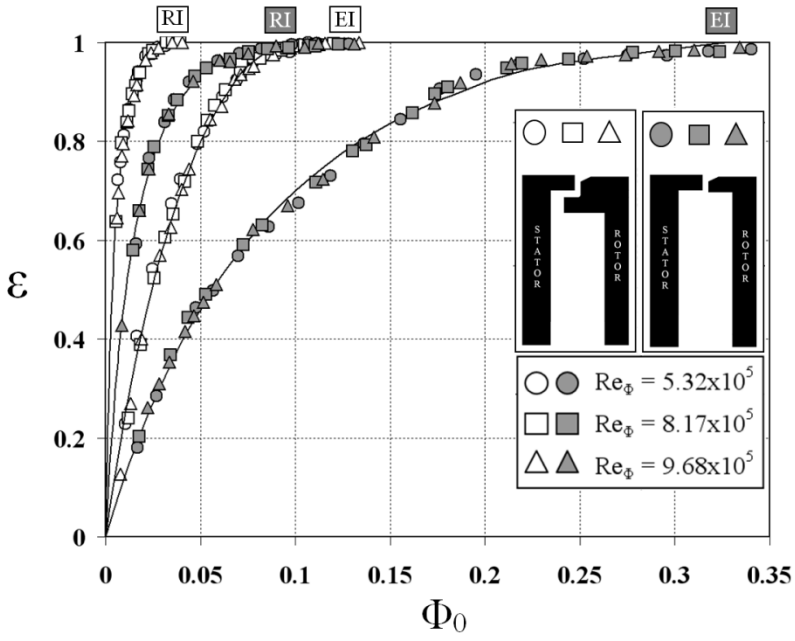

Figure. 2.22: Variation of ε with Φ_0 for axial seal (solid symbols) and radial seal (open symbols) for EI and RI ingress; lines represent optimised fits from Owen (2011a,b) orifice theory (from Sangan *et al.* (2011b)).

Chapter 3. Prediction of combined ingress

This chapter presents analytical and numerical solutions of the orifice equations developed in Owen (2011b) for the case of combined ingress, where external flow and rotational effects are both important in determining ingress levels. The combined ingress orifice model, which is solved for constant and variable egress discharge coefficients, is validated against the experimental data of Phadke and Owen (1988c) using two annular circumferential pressure variations: a saw-tooth profile for the analytical solutions and the measured profile for the numerical solutions. Finally, the possibility of using the model as a tool for extrapolation from rig to engine operating conditions is considered.

3.1 Data used for validation

The experimental data of Phadke and Owen (1988c) was chosen to validate the combined ingress orifice equations. The authors measured the variation of non-dimensional sealing flow rate, $C_{w,min}$, with the axial and rotational Reynolds numbers, Re_W and Re_ϕ respectively, for four seal geometries; only the data for the axial clearance seal will be used here (shown in Fig. 3.1).

Phadke and Owen (1988c) generated pressure asymmetries in the annulus by attaching honeycomb sections to a wire mesh covering the inlet of the external flow feed. The data points in Fig. 3.1 were obtained for the pressure asymmetry presented in Fig. 3.2; the figure shows variation of normalised pressure, f , with non-dimensional circumferential co-ordinate, θ, for the measured data and the theoretical saw-tooth profile used by Owen (2011b) to solve the analytical EI and combined ingress orifice equations. f was defined by Owen as:

$$f = \frac{p_2 - p_{2,min}}{\Delta p} \tag{3.1}$$

in the range $0 \le f \le 1$. For the saw-tooth model:

$$f = 1 - 2\theta \tag{3.2}$$

for $0 < \theta < 0.5$, and

$$f = 2\theta - 1 \tag{3.3}$$

for $0.5 < \theta < 1$. The measured data points were fitted using a cubic spline to provide an empirical relationship between f and θ. The maximum and minimum circumferential static pressure readings (i.e. $p_2 = p_{2,\max}$ at $f = 1$ and $p_2 = p_{2,min}$ at $f = 0$ respectively) gave $C_{p,max} = 0.48$.

3.2 Fundamental equations

The combined ingress orifice equations were formulated in Owen (2011b) and the interested reader is directed towards this paper for a complete derivation from first principles. Only the fundamental orifice equations are included in this section. Any variables not explicitly defined here can be found in the nomenclature.

The ratio of the minimum sealant flow required to seal against combined ingress, $\Phi_{min,CI}$, to the minimum sealant flow required to seal against RI ingress, $\Phi_{min,RI}$, can be expressed as a function of the combined and RI egress discharge coefficients, $C_{d,e,CI}$ and $C_{d,e,RI}$ respectively, the pressure profile integral for combined ingress, I_{min}', and the external pressure parameter, $\Gamma_{\Delta p}$:

$$\frac{\Phi_{min,CI}}{\Phi_{min,RI}} = \frac{C_{w,min,CI}}{C_{w,min,RI}} = \frac{C_{d,e,CI}}{C_{d,e,RI}} I_{min}' \Gamma_{\Delta p}^{1/2} \tag{3.4}$$

where

$$I_{min}' = \int_0^1 \left(1 - f + \Gamma_{\Delta p}^{-1}\right)^{1/2} d\theta \tag{3.5}$$

and

$$\Gamma_{\Delta p} = \frac{\Delta C_p}{C_{\beta_1}} = \frac{C_{p,\max}}{C_{\beta_1}} \left(\frac{Re_W}{Re_\phi}\right)^2 \tag{3.6}$$

For the saw-tooth profile, I_{min}' was solved analytically to give:

$$I_{min}' = \frac{2}{3} \frac{(1+\Gamma_{\Delta p})^{3/2} - 1}{\Gamma_{\Delta p}} \tag{3.7}$$

The variation of I_{min}' with $\Gamma_{\Delta p}$ for the fitted pressure profile was determined using a numerical integral solver.

With reference to the fundamental combined ingress orifice equations (Eqs. 3.4 to 3.7), it is clear that to predict the variation of $\Phi_{min,CI}$ / $\Phi_{min,RI}$ with Re_W / Re_ϕ it is necessary to determine the values of the parameters $C_{\beta I}$, $C_{d,e,CI}$ and $C_{d,e,RI}$ from the Phadke and Owen

(1988c) data; the calculation of these parameters is discussed in Sections 3.3 and 3.4 for the cases of constant and variable discharge coefficients.

3.3 Validation of combined ingress orifice model for constant discharge coefficients

For constant discharge coefficients (i.e. $C_{d,e,CI} = C_{d,e,RI}$) Eq. 3.4 simplifies to:

$$\frac{\Phi_{min,CI}}{\Phi_{min,RI}} = \frac{C_{w,min,CI}}{C_{w,min,RI}} = I_{min}' \Gamma_{\Delta p}^{1/2} \tag{3.8}$$

The value of the egress discharge coefficient for EI ingress, $C_{d,e,EI}$, was determined from the EI orifice model, derived in Owen (2011b), using:

$$C_{w,\min,EI} = 2\pi G_c I_{min} C_{d,e,EI} C_{p,max}^{1/2} Re_W \tag{3.9}$$

where I_{min}, the pressure profile integral for EI ingress, was determined from the value of I_{min}' as $\Gamma_{\Delta p} \rightarrow \infty$; $I_{min} = 2/3$ for the saw-tooth profile and $I_{min} = 0.41$ for the fitted profile. In the Phadke and Owen experiments, $G_c = 0.01$ and $C_{p,max} = 0.48$.

With reference to the data for $Re_\phi = 0$, where rotational effects were negligible and ingress could be considered as pure EI, $C_{w,min,EI}$ was shown to be proportional to Re_W (i.e. the data tended to the EI asymptote). It followed from Eq. 3.9 and the least-squares fit to the data at $Re_\phi = 0$, that $C_{d,e,EI} = 0.448$ and 0.728 for the saw-tooth and fitted pressure profiles respectively; for constant discharge coefficients, $C_{d,e,EI} = C_{d,e,RI}$.

Phadke and Owen (1988a) showed experimentally that in the absence of external flow, $C_{w,min,RI}$ was proportional to Re_ϕ. Figure 3.3 shows the variation of $C_{w,min,RI}$ with Re_ϕ for the experimental data in Fig. 3.1 at $Re_W = 0$; the data was fitted using a least-squares linear polynomial to give the constant of proportionality between $C_{w,min,RI}$ with Re_ϕ. The minimum coolant flow required to seal the wheelspace against RI ingress was derived in Owen (2011a) to be:

$$C_{w,\min,RI} = 2\pi G_c C_{d,e,RI} C_{\beta_1}^{1/2} Re_\phi \tag{3.10}$$

which can be expressed in terms of $\Phi_{min,RI}$ as

$$\Phi_{min,RI} = C_{d,e,RI} C_{\beta_1}^{1/2} \tag{3.11}$$

From Eq. 3.10 and the least-squares fit in Fig. 3.3, the respective values of $C_{\beta 1}$ for the saw-tooth and fitted pressure profiles were calculated as 0.071 and 0.027 for the values of $C_{d,e,RI}$ determined above. It follows that $\Phi_{min,RI} = 0.119$ for both pressure profiles.

Given that $C_{\beta 1}$ and $C_{p,max}$ are constants, it can be seen from Eqs. 3.4 to 3.7 that $\Phi_{min,CI}$ / $\Phi_{min,RI}$ is a unique function of Re_W / Re_ϕ. This is demonstrated in Figs. 3.4 and 3.5 where the Phadke and Owen (1988c) experimental data for the variation $C_{w,min}$ with Re_W and Re_ϕ collapsed onto a single curve when plotted as $\Phi_{min,CI}$ / $\Phi_{min,RI}$ against Re_W / Re_ϕ. In the figures, two curves are shown: a least-squares cubic spline fit to the data (solid line) and the prediction made by the constant discharge coefficient combined ingress orifice model for the saw-tooth pressure profile (dashed line). The combined ingress orifice model solution to the fitted pressure profile is not shown as it was indistinguishable from the saw-tooth solution. It is clear that at low Re_W / Re_ϕ the combined ingress orifice model for constant discharge coefficients does not capture the undershoot of the experimental data.

Phadke and Owen (1988c) and Bohn and Wolff (2003), as discussed in Chapter 2 of this thesis, correlated their results by:

$$C_{w,min,EI} = 2\pi G_c K \left(\frac{1}{2} C_{p,max} Re_W^{\,2} \right)^{1/2} \tag{3.12}$$

where K can be expressed as

$$K = \left(\frac{2}{\Delta C_p} \right)^{1/2} \Phi_{min,EI} \tag{3.13}$$

From the above, $K = 0.42$ for the Phadke and Owen (1988c) data. At a specific value of flow coefficient (Re_W / Re_ϕ), ΔC_p and $\Phi_{min,EI}$—the parameters used to calculate K—are dependent only upon the peak-to-trough pressure in the annulus and the seal geometry (K will therefore the same for any pressure distribution).

The value of K obtained above is comparable with that found by Bohn and Wolff, who used $K = 0.46$ to correlate their axial clearance seal data. Phadke and Owen (1988c) used $K = 0.6$ to correlate their combined data for three seals operating over a range of different annular pressure asymmetries. The value of $K = 0.42$ determined here was for their axial seal data for a single pressure asymmetry. K is not a universal parameter and caution should be exercised when using it to compare data obtained at different operating conditions.

3.4 Validation of combined ingress orifice model for variable discharge coefficients

3.4.1 Discharge coefficient relationship

Chew *et al.* (1994) reported that the egress discharge coefficient, $C_{d,e}$, decreased as Re_W increased. The authors measured the variation of $C_{d,e}$ with the ratio of the axial velocity upstream of the nozzle guide vanes, u_e, to the average radial velocity through the seal clearance, u_m, and correlated their results using a polynomial fit. It follows that when the non-dimensional egress flow rate, $C_{w,e}$, equals $C_{w,min}$, then:

$$\frac{u_e}{u_m} = 2\pi G_c \frac{Re_W}{C_{w,min,CI}} \tag{3.14}$$

If $C_{d,e} = C_{d,e,RI}$ when $u_e / u_m = 0$ and $C_{d,e} = C_{d,e,CI}$ when $u_e / u_m > 0$ then the Chew *et al.* (1994) experimental data (shown in Fig. 2.16 (a)) can be plotted as $C_{d,e,CI} / C_{d,e,RI}$ against u_e / u_m as in Fig. 3.6.

The polynomial fit used by Chew *et al.* (dashed line) and an exponential fit (solid line) are shown alongside the experimental data (open symbols) in the figure. The exponential fit was based upon Eq. 3.15 below:

$$\frac{C_{d,e,CI}}{C_{d,e,RI}} = \exp\left(-A'\frac{u_e}{u_m}\right) \tag{3.15}$$

where $A' = 0.107$ to give the least-squares error to the experimental data. The exponential fit was selected over the polynomial fit as polynomials can produce ambiguous results when used beyond the fitted data range.

Rearranging and substituting Eq. 3.14 into Eq. 3.15 gives the discharge coefficient ratio in the following form:

$$\frac{C_{d,e,CI}}{C_{d,e,RI}} = \exp\left(-A\frac{Re_W}{Re_\phi}\frac{\Phi_{min,RI}}{\Phi_{min,CI}}\right) \tag{3.16}$$

where A, an empirical constant, can be calculated by

$$A = \frac{A'}{\Phi_{min,RI}} = \frac{A'}{C_{d,e,RI}C_{\beta_1}^{1/2}} \tag{3.17}$$

For the experimental data of Phadke and Owen (1988c), where $\Phi_{min,RI}$ = 0.119, and the exponential fit to the Chew *et al.* (1994) discharge coefficient data, where A' = 0.107, then A = 0.89 (a value of A = 0 corresponds to the constant discharge coefficient case).

When $\Phi_{min,CI} \rightarrow \Phi_{min,EI}$ (and therefore $C_{d,e,CI} \rightarrow C_{d,e,EI}$) then, as previously discussed, the data tends to the EI asymptote and Eq. 3.16 can be simplified to:

$$\frac{C_{d,e,EI}}{C_{d,e,RI}} = \exp(-\psi A) \tag{3.18}$$

where ψ, an empirical constant, is calculated from

$$\psi = \left(\frac{2}{C_{p,max}}\right)^{1/2} \frac{\Phi_{min,RI}}{K} \tag{3.19}$$

and K is defined in Eq. 3.13. For the Phadke and Owen (1988c) experimental data, ψ = 0.578. The empirical constants given in Table. 3.1 were calculated using Eq. 3.18 for the saw-tooth and fitted pressure profiles. The values of $C_{d,e,EI}$ and $C_{d,e,RI}$ corresponding to A = 0.89 are not presented for the fitted pressure profile as for this case $C_{d,e,RI} > 1$, which is physically unrealistic.

Pressure profile	A	$C_{d,e,EI}$	$C_{d,e,RI}$
Saw-tooth	0	0.448	0.448
	0.50	0.448	0.598
	0.89	0.448	0.749
Fitted	0	0.728	0.728
	0.50	0.728	0.972

Table 3.1: Empirical constants for different values of A.

3.4.2 Model validation

The CI orifice equation for variable discharge coefficients can be expressed from Eqs. 3.4 and 3.16 as:

$$\frac{\Phi_{min,CI}}{\Phi_{min,RI}} = \exp\left(-A\frac{Re_W}{Re_\phi}\frac{\Phi_{min,RI}}{\Phi_{min,CI}}\right) I_{min}' \Gamma_{\Delta p}^{1/2} \tag{3.20}$$

It can be seen from Eqs. 3.5 and 3.6 that I_{min}' is a function of $\Gamma_{\Delta p}$ and that $\Gamma_{\Delta p}^{1/2} \propto Re_W / Re_\phi$; consequently, for the variable discharge coefficient combined ingress orifice model shown in Eq. 3.20, $\Phi_{min,CI} / \Phi_{min,RI}$ is a unique function of Re_W / Re_ϕ.

Figures 3.7 and 3.8 show the variation of $\Phi_{min,CI}$ / $\Phi_{min,RI}$ with Re_W / Re_ϕ for the Phadke and Owen (1988c) experimental data. In the figures, two curves are shown for the variable discharge coefficient combined ingress orifice model with the saw-tooth pressure profile: the first for A = 0 (bold dashed line), which corresponds to the constant discharge coefficient curve shown in Fig. 3.4; and the second for A = 0.89 (solid line), as calculated from the Chew *et al.* (1994) experimental data above. The curves for the fitted pressure profile are not shown as the solution for A = 0 was indistinguishable from the saw-tooth and for A = 0.89 the discharge coefficients were physically unrealistic. It is clear that at low values of Re_W / Re_ϕ the solution for A = 0.89 provides a better fit to the measurements than for A = 0; however, it does not fully capture dip in the data.

The least-squares cubic spline fit to the Phadke and Owen (1988c) data, which was shown in Figs. 3.4 and 3.5, was within 5 percent of the EI asymptote for $\Phi_{min,CI}$ / $\Phi_{min,RI} \geq 2$. It follows that for $\Phi_{min,CI}$ / $\Phi_{min,RI} \leq 2$ the experimental data of Phadke and Owen (1988c) fell into the combined ingress region where the effects of rotation and external flow were both important in determining ingestion levels.

As mentioned in the previous chapter, the RI and EI orifice equations developed in Owen (2011a, b) were expressed in Sangan *et al.* (2011a, b) in the following form:

$$\frac{\Phi_0}{\Phi_{min,RI}} = \frac{\varepsilon}{[1+(1-\varepsilon)^{1/2}][1+\Gamma_c^{-2}(1-\varepsilon)]^{1/2}} \tag{3.21}$$

and

$$\frac{\Phi_0}{\Phi_{min,EI}} = \frac{\varepsilon}{[1+\Gamma_c^{-2/3}(1-\varepsilon)^{2/3}]^{3/2}} \tag{3.22}$$

Zhou *et al.* (2011b) developed a statistical technique to calculate the optimum values of $\Phi_{min,EI}$, $\Phi_{min,RI}$ and Γ_c to fit the solutions of Eqs. 3.21 and 3.22—referred to as the RI and EI effectiveness equations respectively—to experimental data with minimum uncertainty.

It was shown in Owen (2011b) that the predicted variation of ε with Φ_0 / Φ_{min} is similar for both the RI and EI effectiveness equations; it follows that the variation of ε with Φ_0 / $\Phi_{min,CI}$ is also likely to be similar. It is tentatively proposed that Eq. 3.22 could be used to extrapolate data taken on a test rig to engine conditions for a specific seal geometry. This proposition requires testing, which is beyond the scope of this thesis. The interested reader is referred to Teuber *et al.* (2012) for examination of computational extrapolation of sealing effectiveness from rig to engine conditions.

3.5 Implications

The successful development and validation of the Owen (2011b) combined ingress orifice model carried out in this chapter satisfies Objective 1 of this thesis (see Section 1.5). The model is being incorporated into one-dimensional design codes at Siemens to aid with secondary air-system design; engineers will be able to use the model to estimate ingress levels for various seal designs at full or part load operation (i.e. at a range of values of Re_W / Re_ϕ). To use the saw-tooth combined ingress orifice model, designers will need to estimate $\Phi_{min,EI}$ and $\Phi_{min,RI}$ and the variation of $\Delta C_p^{1/2}$ with Re_W / Re_ϕ in the annulus for their blade and vane setup and rim seal geometry; these can be estimated using the results for generic, but engine representative seals, presented in Sangan *et al.* (2012)—see Appendix D of this thesis—and data from existing engine designs. The model is used in the subsequent chapter to fit the experimental data gathered for off-design operation on the Bath test rig.

3.6 Figures

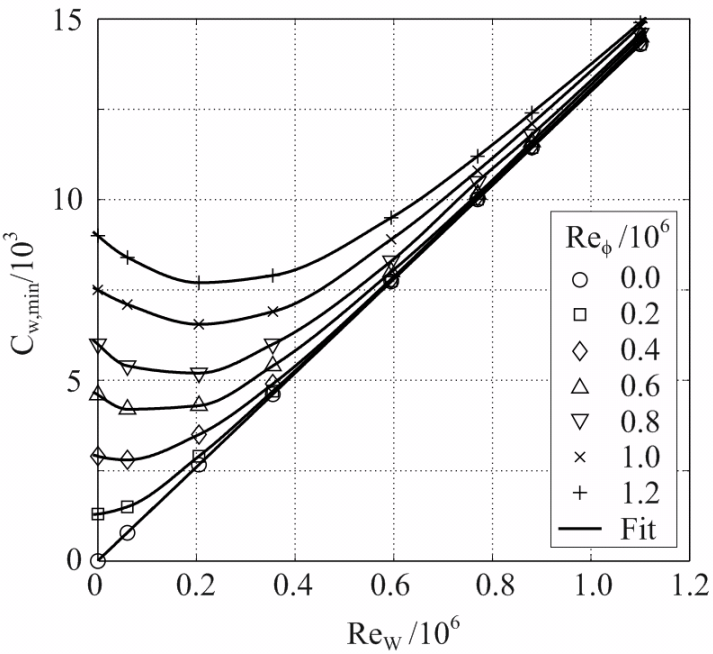

Figure. 3.1: Variation of $C_{w,min}$ with Re_W and Re_ϕ for axial seal with G_c = 0.01; data is taken from Phadke and Owen (1988c).

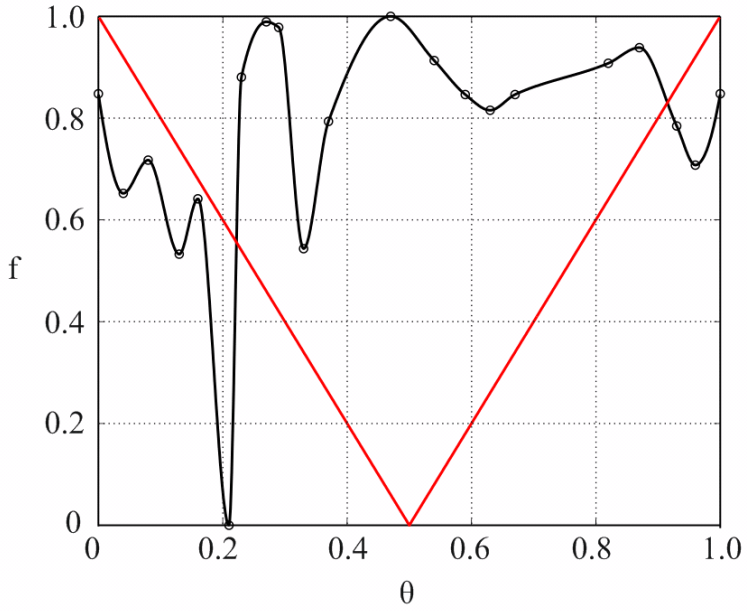

Figure. 3.2: Variation of normalised pressure, f, with non-dimensional circumferential location across the annulus, θ; the experimental data was measured by Phadke and Owen (1988c) and fitted using a cubic interpolant spline.

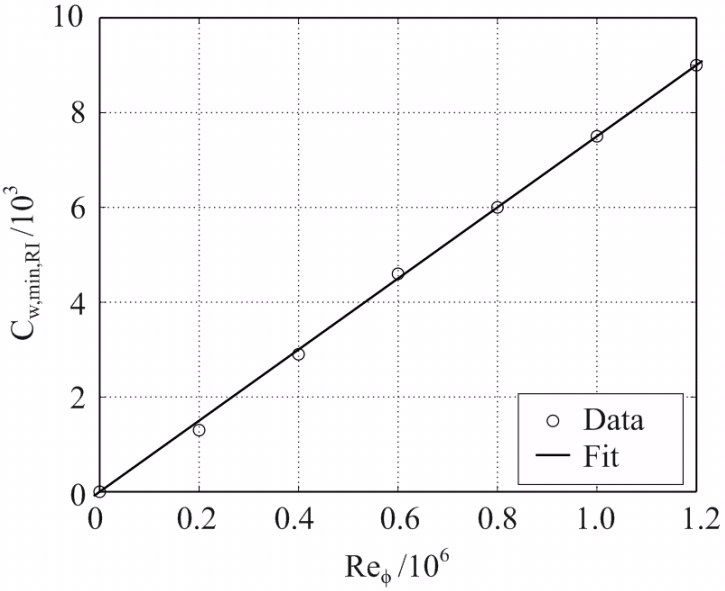

Figure. 3.3: Variation of $C_{w,min,RI}$ with Re_ϕ for $Re_W = 0$; the data was measured by Phadke and Owen (1988c) and fitted using a least-squares linear polynomial.

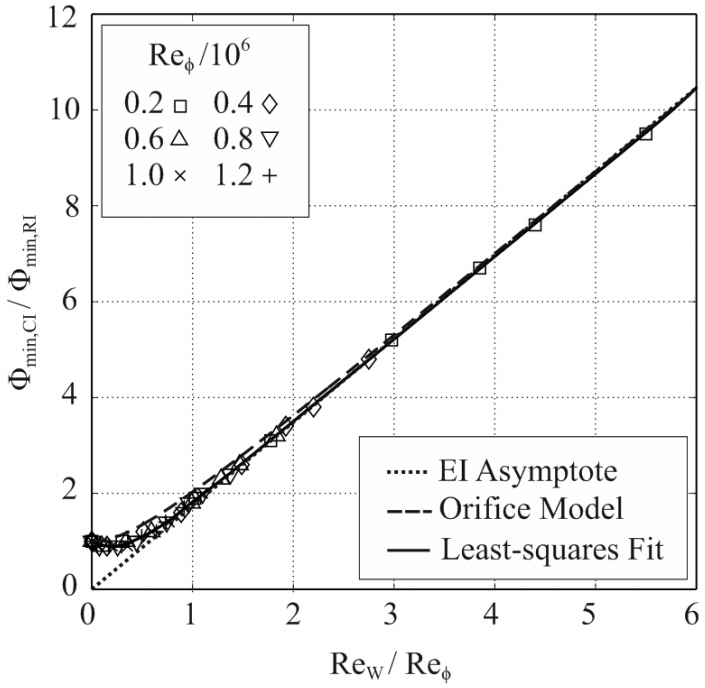

Figure. 3.4: Variation of $\Phi_{min,CI} / \Phi_{min,RI}$ with Re_W / Re_ϕ. Data was measured by Phadke and Owen (1988c) and fitted using both a least-squares cubic spline (solid line) and the constant discharge coefficient combined ingress orifice model (dashed line).

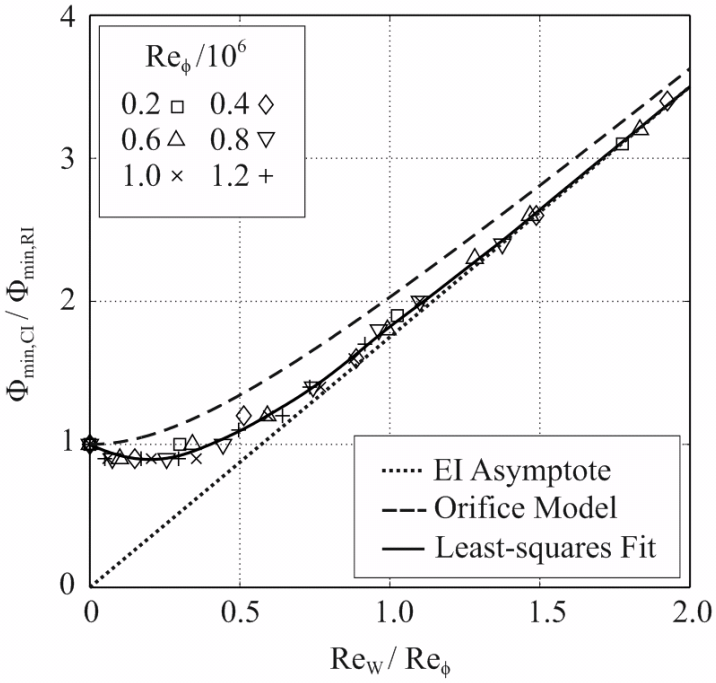

Figure. 3.5: Variation of $\Phi_{min,CI}$ / $\Phi_{min,RI}$ with Re_W / Re_ϕ at low Re_W / Re_ϕ (enlargement of undershoot region shown in Fig. 3.4). Data was measured by Phadke and Owen (1988c) and fitted using both a least-squares cubic spline (solid line) and the constant discharge coefficient combined ingress orifice model (bold dashed line).

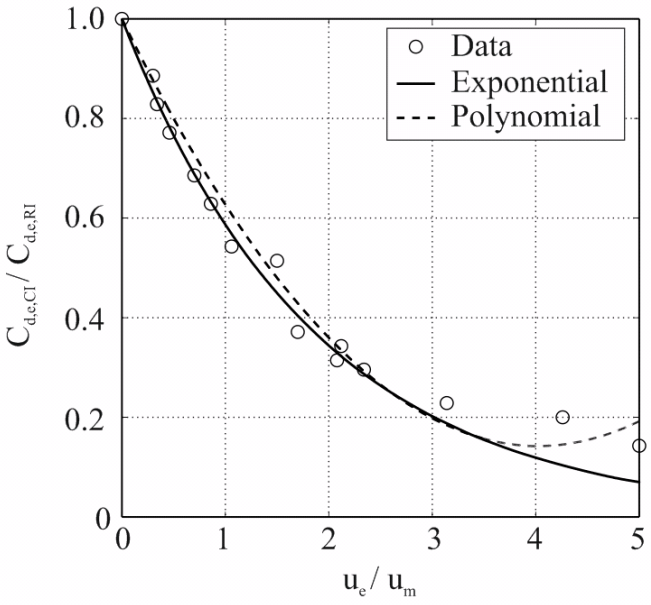

Figure. 3.6: Variation of $C_{d,e,CI}$ / $C_{d,e,RI}$ with u_e / u_m for an axial seal with G_c = 0.01 at Re_ϕ = 0, as measured by Chew *et al.* (1994).

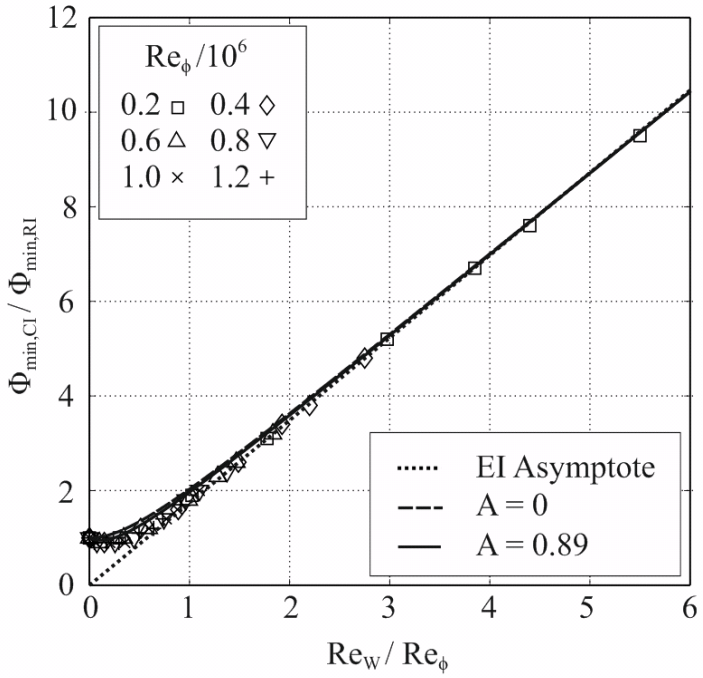

Figure. 3.7: Variation of $\Phi_{min,CI}$ / $\Phi_{min,RI}$ with Re_W / Re_ϕ. Data was measured by Phadke and Owen (1988c) and fitted using the variable discharge coefficient combined ingress orifice model with A = 0 (bold dashed line) and A = 0.89 (solid line).

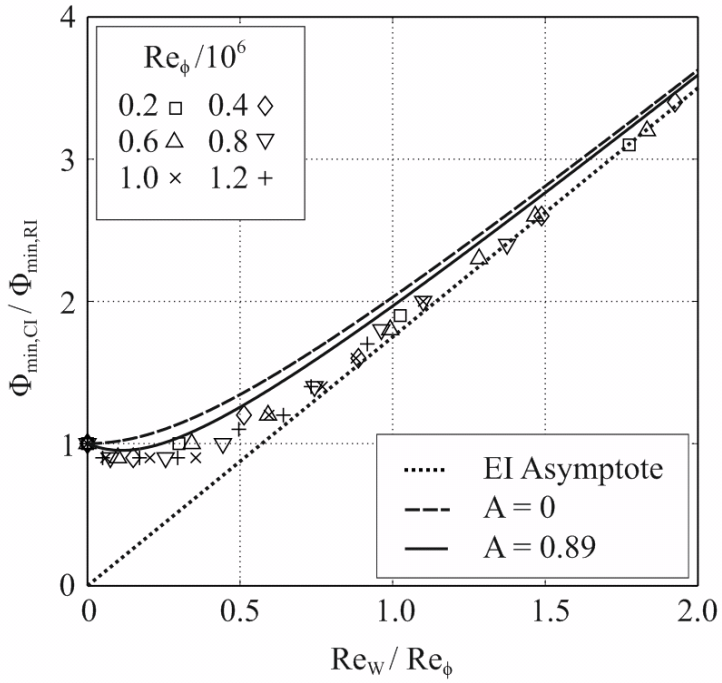

Figure. 3.8: Variation of $\Phi_{min,CI}$ / $\Phi_{min,RI}$ with Re_W / Re_ϕ at low Re_W / Re_ϕ (enlargement of undershoot region shown in Fig. 3.7). Data was measured by Phadke and Owen (1988c) and fitted using the variable discharge coefficient combined ingress orifice model with A = 0 (bold dashed line) and A = 0.89 (solid line).

Chapter 4. Experimental ingress measurements

This chapter presents the concentration sealing effectiveness measurements made on the stator of the University of Bath single-stage gas turbine rig for an axial clearance seal geometry for RI and EI ingress; measurements showing the influence of operating off-design (i.e. varying Re_W/Re_ϕ) on the minimum sealing flow required to purge the wheelspace against ingress are also shown. Details of the test geometry, experimental operating conditions, concentration and pressure measurement techniques and wheelspace fluid dynamics are all discussed in detail prior to the presentation of the experimental measurements. Finally, experimental uncertainty levels and practical implications are considered.

4.1 Experimental test facility

This section, which summarises the University of Bath experimental gas turbine test facility used to make the ingress measurements presented in this chapter, is based upon the 'Experimental Facility' section presented in the paper of Sangan *et al.* (2011a), on which the author of this thesis was a co-author and significant contributor. The design and commissioning of the experimental facility was discussed extensively in Sangan (2011); the interested reader is directed to this reference for a greater level of detail than presented below.

4.1.1 Test section

Figure 4.1 shows a general assembly of the Bath gas turbine test facility (salient experimental elements, including the test section, are labelled in the diagram). The rotor-stator test section shown in Fig. 4.2 featured 32 nozzle guide vanes and 41 NACA 0018 blades; symmetrical blades were chosen to avoid the use of a dynamometer to extract excess power from the turbine. The vanes and blades were manufactured from nylon and attached to the aluminium shrouds encasing the stator and rotor discs. The axial displacement from the vane trailing edge to blade leading edge was 12 mm (note: the distance from the vanes and blades to the seal mid-plane was equal at 6 mm). Both discs were made from transparent polycarbonate to provide optical access to the wheelspace for heat transfer measurements

Figure 4.3 shows the rig test section with the simple axial-clearance seal configuration. Key geometric parameters, which are labelled in the figure, are given in table 4.1. The axial-

clearance seal, which acted as a baseline case for the seal comparisons carried out in Sangan *et al.* (2011a, b) and Sangan *et al.* (2012), was the focus of the off-design measurements presented in this chapter. Sangan (2011) estimated the radial growth of the rotor under rotation to be 0.33 mm at 6000 RPM. The test section was designed with a 0.4 mm step-down between the stator and rotor platforms to ensure that the external flow did not impinge on the edge of the rotor shroud at the maximum operational speed. A chamfer was machined onto the edge of the rotor shroud to further reduce the risk of flow impingement. A laser transducer measured the growth to be 0.23 mm at full speed operation, which indicated that the design was sufficient to prevent flow impingement experimentally.

Geometric Parameter	Value
h (mm)	10
S (mm)	20
$s_{c,ax}$ (mm)	2
b (mm)	190
G	0.105
$G_{c,ax}$	0.0105

Table 4.1: Salient dimensions of Bath test rig. G is the gap ratio (S/b) and $G_{c,ax}$ is the seal clearance ratio ($s_{c,ax}/b$).

External flow was supplied to the annulus via 32 feed pipes (one pipe for each vane) through a convergent transition section. The static pressure of the air in each feed pipe was measured to be axisymmetric to within ± 5%. An electric motor was used to drive the rotor at speeds of up to 3500 RPM, which corresponded to $Re_\phi = 9.68 \times 10^5$. With reference to the velocity triangle diagram in Fig. 4.4, the vane exit and blade inlet angles for the test rig described here were $\alpha = 73.5°$ and $\beta = \beta_0 = 56.7°$ respectively. The rig was considered to be operating 'on-design' when the velocity of the air relative to the blade, V, approached the blade with a relative angle of β_0. It followed that $Re_W / Re_\phi = 0.538$ for the design condition and consequently $Re_W = 5.21 \times 10^5$ at the maximum rotational speed.

The vane exit Mach number, $M = C/a$, was calculated to be approximately 0.4 at the highest value of Re_W; the flow in the annulus was therefore considered virtually incompressible. The values of air density, ρ, and viscosity, μ, used to calculate M, Re_W and Re_ϕ were calculated from static pressure and temperature measurements in the stator wall at $r/b = 0.993$. The measurements of Φ_{min} presented in this chapter were for disc speeds of

2000, 3000 and 3500 RPM. Table 4.2 shows the values of Re_ϕ, Re_W and M for the aforementioned disc speeds at the design condition.

Given the limited supply of compressed air, the annulus height was fixed at 10 mm (see Fig. 4.3 and Table 4.1 above) to achieve the annular mass flow required for the design condition at 3500 RPM. Sangan (2011) estimated that the boundary layer thickness for was less than 3.5% of the total flow area through the annulus. It was therefore suggested that the ingress into the wheelspace was predominantly from the mainstream flow rather than the boundary layer.

Disc Speed (RPM)	**2000**	**3000**	**3500**
$Re_\phi / 10^5$	5.32	8.17	9.68
$Re_W / 10^5$	2.86	4.40	5.21
M	0.23	0.34	0.40

Table 4.2: Tested disc speeds and corresponding values of Re_ϕ, Re_W and M for the design condition ($Re_W / Re_\phi = 0.538$).

4.1.2 Concentration measurements

The sealant flow was seeded with approximately 1% CO_2 and delivered to the wheelspace through an inlet seal at low radius (r/b = 0.65). The radial variation of CO_2 concentration on the stator was measured with ± 1.5% uncertainty through a series of 15 taps in the disc wall over the range $0.55 < r/b < 0.993$ using a Signal Group 9000 MGA dual channel multi-gas analyser. Figure 4.2 shows the concentration taps in the stator wall. Presence of unseeded external flow in the wheelspace (and thereby ingress) was marked by reduction in CO_2 concentration levels at the sample points relative to the measured seed level. Both the sealant and external mass flow rates, $\dot{m}_0$ and $\dot{m}_a$ respectively, were measured using orifice plates manufactured to EN ISO 5167-2. The orifice plates were calibrated using a Rotameter to within ± 3% uncertainty.

Concentration sealing effectiveness, ε_c, was determined from the CO_2 concentration measurements in the stator wall using the following equation:

$$\varepsilon_c = \frac{c_s - c_a}{c_0 - c_a} \tag{4.1}$$

where c_s, c_a and c_0 (shown in Fig. 4.5) were the concentration levels on the stator wall and in the annulus and sealant flows respectively. By definition $\varepsilon_c \rightarrow 0$ as $\Phi_0 \rightarrow 0$ and $\varepsilon_c \rightarrow 1$ as $\Phi_0 \rightarrow \Phi_{min}$.

The definition of effectiveness used in the orifice model is based upon the pressure difference between the annulus and wheelspace. The model does not consider diffusion resulting from the concentration difference across the rim seal. It was assumed that the diffusion term was small and that $\varepsilon_c = \varepsilon$; this allowed the orifice equations to be fitted to the measured variation of ε_c with Φ_0.

4.1.3 Pressure measurements

The circumferential variation of static pressure in the annulus was determined at two locations in the annulus: A, on the stator shroud 2.5 mm axially downstream of the vane trailing edge; and B, in the outer casing at the middle of the seal clearance. At both locations the static pressures were measured from 15 taps equally spaced across a single vane pitch ($0 \leq \theta \leq 1$); Fig. 4.4 shows the arrangement of the static pressure taps on the stator shroud.

The pressure coefficient, C_p, is defined as:

$$C_p = \frac{p_a - \overline{p}_a}{1/2\rho\Omega^2 b^2} \tag{4.2}$$

where p_a is the local static pressure at the measurement location and $\overline{p}_a$ is the arithmetic mean of the measured values of p_a across the vane pitch. The variation of C_p with θ on the stator shroud is plotted in Fig. 4.6 for the design condition with $Re_\phi = 8.17 \times 10^5$ and zero sealant flow.

For the design case, the driving pressure for ingress, ΔC_p, was measured to be 0.82 at location A and 0.42 at location B; these values were invariant with Re_ϕ for $M < 0.4$. It is clear from Eq. 4.3 below, which Owen (2011b) derived for EI ingress with an assumed saw-tooth external pressure profile, that $C_{d,e,EI}$ is determined from $\Phi_{min,EI}$ and $\Delta C_p^{1/2}$. Given that $\Phi_{min,EI}$ is a universal parameter, the calculated value of $C_{d,e,EI}$ will be dependent on the location chosen to measure ΔC_p.

$$\Phi_{min,EI} = \frac{2}{3} C_{d,e,EI} \Delta C_p^{1/2} \tag{4.3}$$

For the measurements of $\Phi_{min,EI}$ made in this thesis, $C_{d,e,EI}$ was different at A and B owing to the different values of ΔC_p measured at the two locations. It follows that caution be taken

when comparing values of $C_{d,e,EI}$ calculated from these experiments with those presented in other studies.

Figure 4.7 shows the measured linear variation of $\Delta C_p^{1/2}$ with Re_W/Re_ϕ and β - β_0 at locations A and B in the annulus for $Re_\phi = 5.32 \times 10^5$ and 8.17×10^5 with $\Phi_0 = 0$. When β - $\beta_0 = 0$, the test rig was operating on-design with $\beta = \beta_0 = 56.7°$ and $Re_W/Re_\phi = 0.538$. The rig was considered to be operating 'off-design' when $\beta \neq \beta_0$; for β - $\beta_0 > 0$, the rig was operating underspeed with $Re_W/Re_\phi > 0.538$ and, conversely, for β - $\beta_0 < 0$, the rig was operating overspeed with $Re_W/Re_\phi < 0.538$.

4.2 Wheelspace fluid dynamics

The Daily and Nece (1960) flow correlations for rotor-stator systems (see Fig. 2.5) showed that the flow regime in the wheelspace is dictated by the gap ratio of the wheelspace, G, and Re_ϕ. For the Bath test rig, where $G = 0.105$ and $Re_\phi = 5.32 \times 10^5$ to 9.68×10^5, the flow in wheelspace cavity would have been turbulent with separate rotor and stator boundary layers, as categorised by Daily and Nece 'Regime 4'. Generally, wheelspaces in gas turbine engines also operate under this flow regime (the rig was designed with this in mind).

The flow structure of the fluid in the wheelspace is predominantly governed by the turbulent flow parameter, λ_T, where:

$$\lambda_T = 2\pi G_c \Phi_0 \, \mathrm{Re}_\phi^{0.2} \tag{4.4}$$

Although the values of Re_ϕ tested on the Bath test rig were an order-of-magnitude lower than for a typical gas turbine engine, λ_T, which is only a weak function of Re_ϕ, was similar in magnitude. It follows that for the same flow regime and similar values of λ_T, the fluid dynamics in the wheelspace of the test rig would have been representative of those in an engine.

For $\lambda_T < 0.22$, the fluid in the wheelspace adheres to Batchelor (1951) type flow: a radially outward flowing rotor boundary layer and a radially inward flowing stator boundary layer with a rotating fluid core located between. The presence of a fluid core was confirmed by measuring the variation of swirl ratio (β) with r/b at seven radial locations in the range $0.65 < r/b < 0.993$, as shown in Fig. 4.8. The core tangential velocity (and hence β) was measured using pitot tubes and static pressure taps: the former located at $z/S = 0.25$ and the latter flush mounted with the stator wall. The Daily *et al.* (1964) correlation presented in Eq. 2.10 predicted $\beta = 0.43$ for the Bath wheelspace geometry with no superposed flow. The experimental measurements showed that $\beta = 0.44$ for $\lambda_T = 0$ when $r/b < 0.8$, which agreed

well with the predicted value. The results for $\lambda_T = 0$ also showed that β increased from 0.44 at $r/b = 0.8$ to 0.9 at $r/b = 0.993$, which indicated the presence of a region where high swirl ingestion was mixing with the fluid in the wheelspace. This 'mixing region' diminished as λ_T was increased and the quantity of ingested fluid reduced.

The experimental measurements also show that β decreased as λ_T increased, which is consistent with the rotor-stator theory discussed in Chapter 2. When λ_T was less than the limit for full disc entrainment (i.e. $\lambda_T < 0.22$) then fluid was drawn into the rotor boundary layer from the core region *and* the source region. As λ_T was increased the amount of fluid entrained from the core region (and thus β) decreased owing to an increase in supply from the source region. For $\lambda_T = 0.242$ (which was above the disc entrainment limit) the core region would have broken down completely.

4.3 Experimental concentration measurements

The concentration measurements presented in this section were made on the stator for $Re_\phi = 5.32 \times 10^5$, 8.17×10^5 and 9.68×10^5 with $Re_W = 0$ for rotationally-induced (RI) ingress, $Re_W / Re_\phi = 0.538$ for externally-induced (EI) ingress and $0 < Re_W / Re_\phi < 0.82$ at the off-design conditions. The results for RI and EI ingress, which were published in Sangan *et al.* (2011a, b), are presented here as they form an important part of the discussion of the off-design measurements.

All measurements (unless stated) were made on the stator wall at $r/b = 0.953$ for an axial clearance seal with $G_c = 0.0105$. It was shown in Sangan *et al.* (2011a, b) that the radial variation of sealing effectiveness on the stator wall was virtually invariant with non-dimensional radius for the axial seal geometry on the Bath test rig for both RI and EI ingress. The chosen location of $r/b = 0.953$ was thus considered to suitably represent the ingress characteristics of the system.

4.3.1 Rotationally-induced ingress

Figure 4.9 shows the measured variation of ε on the stator wall with $C_{w,0}$ and Re_ϕ for RI ingress. The data followed the expected trend: as the wheelspace was supplied with increasing sealant flow, and thus the cavity pressure was raised, the amount of ingress penetrating the seal clearance reduced and thereby ε increased. It is clear from the figure that increasing Re_ϕ led to a reduction in the sealing performance of the system; accordingly, $C_{w,min,RI}$ increased proportionally with Re_ϕ. This agreed with the findings of Bayley and Owen (1970).

The data was also plotted to show the variation of ε with Φ_0, as presented in Fig. 4.10. When plotted in this form the data collapsed upon Re_ϕ to form a single effectiveness curve and thus provide a unique value of $\Phi_{min,RI}$ for the axial geometry. The RI effectiveness equation (Eq. 4.5, as formulated in Sangan *et al.* (2011b)) was used to fit the experimental data using the statistical fitting technique developed by Zhou *et al.* (2011b).

$$\frac{\Phi_0}{\Phi_{min,RI}} = \frac{\varepsilon}{[1+(1-\varepsilon)^{1/2}][1+\Gamma_c^{-2}(1-\varepsilon)]^{1/2}} \tag{4.5}$$

For the axial seal $\Phi_{min,RI}$ = 0.0838 and Γ_c = 0.342; the fit is plotted as a solid line to the ε versus Φ_0 data in Fig. 4.10. The value of $\Phi_{min,RI}$ = 0.0838 compares well with $\Phi_{min,RI}$ = 0.097 found by Bayley and Owen (1970) (also for an axial clearance geometry).

The variation of $\Phi_{i,RI}$ / $\Phi_{min,RI}$ with Φ_0 is also shown in Fig. 4.10. The experimental values of $\Phi_{i,RI}$ were calculated using:

$$\Phi_{i,RI} = \Phi_0\left(\varepsilon^{-1}-1\right) \tag{4.6}$$

These values were fitted using equation 4.7 for $\Phi_{min,RI}$ = 0.0838 and Γ_c = 0.342 as calculated from Eq. 4.5 above.

$$\frac{\Phi_{i,RI}}{\Phi_{min,RI}} = \frac{1-\varepsilon}{[1+(1-\varepsilon)^{1/2}][1+\Gamma_c^{-2}(1-\varepsilon)]^{1/2}} \tag{4.7}$$

With zero sealant flow (i.e. Φ_0 = 0) it follows that $\Phi_{i,RI}$ / $\Phi_{min,RI}$ = 0.17; accordingly, the maximum amount of fluid ingested into the wheelspace was limited to a level of 0.17 of the flow required to seal the system.

4.3.2 Externally-induced ingress

Figure 4.11 shows the measured variation of ε on the stator wall with $C_{w,0}$ and Re_ϕ for EI ingress at Re_W / Re_ϕ = 0.538. The data followed the same trend as the RI data: ε increased as $C_{w,0}$ was increased, and increasing Re_ϕ led to a reduction in the sealing performance of the system.

The measured variation of ε with Φ_0 is presented in Fig. 4.12 for EI ingress; as for the RI ingress data, the EI ingress data collapsed upon Re_ϕ to form a distinct effectiveness curve and provide a single value of $\Phi_{min,EI}$ for the axial geometry. The EI effectiveness equation (Eq. 4.8, as formulated in Sangan *et al.* (2011a)) was used to fit the experimental data using the statistical fitting technique developed by Zhou *et al.* (2011b).

$$\frac{\Phi_0}{\Phi_{min,EI}} = \frac{\varepsilon}{[1+\Gamma_c^{-2/3}(1-\varepsilon)^{2/3}]^{3/2}} \tag{4.8}$$

For the axial seal $\Phi_{min,EI} = 0.326$ and $\Gamma_c = 0.48$; accordingly, for the axial geometry $\Phi_{min,EI} > \Phi_{min,RI}$ by a factor of 3.9. The EI effectiveness equation is plotted as a solid line to the ε versus Φ_0 data in Fig. 4.12.

The non-dimensional ingress flow into the wheelspace for EI ingress, $\Phi_{i,EI}$, was determined from the measurements of ε and Φ_0 using:

$$\Phi_{i,EI} = \Phi_0\left(\varepsilon^{-1} - 1\right) \tag{4.9}$$

The experimental variation of $\Phi_{i,EI} / \Phi_{min,EI}$ with Φ_0 was fitted using Eq. 4.10 below for $\Phi_{min,EI} = 0.326$ and $\Gamma_c = 0.48$; the data and corresponding fit are plotted in Fig. 4.12.

$$\frac{\Phi_{i,EI}}{\Phi_{min,EI}} = \frac{1-\varepsilon}{[1+\Gamma_c^{-2/3}(1-\varepsilon)^{2/3}]^{3/2}} \tag{4.10}$$

With zero sealant flow (i.e. $\Phi_0 = 0$) it follows that $\Phi_{i,EI} / \Phi_{min,EI} = 0.23$; accordingly, the maximum amount of fluid ingested into the wheelspace was limited to a level of 0.23 of the flow required to seal the system.

4.3.3 Off-design ingress

The velocity triangle for the Bath test rig was shown in Fig. 4.4. The rig was operating on-design when the velocity of the air relative to the blade, *V*, approached the blade with a relative angle of $\beta = \beta_0 = 56.7°$, as was achieved when $Re_W / Re_\phi = 0.538$. The off-design experiments, for which the results are presented in this section, were undertaken to investigate the relationship between $\Phi_{min,CI}$ (the minimum purge flow required to seal the wheelspace when against ingress when $\beta \neq \beta_0$) and Re_W / Re_ϕ.

The supply of compressed air restricted the tests to within the following range: $0 < Re_W / Re_\phi < 0.82$. The rig was considered to be operating 'underspeed' when $Re_W / Re_\phi > 0.538$ and overspeed when $Re_W / Re_\phi < 0.538$; consequently, the external flow approached the blade with $\beta > \beta_0$ for the underspeed test cases and $\beta < \beta_0$ for the overspeed test cases. *(n.b. The following limits apply to the blade angle: $\beta \rightarrow \alpha$ as $Re_W / Re_\phi \rightarrow \infty$ and $\beta \rightarrow -\pi/2$ as $Re_W / Re_\phi \rightarrow 0$).*

Zhou *et al.* (2011b) showed that at least 16 data points were required to accurately determine Φ_{min} from the orifice equation fits to the measured variation of ε with Φ_0; approximately 60 data points were used to accurately determine Φ_{min} for the RI and EI

measurements presented above (uncertainties are quantified in the following section). It was not possible to produce full effectiveness curves for all the tested values of Re_W / Re_ϕ owing to time restrictions. Instead, the minimum value of sealant flow required to seal to '95% effectiveness', referred to here as $C'_{w,min,CI}$ or $\Phi'_{min,CI}$, was recorded by manually tuning Φ_0 until ε = 0.95. For RI and EI ingress, $\Phi'_{min,RI}$ = 0.055 and $\Phi'_{min,EI}$ = 0.213 respectively. Diffusion of gas through the rim seal prevented a value of ε = 1 being reached experimentally and so ε = 0.95 was taken as a representative system value for the off-design measurements. Full effectiveness curves were taken at 11 values of Re_W / Re_ϕ and fitted using a least squares cubic spline to ascertain $\Phi'_{min,CI}$.

Figure 4.13 shows the measured variation of $C'_{w,min,CI}$ with Re_W for Re_ϕ = 5.32 × 10^5, 8.17 × 10^5 and 9.68 × 10^5. At low values of Re_W the measured values of $C'_{w,min,CI}$ were influenced strongly by Re_ϕ; this influence diminished at high Re_W where the experimental data tended to the EI asymptote (i.e. $C'_{w,min,CI} \propto Re_W$).

The variable discharge coefficient combined ingress orifice equation (see Chapter 3, Section 3.4) can be expressed as follows for a saw-tooth pressure profile:

$$\frac{\Phi'_{min,CI}}{\Phi'_{min,RI}} = \frac{2}{3}\exp\left(-A\frac{Re_W}{Re_\phi}\frac{\Phi'_{min,RI}}{\Phi'_{min,CI}}\right)\left\{\frac{(1-\Gamma_{\Delta p})^{2/3}-1}{\Gamma_{\Delta p}}\right\} \tag{4.11}$$

where

$$\Gamma_{\Delta p} = \frac{\Delta C_p}{C_{\beta_1}} = \frac{C_{p,\max}}{C_{\beta_1}}\left(\frac{Re_W}{Re_\phi}\right)^2 \tag{4.12}$$

The least-squares fit to the Chew *et al.* (1994) discharge coefficient data in Fig. 3.6 yielded a value of A = 1.95 for $\Phi'_{min,RI}$ = 0.055. With A known, it was necessary to calculate $C_{p,max}$ and $C_{\beta 1}$ for the axial seal geometry so that Eq. 4.11 could be fitted to the off-design experimental data. Given the definition of ΔC_p in Eq. 4.13 below, $C_{p,max}$ was calculated to be 2.74 from the gradient of the least squares linear fit to the measured variation of $\Delta C_p^{1/2}$ with Re_W / Re_ϕ at location A.

$$\Delta C_p = C_{p,max}\left(\frac{Re_W}{Re_\phi}\right)^2 \tag{4.13}$$

$C_{\beta 1}$ was determined from $\Phi'_{min,EI}$, $\Phi'_{min,RI}$ and ΔC_p at Re_W / Re_ϕ = 0.538 using Eqs. 4.14, 4.15 and 4.16:

$$\Phi'_{min,EI} = \frac{2}{3}C_{d,e,EI}\,\Delta C_p^{1/2} \tag{4.14}$$

$$\Phi'_{min,RI} = C_{d,e,RI}\,C_{\beta_1}^{1/2} \tag{4.15}$$

and

$$\frac{C_{d,e,EI}}{C_{d,e,RI}} = \exp\left(- A \frac{Re_W}{Re_\phi} \frac{\Phi'_{min,RI}}{\Phi'_{min,EI}} \right) \tag{4.16}$$

The empirical constants used to fit the variable discharge combined ingress orifice equation to the experimental data are given in Table 4.3.

Constant	Value
A	1.95
$C_{\beta I}$	0.0137
$C_{d,e,EI}$	0.359
$C_{d,e,RI}$	0.471
$C_{p,max}$	2.74

Table 4.3: Empirical constants for variable discharge coefficient combined ingress orifice equation.

Figure 4.14 shows the measured variation of $\Phi'_{min,CI} / \Phi'_{min,RI}$ with Re_W / Re_ϕ for Re_ϕ = 5.32×10^5, 8.17×10^5 and 9.68×10^5; the open symbols represent data obtained using the tuning technique and the solid symbols show data collected from least-squares cubic spline fits to the full effectiveness curves. When plotted in this form the data collapsed upon Re_ϕ to form a single curve. It was shown in Chapter 3 that the EI asymptote was within 5% of the least-squares fit to the Phadke and Owen (1988c) data for $\Phi'_{min,CI} / \Phi'_{min,RI} > 2$. This criterion was assumed to be valid for the measurements presented here; consequently, the gradient of the EI asymptote was calculated from a least-squares linear fit to the data for $\Phi'_{min,CI} / \Phi'_{min,RI} > 2$.

The prediction made by the CI orifice equation, shown as a solid line in Fig. 4.14, agrees well with the experimental data as the EI asymptote is approached; however, it fails to capture the unexplained blip in the data for $Re_W / Re_\phi < 0.1$. This blip was unobserved in studies carried out by Phadke and Owen (1988c) and Khilnani and Bhavnani (2001). It is therefore hypothesised that the anomalous behaviour at low Re_W / Re_ϕ was rig specific. Further experimental and CFD work will be required to confirm this hypothesis.

Figure 4.15 shows the variation of $\Phi'_{min,CI} / \Phi'_{min,RI}$ with Re_W / Re_ϕ as obtained from the full effectiveness curves for the least-squares cubic spline fit (shown as solid symbols in Fig. 4.14) and the EI effectiveness equation (Eq. 4.8). It is apparent that for the overspeed cases the obtained values of $\Phi'_{min,CI} / \Phi'_{min,RI}$ are well-matched for the two fitting techniques; however, the values diverge significantly for the underspeed cases.

Figure 4.16 shows the measured variation of ε with Φ_0 for Re_W / Re_ϕ = 0.734; the least-squares cubic spline fit to the data produced $\Phi'_{min,CI}$ / $\Phi'_{min,RI}$ = 5.27, whereas the fit from the EI effectiveness equation resulted in $\Phi'_{min,CI}$ / $\Phi'_{min,RI}$ = 6.25. The full effectiveness curve for this case (and also the other underspeed cases) displayed a kink which was unobserved for the overspeed, RI and on-design EI cases. It is clear from Fig. 4.16 that the fit produced by the EI effectiveness equation did not capture the kink in the data and therefore overestimated $\Phi'_{min,CI}$. One possible explanation for the kink is that the high sealant flows required to purge the wheelspace for the underspeed cases impacted the discharge coefficients through the seal clearance. The fit from the EI effectiveness equation (Eq. 4.8) was produced by determining Γ_c (the ratio of the ingress and egress discharge coefficients) and Φ_{min} from the experimental data using the statistical technique developed by Zhou *et al.* (2011b). As was stipulated in Owen (2011b): Γ_c does not affect the obtained value of Φ_{min}, but the *shape* of the predicted effectiveness curve. In the EI effectiveness equation Γ_c is assumed to be a constant, which produces a curve of constantly decreasing gradient; to produce a curve with a kink, Γ_c would have to vary with Φ_0. Given the kink in the experimental data, it seems reasonable to suggest that the discharge coefficients (and thus Γ_c) were influenced by the large values of Φ_0 in the underspeed experiments.

4.4 Experimental uncertainties

It was shown in Sangan *et al.* (2012) that the standard deviation, σ, of the gas concentration measurements could be expressed in terms of ε as:

$$\sigma = \frac{2\delta}{c_0 - c_a}\sqrt{\int_0^1 (1+\varepsilon)^2 \,\mathrm{d}\varepsilon} = \frac{3.06\,\delta}{c_0 - c_a} \tag{4.17}$$

where δ is the uncertainty in the measurements and c_0 and c_a are the sealant flow and annular concentration levels respectively; the uncertainty of the gas analyser used to make the measurements presented here was 1.5%. During the experiments the sealant flow was seeded close to the maximum of the analysers 1% range; consequently, δ /(c_0 - c_a) ≈ 0.015 and σ ≈ 0.046.

Table 4.4 shows the parameters used to fit the EI effectiveness equation to the on-design experimental data; these values, including those for the 95% confidence limits, were calculated using the technique of Zhou *et al.* (2011b). $\Phi_{min,EI}^{+}$ and Γ_c^{+} and $\Phi_{min,EI}^{-}$ and Γ_c^{-}, the parameter values for the upper and lower 95% confidence intervals respectively, were input into the EI effectiveness equation to produce the 95% confidence curves plotted in Fig. 4.17. These curves produce an envelope in which 95% of the experimental data would be expected

to fall. The standard deviation of the fit to the on-design data, which was calculated to be σ = 0.0146, is well within the limiting value of σ = 0.046 calculated above.

Parameter	Value
$\Phi_{min,EI}$	0.326
$\Phi_{min,EI}^{+}$	0.344
$\Phi_{min,EI}^{-}$	0.309
Γ_c	0.476
Γ_c^{+}	0.545
Γ_c^{-}	0.421
σ	0.0146

Table 4.4: Parameters used to fit the EI effectiveness equation to the experimentally measured variation of ε_c with Φ_0 for the axially clearance seal at Re_W / Re_ϕ = 0.538, as calculated using the technique of Zhou *et al.* (2011b). + and - represent the upper and lower 95% confidence limits.

4.5 Implications

The work carried out in this chapter fulfils Objectives 1 and 2 of this thesis (see Section 1.5). Experimental sealing flow measurements for an idealised axial seal have been used to further validate the Owen (2011a, b) orifice theory for combined ingress and have shown that the combined effects of the annular pressure asymmetry and rotation in the wheelspace can play significant roles in driving ingestion at low values of Re_W / Re_ϕ (see Section 4.3.3 and Fig. 4.14) . As far as the author of this thesis is aware, the measurements are the first showing the effect of off-design operation on sealing performance for a setup with vanes and blades.

The requirement of industrial gas turbine engines to operate off-design was discussed in Section 1.4. The measurements presented in this chapter inform the engine designer on the relationship between the operational condition (i.e. Re_W / Re_ϕ) and the required sealant flow levels to prevent ingress for an idealised axial seal. Ingress through the inner seal clearance of double seals (which are representative of those used in engines) is driven by the pressure difference between the outer and inner wheelspaces (see Fig. 2.21). Whilst an engine is unlikely to operate far enough off-design for combined ingress to occur through the outer seal clearance, it is hypothesised that ingestion through the inner seal can fall into the combined ingress region when the annular pressure asymmetry is attenuated in the outer wheelspace cavity. It is intended that ingress through double seals at a range of design conditions be explored as part of a future work program.

4.6 Figures

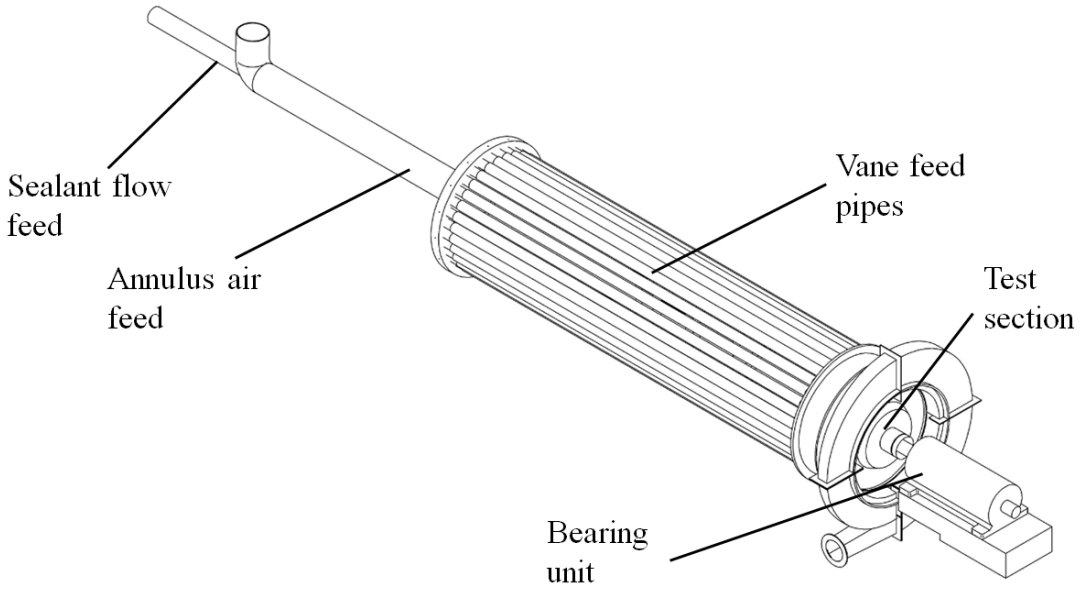

Figure. 4.1: General assembly of Bath gas turbine test rig (adapted from Sangan (2011)).

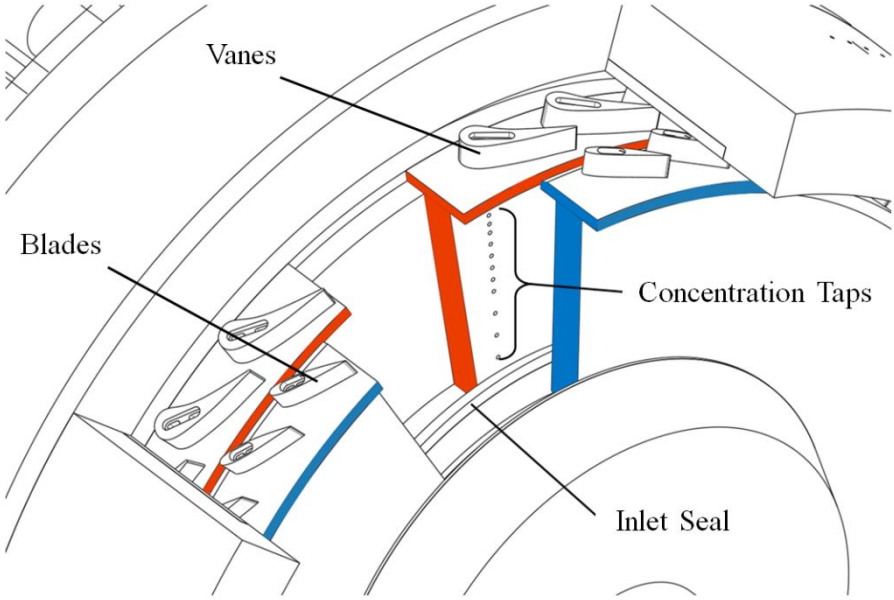

Figure. 4.2: Rig test section showing turbine stage (adapted from Sangan *et al.* (2011a)). The stator is shown in red and the rotor in blue.

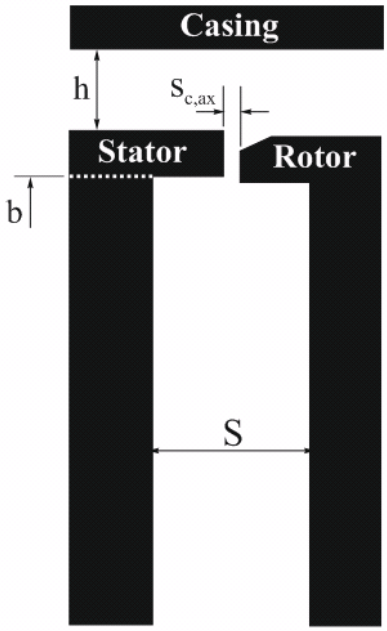

Figure. 4.3: Simple axial seal geometry with key geometric parameters labelled.

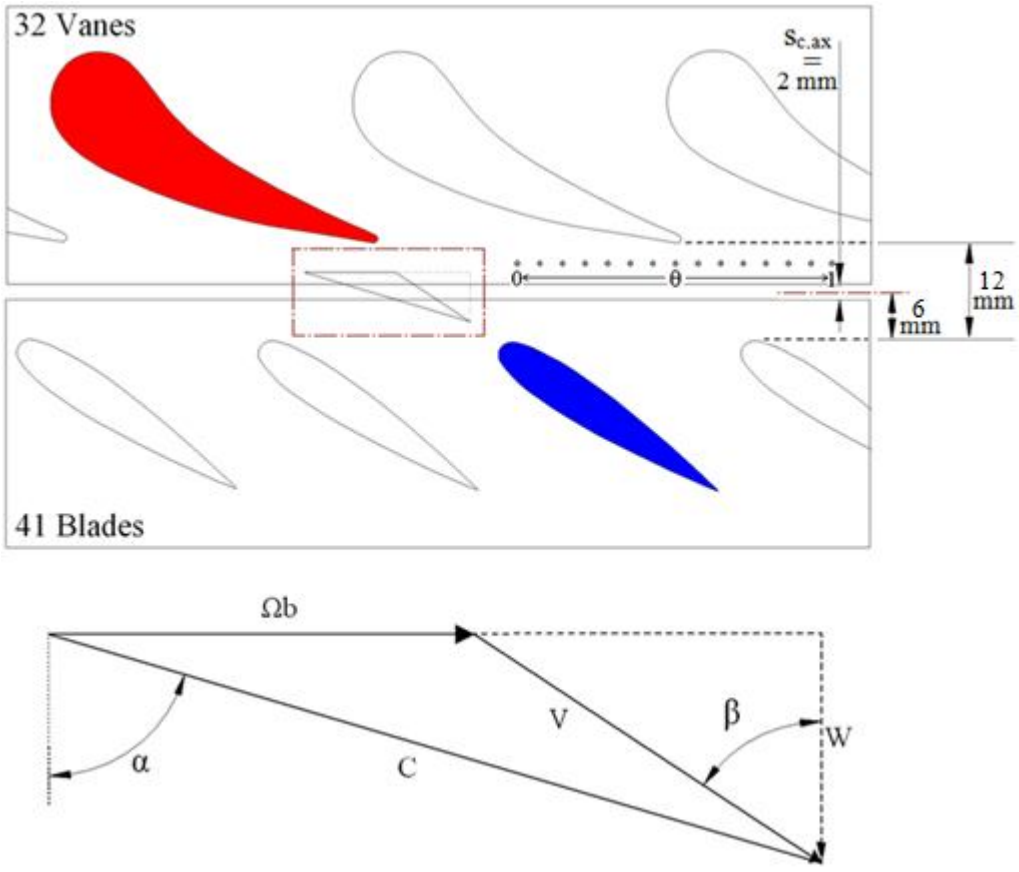

Figure. 4.4: Velocity triangles for vanes and blades (adapted from Sangan *et al.* (2011a)). The static pressure taps are shown on the stator platform across one vane pitch ($0 \leq \theta \leq 1$).

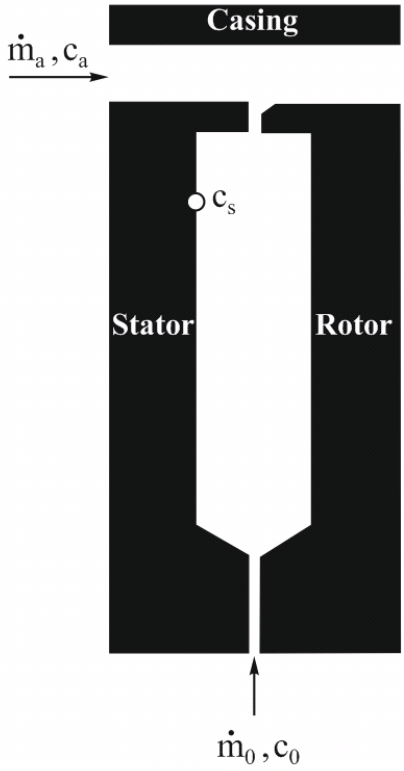

Figure. 4.5: Mass flows and concentrations in the test section of the Bath rig (c_s is shown at r/b = 0.953).

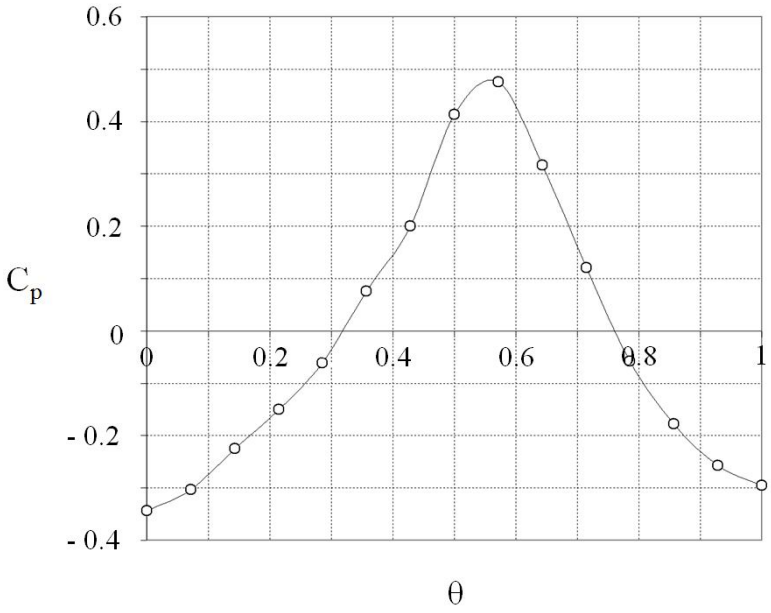

Figure. 4.6: Measured variation of C_p with θ at on the stator shroud (location A) for the design condition with $Re_\phi = 8.17 \times 10^5$ (adapted from Sangan *et al.* (2011a)).

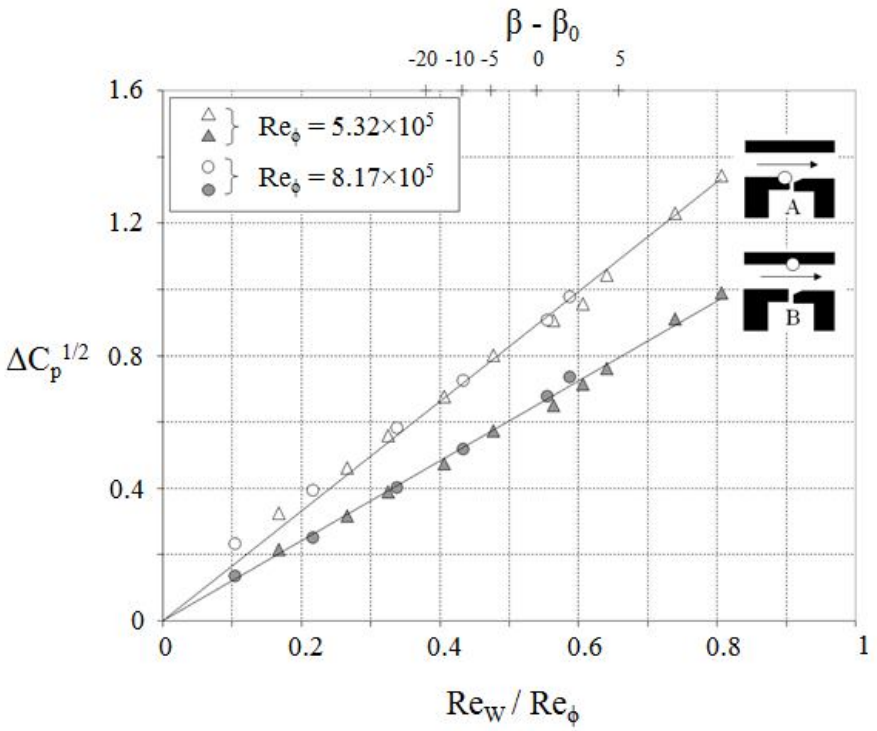

Figure. 4.7: Measured variation of $\Delta C_p^{1/2}$ with Re_W / Re_ϕ at locations A and B for $Re_\phi = 5.32 \times 10^5$ and $Re_\phi = 8.17 \times 10^5$

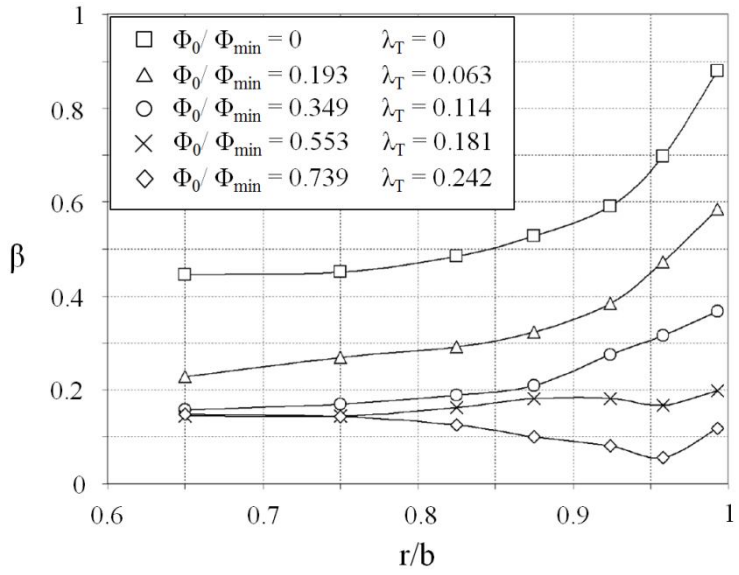

Figure. 4.8: Measured variation of β with r/b for the axial clearance seal for different values of λ_T (adapted from Sangan (2011)).

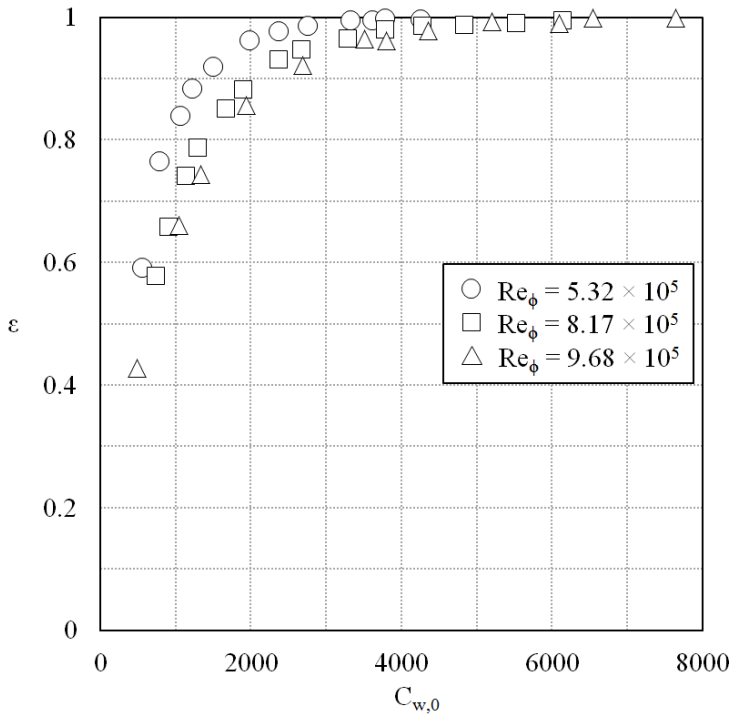

Figure. 4.9: Measured variation of ε with $C_{w,0}$ on the stator wall at r/b =0.953 for the axial clearance seal for RI ingress (i.e. $Re_W = 0$). Three values of Re_ϕ were tested in the range 5.32 to 9.68 × 10^5 .

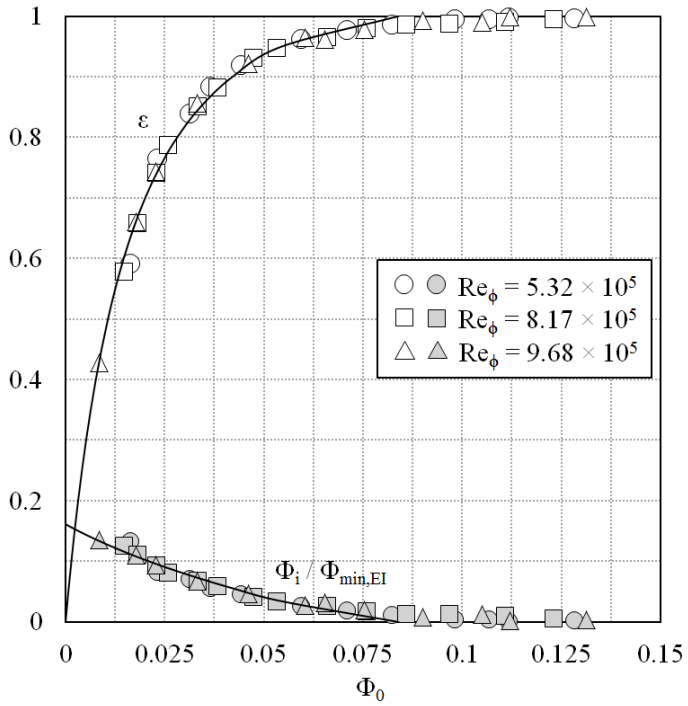

Figure. 4.10: Measured variation of ε and Φ_i / $\Phi_{min,RI}$ with Φ_0 on the stator wall at r/b =0.953 for the axial clearance seal for RI ingress (i.e. $Re_W = 0$). Three values of Re_ϕ were tested in the range 5.32 to 9.68 × 10^5 . Symbols represent experimental data and solid lines show the fits to the data from theory.

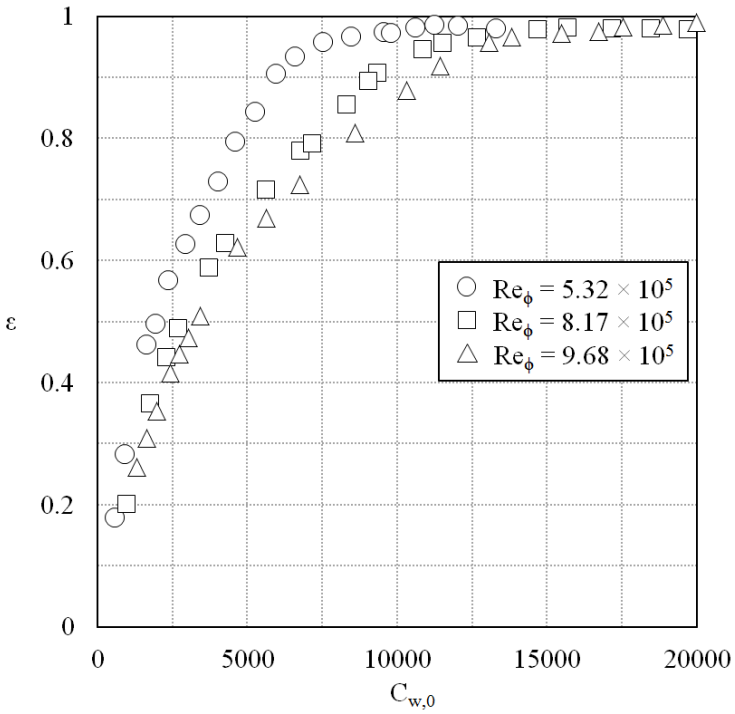

Figure. 4.11: Measured variation of ε with $C_{w,0}$ on the stator at r/b =0.953 for the axial clearance seal for EI ingress (on-design with Re_W / Re_ϕ = 0.538). Three values of Re_ϕ were tested in the range 5.32 to 9.68 × 10^5 .

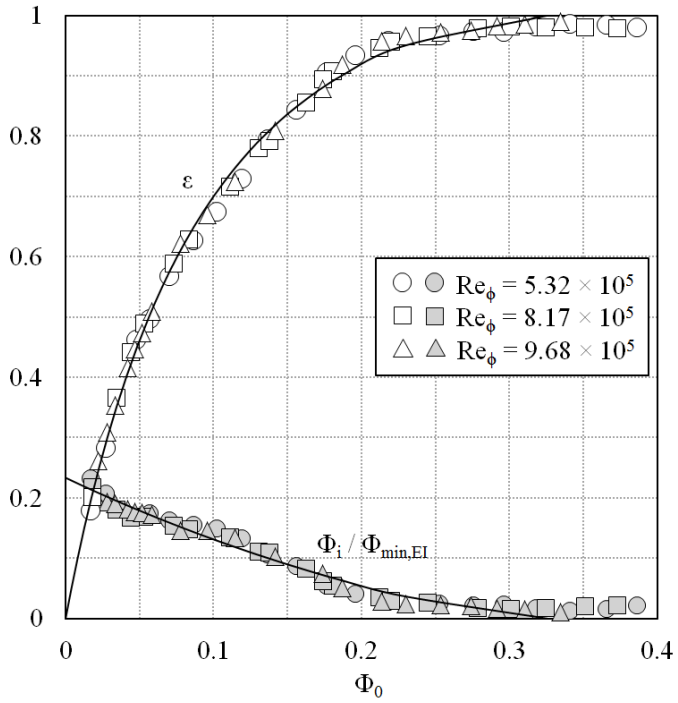

Figure. 4.12: Measured variation of ε and Φ_i / $\Phi_{min,EI}$ with Φ_0 on the stator wall at r/b = 0.953 for the axial clearance seal for EI ingress (on-design with Re_W / Re_ϕ = 0.538). Three values of Re_ϕ were tested in the range 5.32 to 9.68 × 10^5. Symbols represent experimental data and solid lines show the fits to the data from theory.

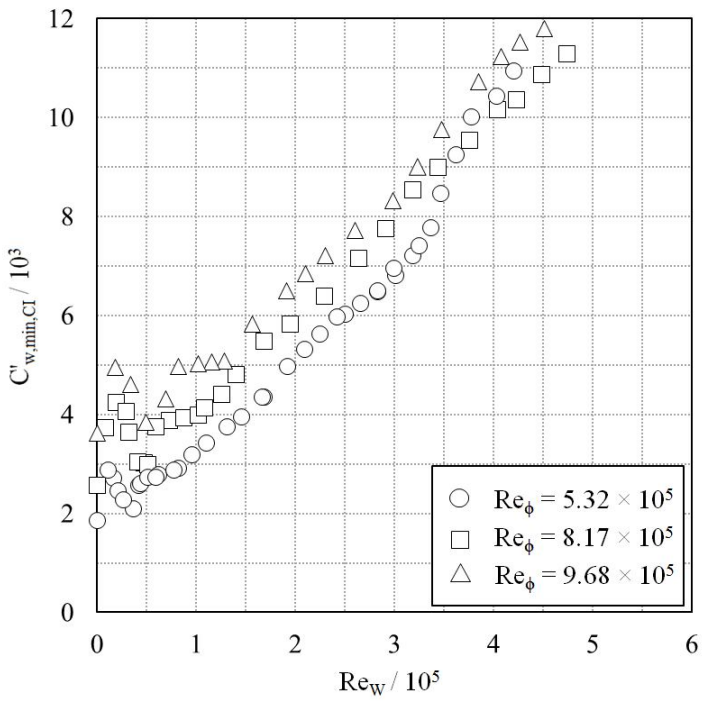

Figure. 4.13: Measured variation of $C'_{w,\,min,CI}$ with Re_W on the stator wall at r/b =0.953 for the axial clearance seal. Three values of Re_ϕ were tested in the range 5.32 to 9.68 × 10^5.

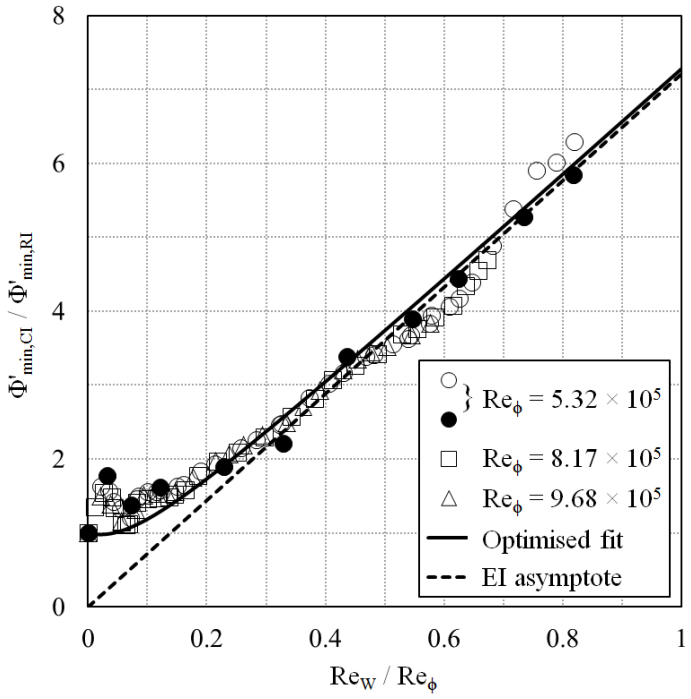

Figure. 4.14: Measured variation of $\Phi'_{min,CI}$ / $\Phi'_{min,RI}$ with Re_W / Re_ϕ on the stator wall at r/b =0.953 for the axial clearance seal. Open symbols represent data obtained using the tuning technique and black symbols represent data obtained using full effectiveness curves. The optimised combined ingress orifice equation and EI asymptote are shown by solid and dashed lines respectively.

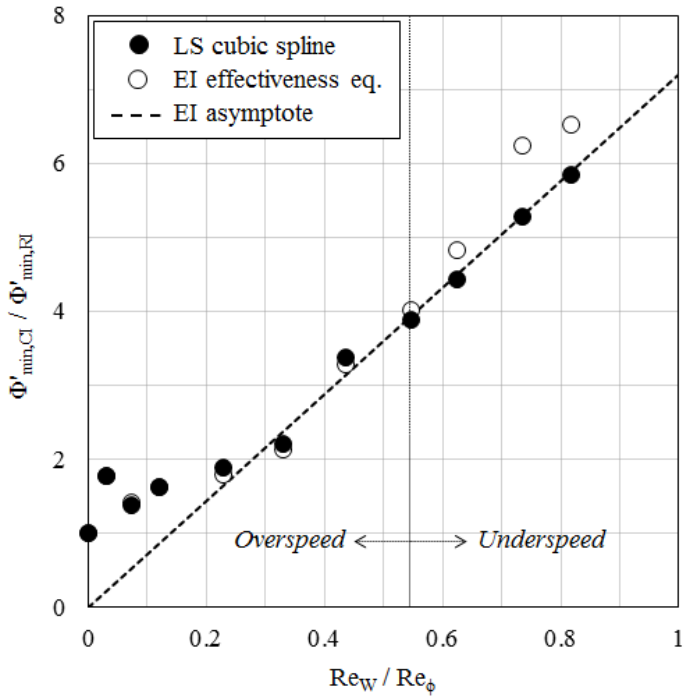

Figure. 4.15: Measured variation of $\Phi'_{min,CI} / \Phi'_{min,RI}$ with Re_W / Re_ϕ on the stator wall at r/b =0.953 for the axial clearance seal. Solid symbols represent data obtained using the least-squares cubic spline fit and open symbols represent data obtained using the fit from the EI effectiveness equations; the fits were applied to full effectiveness curves at each value of Re_W / Re_ϕ.

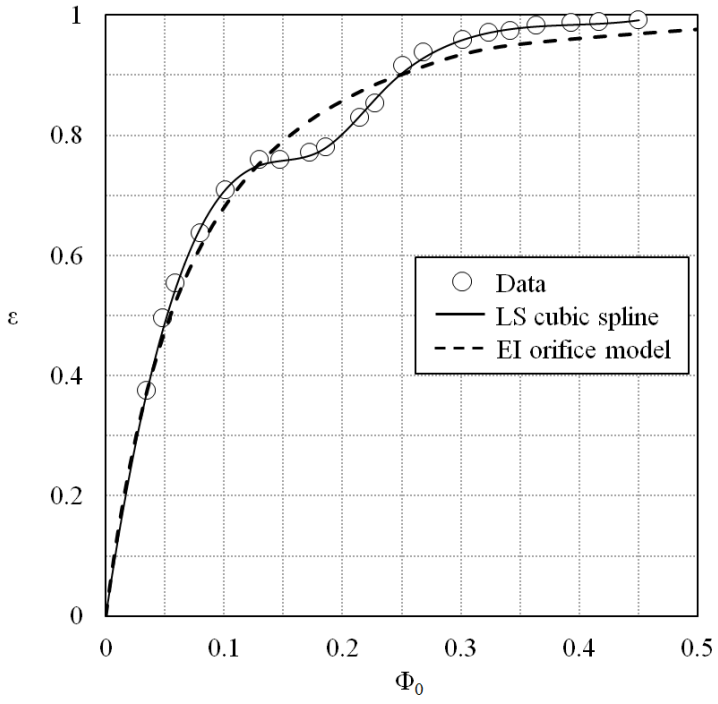

Figure. 4.16: Measured variation of ε with Φ_0 on the stator wall at r/b = 0.953 for the axial clearance seal with $Re_\phi = 5.32 \times 10^5$ and $Re_W / Re_\phi = 0.734$. Symbols represent data and the solid line shows the least-squares cubic spline fit to the data.

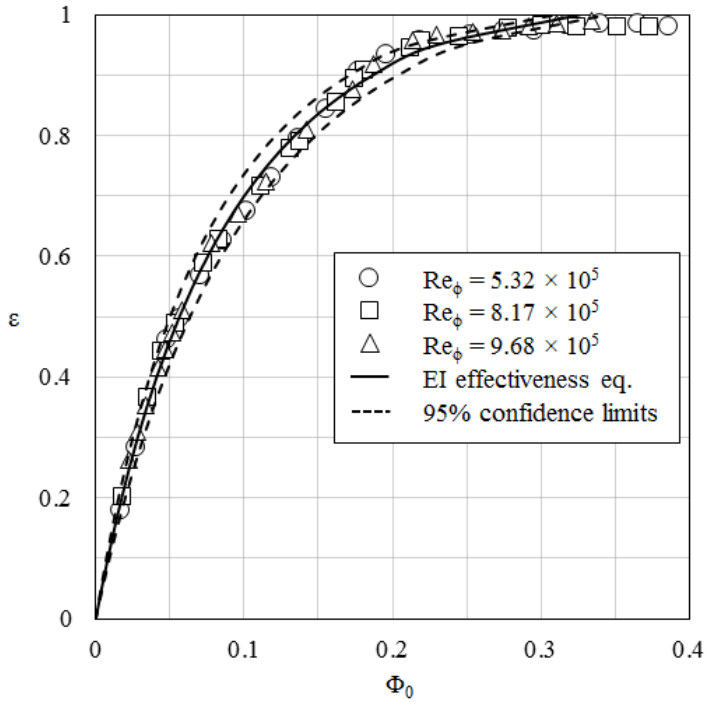

Figure. 4.17: Measured variation of ε with Φ_0 on the stator wall at r/b = 0.953 for the axial clearance seal for EI ingress (on-design with Re_W / Re_ϕ = 0.538). Symbols represent experimental data, the solid lines show the optimised fit to the data from the EI effectiveness equation and the dashed lines show the 95% confidence intervals.

Chapter 5. Literature review part II: heat transfer using thermochromic liquid crystal

The Bath gas turbine test rig was designed for transient heat transfer experiments with thermochromic liquid crystal (TLC) as the rotor surface temperature measurement technique (see Sangan (2011)). This chapter provides an overview of TLC for use in experimental heat transfer studies. The structure, image processing methods and calibration requirements of TLC are considered in detail. It is shown that two TLC surface temperature measurements can be used to determine the heat transfer coefficient and adiabatic wall-temperature from the solution to the one-dimensional Fourier equation for convective heat transfer to a solid of semi-infinite thickness for a step-change and exponential rise in fluid temperature; the uncertainties in the calculated values of the heat transfer coefficient and adiabatic wall temperature are considered for certain combinations of TLCs and for the case where lateral conduction is significant. Alternative surface measurement techniques to TLC and direct heat flux measurement methods are discussed for completeness. Finally, existing research into heat transfer in rotor-stator systems is considered.

5.1 Thermochromic liquid crystals

Liquid crystals are materials that can be used to sense changes in shear stress, pressure or temperature. Cholesteric liquid crystals change colour with temperature; when the crystals change temperature, their optical properties also change owing to a reorganisation of the molecular structure of the material. Thermochromic liquid crystal (TLC), which falls under the cholesteric liquid crystal umbrella, is the most useful to heat transfer experimenters: the material can be applied to a surface, most commonly in micro-encapsulated form, to provide global measurement of wall-temperature during the course of an experiment. Brief overviews of the of the molecular composition and calibration requirements of TLC are provided below. The reader is referred to Kasagi *et al.* (1989), Bahadur (1998) and Ireland and Jones (2000) for a fuller understanding.

5.1.1 Crystal structure

Liquid crystals with nematic structures comprise molecules aligned parallel to one another in planes with a common director (see Fig. 5.1). Cholesteric structured liquid crystals, such as TLC, are also organised into planes where the molecules are aligned

parallel to one another; however, unlike nematic structures, the directors of adjacent planes differ. As described by Hallcrest (1991), during the heating process liquid crystals undergo phase transition: they change from a crystalline solid through to an isotropic liquid. It is in the mesomorphic state (between solid and liquid) that the crystals display their optical properties. In cholesteric structures the director of adjacent planes is rotated through a temperature dependent angle to produce a 'director helix' (see Fig. 5.2). The pitch of the director helix is proportional to the wavelength of visible light; hence, the wavelength of reflected light (and thus colour) is influenced by temperature.

Figure 5.3 demonstrates a typical relationship between wavelength of reflected light and temperature of TLC. TLC colourplay—change from red to yellow to green to blue to violet—typically occurs over a 1 to 20 C range with a starting temperature between -30 and 115 C; the crystals turn colourless when they pass their clearance-point (i.e. when they exceed their colourplay range). The bandwidth of TLC is the temperature range over which the red to blue colour change occurs and is the region where the crystals are most usable in experimental heat transfer. TLC are often categorised by bandwidth: those with a 1–2 C bandwidth are referred to as a 'narrowband crystals', whilst those with a 5–20 C bandwidth are termed 'wideband crystals'. The manufacturers code (see Hallcrest (1991)) is frequently used by experimenters to denote the type of crystal they are using: for example, R40C1W defines a crystal with a red starting temperature of 40 C and bandwidth of 1 C.

TLC are available as unsealed liquids, in microencapsulated form or as printed sheets. The unsealed liquids are generally unsuitable for most applications as they are highly susceptible to degradation from exposure to ultraviolet-light (UV) and air and, owing to the oil-like consistency of TLC during colour change, they easily pick up unwanted dust and fibre particles. Microencapsulated TLC slurries comprise a protective polymer barrier around each crystal molecule; this barrier offers a greater level of protection against degradation relative to the unsealed TLC molecules. Owing to the often harsh operating environments to which measurement surfaces are exposed during heat transfer experiments, microencapsulated TLC is the type most commonly used by experimenters. Printed TLC sheets are used less often as they are less versatile than microencapsulated slurries, which can be applied to complex geometries through various techniques, including airbrushing, dipping and rolling. In a review of liquid crystal methods, Baughn (1995) suggested that airbrushing is the best application method for achieving a coating of uniform thickness, usually on top of a thin layer of black paint, which is used to enhance the brightness of the TLC during their colour change. The colour change is generally recorded on a camera and post-analysed to give a hue–time map of the TLC coated surface. It is important to carefully

calibrate the TLC as there are a number of factors that impact the relationship between the observed colour change and temperature.

5.1.2 Image processing

The change in colour of TLC with time is typically recorded using a CCD video camera and stored as a sequence of images for post-processing. Modern video cameras have three sensors (3CCD), each independently calibrated to a specific range of light wavelengths in the visible spectrum, that detect the components of red, green and blue (RGB) at each pixel in a frame. The RGB components are represented by a value in the range 0–255 and can be extracted from each pixel in the captured frames using software with image processing capabilities.

Some heat transfer experimenters (see Abu Talib *et al.* (2004) and Abdullah *et al.* (2009)) used the green component from RGB as the calibration signal for their crystals. Wang *et al.* (1996) suggested that the Hue-Saturation-Intensity (HSI) index is preferable to RGB as the variation of hue with temperature is monotonic for TLC and is independent of the local illumination strength. The method of conversion from RGB to hue is not covered here; the interested reader is referred to the study of Hay and Hollingsworth (1998) for three definitions of hue and the uncertainties associated with each when used as a parameter for calibration of TLC. It should be noted that hue can be normalised in a number of ways; the authors of the studies discussed in this chapter plotted their hue values over scales of 0–255 or 0–1. Figure 5.4 shows a typical TLC temperature calibration curve for a 30 C narrowband crystal in terms of hue (the definition provided by the Matlab function rgb2hsv) and RGB, as presented by Kakade (2009).

Baughn *et al.* (1999) used a 5 × 5 pixel median filter to process the RGB values of their TLC images. The R, G and B values of each pixel were replaced with the median values of the surrounding 5 × 5 block and then converted to hue using the rgb2hsv function in Matlab. The authors found that applying the median filter to their images reduced calibration uncertainty levels by approximately half compared to the results obtained without the use of the filter.

5.1.3 Calibration considerations

This sub-section provides an overview of the various factors that affect the observed colour change of TLC with temperature. It is important that these factors be taken into

consideration when calibrating TLC if large uncertainties are to be avoided in the experimental measurement of surface temperature.

Film thickness, ageing and high-temperature damage

Wiberg and Lior (2004) calibrated a wideband crystal (R45C10W) to obtain the variation of hue with temperature for four film thicknesses in the range 9–38 μm, as shown in Fig. 5.5. The greatest shift in the calibration curves occurred at hue = 0.37 (close to the peak green intensity): increasing the TLC film thickness from 9 to 38 μm resulted in a decrease in temperature from approximately 55 to 51 C at this value of hue (i.e. a 7% change). The authors suggested that TLC be applied in gradual layers so that the 'magnitude and uniformity' of film thickness can be carefully controlled.

Abdullah *et al.* (2009) investigated the effect of film thickness upon the calibration of green intensity with temperature for a narrowband crystal (R35C1W): thicknesses from 10 to 50 μm were tested in 10 μm increments. The authors observed an 18% increase in peak green intensity and an inconsistent shift of 0.4 C in the temperature at which the peak green intensity occurred when increasing their film thickness from minimum to maximum. It was concluded that film thickness had an insignificant impact upon the value of temperature at which the peak green intensity occurred for narrowband crystals relative to wideband crystals.

Kakade *et al.* (2009a) studied the effect of repeatedly heating narrowband crystals to their clearance-point upon the calibration of hue with temperature for three narrowband TLC (30, 35 and 40 C). The authors discovered that their thinnest TLC layer (15 μm) was subject to ageing—the reduction in intensity and the shift in the hue-temperature calibration of the crystal—at fewer cycles than their thickest TLC layer (45 μm). The calibration curve for the 15 μm layer experienced a shift of around 0.2 C from heating cycles one to five, whereas the calibration curve for 45 μm layer was unchanged after ten heating cycles. The thick layer also proved more resistant than the thin layer to permanent damage from high-temperature exposure (the TLC were heated to 30 C beyond their clearance-point and held at this temperature for 150 minutes before being cooled and re-calibrated). High-temperature exposure resulted in a shift in the peak green temperature of approximately 0.4 C for the 15 μm layer, whereas the shift for the 45 μm layer was significantly less (< 0.1 C). Whilst the authors concluded that it is desirable to have a thin TLC layer so that the temperature of the crystal layer is the same as the surface of the substrate, they also recognised that thicker layers provide the experimenter with the advantage of resistance to ageing. The ability to use TLC repeatedly without sacrifice to the accuracy of the obtained measurements is extremely

useful in experiments that are difficult to setup and re-spraying the crystal after every test is not a feasible option.

Hysteresis

Anderson and Baughn (2004) found evidence of hysteresis in the hue–temperature relationship for narrowband and wideband TLC. The authors observed that the calibration curve obtained during cooling from above the TLC clearance temperature was shifted relative to the calibration curve obtained during heating from below the TLC activation temperature; the shift between the curves increased as the temperature at start of cooling was raised. Kakade *et al.* (2009a), whose results agreed with those of Anderson and Baughn, showed that their TLC 'reset' after a cycle of heating and cooling; the heating and cooling hue–temperature curves were cyclically repeatable provided that the TLC had not started to age or suffer from damage owing to high-temperature exposure (see above). The authors of both studies concluded that errors between calibration and experiment resulting from hysteresis can be negated by calibrating the crystals in the direction of use and from the same initial temperature as to be expected experimentally.

Light source

Farina *et al.* (1994) found that the hue-temperature calibration curves for their wideband TLC (R35C5W) were highly sensitive to the addition of background light to their primary illumination source and the white balance settings on their camera. The authors showed that for their 'ideal' setup (i.e. with their illumination source on full power, no background lighting, a fixed lighting/viewing angle and a constant white balance setting on their camera) that their crystal calibrations could be repeated to within ± 0.25 C accuracy. Varying the background light levels and camera white balance values yielded a shift of up to 2 C in the hue–temperature curves (see Fig. 5.6): an unacceptable level of uncertainty for most heat transfer experimenters. These results showed that the light source, background light levels and white balance of the camera should all be consistent between experiment and calibration if uncertainties are to be minimised.

Anderson and Baughn (2005) investigated the effect of a number of light sources upon the relationship between hue and temperature of their narrowband TLC. The tested illuminates included tungsten, fluorescent and full-spectrum based sources. The authors also examined the impact of background subtraction—a technique which involves subtracting the averaged values of red, green and blue intensity obtained at temperatures below the crystal colourplay from the data captured during the colour changing phase—and white balancing on the obtained hue–temperature curves for the different light sources. The results of the

study revealed that light sources without UV filtering caused damage to the TLC; the source with the highest UV level shifted the hue–temperature calibration curve within minutes of exposure. The background subtraction and white balancing techniques reduced the uncertainty between the calibration curves for the different light sources. Given that modern cameras contain manual white balance modes, white balancing the camera at the beginning of calibrations and experiments is often preferred over background subtraction by experimenters (see Abdullah *et al.* (2009) and Kakade *et al.* (2009a)).

Lighting/viewing angle

Camci *et al.* (1993) found that the calibration of narrowband TLC was insensitive to the angle of illumination in the range 20–40°. As the illumination angle was increased beyond this range the sensitivity of the calibrations increased; at the largest angle (60°) the hue–temperature curve was shifted by 0.2 C relative to the those for the below 20–40°. The authors suggested that the illumination and viewing angles be kept constant between calibration and experiment if an uncertainty in temperature measurement of ±0.1 C is to be obtained using TLC.

Farina *et al.* (1994) showed that wideband crystals were significantly affected by the illumination angle for off-axis lighting (where the illumination angle is varied independently of the viewing angle). As is shown in Fig. 5.7, changing the angle of the light source from 15° to 35° yielded a shift of around 0.6 C over most of the range of hue–temperature calibration curves, whereas calibrations for on-axis viewing—where the illumination and lighting angles are matched—showed a shift of only 0.25 C for the same change in angle. Hay and Hollingsworth (1998) also observed that on-axis lighting produced lower uncertainty levels than off-axis lighting. Sabatino *et al.* (2000) viewed their TLC layer through transparent acrylic and found that on-axis lighting produced reflections off the surface of the viewing window that made their captured images unusable. The authors used off-axis lighting to eliminated the surface reflections and, by having the camera mounted normal to the surface, minimise ‘perspective distortion’.

Kakade *et al.* (2009a) changed the angle of illumination for their calibrations for both narrowband and wideband TLC and found good agreement with the findings of previous studies. The authors found that for a 25 ° angular change in illumination the variation of the hue–temperature curves was within experimental uncertainty for the narrowband crystals and around 0.5 °C for the wideband crystals. Changing the viewing angle had a similar effect to changing the illumination angle upon the measured calibration curves.

Sabatino *et al.* (2000) and Kodzwa and Eaton (2007) developed point-wise calibration techniques for wideband TLC to minimise the uncertainty arising from large changes in viewing/lighting angle that can be present in experimental setups (for example, across a curved surface). Sabatino *et al.* found that from the centre to the edge of their plate the measured hue could vary by up to 20% for a uniform surface temperature. Single point calibration produced an error of 2.5 C across the uniformly heated plate (which was at 31.7 C). By carrying out point-wise calibration—a technique that involves calibrating in cells or points to account for spatial variation of hue across the surface— the variation in measured temperature was reduced to approximately 0.4 C.

Surface rotation

Syson *et al.* (1996) and Camci *et al.* (1998) carried out experiments on rotating discs to determine the effect of centripetal acceleration on the performance of narrowband and wideband TLC. Both studies used an infrared imager to record the surface temperature of the rotating disc to which the TLCs were applied. The results showed that the hue–temperature calibrations for the narrowband and wideband crystals were unaffected by centripetal accelerations of up to 8500g and 16000g respectively. Provided that centripetal acceleration levels are below the aforementioned during a rotating-disc experiment then stationary calibrations can be used for TLC on the surface of the disc.

5.2 Fundamental theory

The heat transfer coefficient between a fluid and solid substrate, h, is determined from the local heat flux, q, and the difference between the surface temperature of the substrate, T_s, and a chosen reference temperature. Moffat (1990) highlighted that it is possible to have two systems with similar fluid velocities and wall temperatures, but different values of h resulting from the difference in the chosen values of reference temperature. Choosing the correct reference temperature is therefore crucial. Moffat suggested that the adiabatic surface temperature—T_{ad}, where all the bounding solids are perfect insulators—is the most appropriate for a system where the injected fluid is at a different temperature to the surface of interest, as would be the case in a typical ingress experiment. h can thus be defined as a function of q, T_{ad} and T_s as follows:

$$h = \frac{q}{(T_{ad} - T_s)} \tag{5.1}$$

Using T_{ad} as the reference temperature ensures that q is zero when $T_s = T_{ad}$ and that h is independent of the magnitude of the temperature of the surface. Often the heat transfer coefficient is expressed in non-dimensional form as the Nusselt number:

$$Nu_r = \frac{hr}{k_{air}} \tag{5.2}$$

where k_{air} is the thermal conductivity of the fluid and, in rotating disc experiments, the characteristic dimension, r, is the radius of the disc.

The heat transfer coefficient can be solved for either steady-state or transient heat transfer. Steady-state experiments generally involve generating and measuring heat flux into the substrate; if q is known and T_{ad} and T_s are measured during an experiment then h can be solved from Eq. 5.1. In transient experiments, the variation of T_s with time, t, is measured for a sudden change in temperature of the air or fluid flowing over the substrate (it is also feasible, but less commonly practiced, to rapidly insert a pre-heated or pre-cooled substrate into an ambient fluid stream). With the variation of T_s and t known Fourier's one-dimensional equation can be solved for h:

$$\frac{\partial T}{\partial t} = \alpha \frac{\partial^2 T}{\partial x^2} \tag{5.3}$$

where $\alpha = k / \rho c_p$ is the thermal diffusivity of the solid and T is the temperature at a distance x from the surface of the solid at time t.

5.3 Analysis of Fourier's equation for a solid of semi-infinite thickness

The analysis of the temperature–time data for transient heat transfer experiments is usually based on the solution of the one-dimensional Fourier equation for convective heat transfer to a solid of semi-infinite thickness with a step-change or exponential rise in the temperature of the fluid. The following initial and boundary conditions apply for the semi-infinite thickness assumption:

$$T = T_{in} \text{ for all } x \text{ at } t = 0 \text{ and as } x \to \infty \text{ for all } t$$

$$\text{and } -k \frac{\partial T}{\partial x} = h(T_{ad} - T_s) \text{ for } x = 0 \text{ for } t > 0$$

where T_{in} is the temperature of the solid prior to the rise in temperature of the fluid.

5.3.1 Solution for a step-change in fluid temperature

Schultz and Jones (1973) showed that for the semi-infinite assumption with a step change in fluid temperature (i.e. from $T_{a,in}$ at $t = 0$ to $T_{a,\infty}$ for $t > 0$), the non-dimensional temperature at the surface of the solid, Θ_s, can be expressed as:

$$\Theta_s = \frac{T_s - T_{in}}{T_{ad} - T_{in}} = 1 - \exp(\chi^2)\,\mathrm{erfc}(\chi) \tag{5.4}$$

where

$$\chi = h\left(\frac{t}{\rho c_p k}\right)^{1/2} \tag{5.5}$$

If T_{ad} is known, as it may be in some heat transfer experiments, then h can be solved from Eq. 5.4 (referred to here as the 'step-change solution') by measuring T_s at a point in time, t, using a single TLC. In the cases where T_{ad} is unknown, then to solve for h and T_{ad} it is necessary measure the surface temperatures $T_{s,1}$ and $T_{s,2}$ at times t_1 and t_2; two TLCs can be used in combination to make these measurements. Appendix A presents the numerical methods used to assess the step-change solution for the cases where T_{ad} is known and unknown.

It was shown in Holman (1990) that for a step-change in fluid temperature at the front face of a solid, the back face non-dimensional temperature can be expressed as:

$$\Theta_L = \frac{T_L - T_{in}}{T_{ad} - T_{in}} = \mathrm{erfc}\left(\frac{1}{2}Fo^{-1/2}\right) - \exp\left(Bi + Bi^2 Fo\right)\mathrm{erfc}\left(\frac{1}{2}Fo^{-1/2} + BiFo^{1/2}\right) \tag{5.6}$$

where the Fourier number, Fo, and the Biot number, Bi, are defined as:

$$Fo = \frac{\alpha t}{L^2} \tag{5.7}$$

and

$$Bi = \frac{hL}{k} \tag{5.8}$$

As mentioned above, the semi-infinite assumption is based upon the premise that the temperature of the back face of the solid, T_L, does not change during the course of an experiment (i.e. $T_L = T_{in}$ and $\Theta_L = 0$); it is therefore required that the specimen be adequately thick and the test time short enough to prevent heat penetrating through to the back face and raising T_L. The commonly used criterion for acceptable use of the step-change solution is, as proposed by Schultz and Jones (1973), that $\Theta_L / \Theta_s < 0.01$. It was suggested by Schultz and

Jones that, based upon the ratio Θ_L / Θ_s, the errors in the semi-infinite solution should be small provided that Fo < 0.1; consequently, Eq. 5.4 should only be used if Fo is within this limit during an experiment.

5.3.2 Solution for an exponential rise and an exponential series rise in fluid temperature

Gillespie *et al.* (1998) developed a solution to Fourier's one-dimensional equation for a semi-infinite solid exposed to an exponential rise in fluid temperature, T_a, from an initial value of $T_{a,in}$ at t = 0, to a value of $T_{a,\infty}$ as $t \rightarrow \infty$. The expression for the exponential rise in fluid temperature and corresponding solution for Θ_s are shown in Eqs. 5.9 and 5.10 respectively.

$$T_a = T_{a,in} + (T_{a,\infty} - T_{a,in})(1 - \exp(-t/\tau)) \tag{5.9}$$

where τ is the time constant of the rise in air-temperature.

$$\begin{aligned}\Theta_s = 1 - \frac{1}{1+\chi_\tau^2}\exp(\chi^2)\operatorname{erfc}(\chi) - \frac{\chi_\tau^2}{1+\chi_\tau^2}\exp(-t/\tau) \\ \times\left(1+\frac{1}{\chi_\tau}\left(\frac{1}{\pi}\sqrt{\frac{t}{\tau}} + \frac{2}{\pi}\sum_1^\infty \frac{1}{n}\exp(-n^2/4)\sinh n\sqrt{\frac{t}{\tau}}\right)\right)\end{aligned} \tag{5.10}$$

where χ was defined in Eq. 5.5 and

$$\chi_\tau = h\left(\frac{\tau}{\rho c_p k}\right)^{1/2} \tag{5.11}$$

If T_{ad} is known then h can be solved numerically from Eqs. 5.9–5.11 using a single TLC measurement of T_s at time t with the values $T_{a,\infty}$ and τ known from the measured fluid temperature history. If T_{ad} is unknown then, as for the step-change solution, two TLC measurements of $T_{s,1}$ and $T_{s,2}$ at times t_1 and t_2 would be required; the equations could then be solved for T_{ad} and h using a Newton-Raphson solver.

Newton *et al.* (2003) extended the semi-infinite solution to Fourier's equation for an exponential rise in fluid temperature to that for an exponential series rise in fluid temperature, where:

$$T_a = T_{a,in} + \sum_{j=1}^{m} T_{a,j}(1 - \exp(-t/\tau_j)) \tag{5.12}$$

$T_{a,j}$ are constant amplitudes, τ_j are time constants and m is the number of exponential series to which the temperature rise is approximated. The authors showed that the solution for Θ_s could be expressed as:

$$\Theta_s = \sum_{j=1}^{m} c_j g(\chi, \chi_{\tau,j}) \tag{5.13}$$

where

$$c_j = \frac{T_{a,j}}{\sum_{j=1}^{m} T_{a,j}} \tag{5.14}$$

$$g(\chi, \chi_{\tau,j}) = 1 - \frac{1}{1+\chi_{\tau,j}^2}\exp(\chi^2)\operatorname{erfc}(\chi) - \frac{\chi_{\tau,j}^2}{1+\chi_{\tau,j}^2}\exp(-t/\tau_j) \times \left(1 + \frac{1}{\chi_{\tau,j}}\left(\frac{1}{\pi}\sqrt{\frac{t}{\tau_j}} + \frac{2}{\pi}\sum_{n=1}^{\infty}\frac{1}{n}\exp(-n^2/4)\sinh n\sqrt{\frac{t}{\tau_j}}\right)\right) \tag{5.15}$$

and

$$\chi_{\tau,j} = h\left(\frac{\tau_j}{\rho c_p k}\right)^{1/2} \tag{5.16}$$

As for the exponential solution described above, T_{ad} and h can be determined for the exponential series solution using Eqs. 5.13–5.16 with two TLC surface temperature measurements and the values of $T_{a,j}$ and τ_j from the measured fluid temperature history. In their study, Newton *et al.* found that m = 3 gave the best fit to their measured fluid temperature profile and, consequently, produced the most accurate estimates of h.

5.4 Uncertainties resulting from TLC for transient heat transfer measurements

Yan and Owen (2002) developed a method for determining the uncertainties in the calculated values of h and T_{ad} resulting from the uncertainties in the TLC surface temperature measurements from which they are calculated. The authors developed a set of uncertainty equations for the semi-infinite solution for a step-change in fluid temperature for two cases: first, when h is unknown and T_{ad} is known; and second, when both h and T_{ad} are unknown. The equations were based upon the theory of Coleman and Steele (1999) for estimating random uncertainties in experiments.

5.4.1 Uncertainty in *h* for a step-change in fluid temperature with T_{ad} known

Yan and Owen showed that for the case where T_{ad} is known, the uncertainties in t and material properties ρ,c_p and k are negligible and the uncertainties in T_{ad}, T_s and T_{in} are equal (i.e. $P_{Tad} = P_{Ts} = P_{Tin} = P_T$), then:

$$\frac{P_h}{h} = \Phi_h \frac{P_T}{T_{ad} - T_{in}} \tag{5.17}$$

where P_h is the uncertainty in h and Φ_h is an amplification parameter calculated from:

$$\Phi_h = \frac{\{2(1 - f(\chi) + f^2(\chi))\}^{1/2}}{\chi f'(\chi)} \tag{5.18}$$

For the semi-infinite solution to a step-change in fluid temperature:

$$\Theta_s = f(\chi) = 1 - \exp(\chi^2)\,\mathrm{erfc}(\chi) \tag{5.19}$$

and

$$f'(\chi) = 2\exp(\chi^2)\left\{\chi\,\mathrm{erfc}(\chi) - \frac{1}{\sqrt{\pi}}\exp(\chi^{-2})\right\} \tag{5.20}$$

Figure 5.8 shows the variation of Φ_h with Θ_s as calculated from Eqs. 5.18–5.20 alongside a set of computed Θ_s–Φ_h values obtained using a 'Monte Carlo' technique; the good agreement between the theoretical prediction and the computed data gave Yan and Owen confidence in their uncertainty theory. A minimum value of $\Phi_h \approx 4.4$ occurs at a value of $\Theta_s \approx 0.52$ and $\Phi_h \leq 5$ for $0.3 < \Theta_s < 0.7$. For a typical experiment, $P_T = 0.2$ C and T_{ad} - $T_{in} = 40$ C; provided that the TLC is selected so that it yields a value of Θ_s in the range 0.3–0.7 then $P_h / h \approx 2.5\%$. This value would be deemed acceptable by most heat transfer experimenters.

5.4.2 Uncertainties in *h* and T_{ad} for a step-change in fluid temperature

When h and T_{ad} are unknown then, as previously mentioned, to solve the semi-infinite solution for a step-change in fluid temperature it is necessary to measure $T_{s,1}$ and $T_{s,2}$ at times t_1 and t_2 using two TLC. The non-dimensional surface temperatures can be expressed as:

$$\Theta_1 = \frac{T_{s,1} - T_{in}}{T_{ad} - T_{in}} = f(\chi_1) \tag{5.21}$$

and

$$\Theta_2 = \frac{T_{s,2} - T_{in}}{T_{ad} - T_{in}} = f(\chi_2) \tag{5.22}$$

where $\Theta_1 < \Theta_2$.

For the case where the uncertainties in t_1, t_2 and material properties ρ, c_p and k are negligible and the uncertainties in temperatures $T_{s,1}$, $T_{s,2}$ and T_{in} are equal (i.e. $P_{Ts,1} = P_{Ts,2} = P_{Tin} = P_T$), then, as shown by Yan and Owen, the uncertainty in h can be calculated from Eq. 5.17 with:

$$\Phi_h = \left\{2(\Phi_1^{-1} - \Phi_2^{-1})^{-2}(\Theta_1^{-2} + \Theta_2^{-2} - \Theta_1^{-1}\Theta_2^{-1})\right\}^{1/2} \tag{5.23}$$

where

$$\Phi_1 = \frac{f(\chi_1)}{\chi_1 f'(\chi_1)} \tag{5.24}$$

and

$$\Phi_2 = \frac{f(\chi_2)}{\chi_2 f'(\chi_2)} \tag{5.25}$$

The uncertainty in the adiabatic wall temperature , P_{Tad}, can be determined from:

$$\frac{P_{Tad}}{T_{ad} - T_{in}} = \Phi_{Tad} \frac{P_T}{T_{ad} - T_{in}} \tag{5.26}$$

where

$$\Phi_{Tad} = \left|\Phi_2 - \Phi_1\right|^{-1}\left\{\Phi_1^{\,2}\Theta_1^{-2} + \Phi_2^{\,2}\Theta_2^{-2} + \left[\Phi_2(\Theta_2^{-1} - 1) - \Phi_1(\Theta_1^{-1} - 1)\right]^2\right\}^{1/2} \tag{5.27}$$

Figures 5.9 and 5.10 show the effect of Θ_2 on the variation of Φ_h and Φ_{Tad} with Θ_1 respectively, as calculated from Eqs. 5.21–5.27, alongside sets of computed values obtained using the aforementioned Monte Carlo technique (which again showed good agreement with the theory). Loci of minima, which are also plotted in the figures, show that in order to minimise Φ_h and Φ_{Tad}, and thus the uncertainties in h and T_{ad}, it is necessary to select two TLC such that Θ_2 is as large as possible and $\Theta_1 \approx 0.5\ \Theta_2$. It is thus necessary that the experimenter make an estimate of T_{ad} for their experiments and select their TLC according to the aforesaid criteria so that the uncertainties in their calculated values of h and T_{ad} are minimised. If an inappropriate TLC pair is used then, as can be seen from Figs. 5.9 and 5.10, the amplification factors can be significant relative to the minimum obtainable values.

5.4.3 Uncertainty in h for an exponential series rise in fluid temperature when T_{ad} is known

Owen *et al.* (2003) developed the uncertainty work of Yan and Owen (2002) for an the semi-infinite solution to an exponential series rise in fluid temperature. For the case where T_{ad} is known, the uncertainties in t and material properties ρ, c_p and k are negligible and the uncertainties in T_{ad}, T_s and T_{in} are equal (i.e. $P_{Tad} = P_{Ts} = P_{Tin} = P_T$), the heat transfer coefficient amplification factor can be calculated from:

$$\Phi_h = \sum_{j=1}^{m} \frac{\Phi_{h,j}}{c_j} \tag{5.28}$$

where

$$\Phi_{h,j} = \frac{\{2(1-\Theta_s+\Theta_s{}^2)\}^{1/2}}{\chi g'(\chi, \chi_{\tau,j})} \tag{5.29}$$

and Θ_s, c_j and $g(\chi, \chi_\tau)$ are given in Eqs. 5.13, 5.14 and 5.15 respectively. When $m = 1$ the equations are applicable to the semi-infinite solution for an exponential rise developed by Gillespie *et al.* (1998). The uncertainty in h can be calculated from the known values of Φ_h, P_{Tad} and T_{ad}-T_{in} using Eq. 5.17. The optimum value of Φ_h, which occurs in the range $0.5 < \Theta_s < 0.6$, increases with χ_τ. Owen *et al.* showed that for $\chi_\tau = 1$, then $\Phi_{h,min} \approx 5$ and for $\chi_\tau = 10$, $\Phi_{h,min} \approx 23$. The experimental setup should be designed to minimise χ_τ so that large uncertainties in h can be avoided.

5.5 Lateral-conduction error

The one-dimensional solution of Fourier's equation, from which the transient solutions presented above were derived, ignores the effect that the lateral variation in surface temperature has on the determined value of h. Kingsley-Rowe *et al.* (2005) provided a correction for the one-dimensional solution to account for the errors in h when lateral-conduction is significant.

Fourier's equation in two-dimensions can be expressed as:

$$\frac{\partial T}{\partial t} = \alpha\left(\frac{\partial^2 T}{\partial x^2} + \frac{\partial^2 T}{\partial y^2}\right) \tag{5.30}$$

where x and y are the co-ordinates normal and parallel to the surface respectively. Alternatively, the two-dimensional equation can be represented in non-dimensional form as:

$$\frac{\partial \Theta}{\partial Fo} = \frac{\partial^2 \Theta}{\partial X^2} + \frac{\partial^2 \Theta}{\partial Y^2} \tag{5.31}$$

where $X=x/L$, $Y=y/L$ and Fo is given by Eq. 5.7. For the one-dimensional case $\partial^2\Theta/\partial Y^2 = 0$.

Kingsley-Rowe *et al.* introduced a correction parameter, $\phi = \phi$ (X, Y, Fo), which was defined by:

$$\phi = \frac{\partial^2 \Theta}{\partial Y^2} \Big/ \frac{\partial^2 \Theta}{\partial X^2} \tag{5.32}$$

With $\overline{\phi}$ assumed to equal the average value of ϕ, the authors developed a quasi-two-dimensional equation:

$$\frac{\partial \Theta}{\partial \overline{Fo}} = \frac{\partial^2 \Theta}{\partial X^2} \tag{5.33}$$

where

$$\overline{Fo} = Fo(1 + \overline{\phi}) \tag{5.34}$$

For the semi-infinite solution to a step-change in fluid temperature then:

$$\Theta_s = f(\overline{\chi}) = 1 - \exp\left(\overline{\chi}^2\right)\mathrm{erfc}\left(\overline{\chi}\right) \tag{5.35}$$

where

$$\overline{\chi} = \overline{Bi}\,\overline{Fo}^{1/2} \tag{5.36}$$

and

$$\overline{Bi} = \frac{\overline{h} L}{k} \tag{5.37}$$

$\overline{h}$ is the value of the heat transfer coefficient with correction for lateral-conduction. The corrected Biot number can be calculated from:

$$\overline{Bi} = Bi_1 (1 + \overline{\phi})^{-1/2} \tag{5.38}$$

where Bi_1 is the value of Bi obtained from the one-dimensional solution.

Kingsley-Rowe *et al*. provided a means of estimating $\overline{\phi}$ from ϕ_0, where ϕ_0 is the value of ϕ at $X = 0$, $Y = 0$ and $Fo = Fo_0$ (Fo_0 is the value of Fo at which the TLC surface temperature measurement is taken). The following relationship between $\overline{\phi}$ and ϕ_0 was assumed:

$$\overline{\phi} = c\phi_0 \tag{5.39}$$

where c is a constant of proportionality. The authors showed that ϕ_0 could be estimated from:

$$\phi_0 = 2\frac{Fo_0}{Bi_1}\left[\frac{\partial^2 Bi_1}{\partial Y^2} + g(\chi_1)Fo_0^{1/2}\left(\frac{\partial Bi_1}{\partial Y}\right)^2\right] \tag{5.40}$$

where

$$g(\chi_1) = \frac{(f(\chi_1)-1)(1+2\chi_1^2)+2\pi^{-1/2}\chi_1}{\chi_1(f(\chi_1)-1)+\pi^{-1/2}} \tag{5.41}$$

and

$$\chi_1 = Bi_1 Fo_0^{1/2} \tag{5.42}$$

To calculate $\overline{Bi}$ it is necessary to use TLC to measure the variation of Bi_1 with Y during an experiment, thereby allowing $\partial\chi_1/\partial Y$ and $\partial^2\chi_1/\partial Y^2$ to be estimated at a specified value of Y from a smoothed fit to the data; with χ_1, Fo_0, $\partial\chi_1/\partial Y$ and $\partial^2\chi_1/\partial Y^2$ known, ϕ_0 can be estimated from Eq. 5.40. Kingsley-Rowe *et al.*, who solved Fourier's two-dimensional equation numerically to validate their technique, found that the constant of proportionality, c, could be approximated by:

$$c = 0.563 - 0.371\Theta_s \tag{5.43}$$

where Θ_s is the value of non-dimensional temperature given by the TLC surface temperature measurement at Fo_0. With c estimated using the above correlation, $\overline{\phi}$ and $\overline{Bi}$ can be determined from Eqs. 5.38 and 5.39. Kingsley-Rowe *et al.* used their numerical model to show that for $\Theta_s = 0.5$ with a polynomial variation of Bi_1 with Y, their technique reduced the error in the calculated value of Bi from 20% to 2%.

5.6 Alternative surface temperature measurement techniques to TLC

The Bath test rig was designed specifically for TLC (see Sangan (2011)) and so this chapter has focused largely on the use of TLC as a surface measurement technique from which h and T_{ad} can be determined. In this section, infrared thermography and thermocouples are considered as alternatives to TLC. As only an overview of each technique is provided, the interested reader is directed to the cited papers for a fuller understanding.

5.6.1 Infrared thermography

Carlomagno *et al.* (1998) and Carlomagno and Cardone (2010) provide detailed accounts of infrared (IR) thermography in experimental heat transfer. The technique comprises the use of an IR camera to detect the energy radiated in the IR spectrum by an object and convert it into hue or intensity based signal. As with TLC, the converted signal can be calibrated to produce a hue–temperature correlation, from which a surface temperature map can be measured during an experiment.

Modern IR cameras are capable of measuring two-dimensional maps of surface temperatures with high sensitivity (down to 20 mK) and fast response-times (as low as 20 μs); this makes them extremely useful for transient heat transfer studies. However, as Carlomagno and Cardone pointed out, the calibration of IR cameras for accurate temperature measurement is notoriously difficult owing to a number of factors. Factors of particular note are the emission of radiation from background objects and the transmissivity of viewing windows; these need to be accounted for between calibration and experiment if errors in the measured temperature are to be avoided.

Although an IR camera would have been suitable for making surface temperature measurements on the rotor of the Bath test rig, there were a number of factors that favoured the use of TLC for the experiments carried out in this thesis. First, IR cameras are expensive and difficult to calibrate; by contrast, TLC is relatively cheap and, provided the factors discussed in Section 5.1.3 are considered, can be accurately calibrated with relative ease. Second, viewing the rotor surface in the wheelspace would have necessitated the installation of a window of high transmissivity in the stator wall. The architecture of the rig would have made this extremely difficult as the back of the stator is heavily instrumented. The use of TLC on the rotor surface was made straightforward by constructing the disc out of transparent polycarbonate.

5.6.2 Thermocouples

The fundamental theory of thermocouples and their application in surface temperature measurement is discussed in detail by Moffat (1990). Figure 5.11 shows a typical thermocouple circuit with details pertinent to the description provided below. A thermocouple comprises two wires of thermoelectrically dissimilar metals welded together to form a measurement junction (termed hot junction) at one end; the unwelded ends of the wires are individually fed into a device that measures the voltage difference between the two terminals (termed reference end). When the hot junction is heated or cooled relative to the

reference end, a voltage difference exists between the two wire terminals. This voltage difference, ΔV, can be measured and correlated to the temperature difference, ΔT, between the hot junction and reference end. The temperature of the two wire terminals, which must be equal, is referred to as the reference temperature, T_{ref} ; it is necessary to measure this temperature and add it to the temperature difference between the hot junction and reference end in order to obtain the absolute temperature value at the welded tip (i.e. $T_{hot} = \Delta T + T_{ref}$).

Thermocouples can be used to make surface temperature measurements in two ways: first, the measurement junction can be attached directly to the surface, typically through welding; and second, the measurement junction can be embedded in the substrate on which the surface is to be measured. Both types of thermocouple require careful installation and calibration (specific error sources and calibration requirements are not discussed here). The design complexities and expense associated with transmitting thermocouple voltages from a rotating disc through slip rings and a telemetry system made them unsuitable for surface temperature measurements on the rotor in this study. TLC was seen as a relatively simple and inexpensive alternative.

5.7 Transient heat transfer methods

The solutions for h and T_{ad} presented in Section 5.3 were for a transient change in fluid temperature relative to the test surface. Transient heat transfer experiments can be setup by either rapidly heating the fluid relative to the test surface or vice versa. Experimenters have achieved these rapid temperature changes in a number of ways, some of which are discussed below.

5.7.1 Transient change in fluid temperature

Metzger *et al.* (1991) measured h on the rotor of a rotor-stator system by raising the temperature of the sealant flow relative to the discs, which were both initially at ambient temperature. The air supply was heated using a variac electric heater and, once the temperature of the air had stabilised, it was rapidly directed to the test section using a ball diverter valve. The authors measured the temperature rise of the air at entry to the wheelspace and reported that it could be closely approximated by a modified version of the semi-infinite step-change solution.

Ireland *et al.* (1996) developed a patent for a mesh heater design that has been used in a number of transient heat transfer studies since. The design comprises fine wire meshes soldered to bus bars through which a current is supplied from a power supply. The supply of

current to the bus bars serves to heat up the mesh wire and thereby heat the fluid as it flows through the mesh sections. Newton *et al.* (2003) and Kakade et *al.* (2009a, b) used the design of Ireland *et al.* to generate exponential rises in fluid temperature for the supply of air to their pre-swirl nozzles. TLC was used around the receiver holes to measure the surface temperature history on the rotating-disc. The solution of Fourier's equation for a solid of semi-infinite thickness exposed to an exponential series rise in fluid temperature was used to determine *h*.

5.7.2 Heated/cooled test sections

Baughn (1995) investigated two methods of surface heating for transient heat transfer. The first, referred to as the 'pre-heated wall transient method' involved heating the test section to a uniform temperature in an oven, before removing it and rapidly inserting it into the ambient fluid. The second, termed the 'shroud-heating technique', comprised heating the test section in a shrouded chamber; once the test section had reached a constant temperature, the shrouds were removed to expose it to the fluid. Reiss and Bolcs (2000) and Wagner *et al.* (2007) used pre-cooling conditioning boxes for their research into showerhead cooling on curved surfaces. Both studies utilised an actuator to thrust the uniformly cooled test piece from the conditioning box into the fluid stream and trigger the transient heat transfer process.

The rapid exposure of a heated/cooled test section to an ambient fluid stream is clearly unsuitable for making transient heat transfer measurements in rotor-stator systems, where precise alignment of axial and radial clearances is time-consuming and critical to the accuracy of the obtained results. Owing to this, the majority of transient rotor-stator heat transfer studies have utilised heated fluid methods as described above. A mesh heater arrangement was chosen for the measurements in this thesis.

5.8 Steady-state heat transfer methods

To determine *h* in steady-state heat transfer experiments (where $\partial T/\partial t = 0$ in Eq. 5.3), it is necessary to measure the heat-flux, q, and the steady-state surface temperature, T_{ss}, from which h can be calculated using Eq. 5.1 (note, T_{ad} must be known to the experimenter). This section considers some of the methods used by experimenters to determine *h* during steady-state experiments.

5.8.1 Thin film heat flux meters

Transducers that directly measure surface heat flux are categorised as 'heat flux meters'. The most widely used by heat transfer experimenters are thin film gauges, a detailed discussion of which is provided by Moffat and Kim (2005).

Thin-film gauges are made from thin sheets of insulating materials across which the steady-state temperature drop, ΔT, is measured. Thermopiles—a series of thermocouples—are bonded to the surfaces of the thin film to measure ΔT. The heat flux through the film is calculated from Fourier's law by :

$$q = \frac{k}{L}\Delta T \tag{5.44}$$

where k is the thermal conductivity of the insulating material and L is the thickness of the film.

Chen *et al.* (1996) used thin film gauges to measure the heat flux through a heated rotating-disc (kept at constant temperature by radiant heaters at the back surface of the disc). Embedded thermocouples were used to measure the steady-state surface temperature of the disc during the experiment. Slip-rings and a telemetry system were required to transmit the thin film gauge and thermocouple signals from the rotating disc to the data acquisition system. Such a system (for the reasons discussed in Section 5.6.2 above) was considered unsuitable for measurements on the rotor of the Bath test rig.

5.8.2 Thin electric foil heaters

Han *et al.* (2000) provide a detailed description on the workings of thin foil heaters. Foil heaters comprise thin stainless-steel strips welded to copper bus bars at their ends. The strips are mounted directly onto the test surface, which must be manufactured from a material of low conductivity. An electric current is passed through the strips to generate a constant heat flux on the surface on which they are mounted; q is determined from the electrical power supplied to the foils. Thermocouples are typically soldered to the underside of the foils to measure T_{ss}.

Cardone *et al.* (1997) glued thin foil heaters to the surface of a polyurethane-aluminium rotating-disc. Electrical power was supplied to the heaters through slip rings located in the rotor shaft. The heaters were used to generate a constant heat flux on the polyurethane

surface; T_{ss} was measured using an IR camera. The system produced repeatable measurements of h, with an uncertainty of ±3% quoted by the authors.

Despite the repeatable results obtained by Cardone *et al.* using the combination of thin foils heaters with IR thermography, the system was deemed unsuitable for use in the Bath test rig. The difficulties associated with making surface temperature measurements on the rotor using an IR camera (discussed in Section 5.6.1) combined with the design complexities required to deliver the electrical power to the rotating heaters were favoured by the simplicity of using TLC with transient heating of the air supply.

5.8.3 Heat and mass transfer analogy

Some heat transfer experimenters (for example, see Eckert *et al.* (2001)) measure the transfer of mass during an experiment and subsequently calculate the convective heat transfer coefficient through the mass and heat transfer analogy. The analogy relates the Nusselt number (Nu_r—defined in Eq. 5.2 above) to the Sherwood number (Sh_r) through the Prandtl (Pr) and Schmidt (Sc) numbers as follows:

$$\frac{Nu_r}{Sh_r} = f\left(\frac{Pr}{Sc}\right) \tag{5.45}$$

where

$$Sh_r = \frac{h_m r}{D} \tag{5.46}$$

$$Pr = \frac{\mu}{\rho\alpha} \tag{5.47}$$

and

$$Sc = \frac{\mu}{\rho D} \tag{5.48}$$

h_m is the mass transfer coefficient, r is the characteristic dimension of the system (for a rotor-stator system this would be taken as the disc radius) and D is the mass diffusivity of the fluid.

Hong and Song (2007) used a naphthalene sublimation technique to measure h_m in their experiments. The technique, which is typically carried out under steady-state heat transfer conditions so that a uniform wall temperature is maintained (see Moffat and Kim (2005)), involves coating a transparent test piece with a naphthalene coating and illuminating it with

a laser; the intensity of red light detected behind the naphthalene coating is calibrated to the thickness of the layer, thereby allowing the change of the coating thickness (and h_m) to be measured during an experiment. Hong and Song used a pre-published correlation between Nu_r and Sh_r to determine h from h_m; a 95% uncertainty level of approximately 10% was quoted in their measured values of h.

TLC was considered much simpler than the naphthalene sublimation technique. The need to illuminate the naphthalene layer with a laser and detect the corresponding signal strength behind the test surface would have been difficult to achieve on the Bath test rig given the lack of optical access to the rotor surface through the stator.

5.9 Heat transfer in rotor-stator systems

The majority of work carried out by researchers into ingress (see Chapter 2) has been to understand the fundamental fluid dynamics of the phenomenon and determine the required coolant flow levels to seal the wheelspace for various rim seal geometries. The effects of ingress on convective heat transfer to the rotor has not been studied by many workers; most existing studies into heat transfer to rotating discs have either been conducted for a free-disc or for rotor-stator systems without ingress.

5.9.1 Free-disc Nusselt numbers

Owen and Rogers (1989) solved the boundary-layer equations for turbulent flow over a free-disc rotating in a stationary fluid (i.e. $\beta = 0$) for a power-law temperature distribution on the surface of the disc. The authors showed that the relationship between the local values of Nu_r and $Re_{\phi,r}$ (subscript r denotes the use of the local radius as the characteristic dimension) could be expressed as:

$$Nu_r = 0.0267\left(\frac{n+2.6}{4.6}\right)^{0.2} Pr^{0.6}[(r/b)^2 Re_{\phi,r}]^{0.8} \tag{5.49}$$

where n is the power term in the power law distribution. For an isothermal disc rotating in air, where $n = 0$ and $Pr \approx 0.71$, Eq. 5.49 simplifies to:

$$Nu_r = 0.0194[(r/b)^2 Re_{\phi,r}]^{0.8} \tag{5.50}$$

Owen and Rogers also showed that the radially-weighted average Nusselt number, Nu_{av}, could be expressed in terms of the moment coefficient, C_M, on the disc by:

$$Nu_{av} = Pr\,\chi_{av}\,\frac{Re_{\phi}C_M}{\pi} \tag{5.51}$$

χ_{av} is a correction factor based upon n and Pr, and

$$C_M = \frac{M}{1/2\rho\Omega^2 b^5} \tag{5.52}$$

where M is the moment on the rotating disc. A correlation for the free-disc value of C_M for turbulent flow with $Re_{\phi} < 4.2 \times 10^6$ was given by Bayley and Owen (1969) as:

$$C_M = 0.0655\,Re_{\phi}^{-0.186} \tag{5.53}$$

5.9.2 Rotor moment coefficients

Childs (2011) presented the following correlation for C_M for turbulent flow inside a shroudless rotor-stator cavity with a rotating fluid core located between separate boundary layers on the rotor and stator (Daily and Nece (1960) Regime 4—see Section 2.2.2):

$$C_M = \varepsilon_M\,Re_{\phi}^{-0.2} \tag{5.54}$$

where ε_M is a dimensionless coefficient that decreases as the swirl ratio, β, in the fluid core increases. C_M increases from approximately half of the free-disc value at $\lambda_T = 0$, to the free-disc value at $\lambda_T = 0.22$; between these extremities, C_M increases monotonically with increasing λ_T. It would be expected that for rotor-stator systems with ingress, where the ingested fluid will have a high level of swirl and thereby increase β in the core even more than for an enclosed rotor-stator system, that C_M, and thereby Nu_{av}, would be less than for the free-disc case.

5.9.3 Experiments

Metzger *et al.* (1991) was one of the first studies to use TLC to measure heat transfer in a rotor-stator system. The authors used TLC surface temperature measurements in conjunction with the semi-infinite step-change solution to measure the variation of Nu_r with radius on a rotating disc in close proximity to a stator through which an impinging air jet was fed. The rotor disc and jet nozzle, which was located normal to the surface of the rotor in the wall of the adjacent stator, were initially at ambient temperature. At the periphery of the stator a shroud was installed to minimise ingestion of fluid into the cavity between the two discs. The air supply was heated using a variac electric heater; once the temperature of the air had stabilised it was rapidly directed to the nozzle using a ball diverter valve. The radial location of the nozzle was varied between tests so that the effect of changing the location of the

impinging jet on the heat transfer to the rotor could be investigated. The authors found that central impingement (at $r/b = 0$) produced the highest average level of heat transfer across the surface of the rotor. Increasing the impingement radius resulted in an increase in the heat transfer at the location of impingement relative to the centre-line supplied case, but resulted in a decrease in the average level of heat transfer to the disc. The authors carried out multiple runs at each test case and found good agreement between the different test sets (uncertainties were not quantified in the paper); this gave them confidence in their experimental technique.

Bunker *et al.* (1992a, b) used the same experimental set up as Metzger *et al.* (1991) to examine the effect of the gap ratio of the wheelspace, G, upon the heat transfer to the rotor in the presence of an impinging jet; the radial location of the jet was varied in the range $r/b = 0$, 0.2, 0.4 and 0.8. Like Metzger *et al.*, the authors used TLC surface temperature measurements alongside the step-change solution to determine the variation of Nu_r with r/b. For the case of centre-line impingement, it was assumed that the flow of air was radially outward on both the rotor and stator (this would only be the case if $\lambda_T > 0.22$ and the fluid core between the two discs had broken down—see Section 2.2) and, based upon this assumption, a correction was applied to account for the effect of heat transfer to the stator on the heat transfer to the rotor. For centre-line impingement, there was evidence of impingement and rotationally dominated heat transfer regions at low and high radii respectively, with an area of low heat transfer between. The radial extent of these regions was dependent upon G, the mass flow rate of the air jet and Re_ϕ. Varying the radial location of the jet showed that the overall heat transfer to the rotor was best optimised by median injection (i.e. $0.4 < r/b < 0.6$) for $G \leq 0.10$ and hub injection for larger values of G. For all radial injection locations the heat transfer distribution was significantly affect by the geometry of the rotor disc.

Chew *et al.* (1994) made gas concentration measurements on the surface of the stator in a rotor-stator system with an axial clearance rim seal. External flow was fed through a set of nozzle guide vanes to generate a circumferential pressure asymmetry in the annulus to drive EI ingress. The authors found good agreement between their CFD model and experimental sealing effectiveness data on the stator; consequently, they used their CFD to interrogate the corresponding effectiveness on the rotor, and found that the effects of ingestion of the rotor were significantly less than on the stator. (Although no heat transfer results were reported in this study, the result showing the protection of the rotor from the ingested fluid in the core is pertinent to the discussion of thermal buffering in Chapter 6 of this thesis.)

Chen *et al.* (1996) carried out steady-state heat transfer experiments on a rotor-stator system open to atmosphere through an axial clearance rim seal for $C_{w,0} < 9680$ and $Re_\phi < 1.6$

$\times 10^6$. Thin film gauges and thermocouples were used to measure the heat flux and surface temperature of the rotating disc; h was calculated from these measurements with the adiabatic wall temperature as the reference temperature. During the experiments, the heat flux was kept constant through the rotor by heating the back face with thirty radiant heaters. The sealant flow, which was unheated, was supplied to the wheelspace at low radius through the stator. At $Re_\phi \approx 1.2 \times 10^6$, the Nusselt numbers were shown to increase with $C_{w,0}$; tangential velocity measurements showed that this was the result of the core swirl decreasing, and thus C_M increasing, with increasing λ_T. The Nusselt numbers for the largest tested value of λ_T approached the free-disc levels; this was explained by the core swirl measurements, which showed that $\beta \rightarrow 0$ for this case.

Roy *et al.* (2001) carried out an experimental study into the effect of varying Re_ϕ and $C_{w,0}$ on the distribution of the convective heat transfer to the rotor in a rotor-stator system with a radial-type clearance seal at the rim; mainstream flow was supplied through an annulus to vanes and blades installed at the peripheries of the discs. The authors used TLC and embedded thermocouples to measure the temperature difference, and thus heat flux, across an insulating coating on the surface of the rotor; the local value of h was calculated from the measured flux using the fluid temperature in the core as the reference temperature. The results showed that ingress into the wheelspace had a significant impact on the obtained Nusselt numbers on the rotor at the radii where the fluid core existed (note: the start of the fluid core is pushed radially outward as $C_{w,0}$ increases). The following correlation was proposed for $1504 < C_{w,0} < 7520$ and $4.6 \times 10^5 < Re_{\phi,r} < 8.6 \times 10^5$:

$$Nu_r = CRe_{\phi,r}^{\ m} \tag{5.55}$$

where $C = 0.0195$ and $m = 0.8$ gave the best fit to the experimental data collected by the authors. The average deviation of the data to the correlation was 16.3% for $C_{w,0} = 1504$ and 7.3% for $C_{w,0} = 7520$. Figure 5.12 shows the Roy *et al.* experimental data and associated correlation.

Boutarfa and Harmand (2005) made convective heat transfer measurements for laminar and turbulent flows in a shroudless rotor-stator system with a central opening in the stator (no sealant flow was supplied to the system). The authors used embedded thermocouples and IR thermography to determine the local heat transfer coefficients on the rotating-disc. Correlations between Nu_r and $Re_{\phi,r}$ were provided for the four flow regimes described by Daily and Nece (1960) in the form:

$$Nu_r = CXRe_{\phi,r}^{\ m} \tag{5.56}$$

where C and m are constants and X is a function of the gap ratio, G. The correlations were applicable for isothermal systems with $0.01 < G < 0.17$ and $5.67 \times 10^4 < Re_\phi < 1.4 \times 10^6$. Although the study was not representative of an engine setup—where shrouds and vanes/blades would be installed at the periphery of the discs, external flow would be fed through an annulus, and sealant flow would be supplied to the wheelspace—it demonstrated the significance of the wheelspace flow structure on the heat transfer to the rotor.

Kakade *et al.* (2009b) used TLC in a pre-swirl rotor-stator system in which a number of nozzles at one radial location in the stator swirled heated air onto the surface of the rotor, and the air left the system through a series of receiver holes in the rotor. The authors used TLC on the surface of the rotor with a stroboscopic light to 'freeze' the rotating surface so that the non-axisymmetric heat transfer around the receiver holes could be measured. A transient increase in air supply to the pre-swirl nozzles was achieved using a mesh heater designed using the technique of Ireland *et al.* (1996). The heat transfer coefficient was solved using the TLC surface temperature measurements with the semi-infinite solution for an exponential series rise in fluid temperature, as described above. The results showed two heat transfer regimes: a viscous regime at low λ_T and an inertial regime at high λ_T.

5.10 Summary

This chapter has discussed experimental heat transfer with particular focus on TLC as a surface temperature measurement technique. The structural composition, image processing methods and calibration requirements of TLC were all considered in detail. It was shown that two TLC surface temperature measurements can be used to solve for h and T_{ad} from the one-dimensional solution of Fourier's equation for a step-change or exponential rise in the temperature of a fluid flowing over a solid of semi-infinite thickness. The uncertainties associated with the use of the semi-infinite solution were shown to be large for certain combinations of TLCs or for cases where the lateral variation in surface temperature makes lateral conduction significant.

Alternative surface measurement methods to TLC and direct heat flux measurement techniques for steady-state heat transfer were discussed. The design complexities arising from the need to transmit measurement signals from the rotating disc through slip rings and a telemetry system excluded many of the techniques from the finalised rig design. TLC was seen as an accurate (provided that calibration requirements are taken into account) and inexpensive method, which was easily implementable with the use of a transparent polycarbonate rotor. Of the transient heat transfer methods considered, the use of a mesh

heater to generate a rapid change in fluid temperature was seen as the most feasible for the Bath rig.

Finally, heat transfer in rotor-stator systems was discussed. A number of existing experimental heat transfer studies on rotating discs were presented, the results of which are used to interpret the measurements presented in the following chapter. The review of literature showed that effects of ingress on convective heat transfer to the rotor has not been studied by many workers; previous studies have tended to focus on the free-disc or rotor-stator systems without ingress. It is clear that there is a gap in knowledge that requires investigation.

5.11 Figures

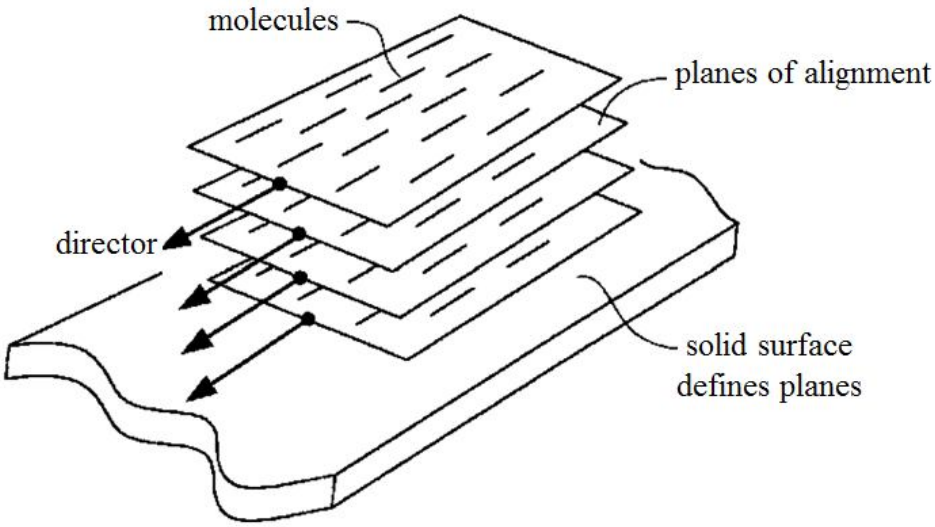

Figure. 5.1: Representation of nematic structure (from Ireland and Jones (2000)).

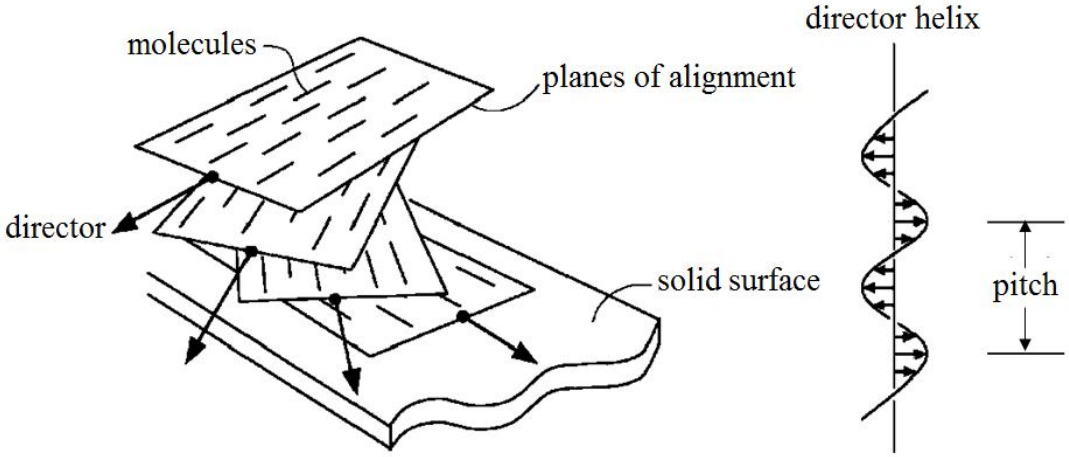

Figure. 5.2: Representation of cholesteric structure (from Ireland and Jones (2000)).

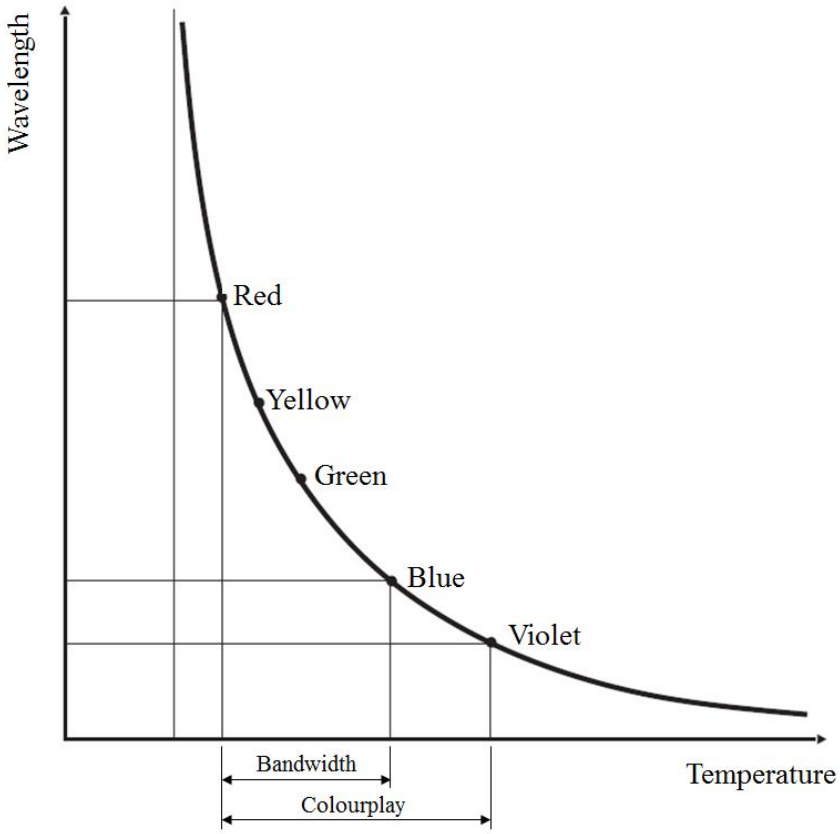

Figure. 5.3: Reflected light wavelength and resultant colour of TLC (from Hallcrest (1991)).

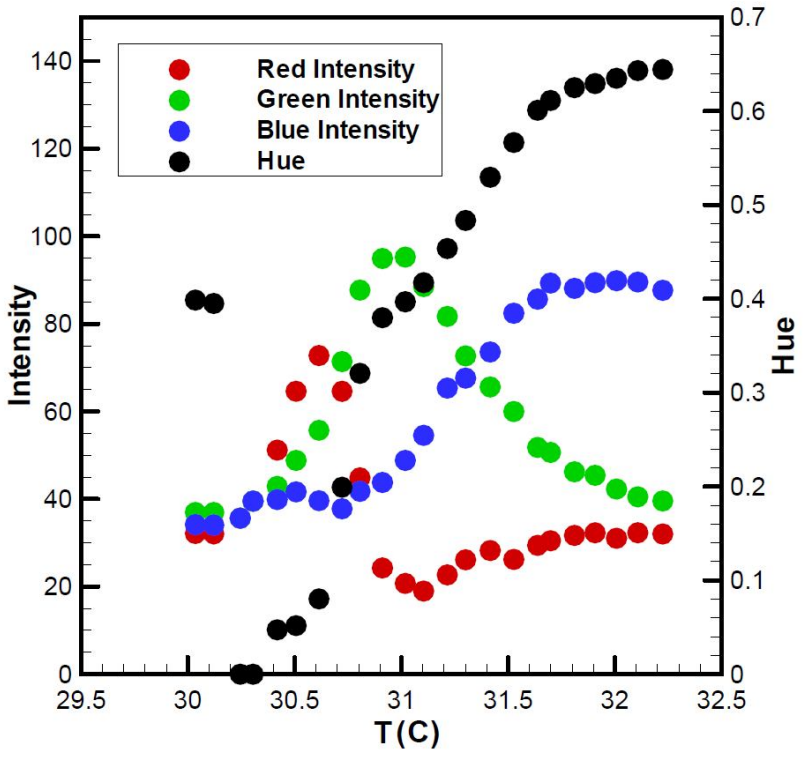

Figure. 5.4: Calibration curve for 30 C narrowband (R30C1W) TLC (from Kakade (2009)).

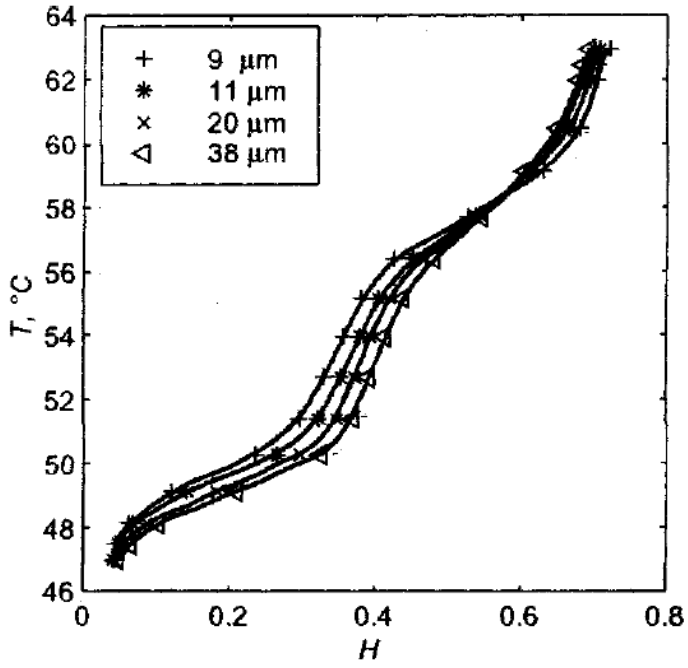

Figure. 5.5: Calibration curve for 40 C wideband (R40C10W) TLC for different film thicknesses (from Wiberg and Lior (2004)).

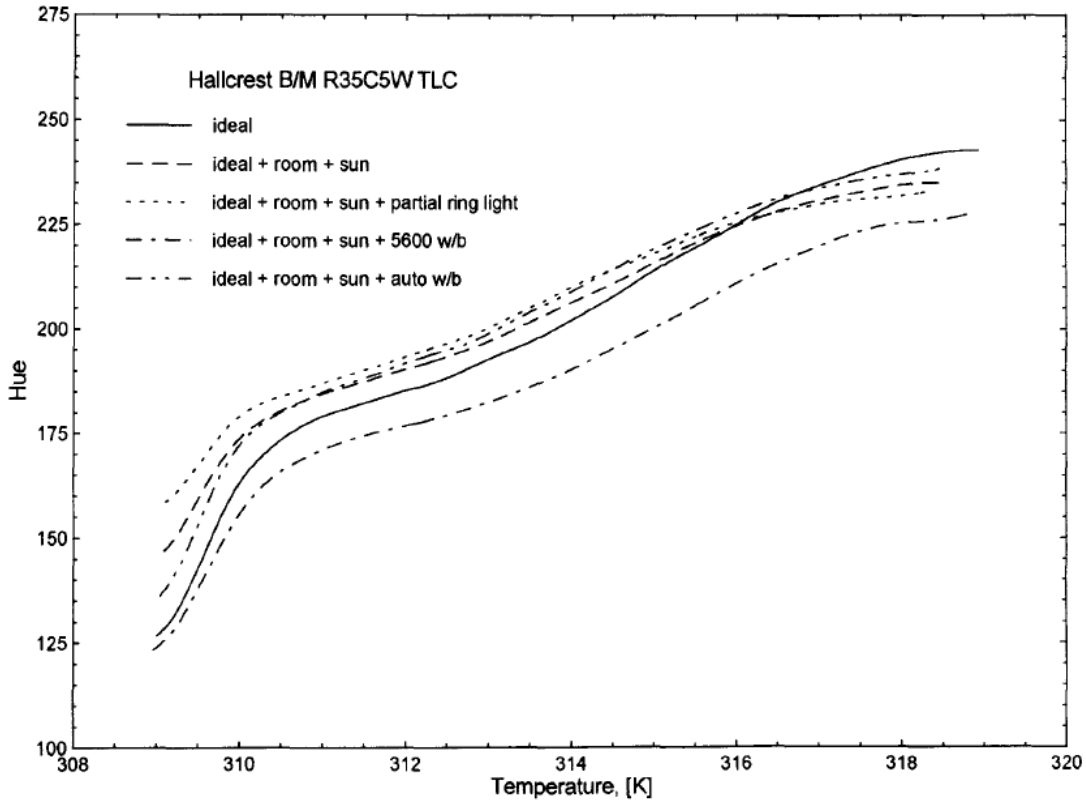

Figure. 5.6: Calibration curve for 35 C wideband (R35C5W) TLC under different lighting conditions (from Farina *et al.* (1994)).

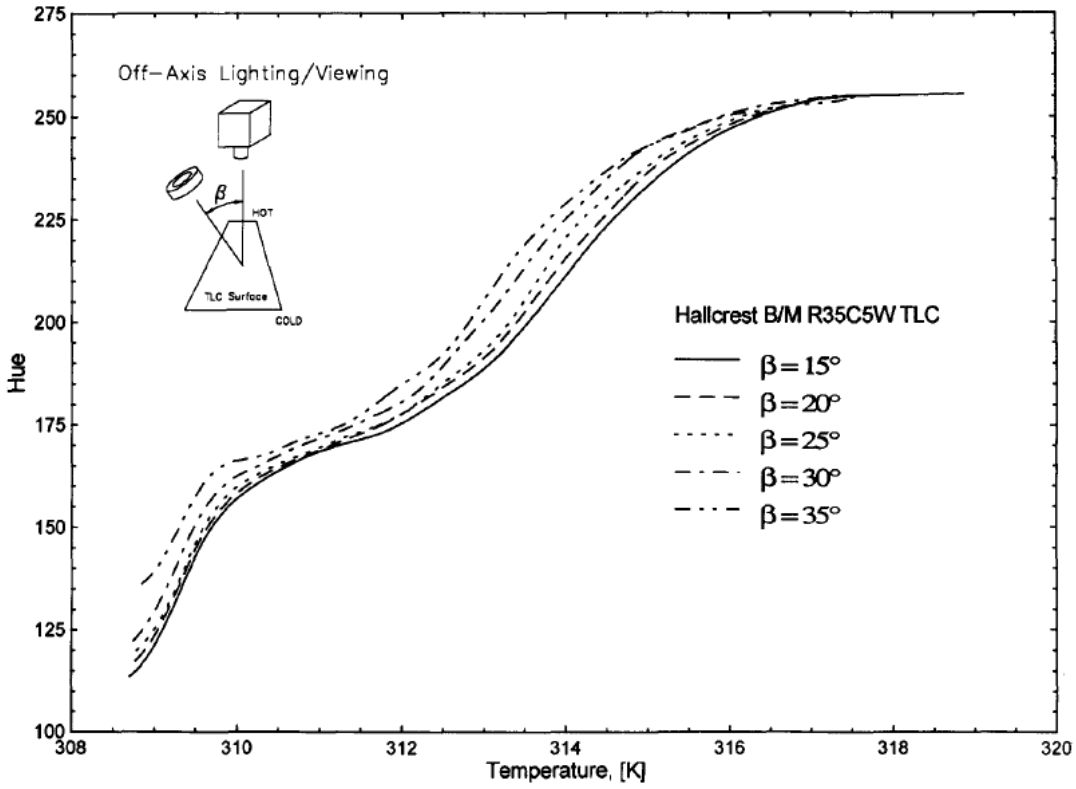

Figure. 5.7: Calibration curve for 35 C wideband (R35C5W) TLC at different off-axis lighting angles (from Farina *et al.* (1994)).

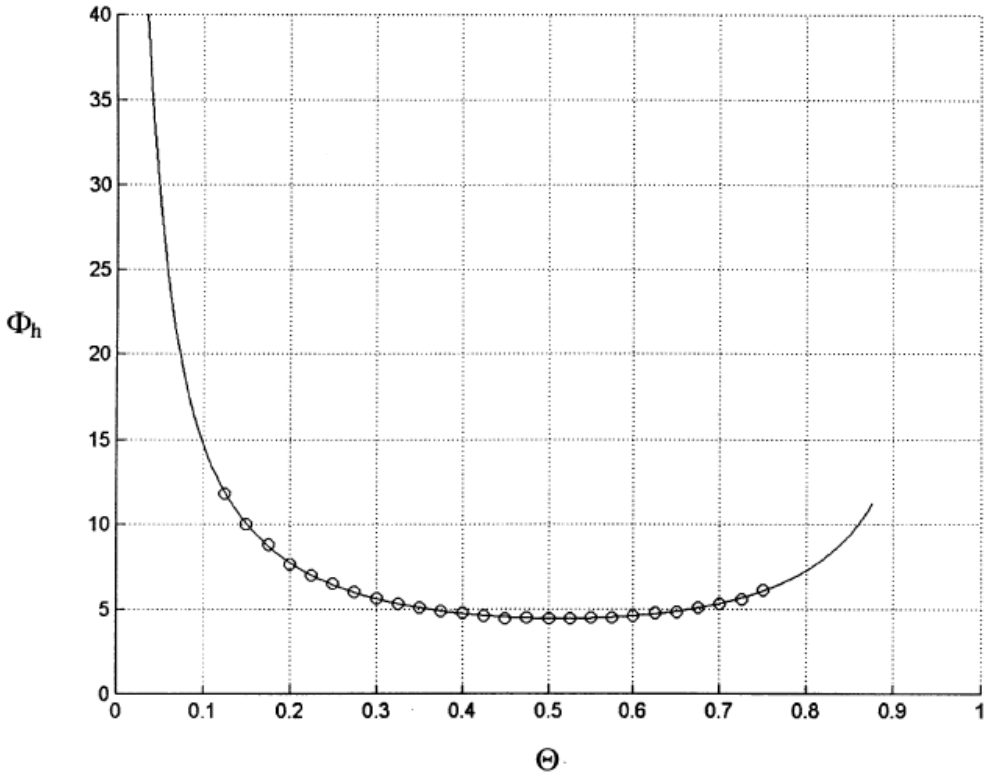

Figure. 5.8: Variation of Φ_h with Θ_s for the semi-infinite solution to a step-change in fluid temperature where T_{ad} is known. The line represents the solution to the uncertainty equations and symbols show computed data (from Yan and Owen (2002)).

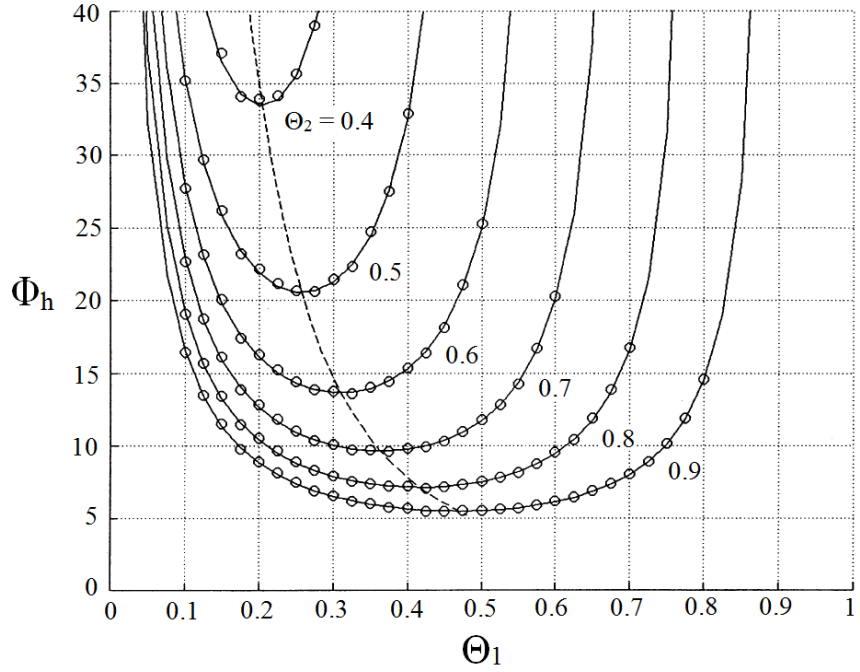

Figure. 5.9: Effect of Θ_2 on the variation of Φ_h with Θ_1 for the semi-infinite solution to a step-change in fluid temperature where h and T_{ad} are unknown. The solid lines represent the solutions to the uncertainty equations, the dashed line shows locus of minima and symbols show computed data (from Yan and Owen (2002)).

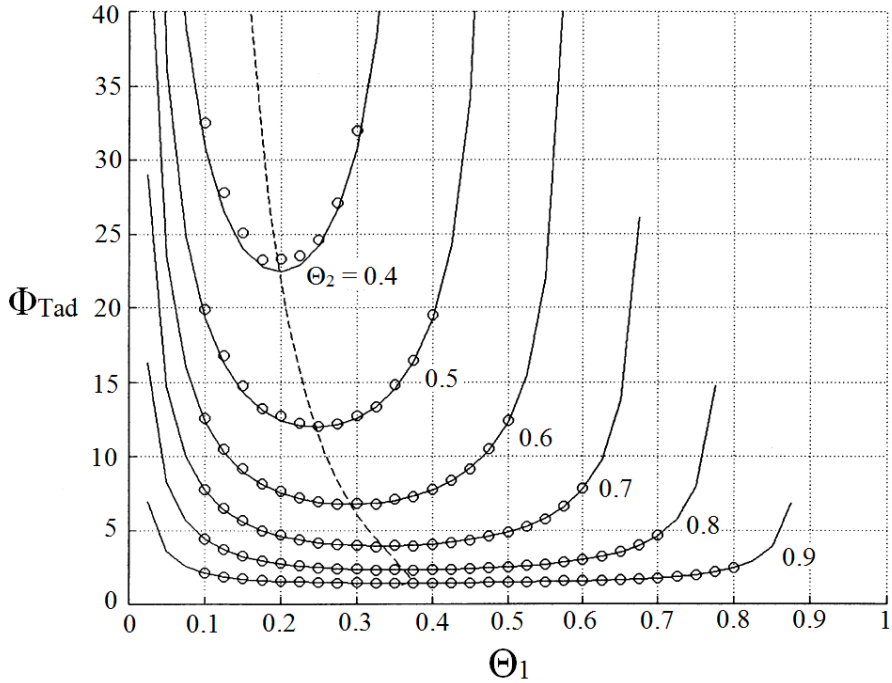

Figure. 5.10: Effect of Θ_2 on the variation of Φ_{Tad} with Θ_1 for the semi-infinite solution to a step-change in fluid temperature where h and T_{ad} are unknown. The solid lines represent the solutions to the uncertainty equations, the dashed line shows locus of minima and symbols show computed data (from Yan and Owen (2002)).

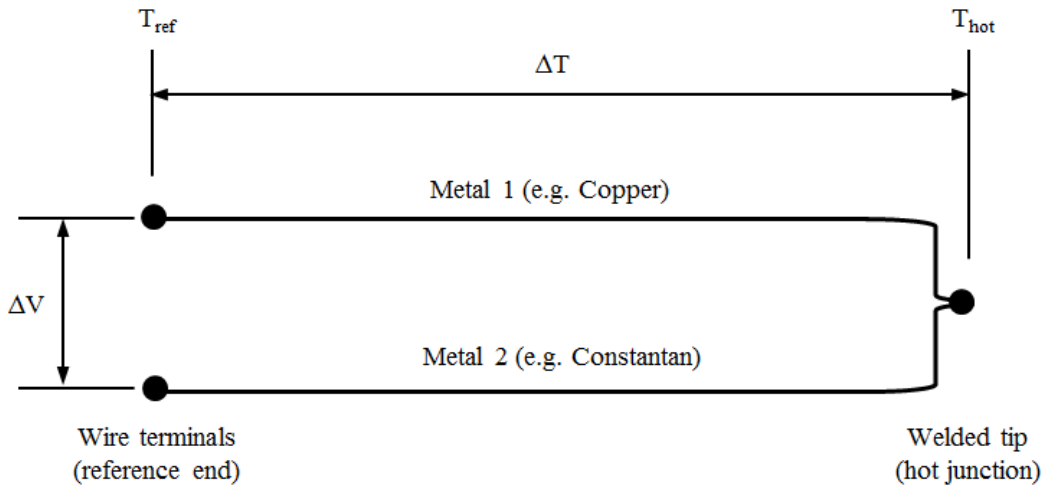

Figure. 5.11: A typical thermocouple circuit (adapted from Moffat (1990)).

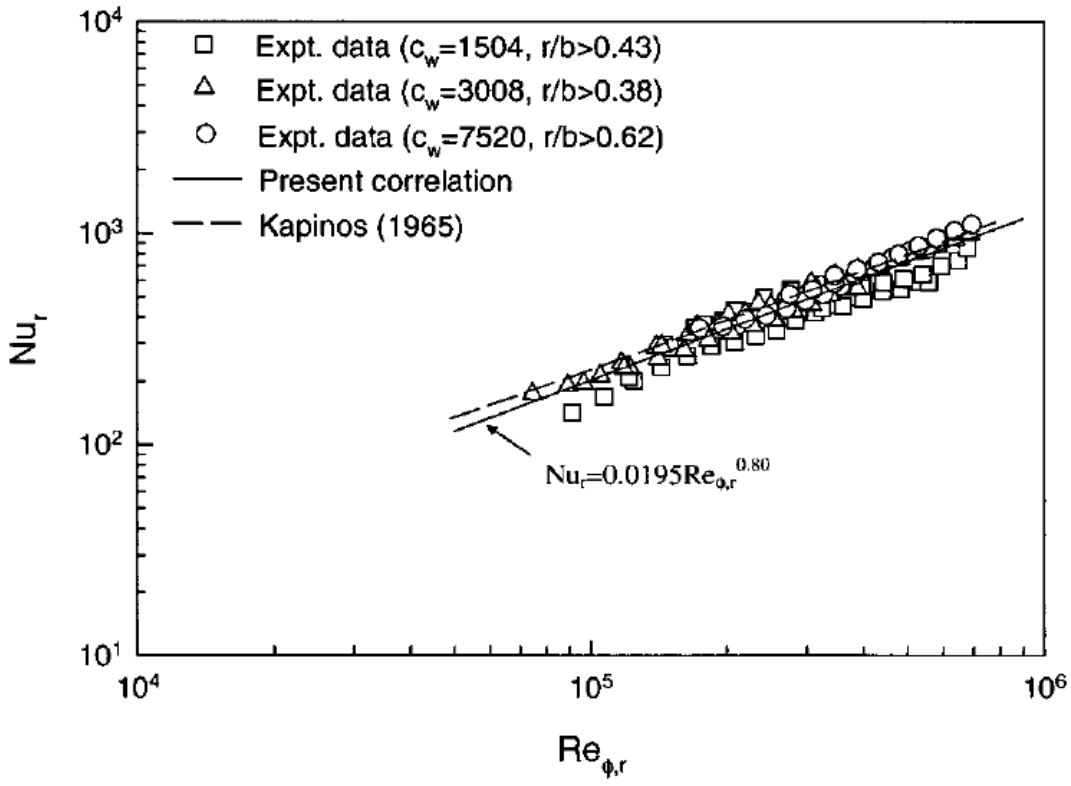

Figure. 5.12: Variation of Nu_r with $Re_{\phi,r}$ for a rotor in a rotor-stator system with mainstream flow and a radial clearance seal at the shroud (from Roy *et al.* (2001)).

Chapter 6. Rotor effectiveness and heat transfer measurements

This chapter presents measurements on the rotor of the Bath gas turbine test rig. Details of the rig relevant to the measurement of h and T_{ad} using TLC are provided. An adiabatic effectiveness based upon the measurements of T_{ad} on the rotor is defined and used to determine the effects of ingress on the rotor. It is shown that the rotor boundary layer, which contains entrained sealant flow from the wheelspace source region, provides a thermal buffer that protects the disc from the ingested fluid in the fluid core. A thermal buffer hypothesis is provided to relate the adiabatic effectiveness on the rotor to the concentration effectiveness on the stator; it is shown that the hypothesis is in good agreement with the experimental measurements. Finally, the local Nusselt numbers on the rotor are presented for different values of λ_T ; these are shown to be consistent with the fundamental fluid dynamics of rotor-stator systems.

6.1 Experimental facility

The reader is referred back to Section 4.1 of this thesis for a detailed description of the single-stage gas turbine facility at the University of Bath. This section will provide additional details pertinent to the measurement of heat transfer on the rotor.

6.1.1 Seal geometry

A simple axial-clearance seal was chosen for the heat transfer tests presented here as it is the datum seal used by most researchers who wish to study the fundamentals of ingress. The vane and blade platforms at the periphery of the stator and rotor form the simple axial-clearance seal used in the tests. To reduce heat loss, polycarbonate inserts were attached to the inner surfaces of the aluminium vane and blade platforms. The inserts had a radial thickness, h_{seal}, of 5 mm and were mitred with an angle of 15^o to the radial direction, as shown in Fig. 6.1 (the values of the geometric parameters shown in the figure were the same as those given in Table 4.1).

The axial deflection of the disc, which was measured using displacement transducers, was < 8% of the seal clearance at 3500 RPM for the highest sealant flow rates tested (the sealant flow pressurised the wheelspace causing the disc to ‘bowl’). The displacement

transducers were also used to measure the radial growth of the disc under rotation; the results showed that the maximum growth was < 0.04% of the radius.

6.1.2 Temperature measurement

Figure 6.2 shows the configuration used in the tests described here. TLC was applied across a 44° segment on the rotor surface (covering 5 of the 41 blades) and illuminated by a stroboscope so as to freeze the rotation. The colour change of the TLC with time was captured using a digital camera (Panasonic NV-MX500) mounted perpendicularly to the test surface. The strobe unit was angled at 30° so as to minimise reflections off the polycarbonate rotor surface. Air temperatures in the sealant flow line, at five radial locations in the wheel-space and upstream of the vanes in the annulus were measured using fast-response thermocouples.

TLC calibration

In the previous chapter, a number of key factors that influence the hue–temperature relationship of TLC were discussed. Of these factors, a selection were relevant to the experiments presented here, namely: ageing, film thickness, light source and lighting/viewing angles. Hysteresis and rotational effects were not considered as the TLC were only used for surface temperature measurements during heating (hence, the cooling cycle was ignored) and the centripetal acceleration levels on the Bath rotor were below the limit where rotational shift is significant.

The TLC calibrations were performed, as conducted by Kakade *et al.* (2009a), using a 65 × 65 × 5 mm copper block and film heater, insulated with Rohacell foam. Heat-sink compound was applied between the film heater and copper block so as to reduce the heat loss across the joining interface. A voltage calibrator was used to raise the temperature of the film heater and thus heat up the copper block from ambient temperature to 45 C in approximately an hour; the temperature of the copper block was measured via an embedded K-type thermocouple.

The embedded K-type thermocouples for TLC calibration (and the fast response K-type thermocouples used to measure the air temperatures—discussed below) were calibrated in a heated water bath using a Druck P600 digital thermometer with Pt100 sensing probe as a reference. The calibrations were performed as the water bath cooled from 80 C down to ambient temperature; during cooling the thermal gradients in the bath were shown to be within 0.1 C. Throughout the calibrations the thermocouple voltages were acquired through the experimental data acquisition system so as to minimise the risk of incurred DC voltage

offsets, which vary from channel to channel. For each thermocouple the calibration procedure was repeated three times and produced uncertainties of 0.1 C.

The copper block was sprayed with a mixture of 30, 35 and 40 C narrowband TLCs using a compressed air spray gun. The mixture comprised 4.5 ml of TLC (1.5 ml of each crystal) and 4.5 ml of water; the water was added to thin the TLC mixture to ease application. A mixture of 1.5 ml black paint and 1.5 ml water was applied prior to the TLC layer to provide a contrast for the TLC colour change. The TLC and black paint layers were built up gradually by repeatedly sweeping the spray gun across the block in alternate horizontal, vertical and diagonal trajectories. Three blocks were sprayed using the aforementioned technique; the blocks were weighed in vacuum scales before and after application of the mixtures so that the accuracy of the spraying technique could be verified. The pre– and post–spray measurements showed that the dry masses of the layers were within 5% of the mean dry mass. Scanning electron microscope images showed that the TLC layers were approximately 30 μm thick (the black paint layer was an order-of-magnitude less).

Figure 6.3 shows the TLC calibration setup. During calibration a 65 × 65 × 15 mm block of polycarbonate (i.e. 15 mm thick—the same as the rotor disc) was positioned on top of the copper block to simulate the view through to the inner rotor surface during the experiments. The camera and stroboscopic light were positioned normal and at an angle of 30° to the surface of the copper block respectively so as to represent the viewing/lighting arrangement of the TLC on the test rig. The strobe was set to 50 Hz (the frequency to freeze the disc at 3000 RPM) during the course of the calibrations; the camera was manually white balanced in the presence of the light source at the start of each calibration run, as it was in the experiments. (n.b. The manual white balance technique was recommended by Farina *et al.* (1994)—see Section 5.1.3.)

Figure 6.4 shows the hue–temperature calibration curves for the 30, 35 and 40 C narrowband TLC mixture for three samples (the same three samples used to check the consistency of the spraying technique). For the experiments, the calibration temperatures of the crystals were taken to be 30.9 C, 35.5 C and 40.2 C respectively, which correspond to a hue of 0.4; this value was used to determine the activation time for the data analysis. The effect of cyclic heating to above the clearance point of the 40 C crystal on the TLC mixture was checked to ensure that the crystals did not suffer from ageing during repeated experimental runs. The results of cyclic heating on the calibration curves of the TLC is shown in Fig. 6.5. The calibration temperatures of the three TLCs at a hue of 0.4 were unchanged within experimental uncertainty for up to ten heating cycles; accordingly, in the experiments the TLC segment on the rotor was kept for ten test runs before being removed

and a new layer applied. The 95% uncertainty in the TLC temperature for each of the three crystals for less than ten heating cycles was estimated to be 0.2 C.

Fast-response thermocouples

The fast response thermocouples used in this study were based on the design of those used in Lock *et al.* (2005) and Kakade *et al.* (2009b). The design comprised a 0.025-mm-diameter K-type unsheathed wire with a beaded junction fed through a twin-bore ceramic protection tube; the ceramic tube was braced by a thin stainless steel sheath (see Fig. 6.6). Lock *et al.* recommended that there be a minimum clearance between the thermocouple bead and metal sheath of at least 3.5 mm to minimise errors resulting from 'transient conduction from the bead to the [metal] tube'. For the thermocouples used here, the bead protruded the end of the metal sheath by approximately 10mm.

The fast response thermocouples were individually calibrated using the water bath technique mentioned above. All thermocouple voltages were acquired through a National Instrument USB-9213 input module using a pre-calibrated platinum-resistance thermometer; the temperature uncertainty, response time and probe recovery factor, *R*, were 0.1 C, 40 ms and 0.78 respectively (see Lock *et al.* (2005)). The total temperature of the air, T_a, was calculated from the fast response thermocouple measurements, T_{TC}, using the following relationship:

$$T_a = T_{TC} + R\frac{V^2}{2c_{p,\text{air}}} \tag{6.1}$$

where V is the velocity of the air at the measurement location and $c_{p,air}$ is the specific heat of the air at constant pressure.

6.1.3 Heat transfer measurements on the rotor

The transient experiments were conducted under carefully-controlled thermal boundary conditions. Prior to each test run, fast-response thermocouple measurements were made in the annulus, wheelspace and sealant flow line in the absence of mainstream or sealant flow to ensure that the rig was in thermal equilibrium (equilibrium was assumed when all thermocouples measured within ± 0.1 C of one another).

Two mesh heaters were installed in series in the sealant flow line to control the temperature of the incoming compressed air. The mesh heaters, which were constructed by Sangan (2011) in accordance with the design provided by Ireland *et al.* (1996), comprised fine wire meshes soldered to brass bus bars through which a current was supplied from

individual welding units. The supply of current to the bus bars served to heat up the mesh wire; consequently, heat was passed to the air as it flowed through the mesh sections. The upstream mesh heater was used to match the temperature of the incoming compressed air to typically within ± 0.2 C of the rig equilibrium temperature (T_{in} was taken as the mean value of the equilibrium and conditioned sealant flow temperatures). A step-change of between 30 and 40 C (see Fig. 6.7) in the sealant flow temperature was achieved using the downstream mesh heater, which is shown in Fig. 6.8. The air temperature reached 97.5% of the final step temperature in approximately 1 s from the trigger of current supply to the downstream mesh; this time was taken as the starting value for the analysis.

Figure 6.9a shows a single frame from a video capturing the colour change of the TLC segment on the rotor surface during a typical transient experiment. The TLC segment was viewed through the transparent polycarbonate disc, which was rotating clockwise at 3000 RPM. Fig. 6.9b shows a schematic of the view from the camera. The mitred seal at the periphery of the wheel-space, the annulus, blades and casing are labelled in the figure. It should be noted that the mainstream flow was exhausted from the test section into the atmosphere.

In Fig. 6.9a the activation of the 35 C and 40 C TLC are shown at high and low radial locations on the rotor respectively; the 30 C crystal had already passed its clearance-point and so is not visible in the image. It is clear from the green bands in the figure (which correspond to a hue of approximately 0.4, to which the TLC were calibrated) that the temperature distribution on the rotor was axisymmetric during the experiments.

The calibrated TLC were used to identify three discrete temperature–time values at a given location on the rotor surface during the course of a transient experiment. The data was captured on the Panasonic NV-MX500 at a rate of 25 frames per second and subsequently analysed frame-by-frame using a 3 x 3 median pixel filter in Matlab to give the hue history across the test segment. The times at which a hue of 0.4 was reached for each of the three TLC were calculated from the smoothed hue–time data, providing three temperature–time pairs at each radius. A cubic-spline interpolation was used to reduce the uncertainty in time to < 10 ms.

Fig. 6.9c shows a typical hue history measured at the three radial locations marked in Fig. 6.9b: r/b = 0.68, 0.79 and 0.90. The 30, 35 and 40 C crystals were active between approximately 5–25, 18–80 and 50–100 seconds respectively. With reference to Eq. 5.1, the heat flux falls as the surface temperature of the disc rises; consequently, as the disc was

heated convectively during the experiments, the higher temperature TLC took longer to pass through the activation range than the lower temperature TLC.

6.2 Analysis of heat transfer data

6.2.1 Adiabatic surface temperature of rotor

The heat transfer coefficient, h, for the rotor was defined in Section 5.2 by:

$$h = \frac{q}{(T_{ad} - T_s)} \tag{6.2}$$

where q is the heat flux into the rotor, T_s is the surface temperature and T_{ad} is the adiabatic surface temperature (where all the bounding solids are perfect insulators). Using T_{ad} as the reference temperature ensures that q is zero when $T_s = T_{ad}$ and that h is independent of the magnitude of the temperature of the surface.

It was shown by Owen and Rogers (1989) that T_{ad} is related to the core temperature and swirl ratio, T_∞ and β respectively, by:

$$T_{ad} = T_\infty + R\frac{\Omega^2 r^2}{2c_{p,air}}(1-\beta^2) \tag{6.3}$$

where R is the fluid dynamic recovery factor; for air, $R \approx Pr^{1/3}$ (Pr is the Prandtl number = $\mu c_{p,air}/k$). Karabay *et al.* (2001) showed that for an adiabatic system without ingress, Eq. 6.3 can be expressed in terms of the total temperature and swirl ratio at inlet to the wheelspace, $T_{0,in}$ and β_{in}, by:

$$T_{ad}^* = T_{0,in} + \frac{\Omega^2 b^2}{2c_{p,air}}\left[R\,x^2 - (1-R)\beta_{in}^{\,2} x_{in}^{\,4} x^{-2} - 2R\,\beta_{in} x_{in}^{\,2}\right] \tag{6.4}$$

where superscript * is used to denote T_{ad} in the absence of ingress and $x = r/b$.

In the experiments discussed below the swirl ratio of the air at inlet to the wheelspace was not measured. It was assumed for analytical purposes that $\beta_{in} < 1/3$; for this case Eq. 6.4 can be approximated by:

$$T_{ad}^* < T_{0,in} + \Delta T \tag{6.5}$$

where

$$\Delta T = Pr^{1/3}\frac{\Omega^2 r^2}{2c_{p,air}} \tag{6.6}$$

For air $Pr^{1/3} \approx 0.89$.

6.2.2 Definition of adiabatic effectiveness

The theoretical effectiveness of a rotor-stator system with ingress was defined in Eq. 2.16 by:

$$\varepsilon = 1 - \frac{\Phi_i}{\Phi_e} \tag{6.7}$$

This definition is based on the ratio of the isentropic mass flow rates of the ingress and egress flow parameters, Φ_i and Φ_i respectively. The orifice equations developed by Owen (2011a, b) ignore the effects of friction, diffusion, heat transfer and mixing that would occur in a real system.

In Chapter 4, the effectiveness based upon concentration, ε_c, was given as:

$$\varepsilon_c = \frac{c_s - c_a}{c_0 - c_a} \tag{6.8}$$

where c_s, c_a and c_0 are the sample, ambient and seed tracer gas concentration levels respectively. By definition $\varepsilon_c \rightarrow 0$ as $\Phi_0 \rightarrow 0$ and $\varepsilon_c \rightarrow 1$ as $\Phi_0 \rightarrow \Phi_{min}$.

For the measurements presented below, ε_c was determined on the stator from the measurements of the CO_2 concentration level at the surface of the stationary disc (c_s), upstream of the guide vanes in the annulus (c_a) and in the sealant flow line (c_0). It was not possible to measure concentration on the rotating disc as the system had been designed without slip-rings for simplicity. Consequently, it was necessary to define an alternative form of effectiveness—referred to here as the 'adiabatic effectiveness', ε_{ad}—for comparison of the impact of ingress on the rotor relative to the stator. ε_{ad} was defined by:

$$\varepsilon_{ad} = \frac{T_{ad} - T_a}{T_{ad}^* - T_a} \tag{6.9}$$

where T_{ad}* is the value of T_{ad} when there is no ingress and T_a is the total temperature of the air in the annulus as measured by the fast response thermocouple located upstream of the nozzle guide vanes. Given that frictional heating was small for the results presented here, T_a is approximately equal to the value of T_{ad} when $\Phi_0 = 0$. The definition of ε_{ad} satisfies the criterion that $\varepsilon_{ad} = 1$ when $\Phi_0 = \Phi_{min,ad}$ and $\varepsilon_{ad} = 0$ when $\Phi_0 = 0$. When $\varepsilon_{ad} = 1$ there is no thermal effect of ingress on the rotor.

6.2.3 Calculating h and T_{ad}

For the experiments presented in this chapter both h and T_{ad} were calculated using the solution of Fourier's equation for a semi-infinite solid with a step-change in fluid temperature. The semi-infinite step-change solution was discussed in detail in Section 5.3.1 and will only be considered briefly here.

For a step-change in fluid temperature, the non-dimensional temperature at the surface of a solid of semi-infinite thickness, Θ_s, can be expressed as:

$$\Theta_s = \frac{T_s - T_{in}}{T_{ad} - T_{in}} = 1 - \exp(\chi^2)\,\mathrm{erfc}(\chi) \tag{6.10}$$

where

$$\chi = BiFo^{1/2} = h\left(\frac{t}{\rho c_p k}\right)^{1/2} \tag{6.11}$$

When ingress was present, T_{ad} was unknown, and so to solve for h and T_{ad} it was necessary measure two surface temperatures, $T_{s,1}$ and $T_{s,2}$, at times t_1 and t_2 so that Θ_1/Θ_2 and χ_1/χ_2 could be determined from:

$$\frac{\Theta_1}{\Theta_2} = \frac{T_{s,1} - T_{in}}{T_{s,2} - T_{in}} \tag{6.12}$$

and

$$\frac{\chi_1}{\chi_2} = \left(\frac{t_1}{t_2}\right)^{1/2} \tag{6.13}$$

It follows that from Eqs. 6.10–6.13 that:

$$\frac{\Theta_1}{\Theta_2} = \frac{1 - \exp(\chi_1^2)\,\mathrm{erfc}(\chi_1)}{1 - \exp(\chi_2^2)\,\mathrm{erfc}(\chi_2)} = \frac{1 - \exp\left((t_1/t_2)^{1/2}\chi_2^2\right)\mathrm{erfc}\left((t_1/t_2)^{1/2}\chi_2\right)}{1 - \exp(\chi_2^2)\,\mathrm{erfc}(\chi_2)} \tag{6.14}$$

χ_2, and thus h, were calculated from Eq. 6.14 using a Newton-Raphson iteration as described in Appendix A2; T_{ad} was subsequently determined from Eq. 6.10 using the calculated value of χ_2.

The uncertainties in h and T_{ad} were calculated using the amplification factors developed by Yan and Owen (2002), as detailed in Appendix B1; for the experiments discussed below, the 95% uncertainties in h and T_{ad} were less than 8% and 1.5 C respectively. 30 C/40 C and 35 C/40 C TLC pairs were used to calculate two values of h and T_{ad} for each test run; a variance weighted mean was taken to given improved estimates of the two parameters.

6.2.4 Definition of the thermal buffer ratio

The tangential velocity measurements presented in section 4.2 (see Fig. 4.8) showed that the fluid dynamics in the wheelspace of the Bath test rig followed the Batchelor (1951) flow model: a rotating fluid core situated between separate boundary layers flowing radially inward and outward on the stator and rotor respectively. The fundamental fluid dynamics of Batchelor flow was discussed in detail in Section 2.2; those details pertinent to the measurements presented in this chapter will be briefly revisited here.

The flow structure of the fluid in a rotor-stator wheelspace is predominantly governed by the turbulent flow parameter, λ_T, where:

$$\lambda_T = 2\pi G_c \Phi_0 Re_\phi^{0.2} \tag{6.15}$$

When fluid is supplied to the wheelspace at low radius, as in the Bath rig, then a source region is formed. The fluid in the source region is drawn into a radially outward flowing boundary layer on the rotor to satisfy disc-pumping. When λ_T is less than the disc entrainment limit (0.22 for a free-disc—this value will be slightly less for a rotor-stator system), then the flow structure in the wheelspace comprises separate rotor and stator boundary layers with a rotating fluid core located between; the tangential velocity component in the core is less than the disc speed, Ωr. The rotor boundary layer is supplemented with fluid from the core region and so thickens with radius. The mass of fluid leaving the core is balanced by entrainment of fluid from the stator boundary layer; consequently, the stator boundary layer thins as it flows radially inwards.

As λ_T is increased the disc-pumping is increasingly satisfied by the supply of fluid in the source region, and so entrainment from the fluid core decreases; as a result, the swirl in the core decreases. When λ_T exceeds the entrainment limit then the disc-pumping will be fully satisfied by the supply of fluid from the source region; consequently, there will be no entrainment into the rotor boundary layer from the stator boundary layer and so the fluid core breaks down.

Ingress affects the flow structure in the wheelspace; the ingested fluid enters the wheelspace and mixes with the sealing flow radially inward of the rim seal. The ingested fluid typically has a higher swirl that the fluid in the wheelspace; conservation of angular momentum results in the fluid in the mixing region having higher swirl than the core region deeper in the wheelspace (the experimental results presented in Fig. 4.8 confirmed this). The fluid in the mixing region is drawn into the radially-inflowing stator boundary layer. If the ingress and sealant flows streams have completely mixed-out then the concentration on the

stator wall will be invariant with radius. For an adiabatic stator with negligible frictional heating, the wall temperature on the stator will also be invariant with radius.

In an engine, ingress levels affect the non-dimensional temperature:

$$\theta_E = \frac{T_a - T}{T_a - T_0} \tag{6.16}$$

where T, T_a and T_0 are the total temperatures of the fluid in the wheel-space, the annulus and the sealing flow respectively. Figure 6.10 shows the radial velocity, concentration and engine temperature boundary layers in a rotor-stator system with ingress. The sealing air, which is drawn into the rotor boundary layer from the source region, thermally buffers the rotor against the ingested fluid in the core. This 'thermal buffering' effect is dependent upon the supply of sealing flow to the wheelspace.

It is useful to define the thermal buffer ratio, η , as the ratio of Φ_0 required to seal the wheelspace to the value of Φ_0 when ingress first affects the surface temperature of the rotor. If $\Phi_{min,c}$ (measured on the stator and thus considered system representative) is the value of Φ_0 as $\varepsilon_c \rightarrow 1$ and Φ_{ad} (measured on the rotor as described above) is the value of Φ_0 as $\varepsilon_{ad} \rightarrow 1$ then:

$$\eta = \frac{\Phi_{min,c}}{\Phi_{min,ad}} \tag{6.17}$$

The sealing flow in the rotor boundary layer forms the thermal buffer from the ingested fluid in the core. The level of protection from ingestion that the thermal buffer provides to the rotor is dependent upon λ_T ; when λ_T is increased, and consequently the entrainment from the core into the rotor boundary layer is reduced, η would be expected to increase. It thereby follows that η would increase as $\lambda_{T,min}$—the value of λ_T at the minimum value of sealing flow required to purge the wheelspace of ingress— is increased, where $\lambda_{T,min}$ is given by:

$$\lambda_{T,\min} = 2\pi G_c \Phi_{min,c} \, \mathrm{Re}_\phi^{0.2} \tag{6.18}$$

At large values of $\lambda_{T,min}$, where the fluid entrained from the core into the boundary layer on the rotor tends to zero, the effect of ingestion on the rotor will be negligible and, as a result, $\eta \rightarrow \infty$. As $\lambda_{T,min}$ decreases the entrainment from the core increases and thus η will decrease; at the limit $\lambda_{T,min} \rightarrow 0$ then $\eta \rightarrow 1$. The following relationship between η and $\lambda_{T,min}$ is hypothesised:

$$\eta = \exp(K\lambda_{T,min}) \tag{6.19}$$

where K is an empirical constant. This hypothesis satisfy the limits at the small and large values of $\lambda_{T,min}$ outlined above.

6.3 Experimental measurements

For the concentration tests, results were obtained at three different rotational speeds (2000, 3000 and 3500 RPM) corresponding to $Re_\phi = 5.32 \times 10^5$, 8.17×10^5 and 9.68×10^5. For each speed, two different external flow rates were used: one on-design and the other off-design. For the design condition, $Re_W / Re_\phi = 0.538$; at the overspeed off-design condition, $Re_W / Re_\phi = 0.326$. The corresponding annular vane-exit absolute Mach numbers are given for the design case in Table 4.2 (see Section 4.1.1) and the overspeed case in Table 6.1 below.

Disc Speed (RPM)	**2000**	**3000**	**3500**
$Re_\phi / 10^5$	5.32	8.17	9.68
$Re_W / 10^5$	1.73	2.66	3.16
M	0.14	0.21	0.24

Table 6.1: Tested disc speeds and corresponding values of Re_ϕ, Re_W and M for the overspeed off-design condition ($Re_W / Re_\phi = 0.326$).

Only one rotational speed (3000 rpm) was used for the heat transfer experiments. The same two external flow rates (and hence values of Re_W / Re_ϕ) used for the concentration tests were used for the heat transfer tests. These two external flow rates created two different values of $\lambda_{T,min}$, which were used to test the thermal buffer ratio hypothesis given above.

6.3.1 Wheelspace air temperatures

The wheelspace temperature measurements presented here were made at five radial locations using the fast response thermocouples described above. The measurement junctions of the thermocouples were located at $z/S = 0.5$, which was considered to be in the fluid core outside the boundary layers on the rotor and stator. During the course of the transient experiments, the temperatures in the core would have been dependent on the heat transfer to the stator; consequently, the measurements are rig specific and would not translate to an engine. Nevertheless, the core temperatures are useful as they give an indication of how ingress affects the distribution of temperature in the wheelspace.

The steady-state core temperatures were obtained by fitting a least-squares three-term exponential series to the temperature–time data and extrapolating to infinity (a caveat is placed upon these extrapolated values as the validity of the exponential fit is uncertain beyond the measured values). Figure 6.11 shows the variation of the non-dimensional core temperature (θ_{core}) with time in the wheelspace for RI ingress at a fully sealed case (i.e. $Re_W = 0$ and $\Phi_i/\Phi_0 = 0$); also shown are the associated exponential series fits to the data. θ_{core} is defined by:

$$\theta_{core} = \frac{T_{core} - T_{in}}{T_0 - T_{in}} \tag{6.20}$$

where T_{core} is the measured core air temperature, T_{in} is the initial temperature of the system, and T_0 is the total temperature of the sealing air after the heater has been activated. $\theta_{core,\infty}$ is the extrapolated value of θ_{core} as $t \rightarrow \infty$.

Figure 6.12 shows the radial variation of $\theta_{core,\infty}$ with r/b for five values of Φ_i/Φ_0 (these values were inferred from the measurements in Sangan *et al.* (2011a, b)). When the system was fully sealed (i.e. $\Phi_i/\Phi_0 = 0$), the core air temperature increased monotonically with radius. This increase can be attributed to the flow structure in the wheelspace: the hot sealant flow is drawn into the rotor boundary layer and is pumped up the disc, before leaving and migrating axially across the wheelspace into the stator boundary layer at high radius. The stator boundary layer, which at the fully sealed case is made up entirely of the hot sealing flow, loses heat to the stator as it flows radially inwards; consequently, as fluid is drawn from the stator boundary layer into the core to satisfy the disc-pumping on the rotor, the temperature in the core decreases as r/b decreases.

The core temperatures are reduced by the ingestion of cold fluid from the annulus into the wheelspace, as can be seen in Fig. 6.12 for $\Phi_i/\Phi_0 > 0$. The reduction in temperature is most pronounced close to the rim seal, where the ingested fluid mixes with the sealing flow as it migrates across the wheelspace from the rotor boundary layer. Once mixed, the fluid is drawn into the stator boundary layer and, as for the fully sealed case, loses heat to the stator as it flows radially inward.

6.3.2 Adiabatic temperature measurements with no ingress

The method for calculating T_{ad} from two TLC temperature measurements was described in detail in Section 6.2.3. To calculate T_{ad}* (the value of T_{ad} when there is no ingress) TLC measurements were made on the rotor without ingress. Previous experimental measurements (see Sangan *et al.* (2011b)) had shown that for an axial seal with RI ingress (i.e. with no

external flow in the annulus) that the wheelspace would be fully sealed when $\Phi_0 > 0.084$. The tests carried out here were for $Re_W = 0$ with $\Phi_0 = 0.090$; these operating conditions ensured that there was no ingestion into the wheelspace cavity.

The values of T_{ad}* obtained for the case without ingress are shown in Table 6.2; the values of ΔT shown in the table were calculated using Eq. 6.6. Frictional heating produced an increase in T_{ad}* with radius; despite the values of ΔT being a similar magnitude to the uncertainties in T_{ad}* (resulting from the semi-infinite step-change solution), the calculated values of T_{ad}* were within the bounds provided by Eq. 6.5. These results gave confidence in the accuracy of the method used to determine T_{ad}*.

r/b	**ΔT (C)**	**$T_{0,\,in} + \Delta T$ (C)**	**T_{ad}* (C)**
0.679	0.7	58.6	58.1
0.715	0.8	58.7	58.0
0.752	0.9	58.8	58.1
0.789	1	58.9	58.0
0.825	1.1	59.0	58.2
0.862	1.2	59.1	58.5
0.898	1.3	59.2	58.7
0.935	1.4	59.3	58.9

Table 6.2: Radial variation of adiabatic surface temperature with zero ingress ($\Phi_0 = 0.090$, $\Phi_i/\Phi_0 = 0$, $T_{0,in} = 57.9$ C, $T_a = 14.5$ C).

As discussed in the previous section, heat transfer from the fluid in the stator boundary layer to the stator affects the temperatures in the core region of the wheelspace. However, as the results in Table 6.2 show, T_{ad}* is unaffected by the core temperature levels for a system without ingress. This exemplifies the thermal buffering effect of the sealant flow in the rotor boundary layer. T_{ad}* can be estimated from $T_{0,in}$ and the frictional temperature rise on the rotating disc using the following equation:

$$T_{ad}^* = T_{0,in} + Pr^{1/3}\frac{\Omega^2 r^2}{2C_p} \tag{6.21}$$

where for air $Pr^{1/3} \approx 0.89$.

6.3.3 Radial variation of effectiveness

Figure 6.13 shows a comparison between the radial variation of concentration and adiabatic effectiveness measured on the stator and the rotor respectively. The tests were conducted for EI ingress at two values of λ_T for the design case (Re_W/Re_ϕ = 0.538).

The concentration measurements on the stator show that, as expected, ε_c increased as λ_T increased. At high radius (r/b > 0.85) ε_c was almost constant, which signifies that the fluid in the stator boundary layer in this region was fully mixed. For r/b < 0.85, ε_c increased slightly as r/b decreased; it is likely that the values of ε_c in this region were influenced by the proximity of the inlet seal through which the seeded sealant flow was supplied.

Figure 6.13 also provides evidence of the thermal buffering hypothesised in Section 6.2.4: the values of ε_{ad} on the rotor were significantly greater than the values of ε_c on the stator for the same λ_T . The entrainment of fluid from the core, which contained the cold ingested fluid, into the rotor boundary layer resulted in a monotonic decrease in ε_{ad} as r/b increased.

The values of ε_{ad} measured on the rotor were determined for a step-change in sealing flow temperature. It should be noted that the step-change assumption is less valid when ingestion occurs and the cold fluid from the annulus penetrates deep into the wheelspace and mixes with the incoming hot sealing flow in the source region (i.e. the step-change in temperature measured at entry to the wheelspace would not translate to the rotor boundary layer). The measurements on the rotor were restricted to cases where ε_{ad} > 0.6 to prevent the step-change assumption becoming invalid. As mentioned in Section 6.2.3, 30 C/40 C and 35 C/40 C TLC pairs were used to calculate two values of T_{ad} (and thus ε_{ad}) for each test run; the two calculated values of ε_{ad} were consistent to within the experimental uncertainties for all tests, which gave confidence in the accuracy of the analytical method.

The comparisons between the variation of ε_{ad} and ε_c with Φ_0 carried out in the following section were based upon the measurements at r/b = 0.898 on the rotor and r/b = 0.958 on the stator; these radii were chosen as they fall in the region where ε_{ad} and ε_c are invariant with radius.

6.3.4 Comparison of concentration and adiabatic effectiveness

Figures 6.14 and 6.15 show the comparisons between the variation of ε_{ad} on the rotor and ε_c on the stator with Φ_0 for the design and overspeed conditions respectively. For both cases, when ingress occurred $\varepsilon_{ad} > \varepsilon_c$, and consequently η > 1.The non-dimensional peak-to-trough

pressure difference in the annulus, ΔC_p, and, as a result, the values of $\Phi_{min,c}$, $\lambda_{T,min}$ and η, were greater for the design condition than those for the overspeed condition. The error bars shown for the ε_{ad} data, which represent the 95% confidence intervals, were calculated using the theory presented in Appendix B2; the typical uncertainty in ε_{ad} was approximately 5.5% for both test conditions.

The EI orifice equations (see Eqs. 4.8–4.10) were fitted to the concentration data using the statistical fitting technique of Zhou *et al.* (2011b); the corresponding fitting parameters are given in Table 6.3. It can be observed from Figs. 6.14 and 6.15 that the fitted curves are in good agreement with the data. $\Phi_{min,c}^{+}$ and Γ_c^{+} and $\Phi_{min,c}^{-}$ and Γ_c^{-}, the parameter values for the upper and lower 95% confidence intervals respectively, were input into the EI effectiveness equation to produce the 95% confidence curves (plotted as dashed lines in the figures). The standard deviations of the fits (σ = 0.0127 and σ = 0.0195 for the on-design and overspeed cases respectively) are within the upper limit of the concentration data (σ = 0.046) calculated in Section 4.4.

Parameter	Case	
	Design	**Overspeed**
$\Phi_{min,c}$	0.275	0.118
$\Phi_{min,c}^{+}$	0.293	0.129
$\Phi_{min,c}^{-}$	0.259	0.109
Γ_c	0.348	0.687
Γ_c^{+}	0.398	0.885
Γ_c^{-}	0.305	0.543
σ	0.0127	0.0195

Table 6.3: Parameters used to fit the EI effectiveness equation to experimentally measured variation of ε_c with Φ_0 for the axially clearance seal with mired inserts for the design and overspeed cases; values were calculated using the technique of Zhou *et al.* (2011b). + and - represent the upper and lower 95% confidence limits.

The EI effectiveness equation (Eq. 4.8) was used to determine the values of $\Phi_{0,c}$ at $\varepsilon_c = \varepsilon_{ad}$ for each of the ε_{ad}–$\Phi_{0,ad}$ data points. For the design case $\Phi_{0,c}/\Phi_{0,ad} \approx 2.1$ and for the overspeed case $\Phi_{0,c}/\Phi_{0,ad} \approx 1.4$; it is therefore suggested that the buffer ratio (see Eq. 6.17) can be generalised by:

$$\eta = \frac{\Phi_{min,c}}{\Phi_{min,ad}} = \left[\frac{\Phi_{0,c}}{\Phi_{0,ad}}\right]_{\varepsilon_c=\varepsilon_{ad}} \tag{6.22}$$

The buffer ratio hypothesis, given in Eq. 6.19, can thus be written as:

$$K_i = \frac{\ln \eta_i}{\lambda_{T,min}} \tag{6.23}$$

where

$$\eta_i = \left[\frac{\Phi_{0,c}}{\Phi_{0,ad}} \right]_i \tag{6.24}$$

The subscript i denotes the i^{th} value of the N effectiveness data points. There were 12 data points for the on-design tests and 8 for the overspeed tests; accordingly: $N = 20$.

For the data presented here, the mean value of K was calculated as $\overline{K} = 2.67 \pm 0.24$ (the uncertainty in $\overline{K}$ was determined using Eq. B11 in Appendix B3). The corresponding mean values for the buffer ratio were $\overline{\eta} = 2.09 \pm 0.14$ and 1.37 ± 0.04 for the design and overspeed cases respectively; the fits to the ε_{ad} data shown in Figs. 6.14 and 6.15 were obtained using these values of $\overline{\eta}$. Whilst the fitted curves show good agreement with the experimental data, the buffer ratio hypothesis was only tested for two test cases and one seal configuration; further experiments and CFD are required to fully validate the theory. Table 6.4 summarises the important buffer ratio data.

Case	$\lambda_{T,min}$	$\overline{K}$	$\overline{\eta}$	$\Phi_{min,ad}$
Design	0.275	0.267	2.09	0.132
Over-speed	0.118	0.267	1.37	0.0863

Table 6.4: Variation of thermal buffer ratio with turbulent flow parameter.

6.3.5 Nusselt number and heat transfer coefficient measurements on the rotor

Figures 6.16 and 6.17 show the effect of λ_T on the radial variation of $Nu_r Re_{\phi,r}^{-0.8}$ and h respectively for the design condition. The local Nusselt number, which was used to non-dimensionalise the heat transfer data, was defined by:

$$Nu_r = \frac{hr}{k_{air}} \tag{6.25}$$

where h is the heat transfer coefficient, determined from two TLC measurements as described in Section 6.2.3, and k_{air} is the thermal conductivity of the air based on the sealing flow temperature.

The free-disc correlation is included in Fig. 6.16 for comparative purposes; this correlation, which was taken from Owen and Rogers (1989) for an isothermal disc, can be expressed as:

$$Nu_r = 0.0194[(r/b)^2 Re_{\phi,r}]^{0.8} \quad (6.26)$$

It can be seen that the measured values of $Nu_r Re_{\phi,r}^{-0.8}$, which were virtually invariant with radius, are significantly less than for the free-disc case. The measurements of heat transfer coefficient presented in Fig. 6.17, which were used to calculate the Nusselt numbers in Fig. 6.16, showed that h on the rotor decreased with radius.

Figure. 6.18 shows the variation of h and $Nu_r Re_{\phi,r}^{-0.8}$ with λ_T at r/b =0.898; it is apparent that h, and thus Nu_r, increased as λ_T was increased. This effect can be explained with reference to the flow structure in the wheelspace: as λ_T is raised, the swirl in the fluid core will reduce, which will result in an increase in the moment coefficient (and thus h and Nu_r) on the rotor. The ingested fluid, which enters the wheelspace with high swirl, will increase the core swirl relative to an enclosed rotor-stator system; this will serve to reduce the moment coefficient on the disc and thereby reduce Nu_r.

Although the Nusselt number measurements results presented here may not be fully representative of those found in engines (owing to the heat transfer to the stator, which is not taken into consideration here), they give some insight into the fluid dynamics of ingestion and should also be useful for the validation of CFD codes.

6.4 Implications

The work carried out in this chapter fulfils Objective 3 of this thesis (see Section 1.5). The performance ranking of rim seal geometries is typically based on the sealant flow levels required to prevent the ingress of fluid into the wheelspace. The work presented in this chapter has shown that the rotor can be protected against ingress by the sealant flow entrained in the radially outflowing rotor boundary layer (see Section 6.3.3 and 6.3.4 and Figs. 6.13 – 6.15). The stator can generally tolerate higher temperatures (and thus ingress levels) than the rotor given that it is under much less mechanical stress; it may be that engine designers can make use of the buffering effect of the rotor boundary layer to allow more ingress into the wheelspace than previously thought without risking thermal damage to the rotor. A caveat is placed on this implication: engine seals have significantly lower values of $\lambda_{T,min}$ than for the axial seal presented here and will consequently have lower values of η.

Nevertheless, designers of secondary air systems should be aware of the protection that the fluid structure in the wheelspace provides the rotating-disc so that cooling air is not wasted.

6.5 Figures

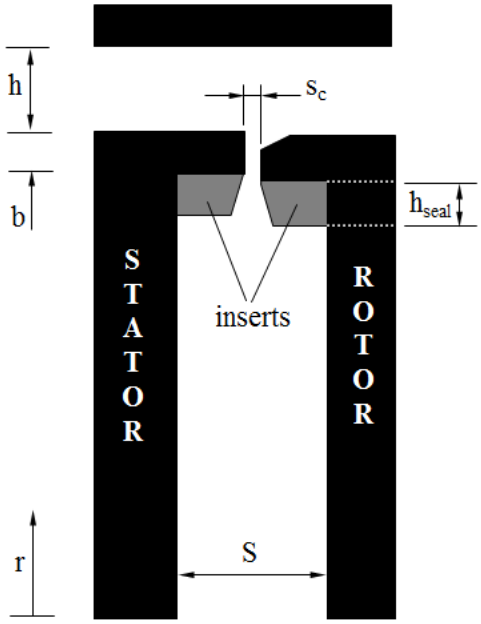

Figure. 6.1: Axial-clearance seal with inserts for heat transfer tests

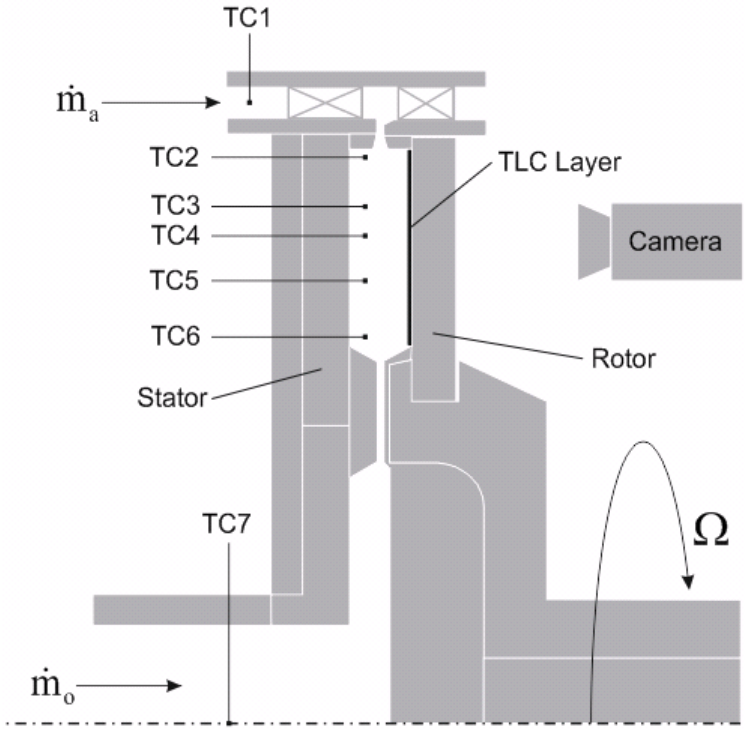

Figure. 6.2: Experimental setup for temperature and TLC measurements; TC1-7 indicate locations of fast-response thermocouples.

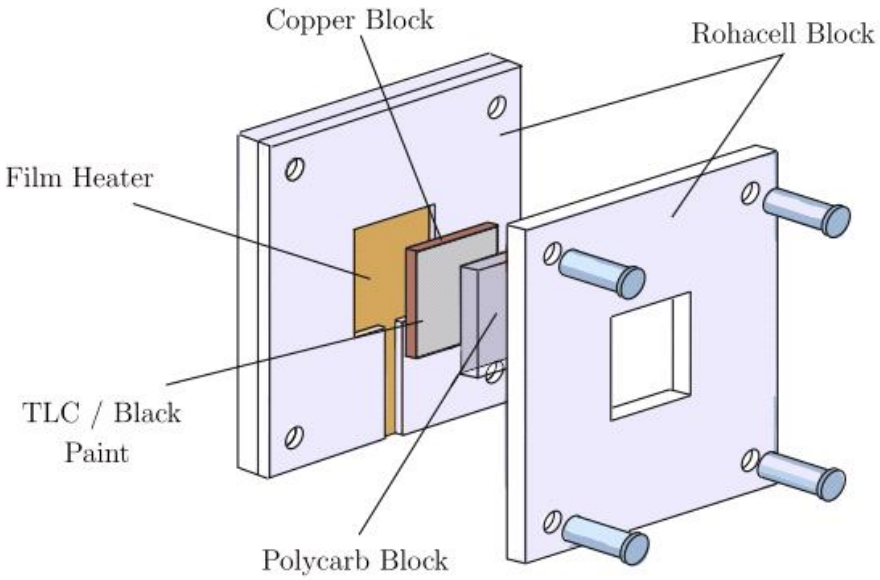

(a)

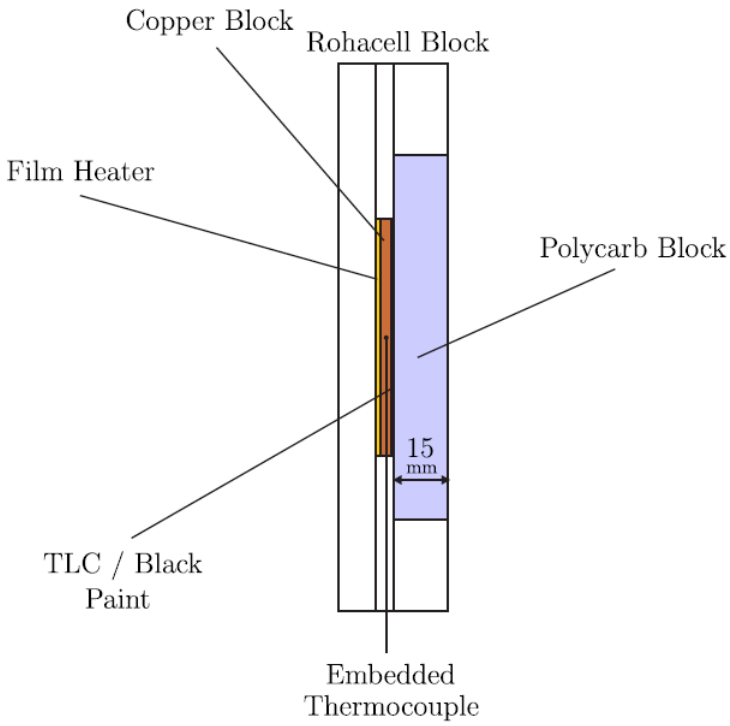

(b)

Figure. 6.3: TLC calibration setup (a) shows an exploded view and (b) shows a cross-sectional view of the test block

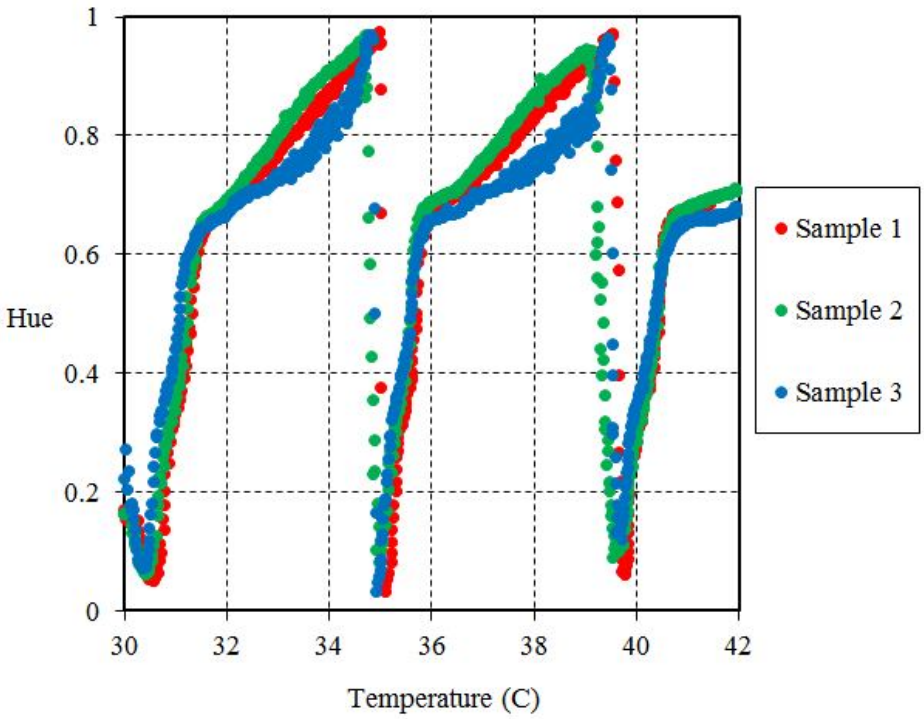

Figure. 6.4: Hue–temperature calibration for three separate samples of a combined 30, 35 and 40 C TLC mixture.

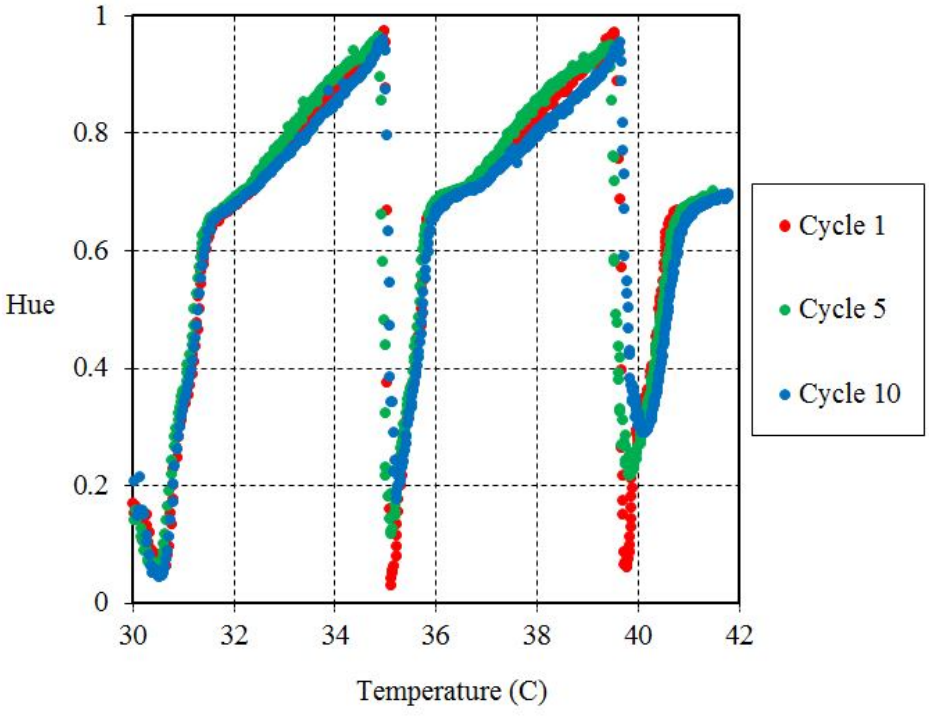

Figure. 6.5: Effect of number of heating cycles on the hue–temperature calibration for a combined 30, 35 and 40 C TLC mixture.

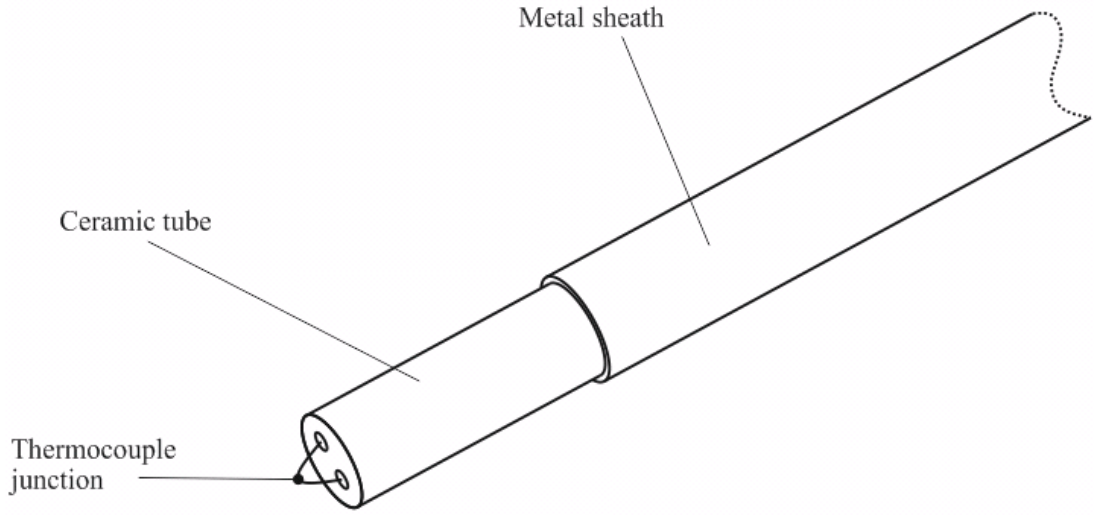

Figure. 6.6: Fast response thermocouple

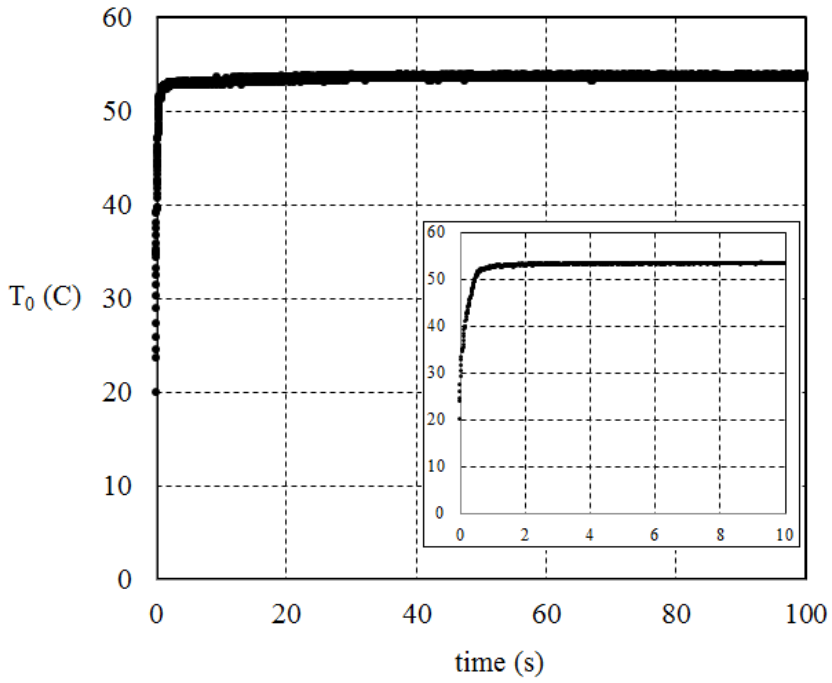

Figure. 6.7: Typical temperature history of sealant flow at inlet to wheelspace. The inset shows a close-up of the transient region.

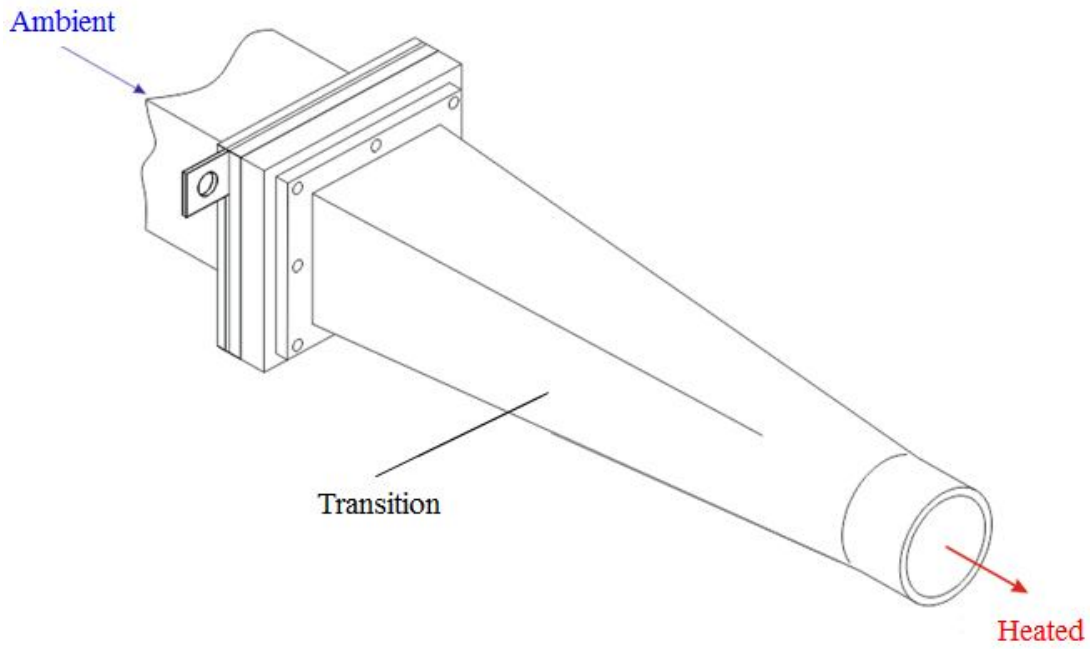

(a)

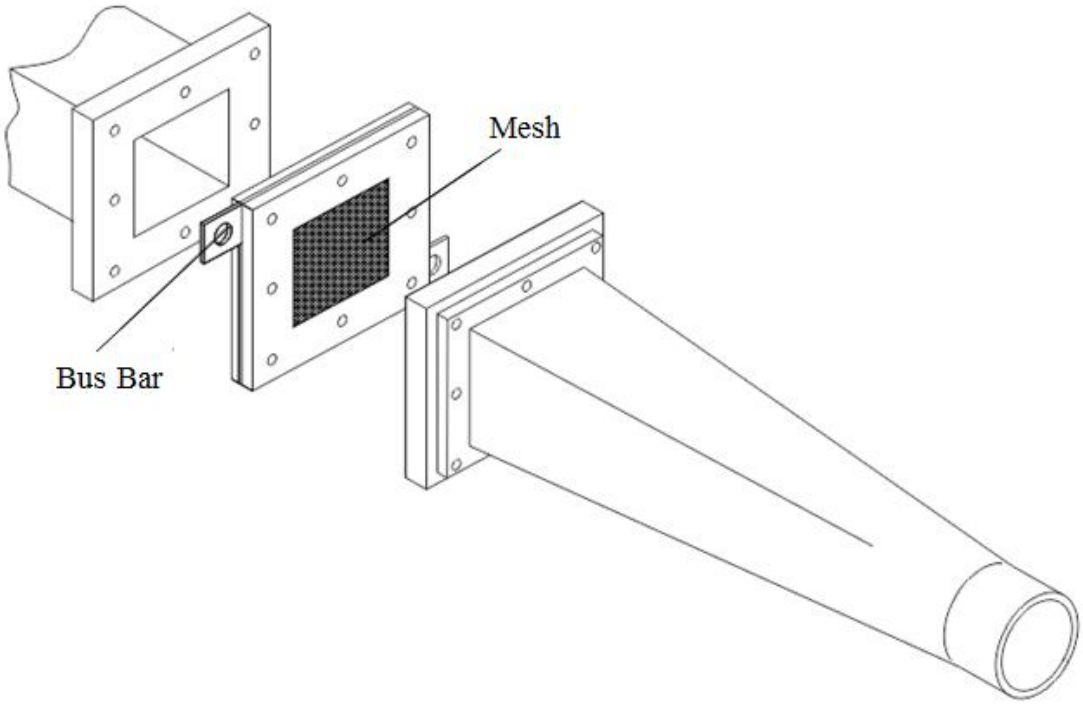

(b)

Figure. 6.8: Mesh-heater arrangement in sealant flow line: (a) shows the assembly with incoming ambient and exiting hot air streams and (b) shows an exploded view with the details of the mesh and bus bars

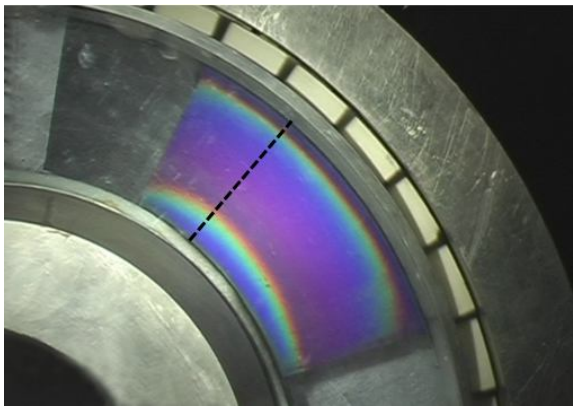

(a)

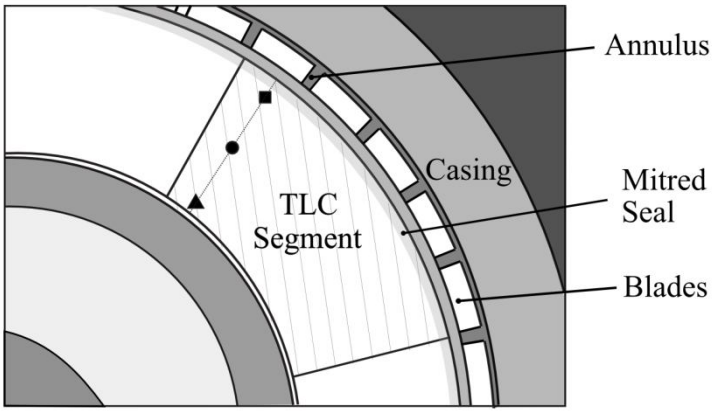

(b)

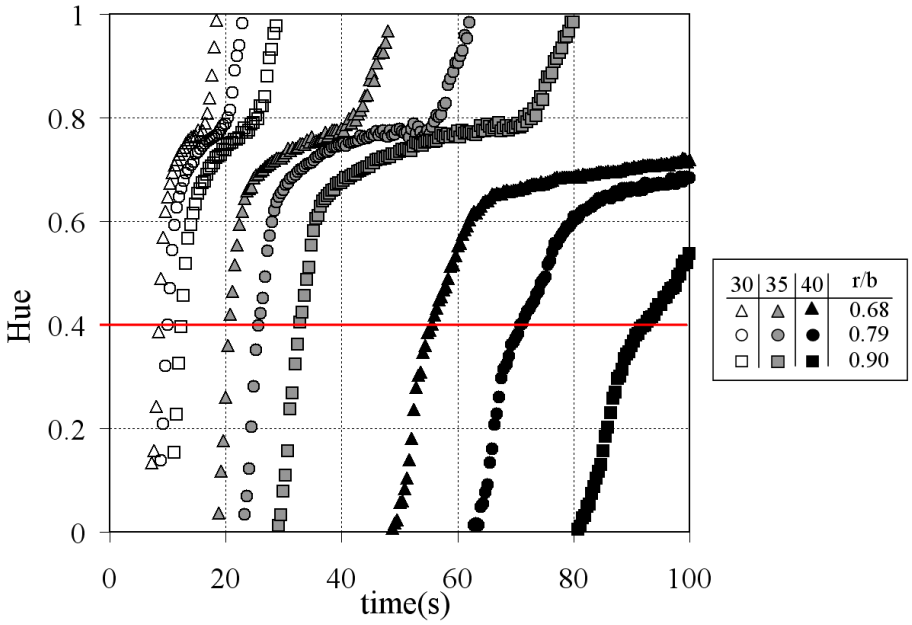

(c)

Figure. 6.9: (a) Photographic image showing colour changes for 35 C and 40 C TLC during experiment (dashed line shows typical measurement arm); (b) schematic of photographic image; (c) variation of hue with time at the three radial locations on the rotor disc marked in (b)

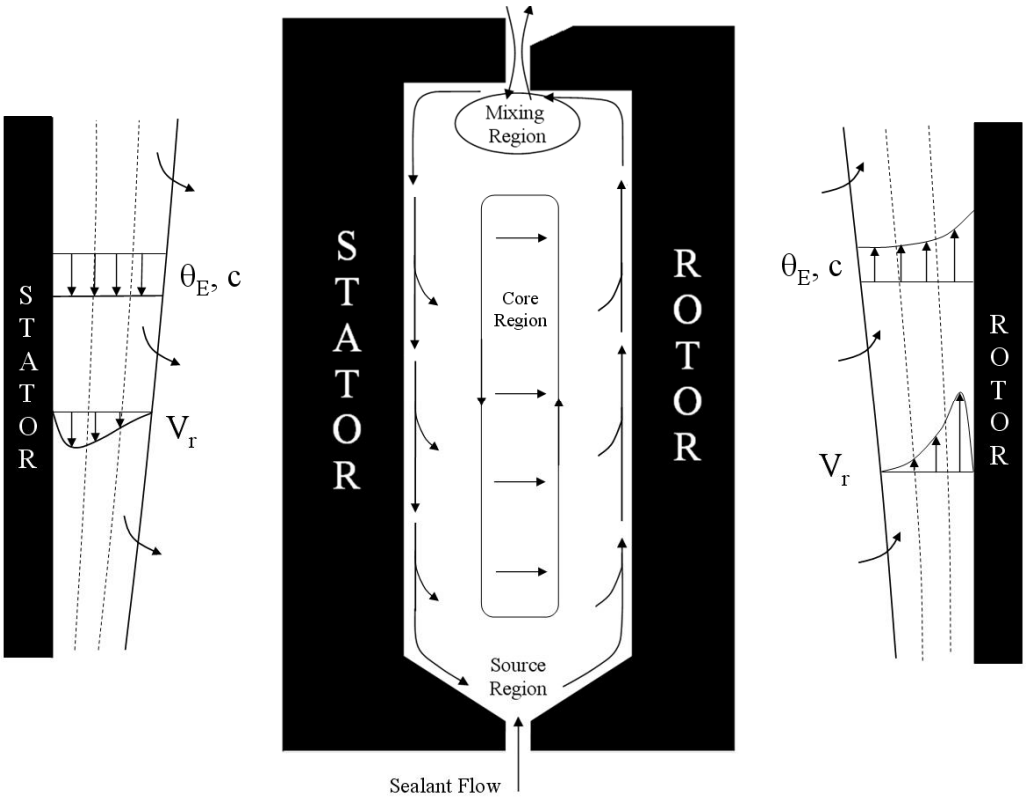

Figure. 6.10: Simplified diagram of ingress and egress, showing boundary layers on the stator and rotor (adapted from Sangan *et al.* (2012)).

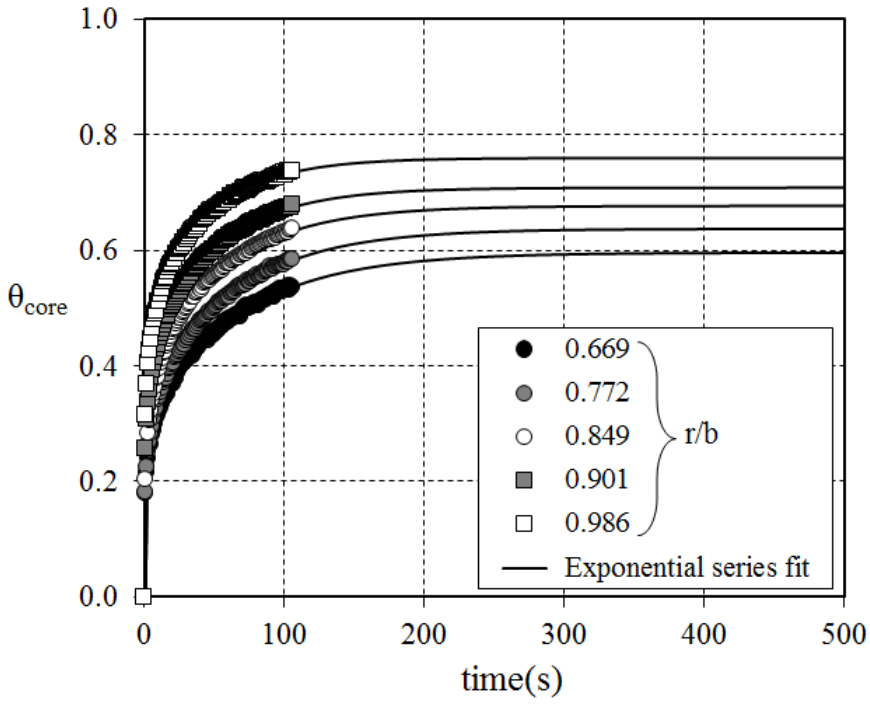

Figure. 6.11 Variation of core temperature with time, as measured by fast response thermocouples in the wheelspace at the specified *r/b* locations. Symbols denote data and solid lines represent a least-squares three-term exponential fit.

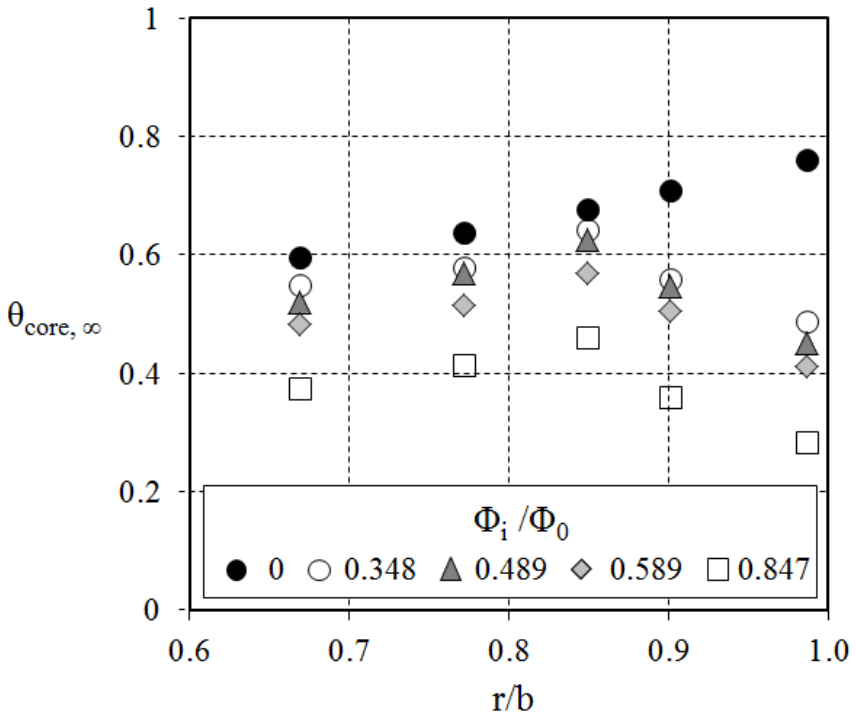

Figure. 6.12 Effect of ingress on radial variation of non-dimensional core temperatures

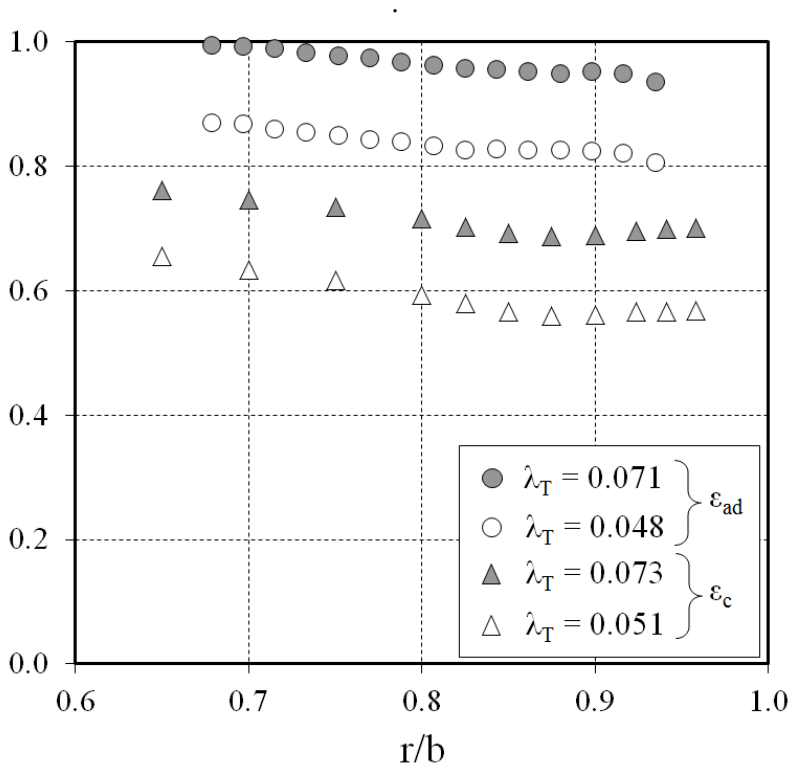

Figure. 6.13 Effect of λ_T on radial distribution of effectiveness at the design condition (Re_W/Re_ϕ = 0.538).

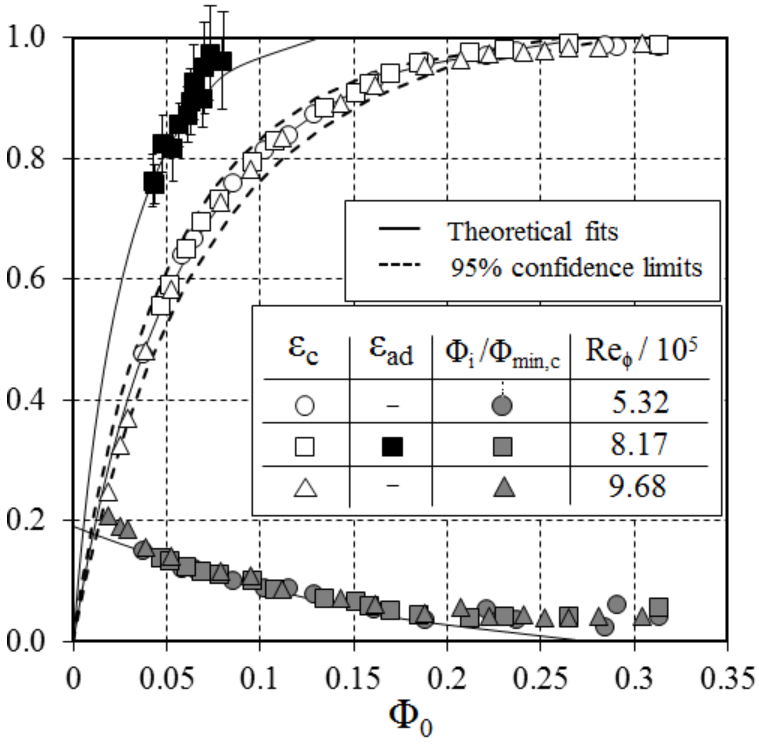

Figure. 6.14 Variation of adiabatic and concentration effectiveness with Φ_0 for the design condition (Re_W/Re_ϕ = 0.538). Symbols represent experimental data, the solid lines show the theoretical fits and the dashed lines show the 95% confidence intervals.

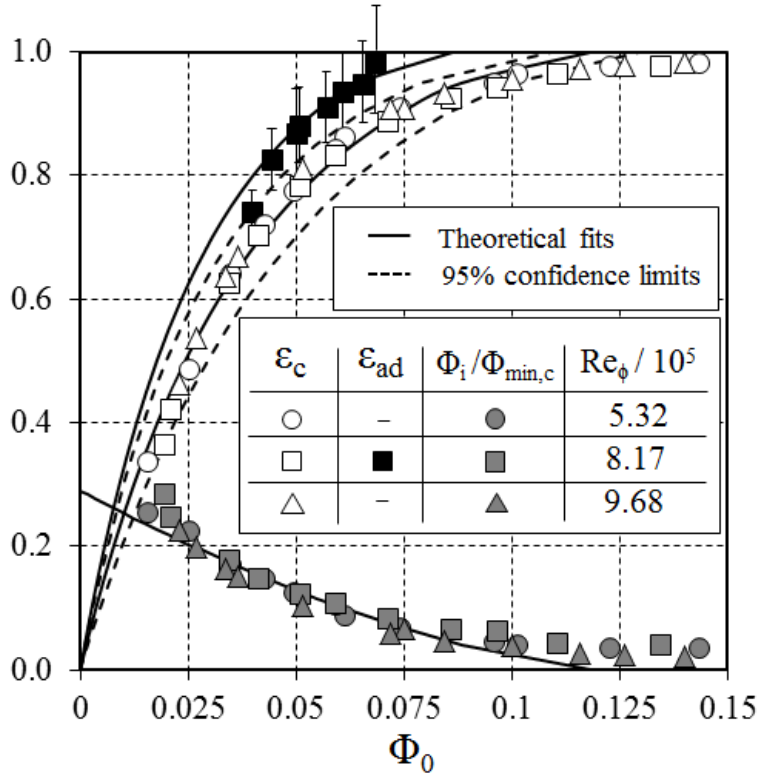

Figure. 6.15 Variation of adiabatic and concentration effectiveness with Φ_0 for the overspeed condition (Re_W/Re_ϕ = 0.326). Symbols represent experimental data, the solid lines show the theoretical fits and the dashed lines show the 95% confidence intervals.

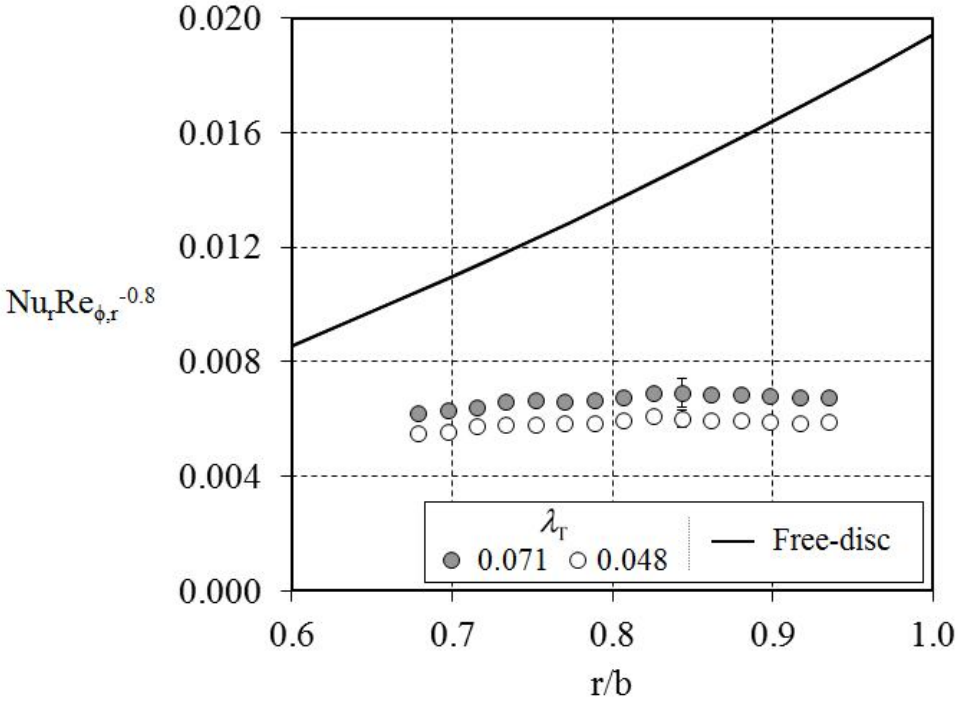

Figure. 6.16 Effect of λ_T on the radial variation of $Nu_rRe_{\phi,r}^{-0.8}$ at the design condition.

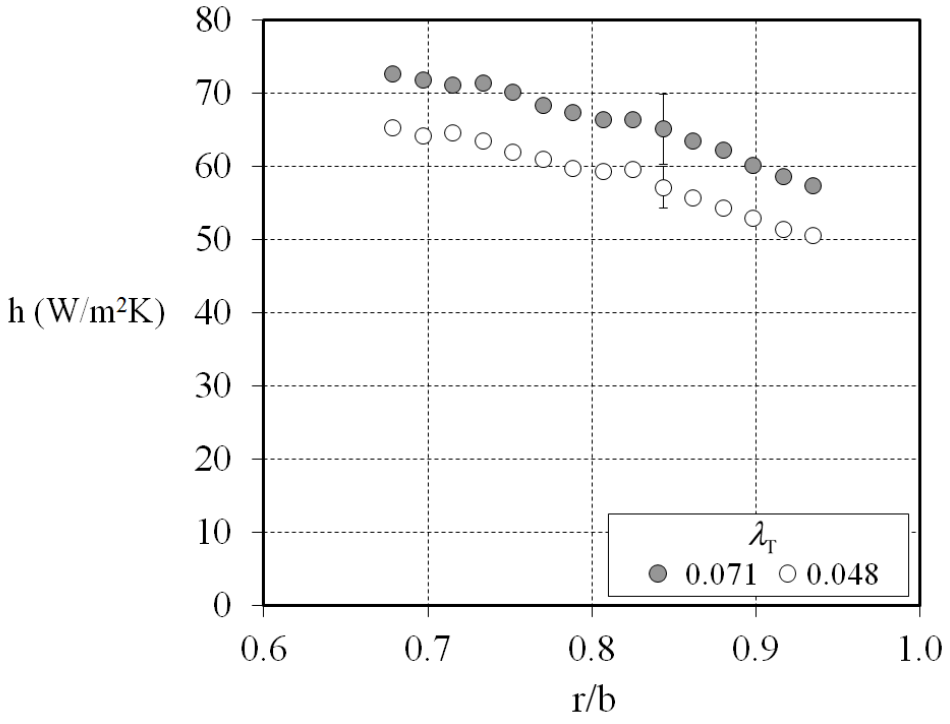

Figure. 6.17 Effect of λ_T on the radial variation of h at the design condition.

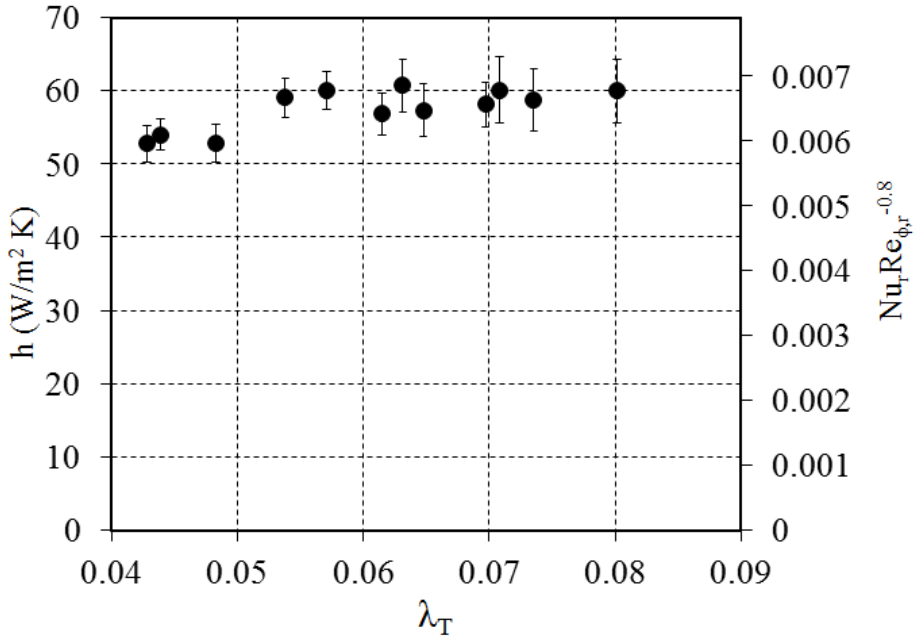

Figure. 6.18 Effect of λ_T on h and $Nu_rRe_{\phi,r}^{-0.8}$ at r/b =0.898 at the design condition.

Chapter 7. Solutions of Fourier's equation for liquid crystal experiments

The work presented in this chapter was prompted from the experimental measurements presented in Chapter 6. The findings will help inform experimenters looking to use thermochromic liquid crystal (TLC) to accurately measure the adiabatic wall temperature, T_{ad}, in transient heat transfer experiments.

The use of TLC to experimentally determine the heat transfer coefficient, h, was discussed in detail in Chapter 5. Most experimenters calculate h using the solution of Fourier's equation for a step-change in the temperature of a fluid flowing over a solid of semi-infinite thickness; solutions also exist for an exponential rise in fluid temperature (see Gillespie *et al.* (1998) and Newton *et al.* (2003)) or for when the heat transfer is not one-dimensional (see Ling *et al.* (2004) and Kingsley-Rowe *et al.* (2005)).

The semi-infinite solutions are based upon the assumption that the back surface temperature of the solid remains unchanged throughout an experiment; this assumption is only valid if the experiential run times are adequately short. It is shown in this chapter that problems arise when T_{ad} is unknown, as longer experimental times are required to accurately calculate T_{ad} than to calculate h. An alternative solution of Fourier's equation, referred to as the 'quenching solution' (which can be used for a substrate of finite thickness with an insulated back surface for a step-change in the fluid temperature at the front surface) is used to quantify the limits of the semi-infinite solution. It is shown that for $Bi < 5$ (which is the case for many experiments), the semi-infinite solution is unlikely to produce accurate estimates of T_{ad} for a substrate made from a single material; however, the solution can be used to produce accurate results over a much larger range of Biot numbers ($Bi > 2$) when a composite substrate is used.

7.1 Relevant solutions of Fourier's equation

7.1.1 Fourier's equation for a step-change in fluid temperature

Fourier's one-dimensional equation can be expressed as:

$$\frac{\partial T}{\partial t} = \alpha \frac{\partial^2 T}{\partial x^2} \tag{7.1}$$

where $\alpha = k / \rho c_p$ is the thermal diffusivity of the solid and T is the temperature at a distance x from the surface of the solid at time t.

As was discussed in Section 5.3, for Fourier's equation for convective heat transfer to a solid of semi-infinite thickness with a step-change in the temperature of the fluid, the following initial and boundary conditions apply :

$$T = T_{in} \text{ for all } x \text{ at } t = 0 \text{ and as } x \rightarrow \infty \text{ for all } t$$

$$\text{and } -k\frac{\partial T}{\partial x} = h(T_{ad} - T_s) \text{ at } x = 0 \text{ for } t > 0$$

where T_{in} is the temperature of the solid prior to the rise in temperature of the fluid (here s denotes the temperature at the surface, where $x = 0$).

The quenching solution is typically used to calculate the temperature at the centre of a solid plunged into a relatively hot or cold fluid. The solution assumes that a solid of finite thickness $2L$ is exposed to a step change in the fluid temperature on both its surfaces. The temperature distribution inside the solid is symmetrical about its centre line; consequently, the problem can be solved using an adiabatic boundary condition at $x = L$. The following initial and boundary conditions apply for the quenching solution:

$$T = T_{in} \text{ for all } x \text{ at } t = 0$$

$$-k\frac{\partial T}{\partial x} = h(T_{ad} - T_s) \text{ at } x = 0 \text{ for } t > 0$$

$$\text{and } -k\frac{\partial T}{\partial x} = 0 \text{ at } x = L \text{ for } t > 0.$$

7.1.2 Fourier's equation in non-dimensional form

The Fourier number, Fo, and the Biot number, Bi, which represent non-dimensional forms of t and h respectively, are defined by:

$$Fo = \frac{\alpha t}{L^2} \tag{7.2}$$

and

$$Bi = \frac{hL}{k} \tag{7.3}$$

The non-dimensional substrate depth, X, is expressed as:

$$X = \frac{x}{L} \tag{7.4}$$

Equation 7.1 can thus be represented in non-dimensional form as:

$$\frac{\partial \Theta}{\partial Fo} = \frac{\partial^2 \Theta}{\partial X^2} \tag{7.5}$$

where

$$\Theta = \frac{T - T_{in}}{T_{ad} - T_{in}} \tag{7.6}$$

The boundary conditions for both the semi-infinite and quenching solution become:

$$\Theta = 0 \text{ at } Fo = 0$$

$$\text{and } -\frac{\partial \Theta}{\partial X} = Bi(1 - \Theta_s) \text{ at } X = 0 \text{ for } Fo > 0.$$

At $X = 1$:

$$\Theta = 0 \text{ for the semi-infinite solution}$$

$$\text{and } \frac{\partial \Theta}{\partial X} = 0 \text{ for the quenching solution.}$$

7.1.3 Semi-infinite solution

It was shown in Holman (1990) that for a step-change in fluid temperature at the front face of a solid of semi-infinite thickness:

$$\Theta = \operatorname{erfc}\left(\frac{X}{2} Fo^{-1/2}\right) - \exp\left(XBi + Bi^2 Fo\right)\operatorname{erfc}\left(\frac{X}{2} Fo^{-1/2} + BiFo^{1/2}\right) \tag{7.7}$$

From this equation, the solution at the front surface ($X = 0$) can be expressed as:

$$\Theta_s = \frac{T_s - T_{in}}{T_{ad} - T_{in}} = 1 - \exp(\chi^2)\operatorname{erfc}(\chi) \tag{7.8}$$

where

$$\chi = Bi\, Fo^{1/2} \tag{7.9}$$

and the solution at the back surface ($X = 1$) can be expressed as

$$\Theta_L = \operatorname{erfc}\left(\frac{1}{2} Fo^{-1/2}\right) - \exp\left(Bi + Bi^2 Fo\right)\operatorname{erfc}\left(\frac{1}{2} Fo^{-1/2} + BiFo^{1/2}\right) \tag{7.10}$$

It was suggested by Schultz and Jones (1973) that, based upon Θ_L / Θ_s < 0.01, the errors in the semi-infinite solution should be small provided that Fo < 0.1. It is shown below that this is a conservative estimate.

7.1.4 Quenching Solution

The quenching solution (given in Holman (1990)) can be expressed in non-dimensional form as:

$$\Theta = 1 - 2\sum_{n=1}^{\infty} \exp(-\beta_n{}^2 Fo)\frac{\sin\beta_n}{\beta_n + \sin\beta_n \cos\beta_n}\cos(\beta_n(1-X)) \tag{7.11}$$

The quenching solution eigenvalues, β_n, are found from:

$$\beta_n = Bi\cot\beta_n \tag{7.12}$$

where $0 < \beta_n < \pi/2$ for $n = 1$ and $\beta_{n+1} \approx \beta_{n+1} + \pi$ for $n >> 1$.

At the surface of the solid (X = 0), Eq. 7.11 can be expressed as:

$$\Theta_s = 1 - 2\sum_{n=1}^{\infty} \exp(-\chi^2 \cot^2\beta_n) f_s(\beta_n) \tag{7.13}$$

where

$$f_s(\beta_n) = \frac{\sin\beta_n \cos\beta_n}{\beta_n + \sin\beta_n \cos\beta_n} \tag{7.14}$$

At the back surface of the solid (X = 1), Eq. 7.11 can be expressed as:

$$\Theta_s = 1 - 2\sum_{n=1}^{\infty} \exp(-\chi^2 \cot^2\beta_n) f_L(\beta_n) \tag{7.15}$$

where

$$f_L(\beta_n) = \frac{\sin\beta_n}{\beta_n + \sin\beta_n \cos\beta_n} \tag{7.16}$$

It can be seen from Eqs. 7.8–7.10 that the semi-infinite solution is a function of χ, whereas, from Eqs. 7.11–7.16 the quenching solution is a function of χ and Fo.

7.2 Comparison between the semi-infinite and quenching solutions

Figure 7.1 shows the variation of χ with *Fo* for various values of Θ_s and Fig. 7.2 shows the variation of Θ_s with *Fo* for various values of *Bi*; the semi-infinite and quenching curves were constructed from Eqs. 7.8 and 7.13 respectively. The error loci, which show the error between the Biot numbers for the two solutions, were calculated from:

$$e = \frac{Bi - Bi'}{Bi} \tag{7.17}$$

where *Bi* and *Bi´* are the Biot numbers calculated from the semi-infinite and quenching solutions respectively.

It should be noted that the quenching solution is only applicable to the case where the back surface of the solid is perfectively insulated. The quenching solution is used here to check when the back face boundary condition starts to affect the values of *Bi* calculated from the semi-infinite solution. It can be seen from Figs. 7.1 and 7.2 that the divergence between the semi-infinite and quenching curves increases as *Fo* increases.

It can also be seen from the error loci in the figures that the limiting Fourier numbers decrease as Θ_s increases. If an experimenter chooses a validity criterion of $e < 0.05$, then this criterion is valid for $Fo < 0.46$ when $\Theta_s = 0.4$ and for $Fo < 0.35$ when $\Theta_s = 0.8$. Alternatively, a criterion of $e < 0.01$ is valid for $Fo < 0.29$ when $\Theta_s = 0.4$ and for $Fo < 0.24$ when $\Theta_s = 0.8$. The Schultz and Jones (1973) criterion of $Fo < 0.1$ is, therefore, overly restrictive.

7.3 Effect of uncertainty in temperature measurement on calculation of *h* and T_{ad}

The effect of the uncertainties in the measured surface temperature on the values of *h* and T_{ad} calculated from the semi-infinite solution using two TLC isotherms was discussed in detail in Section 5.4; the details relevant to this chapter will be presented again here.

As is shown in Appendix A2, the semi-infinite solution can be used with two TLC measured temperature–time pairs to determine *h* and T_{ad}. Yan and Owen (2002) showed that the uncertainties in the calculated values of *h* and T_{ad} , P_h and P_{Tad} respectively, were related to the uncertainty in the TLC surface temperature measurements, P_T, by:

$$\frac{P_h}{h} = \Phi_h \frac{P_T}{T_{ad} - T_{in}} \tag{7.18}$$

and:

$$\frac{P_{Tad}}{T_{ad} - T_{in}} = \Phi_{Tad} \frac{P_T}{T_{ad} - T_{in}} \tag{7.19}$$

where Φ_h and Φ_{ad} are amplification parameters for h and T_{ad} respectively.

The values of Φ_h and Φ_{ad} are related to the values Θ_1 and Θ_2, the non-dimensional temperatures as measured using TLC, by Eqs. 5.23 and 5.27 (note $\Theta_1 < \Theta_2$). Figures 5.9 and 5.10 show the effect of Θ_2 on the variation of Φ_h and Φ_{Tad} with Θ_1 respectively. It can be seen from the figures that Φ_h and Φ_{Tad} can be significantly higher than unity; consequently, small errors in the TLC measurements can produce large errors in h and T_{ad}.

The Yan and Owen analysis shows that P_h and P_{Tad} can be minimised by making Θ_2 as large as possible and $\Theta_1 \approx 0.5\Theta_2$. A successful experiment might yield $\Theta_1 = 0.4$ and $\Theta_1 = 0.8$; these values would result in $\Phi_h = 7.15$ and $\Phi_{Tad} = 2.35$. If the P_T is 0.2 C (which it typically is for carefully calibrated narrowband TLC—see Section 6.1.3) and $T_{ad} - T_{in} = 40$C, then $P_h/h = 3.6$ % and $P_{Tad} = 0.47$C; these values of uncertainty would be considered acceptable by most experimenters. A poor selection of the two TLCs would result in large amplification factors and, as a result, large uncertainties in the calculated parameters.

The curves in Fig. 7.3 show the variation of Bi with Θ_s for 1% and 5% errors in the semi-infinite solution; these curves correspond to the error loci provided in Figs. 7.1 and 7.2. At $\Theta_s = 0.8$, the 1% and 5% errors in the semi-infinite solution occur at $Bi = 5.5$ and 4.5 respectively; if an experiment was carried out at values of Bi lower than these values then the semi-infinite solution could yield significantly larger errors. For experiments where $Bi < 5$, some improvements are suggested below to improve the accuracy of the two TLC measurement technique for determining T_{ad}.

7.4 Improvements for experiments

7.4.1 Limitations of the semi-infinite solution

As was shown above, to accurately determine T_{ad} from the semi-infinite solution using two TLC measurements, large values of Θ_2 are required to minimise Φ_{Tad}. Some experimenters have used alternative techniques to the two TLC method: Wang *et al.* (1996) used wideband TLC with the semi-infinite solution to determine h for when T_{ad} was known. When T_{ad} is unknown, it is possible to compute the variation of the surface heat flux, q_s, with

T_s numerically from the measured temperature history. h and T_{ad} can be subsequently determined from linear regression to the q_s–T_s data using:

$$q_s = h(T_{ad} - T_s) \tag{7.20}$$

where h is the gradient of the fitted line and T_{ad} is the value of T_s at $q_s = 0$ (i.e. the x-axis intercept); T_{ad} is found by extrapolating the fitted line to $q_s = 0$. The problem with the extrapolation technique is that the uncertainty in T_{ad} increases with the difference between the measured values of T_s and the extrapolated value; to accurately determine T_{ad}, it is necessary to measure values of T_s close to T_{ad} during an experiment (this is also the case for the semi-infinite solution where Θ_2 requires maximising). Practically, it is very difficult to measure values of T_s close to T_{ad} or to maximise Θ_2: Θ_s is limited to the steady-state value, Θ_{ss} (i.e. the Θ_s value of when $T_s = T_{ss}$); and Θ_2 is limited by the validity of the semi-infinite solution.

7.4.2 Steady-state solutions

The non-dimensional steady state temperature, Θ_{ss}, is defined as:

$$\Theta_{ss} = \frac{T_{ss} - T_{in}}{T_{ad} - T_{in}} \tag{7.21}$$

If it assumed that the back surface temperature of the solid is unchanged throughout the experiment (i.e. $T_L = T_{in}$ when $t \rightarrow \infty$), then the steady-state heat flux, q_{ss}, is given by:

$$q_{ss} = h(T_{ad} - T_{ss}) = \frac{k}{L}(T_{ss} - T_{in}) \tag{7.22}$$

From the definitions of Bi and Θ_{ss}, given in Eqs. 7.3 and 7.21 respectively, Eq. 7.22 can be expressed as:

$$\Theta_{ss} = \frac{Bi}{1 + Bi} \tag{7.23}$$

where $\Theta_{ss} \rightarrow 1$ as $Bi \rightarrow \infty$.

Appendix C provides a table of the relevant thermal properties for the materials discussed in this section. Consider the experimental case of a block of L = 10 mm to which h = 60 W/m^{2}K. If the block was made from polycarbonate (the material used to construct the rotor disc on which the heat transfer measurements were made in Chapter 6, for which k = 0.20 W/mK) then Bi = 3 and, from Eq. 7.23, Θ_{ss} = 0.75; if it was made from Rohacell 71, for which k = 0.03 W/mK, then Bi = 20 and $\Theta_{ss} \approx 0.95$. Rohacell offers an advantage over

polycarbonate in allowing higher values of Θ_s (and thus Θ_2) to be achieved during an experiment; this is important as the uncertainties in h and T_{ad} decrease as Θ_2 increases. The disadvantage of Rohacell is that its thermal properties result in small time constants, which leads to difficulty in accurately measuring the times at which lower values of Θ_s (and thus Θ_1) are triggered.

For the semi-infinite solution, Θ_s is a unique function of χ; the activation time of the TLC can be expressed in terms of χ and h as:

$$t = \rho c_p k \left(\frac{\chi}{h} \right)^2 \tag{7.24}$$

With reference to the table of thermal properties in Appendix C, $\rho c_p K$ is two orders-of-magnitude smaller for Rohacell than for polycarbonate or acrylic (another material commonly used by heat transfer experimenters). Assuming that an experimenter is aiming for $\Theta_1 = 0.4$ and $\Theta_2 = 0.8$ (which would yield relatively small uncertainties in h and T_{ad}—see above), then for $\Theta_1 = 0.4$, Eq. 7.8 gives $\chi_1 = 0.531$. For h = 60 W/mK, t_1= 24.1, 23.5 and 0.22 s for acrylic, polycarbonate and Rohacell respectively. The mesh heater used in Chapter 6 had a time constant of approximately 1 s, which is greater that the activation time of the Rohacell for the aforementioned example (i.e. the Rohacell could not be used to make measurements of Θ_1).

Acrylic and polycarbonate allow the activation time of the TLC to be accurately measured at low values of Θ_s and Rohacell allows large values of Θ_2 to be obtained; a composite substrate of these materials should be useable at both small and large values of Θ_s.

7.4.3 Composite substrates

Figure 7.4 shows the steady-state temperature profile through a two-layer composite substrate; subscripts A and B refer to the inner and outer material layers respectively. If it is assumed that when the state-state condition has been reached that T_{ss}, T_i and T_{in} are the surface, material interface and back face temperatures respectively, then:

$$q_{ss} = h(T_{ad} - T_{ss}) = \frac{k_A}{L_A}(T_{ss} - T_i) = \frac{k_B}{L_B}(T_i - T_{in}) \tag{7.25}$$

From the definitions of Bi and Θ_{ss}, given in Eqs. 7.3 and 7.21 respectively, Eq. 7.25 can be expressed as:

$$\Theta_{ss} = \frac{Bi_A + Bi_B}{1 + Bi_A + Bi_B} \tag{7.26}$$

which can be rewritten in the form

$$\Theta_{ss} = \frac{\eta Bi_A}{1 + \eta Bi_A} \tag{7.27}$$

where

$$\eta = 1 + \frac{Bi_B}{Bi_A} = 1 + \frac{k_A L_B}{k_B L_A} \tag{7.28}$$

Consider the experimental case of a composite block of $L_A = L_B = 10$ mm to which h = 60 W/m^{2}K. If the outer material is made from polycarbonate and the inner layer from Rohacell then Bi_A = 3 and Bi_B = 20; it follows from Eqs. 7.27 and 7.28 that η = 7.67 and Θ_{ss} = 0.958 (note: this value could only be achieved for a single substrate if Bi > 23).

7.4.4 Solutions of Fourier's equation for a composite substrate

Numerical solution

For the composite substrate, the one-dimensional Fourier's equation could be solved from the measured surface temperature history using a numerical solution (for example, using a Crank-Nicolson solver); a smoothed fit to the T_s–t data would be used as the front face boundary condition with $T_L = T_{in}$ as the back face boundary condition. Continuity of heat flux at the polycarbonate–Rohacell interface would be computed using:

$$k_A \left(\frac{dT}{dx} \right)_A = k_B \left(\frac{dT}{dx} \right)_B \tag{7.29}$$

If the test time was sufficient that $T_s \rightarrow T_{ss}$, then h and T_{ad} could be found accurately from the computed values of q_s using Eq. 7.20. The advantage of the suggested numerical method is that the semi-infinite solution is not used; consequently, the experimenter can ignore the validity criterion and solve for cases where a step-change in fluid temperature is not realisable.

The surface temperature history could be measured using a wideband TLC or a number of narrowband TLCs; the TLCs would require calibration over their full bandwidth (as was carried out by Abu Talib *et al.* (2004)) to provide sufficient T_s–t data to which a smoothed curve could be fitted. If ΔT is the bandwidth of the TLC and δt is the time-step between the video frames showing the colour change of the TLC (for a typical digital camera capturing at

25 frames per second δt = 40 ms), then the maximum number of data points, n, that can be obtained during a test is given by:

$$n = \frac{\Delta t}{\delta t} \tag{7.30}$$

where Δt is the time over which the TLC changes colour. If it is assumed that:

$$\Delta t \approx \frac{\Delta T}{\left(dT_s / dt\right)} \tag{7.31}$$

then Eq. 7.30 becomes

$$n = \frac{\Delta T}{\left(dT_s / dt\right)\delta t} \tag{7.32}$$

As shown in Fig. 7.2, during a transient heat transfer experiment, $d\Theta_s/dFo$ (which is analogous to dT_s/dt) decreases as Θ_s increases; consequently, the activation time of the TLC (and thus the number of captured data points) will increase at higher values of Θ_s. To maximise the number of data points and thereby increase the accuracy of the fitted T_s–t curve, it would be necessary to utilise wideband TLC at low vales of Θ_s where dT_s/dt is large; at larger values of Θ_s narrowband TLCs (which are easier to calibrate accurately relative to wideband TLC) should suffice.

Analytical solution

To analytically solve for h and T_{ad} using a composite substrate it is necessary to measure T_{ss}, T_{in} and T_1 at time t_1 during an experiment. TLCs should be appropriately selected so that T_1 is measured within the validity of the semi-infinite solution for the front material layer (i.e. $Fo_1 = Fo_A < 0.35$) and T_{ss} is accurately measured (it may be necessary to use a wideband TLC to capture T_{ss} if the experimenter cannot estimate its value and select an appropriate narrowband TLC beforehand). From the definition of Θ given in Eq. 7.6, the ratio Θ_1 / Θ_{ss} can be expressed as:

$$\frac{\Theta_1}{\Theta_{ss}} = \frac{T_{s,1} - T_{in}}{T_{ss} - T_{in}} = c \tag{7.33}$$

where c is a known constant. From Eqs. 7.8 and 7.27, Eq. 7.33 can be written in the form

$$\frac{\Theta_1}{\Theta_{ss}} = \frac{Bi_A^{-1} + \eta}{\eta}\left[1 - \exp(\chi_1^2)\,\mathrm{erfc}(\chi_1)\right] \tag{7.34}$$

where

$$\chi_1 = Bi_A \, Fo_1^{1/2} \tag{7.35}$$

As shown in Appendix A3, Bi_A (and thus h) can be estimated using a Newton-Raphson iteration, from which T_{ad} can be solved for using Eq. 7.27.

An improved estimate of h and T_{ad} could be obtained by calculating a mean value of Bi_A from n values of Θ_1 using the entire bandwidth of the TLC in the low temperature region (as discussed above for the numerical technique); as the standard deviation of a sample is inversely proportional to $n^{1/2}$, increasing n would reduce the uncertainty in the calculated value of Bi_A. It should be possible to use the theory of Yan and Owen (2002) to estimate the optimum range over which to measure Θ_1 to minimise the uncertainties in h and T_{ad} for the composite solution (this is beyond the scope of this thesis).

7.5 Implications

The work carried out in this chapter fulfils Objective 4 of this thesis (see Section 1.5). The benefit of using a composite substrate over a single substrate can be demonstrated by way of example. Suppose a TLC is chosen such that $\Theta_1 = 0.5$; provided that $Bi > 2$ the semi-infinite solution will be accurate to within 1% (see Figs. 7.1 and 7.2). For the polycarbonate–Rohacell composite example considered above (where $h = 60$ W/m^{2}K and $L_A = L_B = 10$ mm), Eq. 7.27 shows that $\Theta_{ss} > 0.94$ when $Bi_A > 2$. For a single substrate, to achieve large enough values of Θ_2 to ensure that the semi-infinite solution produces accurate estimates of T_{ad} without invalidating the semi-infinite thickness assumption, then $Bi > 5$. It is clear that a composite substrate allows T_{ad} to be accurately calculated over a greater range of Biot numbers than for a single substrate. It is hoped that these findings will help inform experimenters looking to accurately measure T_{ad} using TLC in transient heat transfer experiments.

The following caveats apply to the work presented in this chapter:

- The errors in the values of Bi obtained from the semi-infinite solution were determined through comparison of the results of the quenching solution. The quenching solution was used as a datum case to see when the back face boundary condition became important in the analysis. Other solutions (e.g. a finite difference model with a known Biot number at the back face) may produce a different range of Fourier numbers for which the semi-infinite solution is valid.

- The accuracy of Bi and T_{ad} obtained from Fourier's equation for a composite substrate is limited by knowledge of the thermal properties of the materials and the contact resistance at the composite interface. Uncertainties in these quantities will result in a bias in the obtained Biot numbers; this bias will be more significant for a composite substrate than a single substrate as the uncertainties in the thermal properties will be compounded.

7.6 Figures

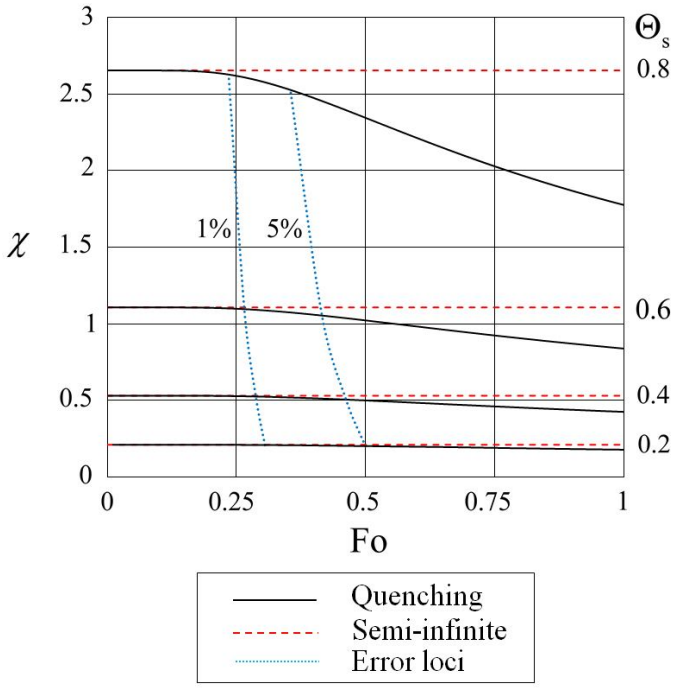

Figure. 7.1: Effect of Θ_s on the variation of χ with *Fo* according to the semi-infinite and quenching solutions.

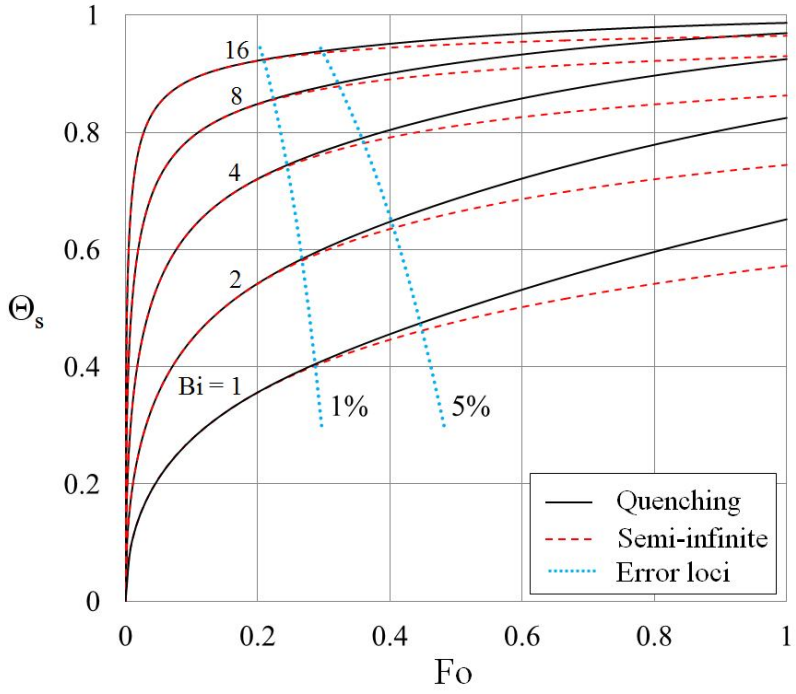

Figure. 7.2: Effect of *Bi* on the variation of Θ_s with *Fo* according to the semi-infinite and quenching solutions.

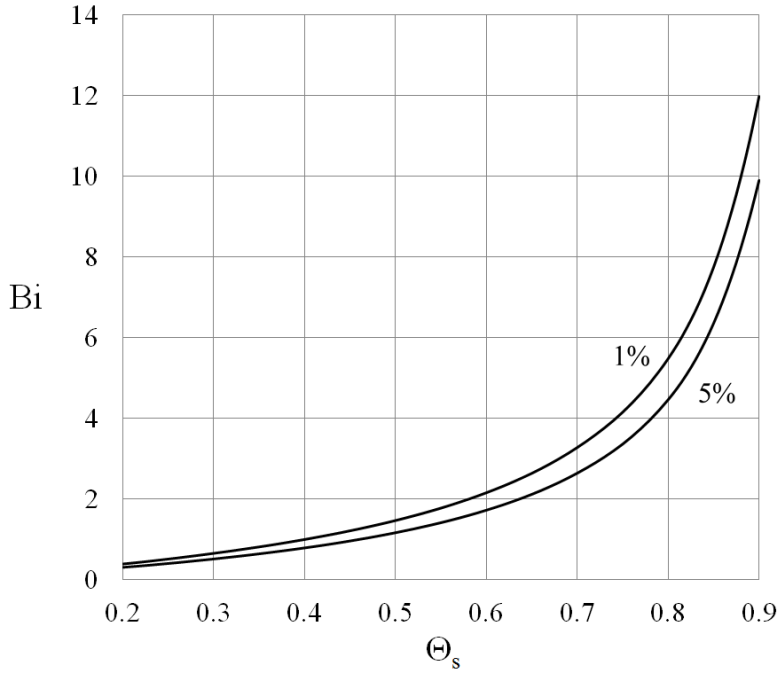

Figure. 7.3: Variation of *Bi* with Θ_s for 1% and 5% errors in the semi-infinite solution

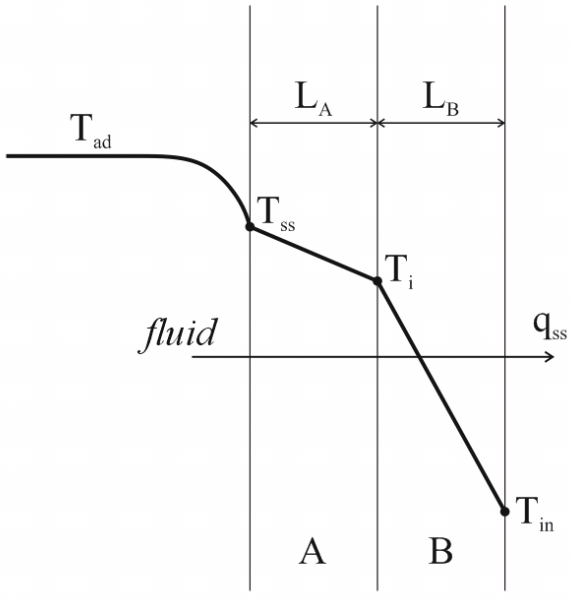

Figure. 7.4: Steady-state temperature profile through a composite substrate

Chapter 8. Conclusions, contributions and future work

This thesis has investigated the effect of hot gas ingress on the fluid dynamics in the wheelspace and the heat transfer to the rotor of a first-stage high-pressure gas turbine. Based upon what engine designers want to know, an extensive review of literature led to the formation of four objectives (see Section 1.5). The findings from the work undertaken to meet these objectives is summarised in the Conclusions section below. It is hoped that the findings will stimulate future research and inform engineers in the design of gas turbine cooling systems.

8.1 Conclusions

8.1.1 Orifice model validation

The findings presented in this sub-section, which are taken from Chapter 3, fulfilled Objective 1 of this thesis.

The CI orifice equations developed in Owen (2011b) were solved for constant and variable egress discharge coefficients to give curves predicting the variation of $\Phi_{min,CI}$ /$\Phi_{min,RI}$ with Re_W /Re_ϕ in Sections 3.3 and 3.4 respectively. Two external pressure profiles were used to solve the equations: a theoretical saw-tooth pressure profile, which was solved analytically; and a fit to the measured pressure profile, which was solved numerically. The equations were preliminarily validated against the data of Phadke and Owen (1988c); additional data for validation was provided from experimental measurements carried out on the Bath single-stage gas turbine rig.

The solutions to the CI constant discharge coefficient orifice equations were found to be in good agreement with the Phadke and Owen data at large values of Re_W /Re_ϕ; at lower values the agreement was less good as the solution failed to capture an undershoot in the data (see Figs. 3.4 and 3.5). The solution for variable discharge coefficients provided a better fit to the Phadke and Owen data than the solution for constant discharge coefficients in the undershoot region at small values of Re_W /Re_ϕ (see Figs. 3.7 and 3.8). For both the constant and variable discharge coefficient CI orifice equations, the solutions for the saw-tooth and

fitted pressure profiles were indistinguishable. It follows that the maximum-to-minimum pressure difference in the annulus is the key criterion in determining ingress levels.

8.1.2 Stator gas concentration measurements

The findings presented in this sub-section, which are taken from Chapter 4, fulfilled Objectives 1 and 2 of this thesis.

Gas concentration measurements were made on the stator of the Bath single stage test rig to measure the variation of ε_c with Φ_0 on the stator for an axial clearance seal geometry at various off-design conditions with Re_ϕ = 5.32 × 10^5, 8.17 × 10^5 and 9.68 × 10^5 (see Section 4.3). The variation of $\Phi'_{min,CI}/\Phi'_{min,RI}$ (where the dash denotes the value of Φ_0 at ε_c = 0.95) with Re_W/Re_ϕ, shown in Fig 4.14, followed the same trend as the Phadke and Owen (1988c) data: at low values of Re_W/Re_ϕ, ingress levels were influenced by the combined effects of the rotation of the disc and the annular pressure profile and were therefore considered to fall into the combined ingress region; the influence of rotation diminished as Re_W/Re_ϕ increased and the data tended to the EI ingress asymptote. The variable discharge coefficient CI orifice equation was in good agreement with the data for $Re_W/Re_\phi > 0.1$; below this value the agreement was less good, owing to an unexplained blip in the experimental data.

A least-squares cubic spline fit to the Phadke and Owen data was within 5% of the EI asymptote for $\Phi_{min,CI}/\Phi_{min,RI} \geq 2$. For $\Phi_{min,CI}/\Phi_{min,RI} \leq 2$ the experimental data was considered to fall into the combined ingress region where the effects of rotation and external flow were both important in determining ingestion levels. Whilst an engine is unlikely to operate far enough off-design to fall into this region, it is possible that ingestion through the inner seal clearance of double seals, which is driven by the pressure difference between the outer and inner wheelspaces, can be categorised as combined ingress when the annular pressure asymmetry is attenuated in the outer wheelspace cavity. It is intended that ingress through double seals at a range of design conditions be explored as part of a future work program.

It was shown in Owen (2011b) that the predicted variation of ε with Φ_0/Φ_{min} is similar for both the RI and EI effectiveness equations; it follows that the variation of ε with $\Phi_0/\Phi_{min,CI}$ is likely to be similar. It is tentatively proposed that the CI orifice equations could be used to extrapolate data taken on a test rig to engine conditions for a specific seal geometry. This proposition requires testing, which is beyond the scope of this thesis.

8.1.3 Rotor temperature and heat transfer measurements

The findings presented in this sub-section, which are taken from Chapter 6, fulfilled Objective 3 of this thesis.

TLC surface temperature measurements were used with a step-change in fluid temperature to solve for h and T_{ad} on the rotor using the one-dimensional solution of Fourier's equation for a solid of semi-infinite thickness; these measurements were made for an axial seal geometry at various sealant flow rates so that the effect of ingress on the rotor could be determined. Concurrent gas concentration measurements were made on the stator for comparison with the rotor. Measurements were made on the stator at rotational disc speeds of 2000, 3000 and 3500 RPM, corresponding to $Re_\phi = 5.32 \times 10^5$, 8.17×10^5 and 9.68×10^5 respectively; measurements were made on the rotor for 3000 RPM only. For each rotational speed, two different external flow rates were used: one on-design and the other off-design. For the design condition, Re_W / Re_ϕ = 0.538; at the overspeed off-design condition, Re_W / Re_ϕ = 0.326. The seal clearance was kept constant at $G_{c,ax}$ = 0.0105 throughout the tests.

The 95% uncertainties in the measured values of h and T_{ad}, which were calculated using the theory of Yan and Owen (2002), were shown to be less than 8% and 1.5 C respectively. A newly defined adiabatic effectiveness, ε_{ad}, was solved for on the rotor using the measurements of T_{ad}. The comparison between ε_{ad} on the rotor and the concentration effectiveness, ε_c, on the stator (presented in Figs. 6.14 and 6.15 in Section 6.3.4), showed that the rotor was protected against the effects of ingress relative to the stator. The sealing air, which is drawn into the rotor boundary layer from the source region, thermally buffers the rotor against the ingested fluid in the core.

A thermal buffer ratio, η, was defined as the ratio of the minimum sealant flow required to purge the stator against ingress, $\Phi_{min,c}$, to the minimum sealant flow required to purge the rotor against ingress, $\Phi_{min,ad}$. The level of protection from ingress that the thermal buffer provides to the rotor is dependent upon the flow structure in the wheelspace, which is governed by λ_T ; when λ_T is increased, and consequently the entrainment from the core into the rotor boundary layer is reduced, η would be expected to increase. A hypothesis relating $\lambda_{T,min}$ (the minimum value of λ_T for which the stator is fully sealed) to η was developed and shown to be in good agreement with the experimental data.

The local Nusselt numbers, Nu_r, were shown to be fairly constant with radius and increased as λ_T was increased (see Figs. 6.16 – 6.18 in Section 6.3.5) . The latter finding can

be explained by the flow structure in the wheelspace: as λ_T is raised, the swirl in the fluid core reduces, which results in an increase in the moment coefficient and Nu_r on the rotor. Although the measured values of Nu_r may not be engine representative, they provide valuable data for validation of CFD codes.

The stator can generally tolerate higher temperatures (and thus ingress levels) than the rotor given that it is under much less mechanical stress; it may be that engine designers can make use of the buffering effect of the rotor boundary layer to allow more ingress into the wheelspace than previously thought without risking thermal damage to the rotor. This would reduce sealant flow requirements and improve engine efficiency.

8.1.4 Improved experimental techniques for TLC

The findings presented in this sub-section, which are taken from Chapter 7, fulfilled Objective 4 of this thesis.

The application of TLC in heat transfer experiments to solve for the Biot number from the solution of Fourier's equation for a step-change in fluid temperature semi-infinite was shown to be restricted to relatively low Fourier numbers (see Section 7.2). The so called 'quenching solution' was used to check when the back face boundary condition starts to affect the values of *Bi* calculated from the semi-infinite solution; it was shown that for a single material substrate, the semi-infinite solution is limited to $Fo < 0.24$ for a 1% error in *Bi* and $Fo < 0.35$ for a 5% error in *Bi*. To minimise the uncertainties in the determined values of T_{ad} it is necessary to measure surface temperatures as close to T_{ad} as possible. This can lead to long experimental run times, resulting in large values of *Fo* that invalidate the semi-infinite solution. For $Bi < 5$ (which is the case for many experiments), the semi-infinite solution is unlikely to produce accurate estimates of T_{ad}.

It was shown in Section 7.4 that a two-layer composite substrate made from, for example, polycarbonate and Rohacell, can be used to achieve accurate estimates of *h* and T_{ad} for $Bi > 2$ (a much greater range of *Bi* than for a single substrate). TLC can be used to measure the surface temperature history of the substrate during an experiment; this would allow *h* and T_{ad} to be solved from the numerical solution of Fourier's equation or from a combination of the semi-infinite and steady-state solutions. These findings will help inform experimenters looking to accurately measure T_{ad} using TLC in transient heat transfer experiments.

8.2 Contributions to scientific understanding

The work is this thesis has made the following significant contributions to scientific understanding:

- The Owen (2011b) combined ingress orifice model was extended and validated. This model is being integrated into industrial 1-D sealing-air-system design codes by Siemens.

- The first published measurements of the minimum sealing flow levels were made for off-design operation for a rotor-stator system with vanes and blades. These results are being used to validate engine designers CFD codes.

- A new adiabatic effectiveness definition was formed and used to make the first measurements of effectiveness on a rotor in a rotor-stator system with ingress.

- The rotor was shown to be thermally buffered against the effects of ingress relative to the stator; this had yet to be shown experimentally in open literature.

- A simple thermal buffer hypothesis was proposed and incorporated into the Owen (2011b) orifice model. The model agreed well with the data in this thesis.

- A new ‘composite substrate’ method for TLC has been suggested. This will help future experimenters to make accurate measurements of adiabatic wall temperature.

8.3 Future work

The research presented in this thesis has opened up a number of opportunities for future work, including:

- Investigation of the sealing performance of different rim seal geometries at off-design operational conditions. This would be particularly interesting for double seal geometries where the annular pressure asymmetry is attenuated in the buffer cavity resulting in the inner seal clearance operating in the combined ingress regime.

- Measurement of adiabatic effectiveness on the rotor for radial and double seal geometries. This would allow the buffer ratio hypothesis to be tested extensively and

would give engine designers an indication of the levels of thermal buffering that may be expected in engine realistic rim seal geometries. It would also be interesting to study the effects of ingress on heat transfer levels to the stator, particularly at the outer radius of the disc where the ingress enters the wheelspace with high swirl.

- Investigation of ingress through rim seals in upstream and downstream wheelspace cavities on a 1.5-stage gas turbine rig (stator-rotor-stator). The measurements in this thesis have been restricted to an upstream wheelspace; the ingress characteristics may differ in downstream wheelspaces where the pressure asymmetry above the rim seal is generated by the flow over the blades (as opposed to the vanes for the upstream cavity). At the time of writing this thesis there is on-going design of a 1.5 stage rig at the University of Bath; gas concentration measurements will be made on both stator discs and TLC surface temperature measurements will be made on both surfaces of the rotor. This will allow the wheelspace fluid dynamics, convective heat transfer to the rotor and performance characteristics of rim seal geometries for the upstream and downstream tests sections to be compared.

References

Abdullah, N., Abu Talib, A. R., Saiah, H. R. M., Jaafar, A. A. and Salleh, M. A. M., 2009, "Film thickness effects on calibrations of a narrowband thermochromic liquid crystal," Exp. Therm. Fluid. Sci., 33(4), pp. 561-578.

Abe, T., Kikuchi, J. and Takeuchi, H., 1979, "An investigation of turbine disk cooling-experimental investigation and observation of hot gas flow into a wheelspace," Paper No. GT-30.

Abu Talib, A. R., Neely, A. J., Ireland, P. T. and Mullender, A. J., 2004, "A novel liquid crystal image processing technique using multiple gas temperature steps to determine heat transfer coefficient distribution and adiabatic wall temperature," ASME J. Turbomach., 126(4), pp. 587-596.

Anderson, M. R. and Baughn, J. W., 2004, "Hysteresis in liquid crystal thermography," ASME J. Heat Transfer, 126(3), pp. 339-346.

Anderson, M. R. and Baughn, J. W., 2005, "Liquid-crystal thermography: Illumination spectral effects. Part 1 - experiments," ASME J. Heat Transfer, 127(6), pp. 581-587.

ASME, 1988, "The world's first industrial gas turbine set at Neuchâtel (1939)," ASME International Historic Mechanical Engineering Landmark, H135.

Bahadur, B., 1998, *Liquid crystals: Applications and uses*, Singapore: World Scientific.

Batchelor, G. K., 1951, "Note on the class of solutions of the Navier-Stokes equations representing steady rotationally symmetric flow," Quarterly Journal of Applied Mathematics, 4((1)), pp. 29-41.

Baughn, J. W., 1995, "Liquid-crystal methods for studying turbulent heat transfer," Butterworth-Heinemann.

Baughn, J. W., Anderson, M. R., Mayhew, J. E. and Wolf, J. D., 1999, "Hysteresis of thermochromic liquid crystal temperature measurement based on hue," ASME J. Heat Transfer, 121(4), pp. 1067-1072.

Bayley, F. J. and Owen, J. M., 1969, "Flow between a rotating and a stationary disc," Aeronautical Quaterly, 20 pp. 333-354.

Bayley, F. J. and Owen, J. M., 1970, "Fluid dynamics of a shrouded disk system with a radial outflow of coolant," ASME J. Eng. Power, 92(3), pp. 335-341.

Bohn, D. E., Johann, E. and Kruger, U., 1995, "Experimental and numerical investigations of aerodynamic aspects of hot gas ingestion in rotor-stator systems with superimposed cooling mass flow," ASME Paper 95-GT-143.

Bohn, D. E., Rudzinski, B., Surken, N. and Gartner, W., 1999, "Influence of rim seal geometry on hot gas ingestion into the upstream cavity of an axial turbine stage," ASME Paper 99-GT-248.

Bohn, D. E., Decker, A., Hongwei, M. and Wolff, M., 2003, "Influence of sealing air mass flow on the velocity distribution in and inside the rim seal of the upstream cavity of a 1.5-stage turbine " ASME Paper GT2003-38459.

Bohn, D. E. and Wolff, M., 2003, "Improved formulation to determine minimum sealing flow - Cw, min – for different sealing configurations," ASME Paper GT2003-38465.

Boutarfa, R. and Harmand, S., 2005, "Local convective heat transfer for laminar and turbulent flow in a rotor-stator system," Exp. Fluids, 38(2), pp. 209-221.

Bunker, R. S., Metzger, D. E. and Wittig, S., 1992a, "Local heat transfer in turbine disk cavities: Part I- rotor and stator cooling with hub injection of coolant," ASME J. Turbomach., 114(1), pp. 211-220.

Bunker, R. S., Metzger, D. E. and Wittig, S., 1992b, "Local heat transfer in turbine disk cavities: Part II- rotor cooling with radial location injection of coolant," ASME J. Turbomach., 114(1), pp. 221-228.

Camci, C., Kim, K., Hippensteele, S. A. and Poinsatte, P. E., 1993, "Evaluation of a hue capturing based transient liquid-crystal method for high-resolution mapping of convective heat-transfer on curved surfaces," ASME J. Heat Transfer, 115(2), pp. 311-318.

Camci, C., Glezer, B., Owen, J. M., Pilbrow, R. G. and Syson, B. J., 1998, "Application of thermochromic liquid crystal to rotating surfaces," ASME J. Turbomach., 120(1), pp. 100-103.

Campbell, D. A., 1978, "Gas turbine disc sealing system design," AGARD-CP-237.

Cardone, G., Astarita, T. and Carlomagno, G. M., 1997, "Heat transfer measurements on a rotating disk," Int. J. Rotating Machinery, 3(1), pp. 1-9.

Carlomagno, G. and Cardone, G., 2010, "Infrared thermography for convective heat transfer measurements," Exp. Fluids, 49(6), pp. 1187-1218.

Carlomagno, G. M., Cardone, G., Meola, C. and Astarita, T., 1998, "Infrared thermography as a tool for thermal surface flow visualization," J. Visualization, 1(1), pp. 37-50.

Chen, J.-X., Gan, X. and Owen, J. M., 1996, "Heat transfer in an air-cooled rotor-stator system," ASME J. Turbomach., 118(3), pp. 444-451.

Chew, J. W., Dadkhah, S. and Turner, A. B., 1992, "Rim sealing of rotor-stator wheelspaces in the absense of external flow," ASME J. Turbomach., 114(2), pp. 433-438.

Chew, J. W., Green, T. and Turner, A. B., 1994, "Rim sealing of rotor-stator wheelspaces in the presence of external flow," ASME Paper 94-GT-126.

Childs, P. R. N., 2011, *Rotating flow*, Oxford: Butterworth-Heinemann.

Coleman, H. W. and Steele, W. G., 1999, *Experimentation and uncertainty analysis for engineers*, 2nd ed. New York: Wiley.

Cumpsty, N., 2003, *Jet propulsion*, 2nd ed. Cambridge: Cambridge University Press.

Dadkhah, S., Turner, A. B. and Chew, J. W., 1992, "Performance of radial clearance rim seals in upstream and downstream rotor-stator wheelspaces," ASME J. Turbomach., 114(2), pp. 439-445.

Daily, J. W. and Nece, R. E., 1960, "Chamber dimension effects on induced flow and frictional resistance of enclosed rotating disks," Journal of Basic Engineering, 82(1), pp. 217-230.

Daily, J. W., Ernst, W. D. and Asbedian, V. V., 1964, "Enclosed rotating disks with superposed throughflow," MIT Hydrodynamics Lab. Rep. 64.

Diakunchak, I., Kiesow, H. J. and McQuiggan, G., 2008, "The history of the Siemens gas turbine," ASME Paper GT2008-50507.

Eckert, E. R. G., Sakamoto, H. and Simon, T. W., 2001, "The heat/mass transfer analogy factor, Nu/Sh, for boundary layers on turbine blade profiles," Int. J. Heat Mass Transfer, 44(6), pp. 1223-1233.

Farina, D. J., Hacker, J. M., Moffat, R. J. and Eaton, J. K., 1994, "Illuminant invariant calibration of thermochromic liquid crystals," Exp. Therm. Fluid. Sci., 9(1), pp. 1-12.

Gillespie, D. R. H., Wang, Z., Ireland, P. T. and Kohler, S. T., 1998, "Full surface local heat transfer coefficient measurements in a model of an integrally cast impingement cooling geometry," ASME J. Turbomach., 120(1), pp. 92-99.

Graber, D. J., Daniels, W. A. and Johnson, B. V., 1987, "Disc pumping test, final report," Air Force Wright Aeronautical Laboratories, Report No. AFWAL-TR-87-2050.

Green, T. and Turner, A. B., 1994, "Ingestion into the upstream wheelspace of an axial turbine stage," ASME J. Turbomach., 116(2), pp. 327-332.

Hallcrest, 1991, *Handbook of thermochromic liquid crystal technology*, Glenview: Hallcrest.

Hamabe, K. and Ishida, K., 1992, "Rim seal experiments and analysis of a rotor-stator system with nonaxisymmetric main flow," ASME Paper 92-GT-160.

Han, J. C., Dutta, S. and Ekkad, S., 2000, *Gas turbine heat transfer and cooling technology*, New York: Taylor & Francis.

Hay, J. L. and Hollingsworth, D. K., 1998, "Calibration of micro-encapsulated liquid crystals using hue angle and a dimensionless temperature," Exp. Therm. Fluid. Sci., 18(3), pp. 251-257.

Holman, J. P., 1990, *Heat transfer*, 7th ed. New York: McGraw-Hill.

Hong, K. and Song, T. H., 2007, "Development of optical naphthalene sublimation method," Int. J. Heat Mass Transfer, 50(19-20), pp. 3890-3898.

Hunt, R. J., 2011, "The history of the industrial gas turbine: Part 1- the first fifty years 1940-1990," IDGTE Paper 582.

Ireland, P. T., Gillespie, D. R. H. and Wang, Z., 1996, "Heater element," European Patent No. 0847679 B1.

Ireland, P. T. and Jones, T. V., 2000, "Liquid crystal measurements of heat transfer and surface shear stress," Meas. Sci. Technol., 11(7), pp. 969-986.

Johnson, B. V., Jakoby, R., Bohn, D. E. and Cunat, D., 2006, "A method for estimating the influence of time-dependent vane and blade pressure fields on turbine rim seal ingestion " ASME Paper GT2006-90853.

Johnson, B. V., Wang, C. Z. and Roy, R. P., 2008, "A rim seal orifice model with two cd's and effects of swirl in seals.," ASME Paper GT2008-50650.

Kakade, V. U., Lock, G. D., Wilson, M., Owen, J. M. and Mayhew, J. E., 2009a, "Accurate heat transfer measurements using thermochromic liquid crystal. Part 1: Calibration and characteristics of crystals," Int. J. Heat Fluid Flow, 30(5), pp. 939-949.

Kakade, V. U., Lock, G. D., Wilson, M., Owen, J. M. and Mayhew, J. E., 2009b, "Accurate heat transfer measurements using thermochromic liquid crystal. Part 2: Application to a rotating disc," Int. J. Heat Fluid Flow, 30(5), pp. 950-959.

Kakade, V. U., 2009, "Fluid dynamic and heat transfer measurements in gas turbine pre-swirl cooling systems," University of Bath, PhD.

Karabay, H., Wilson, M. and Owen, J. M., 2001, "Predictions of effect of swirl on flow and heat transfer in a rotating cavity," Int. J. Heat Fluid Flow, 22(2), pp. 143-155.

Kasagi, N., Moffat, R. J. and Hirata, M., 1989, *Liquid crystals*, In: Handbook of Flow Visualization (Ed. Yang, W.J). New York: Hemisphere.

Khilnani, V. I. and Bhavnani, S. H., 2001, "Sealing of gas turbine disk cavities operating in the presence of mainstream external flow," Exp. Therm. Fluid. Sci., 25(3-4), pp. 163-173.

Kingsley-Rowe, J. R., Lock, G. D. and Owen, J. M., 2005, "Transient heat transfer measurements using thermochromic liquid crystal: Lateral-conduction error," Int. J. Heat Fluid Flow, 26(2), pp. 256-263.

Kodzwa, P. M. and Eaton, J. K., 2007, "Angular effects on thermochromic liquid crystal thermography," Exp. Fluids, 43(6), pp. 929-937.

Ling, J. P. C. W., Ireland, P. T. and Turner, L., 2004, "A technique for processing transient heat transfer, liquid crystal experiments in the presence of lateral conduction," ASME J. Turbomach., 126(2), pp. 247-258.

Lock, G. D., Yan, Y., Newton, P. J., Wilson, M. and Owen, J. M., 2005, "Heat transfer measurements using liquid crystals in a preswirl rotating-disk system," ASME J. Eng. Gas Turb. Power, 127(2), pp. 375-382.

Lock, G. D., 2007, "Aicraft propulsion," Univeristy of Bath Lecture Notes, Course: ME30218

Meher-Homji, C. B., 1998, "The development of the Whittle turbojet," ASME J. Eng. Gas Turb. Power, 120(2), pp. 249-256.

Meher-Homji, C. B. and Prisell, E., 2000, "Pioneering turbojet developments of Dr. Hans von Ohain---from the HeS 1 to the HeS 011," ASME J. Eng. Gas Turb. Power, 122(2), pp. 191-201.

Metzger, D. E., Bunker, R. S. and Bosch, G., 1991, "Transient liquid crystal measurement of local heat transfer on a rotating disk with jet impingement," ASME J. Turbomach., 113(1), pp. 52-59.

Moffat, R. J., 1990, "Some experimental methods for heat transfer studies," Exp. Therm. Fluid. Sci., 3(1), pp. 14-32.

Moffat, R. J. and Kim, J., 2005, *Temperature and heat transfer measurements*, In: The CRC Handbook Of Mechanical Engineering (Eds. Kreith, F. and Goswami, D.Yogi), 2nd ed. Boca Raton: CRC Press.

Newton, P. J., Yan, Y. Y., Stevens, N. E., Evatt, S. T., Lock, G. D. and Owen, J. M., 2003, "Transient heat transfer measurements using thermochromic liquid crystal. Part 1: An improved technique," Int. J. Heat Fluid Flow, 24(1), pp. 14-22.

Owen, J. M. and Rogers, R. H., 1989, *Flow and heat transfer in rotating-disc systems. Volume 1: Rotor-stator systems*, Taunton: Research Studies Press Ltd.

Owen, J. M., Newton, P. J. and Lock, G. D., 2003, "Transient heat transfer measurements using thermochromic liquid crystal. Part 2: Experimental uncertainties," Int. J. Heat Fluid Flow, 24(1), pp. 23-28.

Owen, J. M., 2011a, "Prediction of ingestion through turbine rim seals. Part I: Rotationally induced ingress," ASME J. Turbomach., 133(3), pp. 031005.

Owen, J. M., 2011b, "Prediction of ingestion through turbine rim seals. Part II: Externally induced and combined ingress," ASME J. Turbomach., 133(3), pp. 031006.

Phadke, U. P. and Owen, J. M., 1982, "An investigation of ingress for a simple shrouded rotating disk system with a radial outflow of coolant," ASME Paper 80-GT-49.

Phadke, U. P. and Owen, J. M., 1983, "An investigation of ingress for an air-cooled shrouded rotating-disk system with radial clearance seals," ASME J. Eng. Power, 105(1), pp. 178-183.

Phadke, U. P. and Owen, J. M., 1988a, "Aerodynamic aspects of the sealing of gas-turbine rotor-stator systems. Part 1: The behavior of simple shrouded rotating disk systems in a quiescent environment," Int. J. Heat Fluid Flow, 9(2), pp. 98-105.

Phadke, U. P. and Owen, J. M., 1988b, "Aerodynamic aspects of the sealing of gas-turbine rotor-stator systems. Part 2: The performance of seals in a quasiaxisymmetric external flow " Int. J. Heat Fluid Flow, 9(2), pp. 106-112.

Phadke, U. P. and Owen, J. M., 1988c, "Aerodynamic aspects of the sealing of gas-turbine rotor-stator systems. Part 3: The effect of nonaxisymmetric external flow on seal performance " Int. J. Heat Fluid Flow, 9(2), pp. 113-117.

Pountney, O. J., Sangan, C. M., Lock, G. D. and Owen, J. M., 2012a, "Effect of ingestion on temperature of turbine discs," ASME Paper GT2012-68496, to appear in ASME J. Turbomach.

Pountney, O. J., Cho, G., Lock, G. D. and Owen, J. M., 2012b, "Solutions of Fourier's equation appropriate for experiments using thermochromic liquid crystal," Int. J. Heat Mass Transfer, 55(21-22), pp. 5908-5915.

Reiss, H. and Bolcs, A., 2000, "Experimental study of showerhead cooling on a cylinder comparing several configurations using cylindrical and shaped holes," ASME J. Turbomach., 122(1), pp. 161-169.

Rolls-Royce, 1996, *The jet engine*, 5th ed. Derby: Rolls-Royce plc.

Roy, R. P., Xu, G. and Feng, J., 2001, "A study of convective heat transfer in a model rotor-stator disk cavity," ASME J. Turbomach., 123(3), pp. 621-632.

Sabatino, D. R., Praisner, T. J. and Smith, C. R., 2000, "A high-accuracy calibration technique for thermochromic liquid crystal temperature measurements," Exp. Fluids, 28(6), pp. 497-505.

Sangan, C. M., 2011, "Measurement of ingress through gas turbine rim seals," University of Bath, PhD.

Sangan, C. M., Pountney, O. J., Zhou, K., Wilson, M., Owen, J. M. and Lock, G. D., 2011a, "Experimental measurement of ingestion through turbine rim seals. Part 1: Externally-induced ingress," ASME Paper GT2011-45310, to appear in ASME J. Turbomach.

Sangan, C. M., Pountney, O. J., Zhou, K., Wilson, M., Owen, J. M. and Lock, G. D., 2011b, "Experimental measurements of ingestion through turbine rim seals. Part 2: Rotationally-induced ingress," ASME Paper GT2011-45313, to appear in ASME J. Turbomach.

Sangan, C. M., Pountney, O. J., Scobie, J. A., Wilson, M., Owen, J. M. and Lock, G. D., 2012, "Experimental measurements of ingestion through turbine rim seals. Part 3: Single and double seals," ASME Paper GT2012-68493, to appear in ASME J. Turbomach.

Saravanamuttoo, H. I. H., Rodgers, G. F. C., Cohen, H. and Straznicky, P. V., 2009, *Gas turbine theory*, 7th ed. London: Pearson Prentice Hall.

Schlichting, H., 1979, *Boundary-layer theory*, New York: McGraw-Hill.

Schultz, D. L. and Jones, T. V., 1973, "Heat transfer measurements in short duration hypersonic facilities," Agardograph No. 165.

Stewartson, K., 1953, "On the flow between two rotating coaxial discs," Proceedings of the Cambridge Philosophical Society, 49(1), pp. 333-341.

Syson, B. J., Pilbrow, R. G. and Owen, J. M., 1996, "Effect of rotation on temperature response of thermochromic liquid crystal," Int. J. Heat Fluid Flow, 17(5), pp. 491-499.

Teuber, R., Wilson, M., Lock, G. D., Owen, J. M., Li, Y. S. and Maltson, J. D., 2012, "Computational extrapolation of turbine sealing effectiveness from test rig to engine conditions," ASME Paper GT2012-68490.

Wagner, G., Schneider, E., von Wolfersdorf, J., Ott, P. and Weigand, B., 2007, "Method for analysis of showerhead film cooling experiments on highly curved surfaces," Exp. Therm. Fluid. Sci., 31(4), pp. 381-389.

Wang, C. Z., Johnson, B. V., Mathiyalagan, S. P., Glahn, J. A. and Cloud, D. F., 2012, "Rim seal ingestion in a turbine stage from 360-degree time-dependent numerical solutions," GT2012-68193.

Wang, Z., Ireland, P. T., Jones, T. V. and Davenport, R., 1996, "A color image processing system for transient liquid crystal heat transfer experiments," ASME J. Turbomach., 118(3), pp. 421-427.

Wiberg, R. and Lior, N., 2004, "Errors in thermochromic liquid crystal thermometry," Rev. Sci. Instrum., 75(9), pp. 2985-2994.

Yan, Y. Y. and Owen, J. M., 2002, "Uncertainties in transient heat transfer measurements with liquid crystal," Int. J. Heat Fluid Flow, 23(1), pp. 29-35.

Zhou, K., Wilson, M., Owen, J. M. and Lock, G. D., 2011a, "Computation of ingestion through gas turbine rim seals," ASME Paper GT2011-45314.

Zhou, K., Wood, S. N. and Owen, J. M., 2011b, "Statistical and theoretical models of ingestion through turbine rim seals," ASME Paper GT2011-45139, to appear in ASME J. Turbomach.

Appendix A. Evaluation of the semi-infinite solution

This Appendix present solutions for the heat transfer coefficient, *h*, and the adiabatic wall-temperature, T_{ad}, for the semi-infinite solution to a step-change in fluid temperature for when T_{ad} is known and unknown.

A1. Evaluation of *h* from the semi-infinite solution when T_{ad} is known

In an experiment where the surface temperature, T_s, is measured at a specific time, *t*, and T_{ad} is known then Eq. 5.4 can be solved using the Newton-Raphson method. Equation 5.4 can be written in the form:

$$f(\chi) = \Theta_s - 1 + \exp(\chi^2)\,\mathrm{erfc}(\chi) = 0 \tag{A1}$$

where

$$\Theta_s = \frac{T_s - T_{in}}{T_{ad} - T_{in}} \tag{A2}$$

and

$$\chi = \frac{h\sqrt{t}}{\sqrt{\rho c_p K}} \tag{A3}$$

The iteration for χ can be expressed as:

$$\chi_{n+1} = \chi_n - \frac{f(\chi_n)}{f'(\chi_n)} \tag{A4}$$

where (from Eq. A1)

$$f'(\chi) = 2\exp(\chi^2)\left\{\chi\,\mathrm{erfc}(\chi) - \frac{1}{\sqrt{\pi}}\exp(-\chi^2)\right\} \tag{A5}$$

Provided that for $n = 1$ a reasonable value of χ is assumed then χ can be solved using Eq. A4. With the properties ρ, c_p and k known for the material then *h* can then be found from Eq. A3.

A2. Evaluation of *h* from the semi-infinite solution when T_{ad} is unknown

When T_{ad} is unknown it is common in experiments to measure the time taken for two thermochromic liquid crystals (applied to the surface of the substrate) to reach their pre-calibrated activation temperatures $T_{s,1}$ and $T_{s,2}$. It follows from Eq. 5.4 that:

$$\frac{\Theta_1}{\Theta_2} = \frac{1 - \exp(\chi_1{}^2)\,\mathrm{erfc}(\chi_1)}{1 - \exp(\chi_2{}^2)\,\mathrm{erfc}(\chi_2)} \tag{A6}$$

where from Eq. A2

$$\frac{\Theta_1}{\Theta_2} = \frac{T_{s,1} - T_{in}}{T_{s,2} - T_{in}} \tag{A7}$$

and from Eq. A3

$$\frac{\chi_1}{\chi_2} = \left(\frac{t_1}{t_2}\right)^{1/2} \tag{A8}$$

where t_1 and t_2 are the times taken for the surface of the solid to reach the activation temperatures of the TLCs, $T_{s,1}$ and $T_{s,2}$ respectively. As for the case where T_{ad} is known, when T_{ad} is unknown it is possible to use a Newton-Raphson iteration to find *h*. Equation A6 can be written as:

$$f(\chi_2) = \frac{\Theta_1}{\Theta_2} - \frac{f_1}{f_2} = 0 \tag{A9}$$

where

$$f_1 = 1 - \exp\left(\frac{t_1}{t_2}\chi_2{}^2\right)\mathrm{erfc}\left(\left(\frac{t_1}{t_2}\right)^{1/2}\chi_2\right) \tag{A10}$$

and

$$f_2 = 1 - \exp\left(\chi_2{}^2\right)\mathrm{erfc}\left(\chi_2\right) \tag{A11}$$

Although the non-dimensional surface temperatures, Θ_1 and Θ_2, are unknown, Θ_1 / Θ_2 can be calculated from $T_{s,1}$, $T_{s,2}$ and T_{in} as in Eq. A7 above.

Equation A4 can be rewritten as:

$$\chi_{2,n+1} = \chi_{2,n} - \frac{f(\chi_{2,n})}{f'(\chi_{2,n})} \tag{A12}$$

where

$$f'(\chi_{2,n}) = -\frac{f_2 f_1' - f_1 f_2'}{{f_2}^2} \tag{A13}$$

$$f_1' = 2\left\{\frac{1}{\sqrt{\pi}} - \frac{t_1}{t_2}\chi_2 \exp\left(\frac{t_1}{t_2}{\chi_2}^2\right)\operatorname{erfc}\left(\left(\frac{t_1}{t_2}\right)^{1/2}\chi_2\right)\right\} \tag{A14}$$

and

$$f_2' = 2\left\{\frac{1}{\sqrt{\pi}} - \chi_2 \exp\left({\chi_2}^2\right)\operatorname{erfc}\left(\chi_2\right)\right\} \tag{A15}$$

Having calculated χ_2, then T_{ad} can be calculated from:

$$\Theta_2 = \frac{T_{s,2} - T_{in}}{T_{ad} - T_{in}} = 1 - \exp({\chi_2}^2)\operatorname{erfc}(\chi_2) \tag{A16}$$

A3. Evaluation of h and T_{ad} for a composite substrate

Equation 7.34 can be written in the following form:

$$\lambda = f(Bi_A)g(\chi_1) - c = 0 \tag{A17}$$

where

$$f = \frac{{Bi_A}^{-1} + \eta}{\eta} \tag{A18}$$

and

$$g = 1 - \exp({\chi_1}^2)\operatorname{erfc}(\chi_1) \tag{A19}$$

The subscript 1 denotes the activation time of the first TLC, which should be selected so that it falls within the valid range of the semi-infinite solution. Equation A17 can be solved using a Newton-Raphson iteration:

$$Bi_{A,n+1} = Bi_{A,n} - \frac{\lambda_n}{\lambda'_n} \tag{A20}$$

where

$$\lambda' = \frac{d\lambda}{dBi_A} = g\frac{df}{dBi_A} + f\frac{dg}{d\chi_1}\frac{d\chi_1}{dBi_A} \tag{A21}$$

It can be shown that

$$\lambda' = \frac{1}{\eta Bi_A^{\,2}} \left\{ 2\chi_1 (1 + \eta Bi_A)[\pi^{-1/2} - \chi_1 (1 - g)] - g \right\} \tag{A22}$$

Bi_A (and thus h) can be found from Eqs. A20 and A22; T_{ad} can then be solved for using this value of Bi_A with Eq. 7.27.

Appendix B. Determination of experimental uncertainties

This Appendix presents the equations and assumptions used to estimate the uncertainties in the experimental measurements of the heat transfer coefficient, *h*, the Nusselt number, *Nu*, and the adiabatic effectiveness, ε_{ad}, presented in Chapter 6.

B1. Uncertainties in *h* and *Nu*

For the purpose of the analysis in this section, the uncertainty in the measured values of *h* and *Nu* were assumed to be equal. As discussed in Chapter 5 of this thesis, Yan and Owen (2002) defined an amplification parameter, Φ_h, which related the uncertainty in *h* to the uncertainty in the measured values of the non-dimensional surface temperatures, Θ_1 and Θ_2, obtained from two TLC measurements using the analysis presented in Appendix A2. The following equation was presented by the authors:

$$\frac{P_h}{h} = \Phi_h \frac{P_T}{T_{ad} - T_{in}} \tag{B1}$$

where P_h is the 95% uncertainty in the calculated value of *h* and P_T is the 95% uncertainty in the measured temperatures. For the experiments presented in Chapter 6, P_T was taken to be 0.2 C (from the calibrations of the thermocouples) and $T_{ad} \approx T_0$. Equation 5.23 was used to evaluate P_h from Θ_1 and Θ_2. For example, if $\Theta_1 = 0.382$, $\Theta_2 = 0.702$, $h = 56.9$ W/m^{2}K and $T_0 - T_{in} = 34$ C, then $\Phi_h = 9.61$ and hence $P_h/h = 0.057$.

Three different TLC were used in the experiments to obtain three values of Θ_s; it was thus possible to analyse *h* and T_{ad} from three pairs of Θ_1 and Θ_2. An improved estimate of *h*, referred to here as $\hat{h}$, was obtained by weighting the individual *h* values, h_i, by the inverse of their variance, $P_{h,i}^{-2}$, using the following relationship (S.N. Wood, *pers. comm*, 2011):

$$\hat{h} = \frac{\sum_i P_{h,i}^{-2} h_i}{\sum_i P_{h,i}^{-2}} \tag{B2}$$

The 95% uncertainty, $\hat{P}_h$, of the improved estimate was then calculated from:

$$\hat{P}_h = \sqrt{\frac{1}{\sum_i P_{h,i}^{-2}}} \tag{B3}$$

B2. Uncertainties in adiabatic effectiveness

The adiabatic effectiveness, ε_{ad}, was defined in Eq. 6.9 as:

$$\varepsilon_{ad} = \frac{T_{ad} - T_a}{T_{ad}^* - T_a} \tag{B4}$$

where T_{ad} is the adiabatic surface temperature (obtained from the TLC isotherms with the semi-infinite step change solution—see Appendix A) when ingress occurs, T_{ad}^* is the value of T_{ad} when there is no ingress and T_a is the total temperature of the air in the annulus as measured by the fast response thermocouple located upstream of the nozzle guide vanes. T_a is equivalent to T_{ad} when there is no sealant flow (i.e. $\varepsilon_{ad} = 0$).

If δ_ε, δ_{ad}, δ_{ad}^* and δ_a are the uncertainties in ε_{ad}, T_{ad}, T_{ad}^* and T_a respectively then Eq. B4 can be rewritten as:

$$\varepsilon_{ad} \pm \delta_\varepsilon = \frac{T_{ad} \pm \delta_{ad} - (T_a \pm \delta_a)}{T_{ad}^* \pm \delta_{ad}^* - (T_a \pm \delta_a)} = \varepsilon_{ad} \left\{ \frac{1 + (\pm\delta_{ad} \pm \delta_a)/(T_{ad} - T_a)}{1 + (\pm\delta_{ad}^* \pm \delta_a)/(T_{ad}^* - T_a)} \right\} \tag{B5}$$

If it is assumed that $|(\pm \delta_{ad}^* \pm \delta_a)/(T_{ad}^* - T_a)| << 1$ then:

$$\varepsilon_{ad} + |\delta_\varepsilon| \le \varepsilon_{ad} \left\{ 1 + \frac{|\delta_{ad}| + |\delta_a|}{T_{ad} - T_a} + \frac{|\delta_{ad}^*| + |\delta_a|}{T_{ad}^* - T_a} \right\} \tag{B6}$$

which can be expressed as

$$\frac{|\delta_\varepsilon|}{\varepsilon_{ad}} \le \left\{ \frac{|\delta_{ad}| + |\delta_a|}{T_{ad} - T_a} + \frac{|\delta_{ad}^*| + |\delta_a|}{T_{ad}^* - T_a} \right\} \tag{B7}$$

Owing to the amplification factors arising from the use of the step-change solution to Fourier's one-dimensional equation for a semi-infinite solid (see section 5.4.2), the uncertainty in T_{ad} and T_{ad}^* was typically an order of magnitude higher than the uncertainty in T_a. If it is assumed that $\delta_{ad} = \delta_{ad}^* = \delta$ and $\delta_a << \delta$, then Eq. B7 becomes:

$$\frac{|\delta_\varepsilon|}{\varepsilon_{ad}} \le \delta \left\{ \frac{1}{T_{ad} - T_a} + \frac{1}{T_{ad}^* - T_a} \right\} \tag{B8}$$

which simplifies to

$$|\delta_\varepsilon| \le \frac{\delta}{T_{ad}^* - T_a} (1 + \varepsilon_{ad}) \le \frac{2\delta}{T_{ad}^* - T_a} \tag{B9}$$

In the experiments, T_{ad}* - $T_a \approx T_o$ - T_a (as the frictional heating component was small) and δ was assumed to equal P_{Tad} the 95% uncertainty in T_{ad} calculated from Yan and Owen (2002) using the following equation:

$$\frac{P_{Tad}}{T_{ad} - T_{in}} = \Phi_{Tad} \frac{P_T}{T_{ad} - T_{in}} \tag{B10}$$

where Φ_{Tad} is the amplification parameter for T_{ad}. As an example (from the experimental measurements made in Chapter 6), if Θ_1 = 0.382, Θ_2 = 0.702, h= 56.9 W/m^{2}K, T_0 - T_{in} = 34 C, and P_T = 0.2 C then, from Eq. 5.27, Φ_{ad} = 3.96 and $\delta = P_{Tad}$ = 0.79 C. Improved estimates of adiabatic effectiveness, $\hat{\varepsilon}_{ad}$, and its uncertainty, $\hat{\delta}_{\varepsilon}$, were calculated using the weighed variance method as described above for h.

B3. Uncertainties in *K*

The 95% uncertainty limit in $\overline{K}$ (the mean value of the thermal buffer ratio constant given in Eq. 6.19) was calculated from the theory of Coleman and Steele (1999) for 'confidence intervals in sample populations' using:

$$P_{\overline{K}} = t \frac{\sigma_K}{\sqrt{N}} \tag{B11}$$

where t is the t-value related to the 95% uncertainty limit, σ_K is the standard deviation of the sample and N is the sample size. For N = 20 (the number of data points presented in Section 6.3.4) t = 2.09 from the Coleman and Steele t-value tables.

Appendix C. Properties of some relevant materials

This Appendix presents a table of the properties of the materials relevant to the discussion in Chapter 7.

Materials	k **(W/mK)**	ρ **(kg/m^3)**	c_p **(J/kg K)**	α **(m^2/s) × 10^7**	$\rho c_p k$ **(J^{2}m^{-4}K^{-2}s^{-1})**
Acrylic	0.167	1190	1550	0.91	3.08×10^5
Polycarbonate	0.2	1200	1250	1.33	3.00×10^5
Rohacell 71	0.03	75	1225	3.25	2.76×10^3

Table B1: Properties of some relevant materials

Appendix D. Co-authored journal papers

This Appendix presents the following three journal papers (on all which the author of this thesis was a co-author and significant contributor):

1. Sangan, C. M., **Pountney, O. J.**, Zhou, K., Wilson, M., Owen, J. M. and Lock, G. D., 2011, "Experimental measurement of ingestion through turbine rim seals. Part 1: Externally-induced ingress," ASME Paper GT2011-45310, to appear in ASME J. Turbomach.
2. Sangan, C. M., **Pountney, O. J.**, Zhou, K., Wilson, M., Owen, J. M. and Lock, G. D., 2011, "Experimental measurements of ingestion through turbine rim seals. Part 2: Rotationally-induced ingress," ASME Paper GT2011-45313, to appear in ASME J. Turbomach.
3. Sangan, C. M., **Pountney, O. J.**, Scobie, J. A., Wilson, M., Owen, J. M. and Lock, G. D., 2012, "Experimental measurements of ingestion through turbine rim seals. Part 3: Single and double seals," ASME Paper GT2012-68493, to appear in ASME J. Turbomach.